

---

# AQUINAS Documentation

---

Achilleas Filippidis and Adam Jan Sadowski

Imperial College London

Tuesday 18<sup>th</sup> April, 2023

# Contents

<b>1</b>	<b>Introduction</b>	<b>1</b>
1.1	Motivation . . . . .	1
1.2	Installation . . . . .	3
1.3	Using AQUINAS . . . . .	4
1.4	Developing AQUINAS . . . . .	5
<b>2</b>	<b>Shell finite element formulation</b>	<b>7</b>
2.1	Geometry . . . . .	7
2.2	Kinematic relations . . . . .	10
2.2.1	Linear strain-displacement relations . . . . .	11
2.2.2	Nonlinear strain-displacement relations . . . . .	12
2.3	Constitutive relations . . . . .	13
2.4	Finite Element Formulation . . . . .	15
2.5	Condensation of nodal variables . . . . .	19
2.6	Recovery of nodal variables . . . . .	22
<b>3</b>	<b>Software capabilities</b>	<b>24</b>
3.1	Geometric definitions . . . . .	24
3.1.1	Plate segment geometry . . . . .	24
3.1.2	Conical segment geometry . . . . .	25
3.1.3	Elliptical segment geometry . . . . .	26
3.1.4	Three-point arc segment geometry . . . . .	28
3.1.5	Interpolated segment geometry . . . . .	28
3.2	Analysis types . . . . .	30
3.3	Optimisation . . . . .	30
<b>4</b>	<b>Software architecture</b>	<b>36</b>
4.1	Flow of control in AQUINAS . . . . .	36
4.2	Class descriptions . . . . .	37
4.2.1	AQUINAS Material Object . . . . .	38
4.2.2	AQUINAS Segment Object . . . . .	39
4.2.3	AQUINAS Nodal Force Object . . . . .	42
4.2.4	AQUINAS Distributed Pressure Object . . . . .	43
4.2.5	AQUINAS Constraint Object . . . . .	44
4.2.6	AQUINAS DOF Tracker Object . . . . .	46
4.2.7	AQUINAS Output Mode Object . . . . .	47
4.2.8	AQUINAS Analysis Object . . . . .	48
4.2.9	AQUINAS Solver Object . . . . .	49
4.3	Procedure descriptions . . . . .	57

4.3.1	AQUINAS LA . . . . .	57
4.3.2	AQUINAS LBA . . . . .	58
4.3.3	AQUINAS GNA - MNA - GMNA . . . . .	58
<b>5</b>	<b>Example library</b>	<b>62</b>
5.1	LAs . . . . .	63
5.1.1	Example LA01: Thin cylinder under axial compression and internal pressure . . . . .	64
5.1.2	Example LA02: Thin cylinder with midsurface eccentricity under axial compression and internal pressure . . . . .	65
5.1.3	Example LA03: Multi-strake cylindrical silos with step-wise varying thickness under nonlinear loading . . . . .	67
5.1.4	Example LA04: Conical shell under axial uniform pressure . . . . .	70
5.1.5	Example LA05: Spherical shell segment with an outward radial edge load . . . . .	71
5.1.6	Example LA06: Spherical cap subjected to uniform vertical pressure	73
5.1.7	Example LA07: LA of a thin elliptical shell cap under uniform pressure	75
5.1.8	Example LA08: LA of a thin ogival shell under self weight pressure	77
5.1.9	Example LA09: LA of a thin hyperboloid under an axial edge load	78
5.1.10	Example LA10: LA of a thin multi-segment shell under normal pressure . . . . .	80
5.1.11	Example LA11: Thin circular plate with clamped edges under uniform pressure . . . . .	82
5.1.12	Example LA12 : LA of a thin toroid shell with uniform internal pressure . . . . .	84
5.2	LBAs . . . . .	86
5.2.1	Example LBA01: LBA of a thin cylindrical shell of varying length under uniform axial compression . . . . .	86
5.2.2	Example LBA02: LBA of a thin cylinder under axial compression and direct comparison with the Koiter circle . . . . .	88
5.2.3	Example LBA03: LBA of a thin cylindrical shell under uniform lateral pressure . . . . .	90
5.2.4	Example LBA04: Koiter ellipse for a thin truncated cone under uniform axial compression . . . . .	93
5.2.5	Example LBA05: Bifurcation modes of a thin spherical shell under uniform external pressure . . . . .	95
5.3	MNAs . . . . .	98
5.3.1	Example MNA01: MNA of a thin cylinder under uniform axial compression . . . . .	99
5.3.2	Example MNA02: MNA of a simply-supported circular plate under concentrated load . . . . .	100
5.3.3	Example MNA03: MNA of a clamped spherical caps under uniform external pressure . . . . .	102
5.4	GNAs . . . . .	103
5.4.1	Example GNA01: GNA of a thin cylindrical shell under uniform axial compression . . . . .	104
5.4.2	Example GNA02: GNA of the Belleville spring . . . . .	106

5.4.3	Example GNA03: GNA of a thin spherical cap under uniform external pressure . . . . .	107
5.4.4	Example GNA04: GNA of a ring-loaded thin spherical cap . . . . .	108
5.4.5	Example GNA05: Snap-through of a shallow spherical cap . . . . .	109
5.4.6	Example GNA06: Nonlinear buckling analysis of a clamped shallow spherical cap under uniform external pressure . . . . .	110
5.5	GNIAs . . . . .	111
5.5.1	Example GNIA01: GNIA of a thin unpressurised cylinder under uniform axial compression with a weld depression imperfection . . . . .	112
5.5.2	Example GNIA02: GNIA of a thin pressurised cylinder under uniform axial compression with a weld depression imperfection . . . . .	115
5.6	GMNAs . . . . .	117
5.6.1	Example GMNA01: Nominal capacity curve generation for cylinders of varying slenderness under uniform axial compression . . . . .	117
5.6.2	Example GMNA02: Elastic-plastic collapse load predictions for a pressurised cylinder under uniform axial compression . . . . .	120
5.7	GMNIAs . . . . .	122
5.8	Miscellaneous . . . . .	122
5.8.1	Example MISC01: Parallel scaling analysis . . . . .	122
	<b>Bibliography</b>	<b>123</b>

# Chapter 1

## Introduction

### 1.1 Motivation

Shells of revolution are well established and widely used structural systems, commonly encountered in agricultural and industrial engineering applications, serving as storage containers in the form of silos and tanks, as wind turbine or nuclear reactor towers in the energy sector, or as civilian structures where they take the shape of domes for aesthetically pleasing roofs of churches and public buildings. Axisymmetric shell problems thus correspond to important reference structural systems for many different fields of engineering design and continue to be the subject of research interest (e.g. see [35, 42, 57, 56]).

Historically, the very first step taken towards the better understanding of the structural behaviour of shells was examining the problem using the principle of static equilibrium. This simple approach neglects through-thickness bending action and assumes that loads are equilibrated through in-plane ‘membrane’ forces per unit length. Various membrane theory shell problems are explored by J. Heyman in *Equilibrium of shell structures* [23]. The accuracy of this theory depends on the fact that the inclusion of bending should have only a negligible effect on the complete stress state. While neglecting bending can be a reasonable assumption where the boundary conditions do not introduce compatibility effects (such as for a fully closed sphere or for a cylinder whose meridian is free to axially expand/shorten with no radial displacement restraints), their contribution quickly becomes very important for thicker or shorter shells wherever edge conditions induce compatibility bending. Equilibrium equations are now not enough to describe the mechanical behaviour of the shell due to the additional unknowns, and constitutive and kinematic relations have to be employed which add significant complexity. The problem of shell stress analysis now becomes even more mathematical in nature, necessitating the solution of coupled partial differential equations in terms of displacements rather than stress resultants. These differential equations become significantly simpler, but still not effortless to deal with, when studying the response of shells of revolution under circumferentially uniform loading and boundary conditions. The axisymmetric nature reduces the originally 3D problem into a 2D one, making the stress analysis of specific families of such shells, like cylinders or spherical caps, more feasible. Some notable summative works on the subject are those of S. Timoshenko and S. Woinowsky-Krieger [55], C.R. Calladine [12] and the rather more in depth investigation by W. Flügge [20], with the book’s scope balancing between the mechanical and mathematical nature of shell problems.

When the manufacturing material belongs in the family of structural metals such as

steel, the limit state of thin-walled shells is controlled primarily by buckling. It is laborious to study the buckling of axisymmetric shells undergoing buckling by direct solution of the differential equations, although a few successful investigations have been made on the subject, usually accompanied with some appropriate simplifications like a membrane pre-buckling stress state. The PhD thesis of W.T. Koiter [27] and the work of N. Yamaki [61] are seminal textbooks on the bifurcation behaviour of cylindrical shells, while a few endeavours have also been made to study the buckling response of complete spheres under external pressure [63] - [25]. All of the above analytical approaches to the axisymmetric shell buckling problem assume a harmonic distribution of the circumferential displacement field corresponding to the buckling modes.

Adopting an analytical approach becomes increasingly difficult for more generic axisymmetric shell problems where the pre-buckling structural response is not sufficiently well described by a membrane stress state because the effect of bending cannot be neglected, or for more intricate meridional geometries beyond those of a cylinder or a sphere. The effects of plasticity and geometric nonlinearities that occur as the shell deforms further complicate an already complex structural problem and prevent direct solution of the governing equations. The use of a circumferentially period harmonic distribution of the displacements corresponding to the bifurcation modes in their FE formulations allowed for the development of efficient specialised FE tools for the nonlinear analysis of axisymmetric shells undergoing buckling and beyond. A representative list of such specialised software known to have once been widely used in nonlinear elastic-plastic stability analysis of axisymmetric shells with a Fourier series representation of the unsymmetrical response in the circumferential dimension is as follows:

- The BOSOR (**B**ucking of **S**hells of **R**evolution) suite of advanced finite difference-based programs developed by D. Bushnell and his research group, widely used for computational shell buckling studies in the aerospace sector for many decades starting in the 1960s (e.g. see [11, 9, 10]). The source code appears to have been available for download until about 2021 from its Author's personal website ([www.shellbuckling.com](http://www.shellbuckling.com)), but is now no longer publicly obtainable or supported.
- The FELASH (**F**inite **E**lement **A**nalysis of **A**xisymmetric **S**hells) suite of advanced finite element-based programs developed by J.G. Teng and J.M. Rotter [50, 51] in the late 1980s, and in particular the NEPAS (**N**onlinear **E**lastic-**P**lastic **A**nalysis for **B**ifurcation **S**tability) component that was primarily used in civil engineering shells research (e.g. see [37, 54]). It does not appear to be publicly available.
- The INCA software developed by A. Combescure in the 1980s, used for stability analyses of cooling towers for the nuclear industry until the 2000s (e.g. see [5, 15, 22]). It, too, does not appear to be publicly available.

There are doubtless many others that were developed by individual researchers for internal use, never having been intended for public release. The reader may note that the use of custom-written research-oriented specialised finite element software appears to have largely waned in the past 20 years in structural mechanics research. This appears to correspond to the widespread adoption of powerful commercial and ‘general’ FE software packages such as ABAQUS [1] or ANSYS [4], which benefit from a steady licensing income stream, active development and extensive validation. In the present context, however, while these ‘general’ FE packages do offer axisymmetric shell elements as part of their

finite element library (e.g. SAX1 or SAX2 in ABAQUS, and SHELL208 or SHELL209 in ANSYS), these elements are typically not enhanced with the ability to represent arbitrary unsymmetrical deformation modes through the use of a circumferential Fourier series expansion. ABAQUS additionally offers the SAXA1 $n$  or SAXA2 $n$  axisymmetric shell elements which support circumferentially asymmetric loading and deformation in the form of a circumferential Fourier harmonic  $n$ , but only up to  $n = 4$ . Similarly, ANSYS offers the SHELL61 ‘harmonic’ axisymmetric shell element supporting loading and deformation into arbitrary  $n$ , but only for linear elastic stress analyses.

The reader is invited to see a fuller discussion of the background to the above given in Sadowski et al. [42]. This source includes a workaround implemented in ABAQUS to allow the detection of the critical unsymmetrical bifurcation buckling mode on the basis of the so-called ‘panel analysis’ technique, where conditions of circumferential symmetry are applied to a 3D shell panel that is designed to have an angular spread commensurate with a target circumferential mode into which buckling is being triggered. Yet this workaround is only partially successful at countering the fundamental limitation of having to use a 3D modelling space for axisymmetric shell systems, namely that the need for an explicit discretisation of the circumferential dimension is parasitic and detrimental to the quality of the analysis, and its application is tedious to the extreme.

The accurate and efficient buckling analysis of natively axisymmetric shells thus constitutes a challenging task for the structural analyst. The circumferentially uniform pre-buckling stress state theoretically offers an infinite number of possible locations for an asymmetric buckle, an uncomfortable prospect for classical computers working on finite precision. Aiming to answer the need for a computational tool able to handle the problem of shell buckling with a uniform pre-buckling stress state, the Authors hereby introduce and release AQUINAS, a custom-written FE MATLAB toolbox inspired from a past era of shell research for the bifurcation analysis of nonlinear axisymmetric shell problems. In doing so, they hope to rekindle awareness of this very particular treatment of the buckling of axisymmetric shells systems, which even today occupies a special niche among the mighty ‘general’ FE software and widely-accessible computational power.

While the main motivation for the development of AQUINAS has been the accurate detection of the critical circumferential mode number together with the associated load level, the software Git repository (see below) comes with a library of more than 30 validation examples at the time of release (April 2023) where comparisons are made with numerous well-established literature resources on the topic of shell buckling. This library is in itself an important resource that may be used for the verification and validation of models of thin-walled shells created by other FE software, as is now required by prEN 1993-1-6 [14] and prEN 1993-1-14 [13] for structural steel design assisted by FE, and more examples will be added periodically.

## 1.2 Installation

Setting up AQUINAS for the analysis of an axisymmetric shell problem is very straightforward. The AQUINAS toolbox has been developed and tested in the MATLAB 2022a [30] programming environment, which is the only requirement for the usage of the AQUINAS. Unfortunately, it may not be backwards compatible with previous MATLAB versions as some of the new programming features introduced in recent releases of the coding environment (such as the input validation functions) have been used during development of

the software. The toolbox has been tested to run on Windows, Mac and Linux distributions with MATLAB 2022a installed.

To obtain AQUINAS the user may either pull a ‘clone’ from the online Github repository or download a .zip file of the code, containing both the source code and the manual of the software. The online address of AQUINAS repository, as well as all of the software metadata are presented in Table 1.1, where the development requirements are only relevant if the user is interested in altering any of the internal workings of the toolbox.

Nr.	Metadata description	Metadata value
S1	Current software version	0.10.0
S2	Permanent link to executables of this version	<a href="https://github.com/AchilleasF/AQUINAS-FE">https://github.com/AchilleasF/AQUINAS-FE</a>
S3	Legal Software License	BSD 3-Clause License
S4	Operating Systems	Microsoft Windows, Linux, MacOS
S5	Dependencies	MATLAB R2022a or later
S6	Link to user manual	<a href="https://github.com/AchilleasF/AQUINAS-FE">https://github.com/AchilleasF/AQUINAS-FE</a>
S7	Support email for questions	a.filippidis@imperial.ac.uk a.sadowski@imperial.ac.uk
S8	Development requirements	MinGW-w64 6.3 - Boost C++ libraries - (Maple 2022 or later)

Table 1.1: Executable software metadata

### 1.3 Using AQUINAS

AQUINAS is an open source MATLAB toolbox that permits efficient stress, small/large displacement theory plastic collapse and non-symmetric bifurcation buckling analyses of geometrically nonlinear elastic-plastic axisymmetric shells. The doubly-curved axisymmetric shell finite element formulation presented by J.G. Teng and J.M. Rotter [50, 51] was adopted for AQUINAS, with additional details sourced from Jumikis [26] and the Authors’ own derivations. This formulation was chosen in preference over others because it offers very complete strain-displacement relations, an independent definition of the meridional curvature of the shell and an established track record of successful use in scientific publications [50, 51, 26, 54, 37, 49, 35, 53, 52] for the purposes of software verification. Torsional or non-symmetric loading has not been implemented at present. Full details of the formulation may be found in the accompanying documentation, as well as in the source references.

The AQUINAS Git repository also contains an extensive library of over 30 example .m MATLAB ‘input’ files which are intended to illustrate usage on how to perform each one of the above specialised FE analyses on a selection of classical axisymmetric shells of revolution (cylinders, cones, spheres, ellipsoids, ogivals and more complex custom shapes), while acting as a comprehensive record of verification and validation of the various capabilities of AQUINAS against algebraic predictions from classical shell membrane and / or bending theory (where available), ABAQUS simulations (where appropriate) and physical experiments (where possible). This library is a valuable resource in and of itself

as it may also aid in the validation of other FE software and it's capabilities to solve axisymmetric shell problems.

## 1.4 Developing AQUINAS

The open source nature of the AQUINAS toolbox allows its users to examine or even change different parts of the analysis procedure. Assembly of the finite element system is accelerated through the use of compiled C++ code via the MEX functionality (the release includes standard Windows .`mexw64` and Linux .`mexa64` 64-bit MATLAB executables) which invokes OpenMP threaded parallelism for additional performance. A native MATLAB-only serial execution is possible, but it is much slower. The modular and open source nature of AQUINAS makes the source code accessible to anyone who wishes to add specific functionality, though any changes made to the C++ accelerated matrix assembly will require re-compilation with a GCC 6.3 compiler or later (to support OpenMP 4.5 features such as array reductions), as can be seen from Table 1.1. The MinGW-w64 compiler can be easily installed through MATLAB's `Add-Ons` function from the `Home` tab of the programming UI. The Boost C++ libraries <https://www.boost.org/> need also be added to the path during compilation of the MEX files. The commented line in the beginning of every .`cpp` provides the command for the compilation of the C++ assembly files, where the path to the Boost libraries should be altered to reflect the actual path of these libraries in the user's personal computer.

The stiffness matrices are generated in AQUINAS by deriving the individual terms through a run of the Maple [29] worksheets, also included in the Git repository. While the files containing the stiffness terms may be manually modified through any text editor, either for the MATLAB or C++ version of the assembly, they may be also be generated by altering and running the corresponding Maple worksheets provided that the (proprietary) Maple mathematical programming environment is available to the user.

The Authors of the current document aim for AQUINAS to be an actively updated and maintained toolbox for the analysis of nonlinear axisymmetric shell problems with a uniform pre-buckling stress state. To this end, the reader who would like to report a bug in the software, as a question or contribute in any way is encouraged to contact the Authors at `a.filippidis@imperial.ac.uk`.

## Acknowledgements

The Authors wish to extend their gratitude to Professor Bassam Izzuddin of their Department for his help and support in the development of AQUINAS. The useful recommendations of Paris Stylianidis on the software engineering part of the process are also appreciated.

This research was made possible thanks to a Skempton scholarship, kindly awarded by the Department of Civil and Environmental Engineering of Imperial College London.

## License

BSD 3-Clause License

Copyright (c) 2023, Mr Achilleas Filippidis and Dr Adam Jan Sadowski of Imperial College London. All rights reserved.

Redistribution and use in source and binary forms, with or without modification, are permitted provided that the following conditions are met:

1. Redistributions of source code must retain the above copyright notice, this list of conditions and the following disclaimer.
2. Redistributions in binary form must reproduce the above copyright notice, this list of conditions and the following disclaimer in the documentation and/or other materials provided with the distribution.
3. Neither the name of the copyright holder, nor of Imperial College, nor the names of its contributors may be used to endorse or promote products derived from this software without specific prior written permission.

THIS SOFTWARE IS PROVIDED BY THE COPYRIGHT HOLDERS AND CONTRIBUTORS "AS IS" AND ANY EXPRESS OR IMPLIED WARRANTIES, INCLUDING, BUT NOT LIMITED TO, THE IMPLIED WARRANTIES OF MERCHANTABILITY AND FITNESS FOR A PARTICULAR PURPOSE ARE DISCLAIMED. IN NO EVENT SHALL THE COPYRIGHT HOLDER OR CONTRIBUTORS BE LIABLE FOR ANY DIRECT, INDIRECT, INCIDENTAL, SPECIAL, EXEMPLARY, OR CONSEQUENTIAL DAMAGES (INCLUDING, BUT NOT LIMITED TO, PROCUREMENT OF SUBSTITUTE GOODS OR SERVICES; LOSS OF USE, DATA, OR PROFITS; OR BUSINESS INTERRUPTION) HOWEVER CAUSED AND ON ANY THEORY OF LIABILITY, WHETHER IN CONTRACT, STRICT LIABILITY, OR TORT (INCLUDING NEGLIGENCE OR OTHERWISE) ARISING IN ANY WAY OUT OF THE USE OF THIS SOFTWARE, EVEN IF ADVISED OF THE POSSIBILITY OF SUCH DAMAGE.

THE USE OF THE MATLAB LANGUAGE DOES NOT IMPLY ENDORSEMENT BY MATHWORKS.

# Chapter 2

## Shell finite element formulation

The thin shell finite element formulation adopted for AQUINAS is presented in the original article by J.G. Teng and J.M. Rotter ‘*Elastic-plastic large deflection analysis of axisymmetric shells*’ [50]. The reader may find that the contents of this chapter are similar to those of the publication which this work is based upon. Nevertheless, the necessary definitions for the thin axisymmetric finite element shell formulation are presented here for completeness of the current work, with additional comments to elaborate on the details of the more complex steps where necessary. An attempt to adopt the European standard’s prEN 1993-1-6 [14] notation is made throughout AQUINAS, over any other nomenclature used in relevant literature, including the shell finite element publication [50].

### 2.1 Geometry

The axisymmetric shell’s geometry is defined in a cylindrical coordinate system by the radial and axial coordinates  $r$  and  $z$  as well as the meridional slope  $d\phi/ds$ . The geometry of the shell’s meridian is presented in Figure 2.1 below.

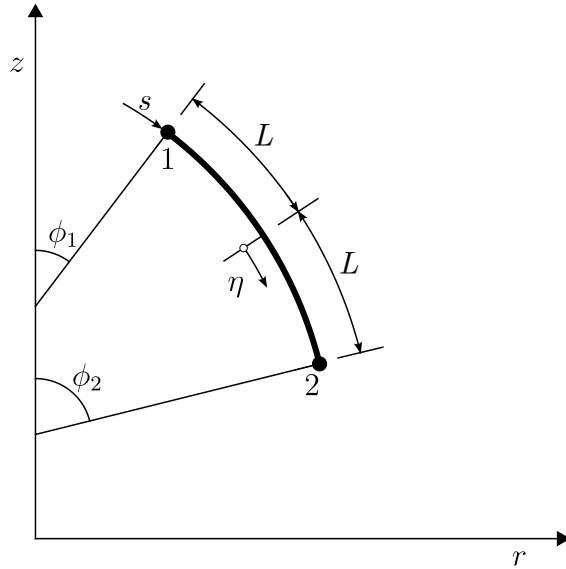


Figure 2.1: Meridional geometry of a curved shell finite element

The nodal values of these geometric properties are then used to interpolate and compute the geometry along the element using Hermitian cubic functions as follows:

$$r = \sum_{i=1,2} N_{0i} r_i + N_{1i} \left( \frac{dr}{ds} \right)_i \quad (2.1a)$$

$$z = \sum_{i=1,2} N_{0i} z_i + N_{1i} \left( \frac{dz}{ds} \right)_i \quad (2.1b)$$

$$\left( \frac{d\phi}{ds} \right) = \sum_{i=1,2} N_{0i} \left( \frac{d\phi}{ds} \right)_i + N_{1i} \left( \frac{d^2\phi}{ds^2} \right)_i \quad (2.1c)$$

The element shape functions  $N_{0i}$  and  $N_{1i}$  for obtaining the interpolated geometric properties within an element are given as

$$N_{01} = \frac{1}{4}(2 - 3\eta + \eta^3) \quad (2.2a)$$

$$N_{11} = \frac{L}{4}(1 - \eta - \eta^2 + \eta^3) \quad (2.2b)$$

$$N_{02} = \frac{1}{4}(2 + 3\eta - \eta^3) \quad (2.2c)$$

$$N_{12} = \frac{L}{4}(-1 - \eta + \eta^2 + \eta^3) \quad (2.2d)$$

where  $\eta$  is a dimensionless curvilinear meridional coordinate defined in terms of the curvilinear meridional coordinate  $s$  and the element's half length  $L$  as

$$\eta = \frac{2s - s_1 - s_2}{2L} \quad (2.3)$$

with the half-length of the element's meridian given as

$$L = \frac{s_2 - s_1}{2} \quad (2.4)$$

A reader who looks into the original publication by J.G. Teng and J.M. Rotter [50] may notice that the element's half-length  $L$  is not included in the equations  $N_{11}$  and  $N_{12}$  there. However, one can appreciate that interpolating derivatives of variables requires the element's length in order to scale said derivatives to the element's size (see Eqs (2.1a)-(2.1c)). The same principle is also considered in the presentation of the element's shape functions by Jumikis P.T. in his PhD thesis [26], one of the researchers that worked on developing the FELASH suite and the axisymmetric shell finite element of [50].

While the curvature of the shell's meridian could be obtained through differentiation of the Cartesian coordinates in Eqs (2.1a) - (2.1b), the curvature here is defined as an independent variable in Eq. (2.1c). This over-complete meridional geometry definition allows for a stable and precise element, avoiding a consequent loss of accuracy in the strain matrix due to a poor definition of meridional curvature.

The Hermitian interpolation field is also adopted for obtaining the displacements, expressed in the global cylindrical coordinate system, along the meridian of an element based on the end-node Degrees Of Freedom (DOF). The end-node DOFs for all elements are  $u_i$ ,  $(du/ds)_i$ ,  $v_i$ ,  $(dv/ds)_i$ ,  $w_i$  and  $(dw/ds)_i$  as illustrated in Figure 2.2a. The displacement interpolation field within an element, as shown in Figure 2.2b, using the shape functions of Eqs (2.2a)-(2.2d), is given as:

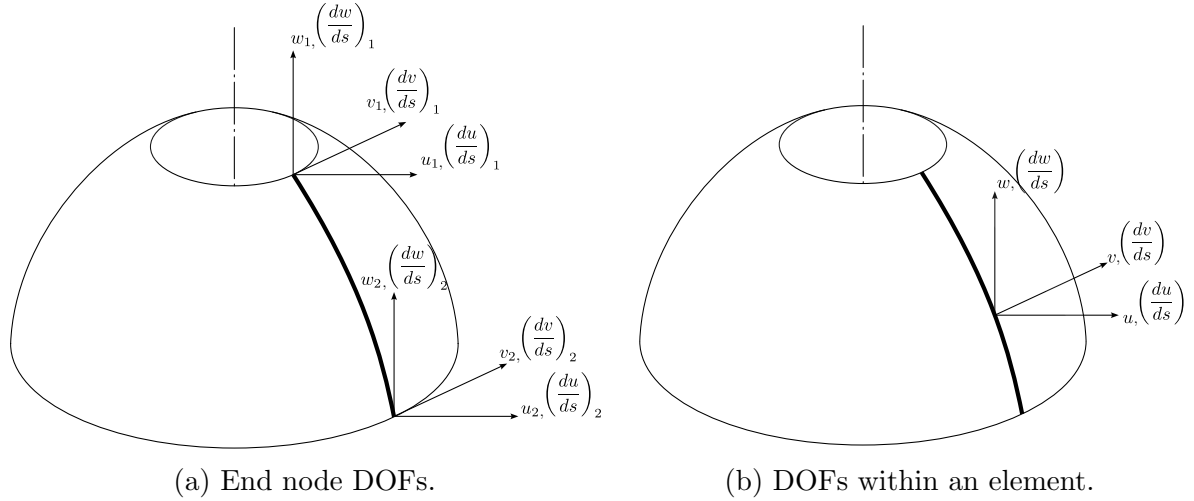


Figure 2.2: Element Degrees of Freedom.

$$u = \sum_{i=1,2} N_{0i} u_i + N_{1i} \left( \frac{du}{ds} \right)_i \quad (2.5a)$$

$$v = \sum_{i=1,2} N_{0i} v_i + N_{1i} \left( \frac{dv}{ds} \right)_i \quad (2.5b)$$

$$w = \sum_{i=1,2} N_{0i} w_i + N_{1i} \left( \frac{dw}{ds} \right)_i \quad (2.5c)$$

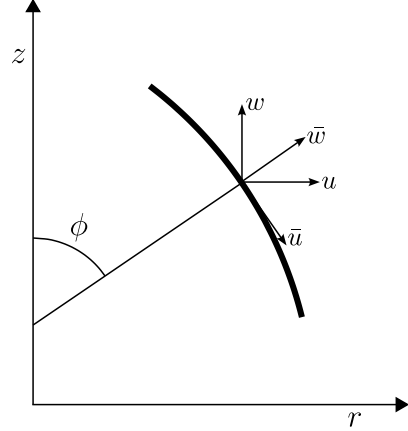


Figure 2.3: Local and global Degrees of Freedom.

Global displacements  $u$ ,  $v$  and  $w$  are related to the corresponding local  $\bar{u}$ ,  $\bar{v}$  and  $\bar{w}$  ones, also defined in curvilinear coordinates, through a transformation matrix  $T$ :

$$\begin{Bmatrix} \bar{u} \\ \bar{v} \\ \bar{w} \end{Bmatrix} = \begin{bmatrix} \cos(\phi) & 0 & -\sin(\phi) \\ 0 & 1 & 0 \\ \sin(\phi) & 0 & \cos(\phi) \end{bmatrix} \begin{Bmatrix} u \\ v \\ w \end{Bmatrix} = [T] \begin{Bmatrix} u \\ v \\ w \end{Bmatrix} \quad (2.6)$$

The global cylindrical coordinate system is used for the definition of the element displacements. On the other hand, stresses and strains are expressed in the local curvilinear system of each element such that the transformation matrix of Eq. (2.6) must be used to obtain the displacements in the local coordinate system of the element. This transformation is implicitly applied with the use of the strain-displacement matrix  $[B]$ , which relates end-node displacements expressed in the global cylindrical coordinate system, to the strains at a dimensionless meridional coordinate  $\eta$  along the element.

In the present finite element formulation for axisymmetric shells, the displacement field is assumed to follow a symmetric Fourier series variation in the circumferential direction. The antisymmetric terms, also included in the original publication by J.G. Teng and J.M. Rotter [50], are here dropped since they are only relevant to describe the displacement field of shells under torsional effects, currently considered out of the scope of the software. Therefore, the circumferential displacements, only included the symmetric variation of the Fourier series, are given as:

$$u = \sum_{n=0}^N u_n \cos(n\theta) \quad (2.7a)$$

$$v = \sum_{n=0}^N v_n \sin(n\theta) \quad (2.7b)$$

$$w = \sum_{n=0}^N w_n \cos(n\theta) \quad (2.7c)$$

It should be noted that the notation used for a circumferential wave-number here is ‘ $n$ ’, instead of the ‘ $m$ ’ letter used in [50]. This is done to adopt the notation used most often in classical texts on shell theory (though ‘ $m$ ’ may also be encountered in some of them), but is also a decision based on the follow-up publication by J.G. Teng and J.M. Rotter [51], where the notation for a circumferential wave-number is changed from ‘ $m$ ’ to ‘ $n$ ’.

The circumferential wave-number is embedded in the finite element formulation of this software, meaning that each stiffness matrix assembled corresponds to a specific wave-number and has an underlying assumption about the circumferential displacement field. For most tasks handled by the software, the axisymmetric wave-number ( $n = 0$ ) is considered, with non-zero wave-numbers being only relevant for analyses including bifurcation checks.

## 2.2 Kinematic relations

Thin shell theory dictates that the strain state at any distance  $z$  normal to the reference surface of the shell can be defined in terms of three membrane strains and three bending strain components. For the formulation of the shell element employed here it is considered that the shell’s reference surface and its mid-surface coincide, hence the normal coordinate  $z$  may take values in the range  $[-t/2, t/2]$  (where  $t$  is the thickness of the shell’s meridian). The membrane strains and curvatures (bending strain components) that may be used to define the strain state at any point within the shell wall of an element are

$$\{\epsilon\} = \{\epsilon_\phi^0, \epsilon_\theta^0, \gamma_{\phi\theta}^0, \kappa_\phi^0, \kappa_\theta^0, \kappa_{\phi\theta}^0\}^T \quad (2.8)$$

where the ‘0’ superscript is used for indicating strains corresponding to the shell’s mid-surface. The initial strains that the reader may notice to be included in the corresponding equation in [50] are here neglected as currently out of scope for the software. Transverse shear strain terms (relevant to a thick shell response) are also currently omitted from the formulation. The six strain terms of Eq. (2.8) may now be used to obtain the strains  $\{\epsilon^z\} = \{\epsilon_\phi^z, \epsilon_\theta^z, \gamma_{\phi\theta}^z\}^T$  at any point  $z$  as

$$\{\epsilon^z\} = [Z]\{\epsilon\} \quad (2.9)$$

where the  $[Z]$  matrix is given as

$$[Z] = \begin{bmatrix} 1 & 0 & 0 & z & 0 & 0 \\ 0 & 1 & 0 & 0 & z & 0 \\ 0 & 0 & 1 & 0 & 0 & z \end{bmatrix} \quad (2.10)$$

with  $z$  in the current context referring to the distance from shell’s midsurface, not to be confused with the  $z$  axial coordinate of Eq. (2.1b). The generalised strains of Eq. (2.8) can be separated into two parts, the linear  $\{\epsilon_l\}$  components given as linear functions of the displacements, and the nonlinear  $\{\epsilon_{nl}\}$  components given as quadratic relations of the displacements

$$\{\epsilon\} = \{\epsilon_l\} + \{\epsilon_{nl}\} \quad (2.11)$$

where the linear and nonlinear strain vectors are

$$\{\epsilon_l\} = \{\epsilon_{\phi l}^0, \epsilon_{\theta l}^0, \gamma_{\phi\theta l}^0, \kappa_{\phi l}, \kappa_{\theta l}, \kappa_{\phi\theta l}\}^T \quad (2.12a)$$

$$\{\epsilon_l\} = \{\epsilon_{\phi l}^0, \epsilon_{\theta l}^0, \gamma_{\phi\theta l}^0, 0, 0, 0\}^T \quad (2.12b)$$

### 2.2.1 Linear strain-displacement relations

The linear strains  $\{\epsilon_l\}$  of the shell’s mid-surface, according to small deflection theory, are given as:

$$\epsilon_{\phi l}^0 = \frac{\partial \bar{u}}{\partial s} + \frac{\partial \phi}{\partial s} \bar{w} \quad (2.13a)$$

$$\epsilon_{\theta l}^0 = \frac{\cos\phi}{r} \bar{u} + \frac{1}{r} \frac{\partial \bar{v}}{\partial \theta} + \frac{\sin\phi}{r} \bar{w} \quad (2.13b)$$

$$\gamma_{\phi\theta l}^0 = \frac{1}{r} \frac{\partial \bar{u}}{\partial \theta} - \frac{1}{r} \cos\phi \bar{v} + \frac{\partial \bar{v}}{\partial s} \quad (2.13c)$$

$$\kappa_\phi = \frac{\partial^2 \phi}{\partial s^2} \bar{u} + \frac{\partial \phi}{\partial s} \frac{\partial \bar{u}}{\partial s} - \frac{\partial^2 \bar{w}}{\partial s^2} \quad (2.13d)$$

$$\kappa_\theta = \frac{1}{r} \frac{\partial \phi}{\partial s} \cos\phi \bar{u} + \frac{1}{r^2} \sin\phi \frac{\partial \bar{v}}{\partial \theta} - \frac{\cos\phi}{r} \frac{\partial \bar{w}}{\partial s} - \frac{1}{r^2} \frac{\partial^2 \bar{w}}{\partial \theta^2} \quad (2.13e)$$

$$\kappa_{\phi\theta} = \frac{1}{r} \frac{\partial \phi}{\partial s} \frac{\partial \bar{u}}{\partial \theta} + \left( \cos\phi \frac{\partial \phi}{\partial s} - \frac{2}{r} \sin\phi \cos\phi \right) \frac{\bar{v}}{r} + \frac{\sin\phi}{r} \frac{\partial \bar{v}}{\partial s} + \frac{2}{r^2} \cos\phi \frac{\partial \bar{w}}{\partial \theta} - \frac{2}{r} \frac{\partial^2 \bar{w}}{\partial s \partial \theta} \quad (2.13f)$$

While the resource cited in [50] for their derivation [40] is presently inaccessible, their derivation may also be found in the PhD thesis of P.T. Jumikis [26]. These linear strains can be found to be identical to those derived in the classical book by W. Flügge *Stresses in Shells* [20] (Chapter 6.1.2 therein), as well as those of Reissner [28, 44] cited in the original publication [50].

## 2.2.2 Nonlinear strain-displacement relations

The nonlinear strain components  $\{\epsilon_{nl}\}$  may be defined as quadratic functions of the shell's mid-surface pseudo-rotations. The reference provided for the derivation of the nonlinear strains in [50] is once again found to be the currently inaccessible report [40], but the same derivation is also included in [26]. The nonlinear strains are given in terms of the pseudo-rotations  $\beta_1\text{-}\beta_6$  as

$$\epsilon_{\phi nl}^0 = \frac{1}{2}(\beta_1^2 + \beta_2^2 + \beta_3^2) \quad (2.14a)$$

$$\epsilon_{\theta nl}^0 = \frac{1}{2}(\beta_1^2 + \beta_2^2 + \beta_3^2) \quad (2.14b)$$

$$\gamma_{\phi\theta nl}^0 = (\beta_1\beta_4 + \beta_2\beta_5 + \beta_3\beta_6) \quad (2.14c)$$

with the pseudo-rotations being

$$\beta_1 = \frac{\partial \bar{w}}{\partial s} - \bar{u} \frac{\partial \phi}{\partial s} \quad (2.15a)$$

$$\beta_2 = \frac{\partial \bar{v}}{\partial s} \quad (2.15b)$$

$$\beta_3 = \frac{\partial \bar{u}}{\partial s} + \bar{w} \frac{\partial \phi}{\partial s} \quad (2.15c)$$

$$\beta_4 = \frac{1}{r} \left( \frac{\partial \bar{w}}{\partial \theta} - \bar{v} \sin \phi \right) \quad (2.15d)$$

$$\beta_5 = \frac{1}{r} \left( \frac{\partial \bar{v}}{\partial \theta} + \bar{w} \sin \phi + \bar{u} \cos \phi \right) \quad (2.15e)$$

$$\beta_6 = \frac{1}{r} \left( \frac{\partial \bar{u}}{\partial \theta} - \bar{v} \cos \phi \right) \quad (2.15f)$$

It should be noted that these relations hold for moderate rotations. The vector of pseudo-rotations  $\Theta$  can now be defined as

$$\{\Theta\} = \{\beta_1, \beta_2, \beta_3, \beta_4, \beta_5, \beta_6\}^T \quad (2.16)$$

and the matrix  $[A]$  of pseudo-rotations as

$$[A] = \begin{bmatrix} \beta_1 & \beta_2 & \beta_2 & 0 & 0 & 0 \\ 0 & 0 & 0 & \beta_4 & \beta_5 & \beta_6 \\ \beta_4 & \beta_5 & \beta_6 & \beta_1 & \beta_2 & \beta_3 \end{bmatrix} \quad (2.17)$$

It can be easily proven that the following relation holds for the nonlinear strains

$$\{\epsilon_{nl}\} = \frac{1}{2}[\Omega]\{\Theta\} \quad (2.18)$$

where  $\Omega$  is given as

$$[\Omega] = [A^T, 0]^T \quad (2.19)$$

with 0 in the above relation being a 6x3 matrix with zero entries.

## 2.3 Constitutive relations

The J2 flow rule of plasticity has been implemented to model the nonlinear behaviour of materials, the yielding of which is determined according to the von Mises yield criterion. The J2 deformation theory of plasticity, presented in the second publication by J.G. Teng and J.M. Rotter [51] has not been implemented in AQUINAS since the pre-buckling configurations that would lead to elastic-plastic shear strains and stresses, such as those arising in axisymmetric shells under torsional effects that would require the determination of the effective shear modulus  $G_{ef}$ , are currently out of scope for the software.

Isotropic hardening can be included through the definition of a nonlinear uniaxial stress-strain curve that will be used to determine the hardening parameter based on the value of the equivalent plastic strain of the material point. However, kinematic hardening effects are neglected in the current version of AQUINAS, mainly because they are, for the most part, only significant in cases where cyclic plasticity occurs. These cases are not currently studied by AQUINAS, which focuses at present on the monotonic applications of loads.

The von Mises yield criterion is defined as

$$F(\sigma, k) = \bar{\sigma} - \sigma_y = 0 \quad (2.20)$$

with  $k$  being the hardening parameter and  $\bar{\sigma}$  the equivalent von Mises stress

$$\bar{\sigma} = \sqrt{\sigma_\phi^2 + \sigma_\theta^2 - \sigma_\phi \sigma_\theta + 3\tau_{\phi\theta}^2} \quad (2.21)$$

where the stresses in the meridional and circumferential directions are  $\sigma_\phi$  and  $\sigma_\theta$  respectively while  $\tau_{\phi\theta}$  is the shear stress. The yield stress  $\sigma_y$  is given as a function of the plastic strains at any material point, which for isotropic hardening can be defined as:

$$\sigma_y = \sigma_{y0} + \int H' d\bar{\epsilon}_p \quad (2.22)$$

In Eq. (2.22) above,  $\sigma_{y0}$  is the material stress at the point of first yielding (zero plastic strain), while the plastic strain increment  $\bar{\epsilon}_p$  is

$$d\bar{\epsilon}_p = \frac{2}{\sqrt{3}} \sqrt{(d\epsilon_{\phi p}^z)^2 + (d\epsilon_{\theta p}^z)^2 + d\epsilon_{\phi p}^z d\epsilon_{\theta p}^z + (d\gamma_{\phi\theta p}^z)^2 / 4} \quad (2.23)$$

where  $d\epsilon_{\phi p}^z$ ,  $d\epsilon_{\theta p}^z$  and  $d\gamma_{\phi\theta p}^z$  are the meridional, circumferential and shear plastic strain increments respectively at any location  $z$  through the shell wall. The isotropic hardening parameter  $H'$ , relating the elastic and tangent moduli of the material, is defined as:

$$H' = \frac{EE_t}{E - E_t} \quad (2.24)$$

Where the elasticity modulus  $E$  (Young's modulus) in Eq. (2.24) is constant throughout the analysis for a specific material point, the tangent modulues  $E_t$  may depend on the magnitude of the plastic strain  $\bar{\epsilon}_p$  and be obtained through a uniaxial stress-strain curve as presented in Figure 2.4.

The flow rule, which can be found on classical texts on plasticity [16, 45], is given as

$$d\{\epsilon_p\} = d\bar{\epsilon}_p \frac{\partial F}{\partial \{\sigma\}} = d\bar{\epsilon}_p \frac{3}{2\bar{\sigma}} \{s\} \quad (2.25)$$

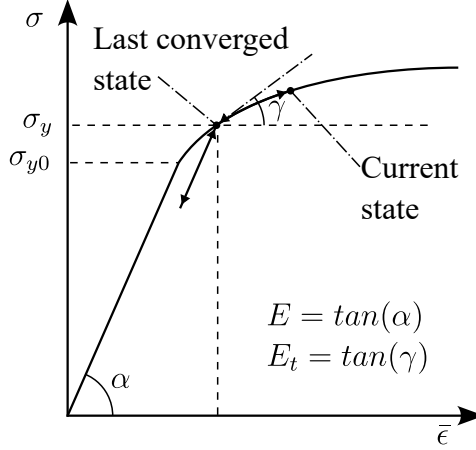


Figure 2.4: Uniaxial stress-strain curve and incremental plastic reversibility assumption.

with the vectors of plastic strains  $\epsilon_p$ , stresses  $\sigma$  and deviatoric stresses  $s$  being:

$$\{\epsilon_p\} = \{\epsilon_{\phi p}^z, \epsilon_{\theta p}^z, \gamma_{\phi \theta p}^z\}^T \quad (2.26a)$$

$$\{\sigma\} = \{\sigma_\phi^z, \sigma_\theta^z, \tau_{\phi \theta}^z\}^T \quad (2.26b)$$

$$\{s\} = \{s_\phi^z, s_\theta^z, s_{\phi \theta}^z\}^T \quad (2.26c)$$

The deviatoric stresses  $s$ , which correspond to the difference between the total stress component  $\sigma$  and the hydrostatic stresses, are given as:

$$s_\phi = \frac{1}{3}(2\sigma_\phi - \sigma_\theta) \quad (2.27a)$$

$$s_\theta = \frac{1}{3}(2\sigma_\theta - \sigma_\phi) \quad (2.27b)$$

$$s_{\phi \theta} = 2\tau_{\phi \theta} \quad (2.27c)$$

An increment of the stress vector is then defined as

$$d\sigma = [D_{ep}]d\{\epsilon^z\} \quad (2.28)$$

where the elastic-plastic modulus matrix  $[D_{ep}]$  is:

$$[D_{ep}] = [D_e] - a[D_p] \quad (2.29)$$

The factor  $a$  in Eq. (2.29) is set to  $a = 0$  for elastic material points, while  $a = 1$  for plastic-hardening ones. The elastic rigidity matrix for plane stress conditions is given as

$$[D_e] = \frac{E}{(1 - \nu^2)} \begin{bmatrix} 1 & \nu & 0 \\ \nu & 1 & 0 \\ 0 & 0 & (1 - \nu)/2 \end{bmatrix} \quad (2.30)$$

where  $E$  is the elastic modulus (Young's modulus) and  $\nu$  is the Poisson ratio of the material. The plastic matrix component of Eq. (2.29) is then

$$[D_p] = \frac{E}{(1 - \nu^2)S_5} \begin{bmatrix} S_1 S_1 & S_1 S_2 & S_1(1 - \nu)\tau_{\phi \theta} \\ S_1 S_2 & S_2 S_2 & S_2(1 - \nu)\tau_{\phi \theta} \\ S_1(1 - \nu)\tau_{\phi \theta} & S_2(1 - \nu)\tau_{\phi \theta} & \tau_{\phi \theta}^2(1 - \nu)^2 \end{bmatrix} \quad (2.31)$$

with the parameters  $S_1$  to  $S_5$  being:

$$S_1 = s_\phi + \nu s_\theta \quad (2.32a)$$

$$S_2 = s_\theta + \nu s_\phi \quad (2.32b)$$

$$S_3 = S_1 d\epsilon_\phi^z + S_2 d\epsilon_\theta^z + (1 - \nu) \tau_{\phi\theta} d\gamma_{\phi\theta}^z \quad (2.32c)$$

$$S_4 = s_\phi^2 + s_\theta^2 + 2\nu s_\phi s_\theta + 2(1 - \nu) \tau_{\phi\theta}^2 \quad (2.32d)$$

$$S_5 = \frac{2\bar{\sigma}^2(1 - \nu)H'}{9G} + S_4 \quad (2.32e)$$

An increment of the equivalent plastic strains of a material point can be found to be:

$$d\bar{\epsilon}_p = \frac{2\bar{\sigma}}{3} \frac{S_3}{S_5} \quad (2.33)$$

The process for formulating  $[D_{ep}]$  and  $[D_p]$  of Eqs (2.29) - (2.31), as well as for computing an increment of the equivalent plastic strains of a material point, can be found in Chapter 6 *Basic plasticity* of [16] as well as other classical texts on plasticity [45]-[31]. Once the stresses at all material points across the thickness of the shell wall have been computed, the vector of generalised stress resultants  $\{\Sigma\}$  can be integrated according to classical shell theory relations. The three membrane stress resultants and three bending stress resultants that comprise  $\{\Sigma\}$  are

$$\{\Sigma\} = \{N_\phi, N_\theta, N_{\phi\theta}, M_\phi, M_\theta, M_{\phi\theta}\} \quad (2.34)$$

where  $N_\phi$  and  $N_\theta$  are the meridional and circumferential membrane stress resultants respectively,  $N_{\phi\theta}$  is the in-plane shear stress resultant (not to be confused with transverse shear),  $M_\phi$  and  $M_\theta$  are the bending stress resultants in the meridional and circumferential directions respectively while  $M_{\phi\theta}$  is the twisting moment. An increment of generalised stress resultants can be related to an increment of reference surface strains of Eq. (2.11) through the tangent modulus matrix  $[D_T]$  as

$$\{d\Sigma\} = [D_T]d[\{\epsilon\} - \{\epsilon_0\}] \quad (2.35)$$

with the tangent modulus  $[D_T]$  given by:

$$[D_T] = \int_{-t/2}^{t/2} [Z]^T [D_{ep}] [Z] dz \quad (2.36)$$

As can be seen from the relation above, in order to obtain the tangent modulus matrix  $[D_T]$  the elastic-plastic modulus matrices  $[D_{ep}]$  of Eq. (2.29) must be integrated across the thickness of the shell wall. This integration is carried out using Simpson's 1/3 rule, as advised in [50], but also most commonly encountered as the through thickness integration scheme when material nonlinearities are considered due to their discontinuous nature that invalidates the use of a Gauss-Legendre scheme (which assumes an  $n^{th}$  order polynomial behaviour).

## 2.4 Finite Element Formulation

With reference to Figure 2.2a, the end node degrees of freedom vector of the axisymmetric shell element presented here is:

$$\{\delta\} = \left\{ u_1, \left( \frac{\partial u}{\partial s} \right)_1, v_1, \left( \frac{\partial v}{\partial s} \right)_1, w_1, \left( \frac{\partial w}{\partial s} \right)_1, u_2, \left( \frac{\partial u}{\partial s} \right)_2, v_2, \left( \frac{\partial v}{\partial s} \right)_2, w_2, \left( \frac{\partial w}{\partial s} \right)_2 \right\} \quad (2.37)$$

Adopting a total Lagrangian formulation, all quantities relate to the original undeformed geometry of the thin shell. The principle of virtual displacements yields

$$\int_V d\epsilon^T \sigma dV = \Pi \quad (2.38)$$

with the work done by external body forces  $p$  and tractions  $q$  being equal to

$$\Pi = \int \rho du^T q dV + \int du^T p dA \quad (2.39)$$

In the above relations,  $\epsilon$  and  $\sigma$  are the vectors of Green strains and Piola-Kirchoff stresses respectively,  $\rho$  is the density of the body,  $u$  is the vector of displacements while  $dA$  and  $dV$  are the elements of surface area and volume respectively, referring to the undeformed configuration.

Following classical finite element theory concepts for the solution of nonlinear problems, the tangent stiffness matrix of the shell elements is split into the material and geometric stiffness components which, when added, formulate the tangent stiffness matrix of an element. The formulation of the individual stiffness components will be described in the following paragraphs.

Revisiting Eq. (2.11) and taking variations while accounting for the relation of Eq. (2.18), an increment of strain can be defined as:

$$d\{\epsilon\} = d\{\epsilon_l\} + \frac{1}{2}[\Omega]d\{\Theta\} + \frac{1}{2}d[\Omega]\{\Theta\} \quad (2.40)$$

Through substitution and differentiation, it can be proven that:

$$[\Omega]d\{\Theta\} = \{\Theta\}d[\Omega] \quad (2.41)$$

Hence, an increment of strain may be given as:

$$d\{\epsilon\} = d\{\epsilon_l\} + [\Omega]d\{\Theta\} \quad (2.42)$$

Observing Eq. (2.42) above, the increment of the linear strains  $d\{\epsilon_l\}$  and the term  $[\Omega]d\{\Theta\}$  will now need to be related to the nodal displacements of an element,  $\{\delta\}$  in order to formulate the linear-nonlinear strain-displacement matrix  $[B]$  and eventually compute the material stiffness of the shell element. The strain-displacement matrix  $[B]$ , used to relate a strain increment to a nodal displacement increment, is given as:

$$d\{\epsilon\} = [B]d\{\delta\} \quad (2.43)$$

Denoting as  $[B_0]$  the strain-displacement matrix corresponding to the linear components of the strains, which is independent of the nodal displacements developing during the solution process, an increment of the linear strain can be found to be:

$$d\{\epsilon_l\} = [B_0]d\{\delta\} \quad (2.44)$$

Before going into the formulation of the strain-displacement matrix corresponding to nonlinear strains, it is important to note that a total Lagrangian formulation for thin shells

has been adopted in [50], and consequently here, where all quantities relate to the initial undeformed configuration of the meridian. Hence, no updating of nodal positions should be expected by the reader when tracing the prebuckling axisymmetric state of the shell when geometrical nonlinearities are considered, and the only place where the nonlinear changes in the geometry are accounted for is through the nonlinear strain-displacement matrix.

A combination of Eqs (2.5), (2.6), (2.15) and (2.16) leads to:

$$\{\Theta\} = [G]\{\delta\} \quad (2.45)$$

with  $[G]$  being an array of shape functions and their derivatives, relating the pseudo-rotations of Eq. (2.15) to the nodal displacement vector  $\{\delta\}$ . By taking variations in Eq. (2.45):

$$d\{\Theta\} = [G]d\{\delta\} \quad (2.46)$$

An increment of the nonlinear strain components can now be found as

$$d\{\epsilon_{nl}\} = [B_L]d\{\delta\} \quad (2.47)$$

where the strain-displacement matrix  $[B_L]$ , relating the nonlinear strains increment  $d\{\epsilon_{nl}\}$  to the nodal displacement vector  $\{\delta\}$ , can be obtained from Eqs. (2.42) and (2.46) as:

$$[B_L] = [\Omega][G] \quad (2.48)$$

The strain-displacement matrix  $[B]$ , relating the reference surface strains  $\{\epsilon\}$ , including both the linear and nonlinear components  $\{\epsilon_l\}$  and  $\{\epsilon_{nl}\}$  to the end node displacements  $\{\delta\}$ , is now defined from Eq. (2.42) as:

$$[B] = [B_0] + [B_L] \quad (2.49)$$

For a single element, Eq. (2.38) can be written as

$$d\{\delta\}^T = \int [B]^T \{\Sigma\} dV = d\{\delta\}^T \{R\} \quad (2.50)$$

where  $\{R\}$  is a vector of equivalent nodal forces because of body forces  $q$  and surface tractions  $p$ . The vector of virtual displacements  $\{d\delta\}^T$  is arbitrary, hence the nonlinear equations for an element can be written as:

$$\{\Phi(\delta)\} = \{R\} - \int [B]^T \{\Sigma\} dV = 0 \quad (2.51)$$

The above expression for the vector of nodal residual forces  $\{\Phi(\delta)\}$  will be the fundamental nonlinear equation for which a solution is sought, for problems where either material or geometric nonlinearities are to be considered. The assumption that the equivalent nodal forces  $\{R\}$  are conservative is made for all that follows.

For a known increment of the total displacements  $\delta_i$ , such that the residual forces are non-zero ( $\Phi(\delta_i) \neq 0$ ), the value of  $\Phi$  for an increment  $\Delta\delta_i$  in  $\delta_i$  can be expressed as a Taylor series expansion of  $\Phi$  about  $\delta_i$ :

$$\Phi(\delta_i + \Delta\delta_i) = \Phi(\delta_i) \left[ \frac{\partial\Phi}{\partial\delta} \right]_{\delta=\delta_i} \Delta\delta_i + \dots = 0 \quad (2.52)$$

Ignoring the second and higher order terms, a linear approximation of the residual force vector with respect to the nodal displacement increments can be obtained as:

$$\{\Phi(\delta_i)\} = [K_T]\{\Delta\delta_i\} \quad (2.53)$$

In Eq. (2.52) above  $[K_T]$  is the tangent stiffness matrix of the axisymmetric shell and is defined as:

$$[K_T] = - \left[ \frac{\partial \Phi}{\partial \delta} \right]_{\delta=\delta_i} \quad (2.54)$$

Due to the truncation of the Taylor series of Eq. (2.52) just after the first order term, the solution obtained for  $\Delta\delta_i$  will be only a linear approximation of the set of nonlinear equations. A series of iterations needs to be performed to obtain a solution of sufficient accuracy, most commonly adopting a Newton-Raphson scheme.

Through manipulation of Eq. (2.51), a relation for the tangent stiffness matrix  $[K_T]$  can be obtained as:

$$-\frac{d\{\Phi\}}{d\{\delta\}} = \int [B]^T \frac{d\{\Sigma\}}{d\{\delta\}} dA + \int \frac{d[B]^T}{d\{\delta\}} \{\Sigma\} dA \quad (2.55)$$

Taking variations of Eq. (2.49), by considering Eq. (2.48), one may find that

$$d[B]^t = d[B_L]^T = [G]^T [\Omega]^T \quad (2.56)$$

since  $[B_0]$  only contains terms of shape functions and their derivatives, and therefore vanishes in a differentiation with respect to the nodal displacements. Substituting Eqs (2.35) and (2.56) into Eq. (2.55) leads to:

$$-\frac{d\{\Phi\}}{d\{\delta\}} = \int [B]^T [D_T] [B] dA + \int [G]^T \frac{d[\Omega]^T}{d\{\delta\}} \{\Sigma\} dA \quad (2.57)$$

The terms in the second integrand can be rewritten in the form

$$\frac{d[\Omega]}{d\{\Sigma\}} = [N_0] \frac{d\{\Theta\}}{d\{\delta\}} = [N_0][G] \quad (2.58)$$

where  $[N_0]$  is a  $6 \times 6$  matrix of membrane stress resultants, corresponding to the pseudo rotations according to the nonlinear strains  $\{\epsilon_{nl}\}$  of Eqs (2.14), given as:

$$[N_0] = \begin{bmatrix} N_\phi & 0 & 0 & N_{\phi\theta} & 0 & 0 \\ 0 & N_\phi & 0 & 0 & N_{\phi\theta} & 0 \\ 0 & 0 & N_\phi & 0 & 0 & N_{\phi\theta} \\ N_{\phi\theta} & 0 & 0 & N_\theta & 0 & 0 \\ 0 & N_{\phi\theta} & 0 & 0 & N_\theta & 0 \\ 0 & 0 & N_{\phi\theta} & 0 & 0 & N_\theta \end{bmatrix} \quad (2.59)$$

Substituting Eq. (2.58) into Eq. (2.57) yields:

$$-\frac{d\{\Phi\}}{d\{\delta\}} = \int_A [B]^T [D_T] [B] dA + \int_A [G]^T [N_0] [G] dA \quad (2.60)$$

Since the variation of an element's residual forces with respect to its nodal displacements is equivalent to the tangent stiffness  $[K_T]_e$ , Eq. (2.60) leads to:

$$[K_T]_e = [\bar{K}]_e + [K_\sigma]_e \quad (2.61)$$

where

$$[\bar{K}]_e = \int_A [B]^T [D_T] [B] dA \quad (2.62a)$$

$$[K_\sigma]_e = \int_A [G]^T [N_0] [G] dA \quad (2.62b)$$

The tangent stiffness matrix  $[K_T]_e$  of an element is formed in Eq. (2.61) through the addition of two individual stiffness matrix components, the material stiffness  $[\bar{K}]_e$ , accounting for changes in element geometry through the nonlinear strain corresponding terms in the strain-displacement matrix from Eq. (2.49), and the geometric stiffness  $[K_\sigma]_e$  which accounts for the effects of internal stresses in the stiffness of the element.

The tangent stiffness of the structure is assembled through the insertion of each element's stiffness terms in the appropriate cells of the global stiffness array, a common procedure in matrix structural analysis. Before going into the assembly of the global tangent stiffness matrix however, the end-node DOFs  $du/ds$  and  $dw/ds$  need to be statically condensed, in order to avoid connecting wrong variables at segment junctions with an abrupt change of meridional slope. The process of statically condensing these nodal DOFs is thoroughly presented in the following section.

## 2.5 Condensation of nodal variables

For shells with continuous meridional curvature, the six nodal DOFs of  $u_i$ ,  $(du/ds)_i$ ,  $v_i$ ,  $(dv/ds)_i$ ,  $w_i$ ,  $(dw/ds)_i$  Eq. (2.37) (6 per node, 12 per element) are indeed appropriate for use in the assembled global stiffness matrix. In cases however that there are sudden changes of slope between segments of the shell's meridian, associating the  $(du/ds)_i$  and  $(dw/ds)_i$  DOFs at the intersection can lead to errors in the analysis due to the excessive continuity that is imposed between elements, as illustrated in Figure 2.5.

For this reason, the  $(du/ds)_i$  and  $(dw/ds)_i$  nodal DOFs are disassociated between shell segments. These two nodal variables are first transformed according to the following relation:

$$\begin{Bmatrix} \beta_i \\ \gamma_i \end{Bmatrix} = \begin{bmatrix} -\sin\phi & -\cos\phi \\ \cos\phi & -\sin\phi \end{bmatrix} \begin{Bmatrix} (du/ds)_i \\ (dw/ds)_i \end{Bmatrix} \quad (2.63)$$

where  $\beta_i$  corresponds to the rotation and  $\gamma_i$  to the meridional stretching of node  $i$ . Once the transformation has been applied, the nodal DOFs  $\gamma$  and  $dv/ds$  are condensed out of the stiffness matrix of the element, before the global stiffness matrix is assembled.

At this point, it is important to note that a different procedure is adopted for condensing out the desired DOFs, depending on the type of the element's stiffness matrix the static condensation is applied upon. For application in the tangent stiffness matrix, which in the absence of geometric nonlinearities in the analysis is indistinguishable from the element's material stiffness components, the process takes its classic form, presented in the 1st article by J.G. Teng and J.M. Rotter [50] and also most commonly found in matrix structural analysis textbooks. However, when the DOFs need to be condensed out from the geometric

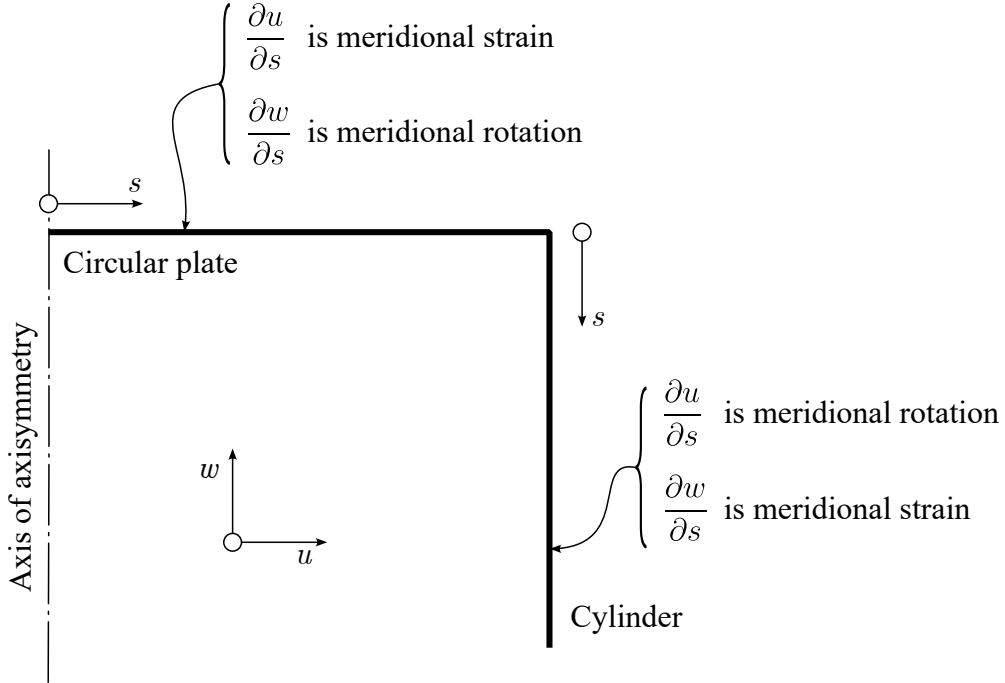


Figure 2.5: Segment intersection with discontinuous meridional curvature

stiffness matrix, the steps and formulas need to be applied are considerably more complex, as outlined in the P.T. Jumikis' PhD Thesis [26].

In the case of the tangent stiffness, after the transformation of the nodal variables takes place, the  $[K_T]_e$  matrix of the element is partitioned as presented in the following relation, where the remaining DOFs are denoted with a subscript  $a$  and the ones to be condensed out (i.e. nodal variables  $(dv/ds)_i$  and  $\gamma$ ) are denoted with a subscript  $b$ :

$$[K_T]_e \{d\delta\} = \begin{bmatrix} K_a & K_{ab} \\ K_{ab}^T & K_b \end{bmatrix} \begin{Bmatrix} d\delta_a \\ d\delta_b \end{Bmatrix} = \begin{Bmatrix} \Phi_a \\ \Phi_b \end{Bmatrix} \quad (2.64)$$

Expanding Eq. (2.64) above yields:

$$d\delta_b = K_b^{-1} [\Phi_b - K_{ab}^T d\delta_a] \quad (2.65)$$

Substituting  $d\delta_b$  from Eq. (2.65) into Eq. (2.64) leads to

$$K_{Tc} d\delta_a = \Phi_c \quad (2.66)$$

where  $K_{Tc}$  is the condensed stiffness matrix of the element, given as

$$K_{Tc} = K_a - K_{ab} K_b^{-1} K_{ab}^T \quad (2.67)$$

and the condensed residual forces vector  $\Phi_c$  of the element being

$$\Phi_c = \Phi_a - K_{ab} K_b^{-1} \Phi_b \quad (2.68)$$

After application of Eqs (2.67) and (2.68), the condensed tangent stiffness matrix and residual force vector of the element may be obtained and used in the assembly of the global stiffness matrix and force vector of the axisymmetric shell model, hence the equilibrium equation of Eq. (2.53) for the displacements of the current load increment can now be solved for.

However, in the case of performing bifurcation checks for any competing circumferential modes, the  $\gamma$  and  $dv/ds$  DOFs need to be condensed out from both the material (which may or may not include the contribution of nonlinear strains) and the geometric stiffness matrices. As discussed in [26], the geometric (or stability) matrix of an element is in general not positive definite, and the procedure outlined above cannot be applied for its condensation. Instead, the technique presented in [62] - [21] is adopted, where the condensation is applied to the equilibrium equation as a whole. Splitting the material and geometric components of the element's stiffness matrix, the equilibrium equation is given as

$$[\bar{K} + K_\sigma]_e \{\delta\} = \{\Phi\} \quad (2.69)$$

where the notation of [50] for the material and geometric stiffness matrices, instead of [26], is used. The same reordering and partition of the DOFs in the element is performed, as in Eq. (2.64). It is assumed that the condensed out variables  $\delta_a$  depend on the remaining DOFs  $\delta_b$  through an auxiliary matrix  $[L]$  so that

$$\{\delta_b\} = [L]\{\delta_a\} \quad (2.70)$$

or

$$\{\delta\} = \begin{bmatrix} I \\ L \end{bmatrix} \{\delta_a\} \quad (2.71)$$

The assumption that the forces applied on the system perform the same amount of work on either the full or condensed system [62] is also made:

$$\{\Phi\}^T \{\delta\} = \{\Phi_c\}^T \{\delta_a\} \quad (2.72)$$

Substitution of Eq. (2.71) into Eq. (2.72) leads to

$$\{\Phi\}^T \begin{bmatrix} I \\ L \end{bmatrix} \{\delta_a\} = \{\Phi_c\}^T \{\delta_a\} \quad (2.73)$$

which leads to the following relation for the condensed vector of nodal forces:

$$\{\Phi_c\} = \begin{bmatrix} I \\ L \end{bmatrix}^T \{\Phi\} \quad (2.74)$$

Substitution of Eqs (2.69) and (2.71) into Eq. (2.74) yields

$$K_{Tc} = \begin{bmatrix} I \\ L \end{bmatrix}^T [\bar{K} + K_\sigma] \begin{bmatrix} I \\ L \end{bmatrix} \quad (2.75)$$

which may be rewritten as:

$$[K_{Tc}] = \begin{bmatrix} I \\ L \end{bmatrix}^T [\bar{K}] \begin{bmatrix} I \\ L \end{bmatrix} + \begin{bmatrix} I \\ L \end{bmatrix}^T [K_\sigma] \begin{bmatrix} I \\ L \end{bmatrix} \quad (2.76)$$

In order to obtain a relation between the condensed DOFs  $\{\delta_a\}$  and  $\{\delta\}$ , it is assumed that the general pattern of deformation will follow that which would be obtained by imposing displacements  $\{\delta_a\}$  on an otherwise unloaded structure [26], which by taking into account the partitioning of Eq. (2.64) gives

$$[K_{ab}]^T \delta_a + [K_b]\{\delta_b\} = 0 \quad (2.77)$$

since the eliminated DOFs are unloaded, which in turn leads to:

$$\{\delta_b\} = -[K_b]^{-1}[K_{ab}]^T \delta_a \quad (2.78)$$

A relation for the  $[L]$  matrix may now be obtained by comparing the above equation with Eq. (2.70):

$$[L] = -[\bar{K}_b]^{-1}[\bar{K}_{ab}]^T \quad (2.79)$$

Substitution of  $[L]$  into the first term of Eq. (2.76) can be used to verify the relation for condensed tangent stiffness matrix of an element of Eq. (2.67). Partitioning the geometric stiffness matrix in the same manner the tangent stiffness was partitioned in Eq. (2.64), its condensed form may be obtained after substituting it and  $[L]$  it into the second term of Eq. (2.76), yielding:

$$\begin{aligned} [K_{\sigma c}] &= \begin{bmatrix} I \\ -\bar{K}_b^{-1}\bar{K}_{ab}^T \end{bmatrix}^T \begin{bmatrix} K_{\sigma,a} & K_{\sigma,ab} \\ K_{\sigma,ab}^T & K_{\sigma b} \end{bmatrix} \begin{bmatrix} I \\ -\bar{K}_b^{-1}\bar{K}_{ab}^T \end{bmatrix}^T \\ &= [I - \bar{K}_{ab}^{-1}\bar{K}_b^{-T}] \begin{bmatrix} K_{\sigma,a} - K_{\sigma,ab}\bar{K}_b^{-1}\bar{K}_{ab}^T \\ K_{\sigma,ab}^T - K_{\sigma,b}\bar{K}_b^{-1}\bar{K}_{ab}^T \end{bmatrix} \\ &= K_{\sigma,a} - K_{\sigma,ab}\bar{K}_b^{-1}\bar{K}_{ab}^T - \bar{K}_{ab}\bar{K}_b^{-T}K_{\sigma,ab}^T + \bar{K}_{ab}\bar{K}_b^{-T}K_{\sigma,b}\bar{K}_b^{-1}\bar{K}_{ab}^T \end{aligned} \quad (2.80)$$

As a consequence of the material matrix  $\bar{K}$  being symmetric, Eq. (2.80) may be rewritten as:

$$[K_{\sigma c}] = K_{\sigma,a} - K_{\sigma,ab}\bar{K}_b^{-1}\bar{K}_{ab}^T - (K_{\sigma,ab}\bar{K}_b^{-1}\bar{K}_{ab}^T)^T + \bar{K}_{ab}\bar{K}_b^{-1}K_{\sigma,b}\bar{K}_b^{-1}\bar{K}_{ab}^T \quad (2.81)$$

The grouping of the partitioned components in Eq. (2.81) allows for some additional saving in computational effort, in comparison to the form presented in Eq. (2.80), due to the third term being the transpose of the second one. After condensing out the  $\gamma$  and  $dv/ds$  DOFs, the geometric stiffness matrix of the element can now be assembled into the global geometric stiffness matrix to be used for solving the eigenvalue problem for a given circumferential mode  $n$ , expressed as:

$$[\bar{K}_c + \lambda K_{\sigma c}]\{\phi\} = \{0\} \quad (2.82)$$

## 2.6 Recovery of nodal variables

Once the equilibrium equation of Eq. (2.66) has been solved for and the nodal variables remaining in the system after condensation have been computed, the full set of element DOFs need to be evaluated in order to determine the linear-nonlinear strain increments according to Eqs (2.13) and (2.14). This process is one of undoing the static condensation and obtaining the nodal variables that were eliminated from the stiffness matrix, which can be done through Eq. (2.65), using the same partitioned components of the tangent stiffness matrix.

It is important to note that at this point the element DOFs vector, just after having worked out the condensed out components, is still under the effect of the transformation of Eq. (2.63). The  $(du/ds)_i$  and  $(dw/ds)_i$  nodal variables can be found through multiplication with the transpose of the transformation matrix of Eq. (2.63), that is:

$$\begin{Bmatrix} (du/ds)_i \\ (dw/ds)_i \end{Bmatrix} = \begin{bmatrix} -\sin\phi & \cos\phi \\ -\cos\phi & -\sin\phi \end{bmatrix} \begin{Bmatrix} \beta_i \\ \gamma_i \end{Bmatrix} \quad (2.83)$$

As a consequence of the condensation process applied in the before the solution of the equilibrium equation, the derivatives of the displacements  $du/ds$ ,  $dv/ds$  and  $dw/ds$  are discontinuous between elements meeting at a common node, as highlighted in [50]. This results to 12 degrees of freedom being necessary to define the deformed state of the shell rather than 6 per node. In turn, this may lead to discontinuities of the strain-stress fields across different elements of the shell's meridian.

In the case of bifurcation checks however there is no need to recover the nodal variables that were condensed out from the stiffness matrices, since the chief goal of the analysis is one of obtaining a number of eigenvalues for a competing circumferential mode  $n$  and there are no strains-stresses to be determined after a solution is obtained.

# Chapter 3

## Software capabilities

AQUINAS has been designed to be a versatile and efficient Finite Element Analysis tool for solving linear or nonlinear axisymmetric shell problems. Having the productivity of its users in mind, it provides an array of tools for the generation of an axisymmetric shell problem, all of which can be accessed and programmed through a single MATLAB [30] script. From different ways to define the meridional geometry of a shell segment to the optimisation procedures applied for identifying the critical circumferential mode  $n$ , it all starts with the generation of an AQUINAS object. In the following paragraphs, the capabilities of the software will be outlined with some hints and tips provided on the internal processes of AQUINAS.

### 3.1 Geometric definitions

Definition of an axisymmetric shell element in AQUINAS requires that the first and second derivatives of geometrical components be known at the nodes along the meridian of a segment, as can be appreciated from the FE formulation of [50]. In order to reduce the analyst's effort for the computational modelling of a shell problem, these derivatives can be automatically evaluated at nodal positions for reference meridional geometries and their combinations.

An important point for all of the following geometric definitions is that condition of axisymmetry of the shell problems should not be violated under any circumstances, for nodes existing in the negative plane of radial coordinates. Failing to do so will result in an error in the construction of the segment object and the analysis will not proceed.

#### 3.1.1 Plate segment geometry

One of the most basic types of axisymmetric shell geometry is that of a circular plate, with or without an opening at its centre. The definition of one is simple with the 'Plate' option of a segment object (see the following chapter for available options of an AQUINAS\_Segment\_Object). Only the radial  $r$  and axial  $z$  coordinates of the plate's ends are required to fully define a segment, illustrated in Figure 3.1, while the derivatives of the meridional geometric components necessary for the formulation are given in Eq (3.1) below, to be computed at the nodal positions. It is important, for the optimal behaviour of the solver, for the '*top*' end of the plate segment to be the one closest to the axis of revolution.

$$\left( \frac{\partial r}{\partial z} \right)_i = \infty \quad (3.1a)$$

$$\left( \frac{\partial^2 r}{\partial z^2} \right)_i = 0 \quad (3.1b)$$

$$\left( \frac{\partial^3 r}{\partial z^3} \right)_i = 0 \quad (3.1c)$$

$$\left( \frac{\partial r}{\partial s} \right)_i = 1 \text{ if } r_{bot} > r_{top}, \quad -1 \text{ if } r_{bot} < r_{top} \quad (3.1d)$$

$$\left( \frac{\partial z}{\partial s} \right)_i = 0 \quad (3.1e)$$

$$\phi_i = 0 \quad (3.1f)$$

$$\left( \frac{\partial \phi}{\partial s} \right)_i = 0 \quad (3.1g)$$

$$\left( \frac{\partial^2 \phi}{\partial s^2} \right)_i = 0 \quad (3.1h)$$

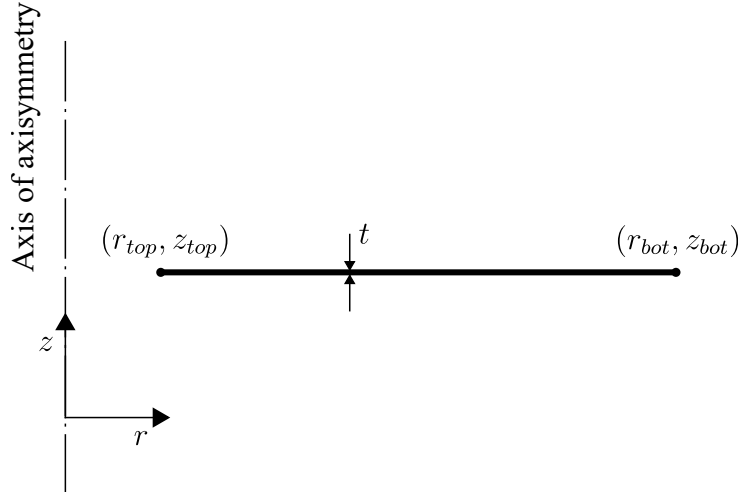


Figure 3.1: Meridional geometry definition of a plate segment.

### 3.1.2 Conical segment geometry

Perhaps the most encountered types of axisymmetric shell in real-life civil engineering applications, cylinders and cones can be easily and accurately defined with the aid of the 'Cone' of the segment object in AQUINAS. Due to the straight meridian of conical segments, as was the case with the plate segment earlier, the coordinates of just the two end points are sufficient for modelling of an axisymmetric cone problem as illustrated in Figure 3.2. Cylinders can be regarded as a special case of conical segments, where the radial coordinates of its top and bottom edges are equal i.e.  $r_{top} = r_{bot}$ .

The relationships that govern the geometric definition of a cone shell element, as coded in `AQUINAS_Segment_Object`, are given in Eq (3.2) below:

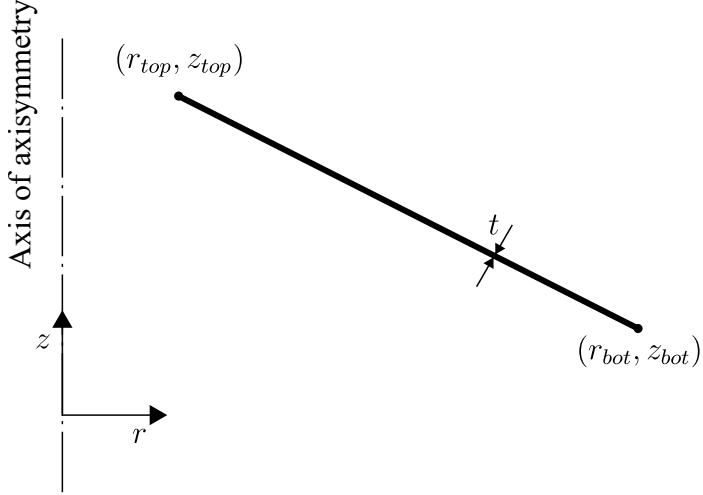


Figure 3.2: Meridional geometry definition of a conical segment.

$$\left( \frac{\partial r}{\partial z} \right)_i = \frac{r_{bot} - r_{top}}{z_{bot} - z_{top}} \quad (3.2a)$$

$$\left( \frac{\partial^2 r}{\partial z^2} \right)_i = 0 \quad (3.2b)$$

$$\left( \frac{\partial^3 r}{\partial z^3} \right)_i = 0 \quad (3.2c)$$

$$\left( \frac{\partial r}{\partial s} \right)_i = 1 \text{ if } \left( \frac{\partial r}{\partial z} \right)_i \equiv \infty, \frac{-\left( \frac{\partial r}{\partial z} \right)_i}{\sqrt{1 + \left( \frac{\partial r}{\partial z} \right)_i^2}} \text{ otherwise} \quad (3.2d)$$

$$\left( \frac{\partial z}{\partial s} \right)_i = 0 \text{ if } \left( \frac{\partial r}{\partial z} \right)_i \equiv \infty, \frac{-1}{\sqrt{1 + \left( \frac{\partial r}{\partial z} \right)_i^2}} \text{ otherwise} \quad (3.2e)$$

$$\phi_i = \frac{\pi}{2} - \tan^{-1} \left( -\left( \frac{\partial r}{\partial z} \right)_i \right) \quad (3.2f)$$

$$\left( \frac{\partial \phi}{\partial s} \right)_i = 0 \quad (3.2g)$$

$$\left( \frac{\partial^2 \phi}{\partial s^2} \right)_i = 0 \quad (3.2h)$$

### 3.1.3 Elliptical segment geometry

Not as common as cylindrical or conical shell segments, but still widely used owing to the efficient load bearing behaviour of their doubly curved surfaces or natural architectural beauty, spherical shells and ellipsoids are a fundamental form of axisymmetric shell structures that could not be missing from AQUINAS. The governing equation for the meridional geometry of an elliptical segment is provided in Eq. (3.3), where the reader may appreciate that the current software supports ellipses without the need for their centre to be on the origin of the radial/axial axes, but it does not currently support a rotated ellipse in the 2D modelling space. The governing equation is

$$\frac{(r - r_C)^2}{\rho_r^2} + \frac{(z - z_C)^2}{\rho_z^2} = 1 \quad (3.3)$$

where  $r_C$  and  $z_C$  are the coordinates of the centre of the elliptical segment, while  $2\rho_r$  and  $2\rho_z$  are the length and width of the full ellipse (even if the entire ellipse is not modelled). Spherical segments, which can be either fully closed spheres or truncated spherical caps, may be generated by setting the major and minor axes of the ellipse to be of equal length for  $\rho_r = \rho_z$ . The meridional geometric definition of an elliptical segment in AQUINAS is given in the following Figure 3.3. The radial and axial coordinates of the top  $(r_{top}, z_{top})$  and bottom  $(r_{bot}, z_{bot})$  edges of the shell segment can aid in defining truncated spherical or elliptical segments.

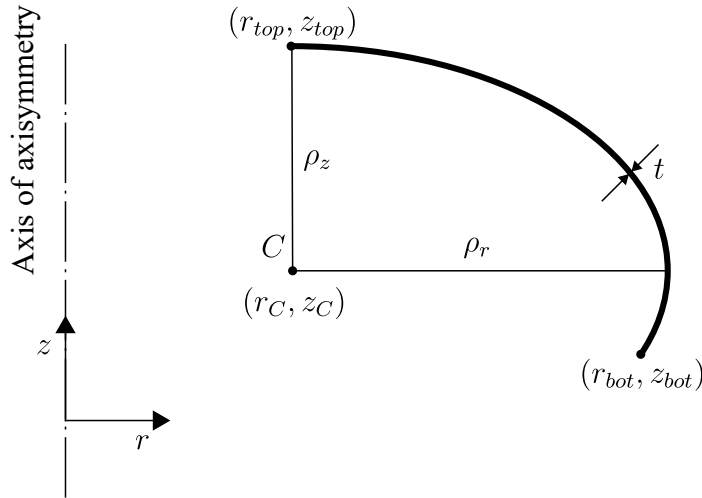


Figure 3.3: Meridional geometry definition of an elliptical segment.

The reader should be advised that meridional regions from both sides of an apex of an elliptical segment should not be modelled into the same object. Instead, two segments should be used, meeting at a common node at the apex, each modelling a portion of the shell that has a meridional curvature of opposite sign (as measured from the axis of revolution). This is done for purely logistical reasons of AQUINAS' inner proceedings so that the same elliptical segment class can capture the behaviour of axisymmetric of both positive and negative Gaussian curvature.

The equations that fully describe the geometric components of a sphere or an ellipse are presented in Eqs (3.4), which may be re-derived having Eq. (3.3) as a starting point.

$$\left(\frac{\partial r}{\partial z}\right)_i = \kappa_m \frac{\rho_r}{\rho_z} \frac{z_C - z_i}{\sqrt{(z_C + \rho_z - z_i)(z_C - \rho_z + z_i)}} \quad (3.4a)$$

$$\left(\frac{\partial^2 r}{\partial z^2}\right)_i = -\kappa_m \frac{\rho_r \rho_z}{\sqrt{(z_C + \rho_z - z_i)(z_C - \rho_z + z_i)}}^3 \quad (3.4b)$$

$$\left(\frac{\partial^3 r}{\partial z^3}\right)_i = -3\kappa_m \frac{\rho_r \rho_z (z_C - z_i)}{\sqrt{(z_C + \rho_z - z_i)(z_C - \rho_z + z_i)}}^5 \quad (3.4c)$$

$$\left(\frac{\partial r}{\partial s}\right)_i = \begin{cases} 1 & \text{if } \left(\frac{\partial r}{\partial z}\right)_i \equiv \infty \\ -\frac{\left(\frac{\partial r}{\partial z}\right)_i}{\sqrt{1+\left(\frac{\partial r}{\partial z}\right)_i^2}} & \text{otherwise} \end{cases} \quad (3.4d)$$

$$\left(\frac{\partial z}{\partial s}\right)_i = \begin{cases} 0 & \text{if } \left(\frac{\partial r}{\partial z}\right)_i \equiv \infty \\ -\frac{1}{\sqrt{1+\left(\frac{\partial r}{\partial z}\right)_i^2}} & \text{otherwise} \end{cases} \quad (3.4e)$$

$$\phi_i = \frac{\pi}{2} - \tan^{-1} \left( - \left(\frac{\partial r}{\partial z}\right)_i \right) \quad (3.4f)$$

$$\left(\frac{\partial \phi}{\partial s}\right)_i = \begin{cases} \kappa_m \frac{\rho_z}{\rho_r^2} & \text{if } \left(\frac{\partial r}{\partial z}\right)_i \equiv \infty \\ \frac{\left(\frac{\partial z}{\partial s}\right)_i \left(\frac{\partial^2 r}{\partial z^2}\right)_i}{1+\left(\frac{\partial r}{\partial z}\right)_i^2} & \text{otherwise} \end{cases} \quad (3.4g)$$

$$\left(\frac{\partial^2 \phi}{\partial s^2}\right)_i = \begin{cases} 0 & \text{if } \left(\frac{\partial r}{\partial z}\right)_i \equiv \infty \\ -\left(\frac{\partial z}{\partial s}\right)_i \left( \frac{\left(\frac{\partial^3 r}{\partial z^3}\right)_i}{\sqrt{1+\left(\frac{\partial r}{\partial z}\right)_i^2}^3} - 3 \left(\frac{\partial r}{\partial z}\right)_i \frac{\left(\frac{\partial^2 r}{\partial z^2}\right)_i^2}{\sqrt{1+\left(\frac{\partial r}{\partial z}\right)_i^2}^5} \right) & \text{otherwise} \end{cases} \quad (3.4h)$$

### 3.1.4 Three-point arc segment geometry

While spherical shells can be generated with the 'Ellipse' options of the segment object, in some cases it is more convenient to generate their curved meridians as a circular arc passing through three non-collinear points. This can be done in AQUINAS using the '3pointArc' option, together with the additional input field for the radial and axial coordinates of the third point that the arc will pass through. This option can be very handy when it comes to scripting an axisymmetric shell problem quickly, without the need of evaluating the centre and radius of an arc, for which the analyst does know at least one additional point on top of the top and bottom edges. There is no requirement that the third point defining the arc should be set midway along the meridian between the other two, but it does need to be at an axial coordinate lower than that of the top edge but higher than the bottom one. Once the segment has been constructed, and the centre and radius of the implied circle on the 2D space of the meridian have been computed, the segment will be turned into an 'Ellipse', and be treated as such thereafter, using the derivatives of Eqs (3.4) for the formulation of the element's geometry.

### 3.1.5 Interpolated segment geometry

An option encompassing all of the previous ones, as well as cases of more arbitrary meridians that cannot be categorised into any of the previously presented families of

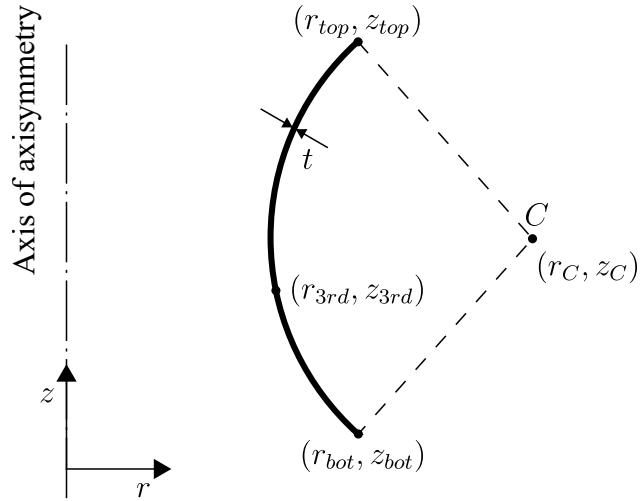


Figure 3.4: Meridional geometry definition of a circular arc segment defined through three points.

geometries, is that of a segment defined through an ‘Akima interpolation’ of a series of points. The ‘Interp’ option will initiate the generation of such a segment that has to go through all of the provided point coordinates, fitting a piecewise polynomial of up to third order (cubic). The procedure applied is considerably different compared to that of the cubic spline, as it allows for a quick regression into a linear portion of the fitted line, without the oscillations in the neighbourhood near this transition that the spline algorithm is usually associated with. The mathematics of the Akima interpolation have been meticulously presented by H. Akima in *A New Method of Interpolation and Smooth Curve Fitting Based on Local Procedures* [2], the formulation of which has been adopted here. It is important to note that the interpolation algorithm coded here has some minor differences compared to the modified Akima interpolation included with MATLAB’s distribution (which could not be used as there are special cases that have to be handled here). The interpolated geometry of a segment is illustrated in Figure 3.5 below.

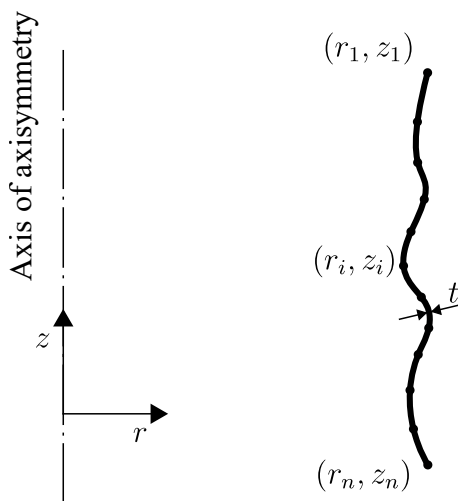


Figure 3.5: Meridional geometry definition of an interpolated segment, defined through a series of points.

While the locations of the points provided for the generation of an interpolation does

not have to coincide with the nodal ones, it should be done so whenever possible, to utilise the best performance attainable by the Akima interpolation algorithm implemented. It is important for the first node in the series to be the topmost one and the last one to be at the bottom. If this does not hold in the point series provided, it will be reversed internally with a warning message displayed to the command window to alert the user.

The interpolation results in a function of the radial coordinate  $r$  with respect to the axial coordinate  $z$ . This leads to a straightforward computation of all derivatives of  $r$  with respect to  $z$ . The remaining geometric derivatives may then be computed using the relationships of Eq. (3.4) for derivatives with respect to the arc coordinate  $S$ .

## 3.2 Analysis types

The AQUINAS toolbox is presently capable of carrying out the following computational structural analyses as defined by the Eurocode prEN 1993-1-6 [14] on the strength and stability of metal shells:

- LA: Linear elastic analysis to obtain the complete primary (membrane) and secondary (bending) stress state;
- LBA: Linear bifurcation analysis to obtain the critical and near-critical bifurcation buckling eigenvalues and associated eigenmodes;
- MNA: Materially nonlinear analysis to obtain the small-displacement plastic collapse mechanism;
- GNA: Geometrically nonlinear elastic analysis to obtain the deformation and stress state assuming large deflections, and to detect axisymmetric limit point and / or potentially non-symmetric bifurcation buckling;
- GMNA: Geometrically and materially nonlinear analysis which extends a GNA to include plasticity;
- GNIA: Geometrically nonlinear elastic analysis which extends a GNA to include imperfections (primarily unintended geometric deviations of the shell midsurface);
- GMNIA: Geometrically and materially nonlinear analysis which extends a GMNA to include imperfections.

By convention, LAs, LBAs, MNAs, GNAs and GMNAs are performed on a reference shell geometry defined by a ‘perfect’ midsurface assuming no imperfections of any kind, although a number of recent research works have undertaken ‘LBIAs’ [42] and ‘MNIs’ [58] under special circumstances. All (G)(M)N(I)As are implemented in AQUINAS as incremental path-tracing analyses using the arc-length algorithm. Every bifurcation buckling check assumes an axisymmetric pre-buckling stress state.

## 3.3 Optimisation

The buckling strength of an axisymmetric shell may be identified as a function  $F(n)$  of the circumferential full wave-number  $n$  associated with its bifurcation. Further capitalising

on the capability of AQUINAS to explicitly obtain the buckling load for any mode  $n$ , a minimisation approach on  $F(n)$  for the computation of the critical buckling resistance and circumferential mode can be established. This minimisation has to be performed in a computational manner, aiming at reducing the exhaustive evaluation of bifurcation loads corresponding to all competing harmonics for a specific shell problem.

The surrogate optimisation algorithm has been employed in AQUINAS in order to perform this minimisation. While this is a machine learning algorithm that is included in MATLAB's [30] Global Optimization Toolbox, the algorithm has been independently coded in AQUINAS, found in `AQUINAS_SO.m`, not only to reduce the number of dependencies for execution of the solver (since MATLAB toolboxes are not included in its basic distribution), but also in order to have full control over the parameters of the optimisation process.

A brief outline of the surrogate optimisation algorithm, as well as all of the parameters that govern its behaviour, is presented here. This section should not be viewed as a presentation of the surrogate optimisation process itself, but rather a description of the algorithm in the context of computing the critical bifurcation load and associated harmonic  $n$  in an efficient, less time consuming manner. The principles of *Engineering Design via Surrogate Modelling* by A. Forrester, A. Sóbester and A. Keane[46], are adopted in the current implementation of the surrogate optimisation algorithm. The surrogate model is obtained through a Gaussian process regression scheme, as is the most popular case for such models, with a Radial Basis Function kernel being used for obtaining the covariance of the Gaussian process.

The chief concept of the surrogate modelling approach to the optimisation of an unknown function, in this case that of the bifurcation load with respect to the harmonic number  $n$ , is the application of the minimisation procedure on a substitute ‘surrogate’ function that approximates the original over a range of  $n$  values. This model can be obtained through computing the value of the  $F(n)$  function for a few circumferential modes  $n$  and then fitting the approximate surrogate model on them through a Gaussian process. This stage can be thought of as the training of the surrogate model, with the bifurcation load acting as the dependent variable  $y$  and its associated harmonic  $n$  acting as the independent one  $x$  of the training range.

Training of the surrogate model is performed by computing one more bifurcation load for a circumferential mode that the model is not already trained on. Deciding which harmonic should be used to enhance the surrogate model is done on the basis of an Expected Improvement (EI) function, as presented in [46], that aims on maximising the accuracy of the prediction on the global minimum of the original function. The amount of improvement expected is evaluated based on the mean  $\hat{y}(x)$  and variance  $\hat{s}^2(x)$  of the surrogate model [46], given as

$$E[I(x)] = (y_{min} - \hat{y}(x))\Phi\left(\frac{y_{min} - \hat{y}(x)}{\hat{s}(x)}\right) + \hat{s}\phi\left(\frac{y_{min} - \hat{y}(x)}{\hat{s}(x)}\right) \quad (3.5)$$

where  $\Phi()$  is the cumulative distribution function and  $\phi()$  is the probability density function.

The harmonic  $n$  corresponding to the maximum value of the EI function will be used as the new training data point in order to update the surrogate model. Once the maximum Expected Improvement is below some threshold tolerance, the surrogate optimisation has converged into a reasonable approximation of the original function. The minimum of the surrogate model constitutes a prediction for the critical bifurcation load of the axisymmetric shell model. The surrogate optimisation algorithm may also be terminated by exhausting a number of iterations without achieving convergence of the surrogate model,

in which case the already computed data will be used for an estimation of the critical bifurcation load.

In its most basic form, the lower and upper bounds of the training range for the surrogate models are kept constant throughout the optimisation process. This is not the case for the current implementation of the algorithm, as it may not be apparent how high of a circumferential wave-number  $n$  should be considered as competing for the bifurcation of thin axisymmetric shells. A way to deal with this issue could potentially be to consider an extremely high harmonic as the upper bound of the range. Such an approach has the major drawback of spending considerable computational time for training of the model over an extensive range of harmonics. Instead, a harmonic is to be used as an initial upper bound, only to be updated if the surrogate model expects improvement toward the higher end of its training range. A step for expanding the upper bound of the range of competing harmonics will be used in such a case, the value of which can be set by the analyst before submission of an analysis.

It is not uncommon in Gaussian processes, when used in the context of machine learning algorithms, to have their hyper-parameters optimised as the surrogate model develops, so that the best possible approximation to the original function can be achieved. This technique is also applied here, with the optimisation of the hyper-parameters performed through a maximising process of the log marginal likelihood function, as per the algorithmic procedures presented in *Gaussian Processes for Machine Learning* by C.A. Rasmussen and C.K.I. Williams [59]. It is important to note that the step of hyper-parameter optimisation is an optional one in the overall course of the surrogate model training, and the hyper-parameters may be kept constant at their initial values, before entering the surrogate optimisation loop.

Once the surrogate model has been trained for the current loop of the optimisation process, and the non-compulsory operations of updating the upper bound of the training range or optimising the hyper-parameters have either been carried out or skipped, it is time to update the surrogate function itself, through a Gaussian Process Regression scheme, in preparation of the next iteration in the optimisation process. A Radial Basis Function (RBF) constitutes the most basic, but also popular, choice of a kernel for the Gaussian process for computing the covariance between points. The kernel will in turn help in the approximation of the ‘true’ function form between trained data points. For a more in depth presentation of the underlying mathematics of Gaussian processes, the interested reader is encouraged to examine the formulations of [59] as a valuable and well established resource for such methods.

A practical example of the surrogate optimisation process in the context of computing the critical bifurcation load of an axisymmetric shell is illustrated in the following Figures 3.6 - 3.11. As showcased, there are two ways to approach the problem of evaluation of the linear bifurcation strength for a cylindrical shell under axial compression, a problem that will be further investigated in Chapter 5 while studying the results of `input_Example_LBA01.m`. The first, and rather laborious one, is the extensive computation of the eigenvalues (corresponding the bifurcation LPF for LBA problems) for all competing harmonics  $n$ . This approach gets increasingly expensive in computational time as the cylinders increase in slenderness. For a cylinder with an  $r/t$  ratio of 2000, the competing circumferential modes may go all the way up a harmonic  $n$  of 61.

The alternative of using a surrogate model to perform the minimisation has considerable advantages, as only a fraction of the modes need to be actually processed through the FE solver of AQUINAS. Starting with an initial number of 8 data points to generate

the surrogate model, the optimisation process is applied, gradually obtaining a better approximation of the true eigenvalue distribution in the neighbourhood of its global minima. The 95% confidence intervals are also plotted, showing the ‘confidence’ of the Gaussian process’s estimation. These intervals get closer to the mean distribution of the prediction, as more steps are taken in the optimisation process and the model is trained. Only a mere 13 modes are actually computed (with the axisymmetric one evaluated after convergence of the model), leading to a 78.7 % percent save in FE computational time.

This case also serves as a warning statement of the limitations of this machine learning algorithm. Even though the actual global minima is located, a second convex region exists for ‘low’ circumferential mode numbers, which is completely missed during the optimisation process. While this is of no severe consequence for the current investigation, the results of the surrogate optimisation process are not to be trusted blindly, and a ‘sanity check’ should be performed at the end of the procedure.

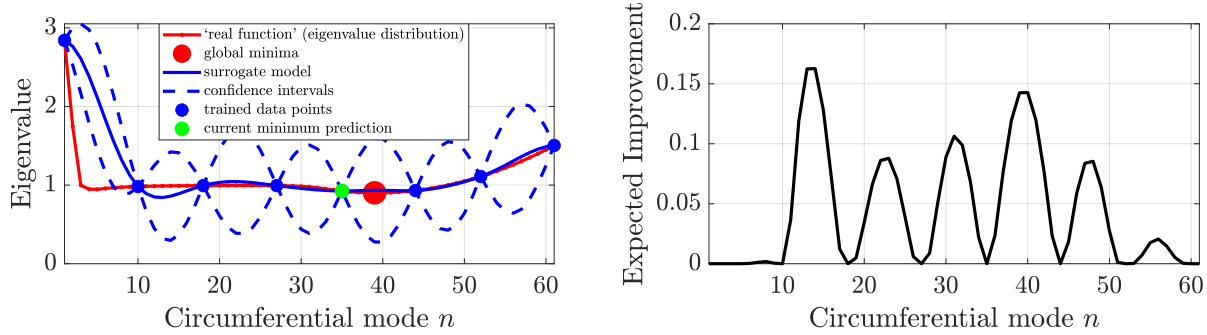


Figure 3.6: Initial training of surrogate model.

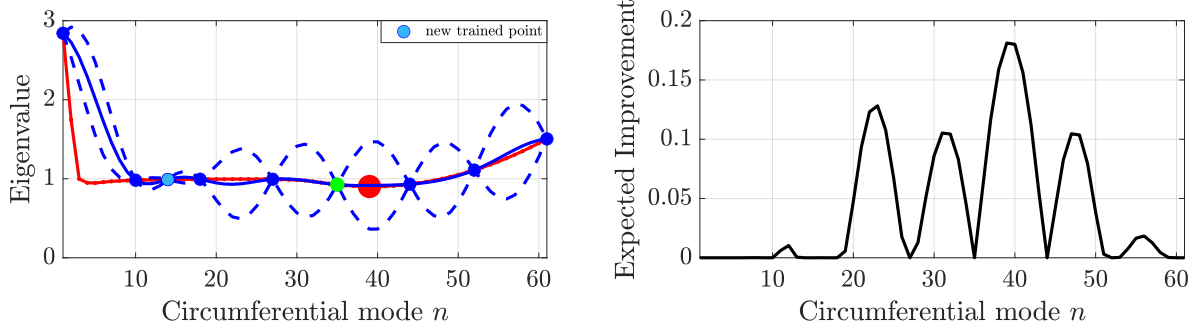


Figure 3.7: First training step in the surrogate optimisation process.

The flow of control for the surrogate optimisation algorithm, as coded in the `AQUINAS_SO.m` script, is presented in Figure 3.12, where the steps with a dashed line correspond to optional actions, that may or may not be undertaken in the process of training the surrogate model.

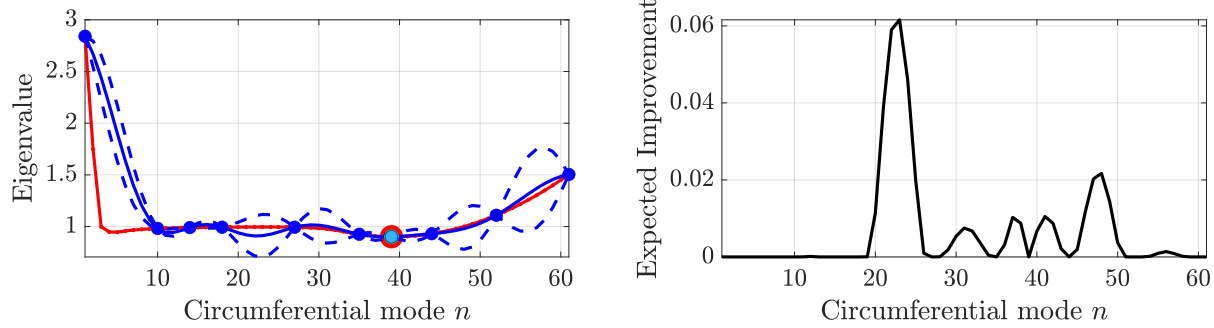


Figure 3.8: Second training step in the surrogate optimisation process.

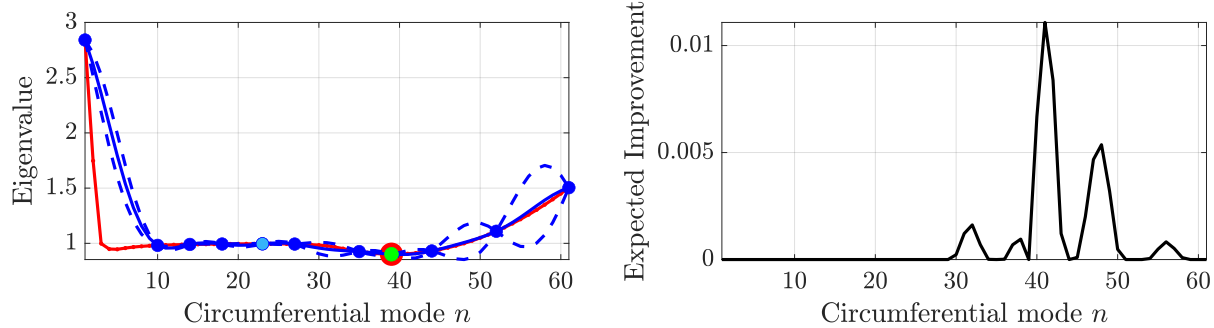


Figure 3.9: Third training step in the surrogate optimisation process.

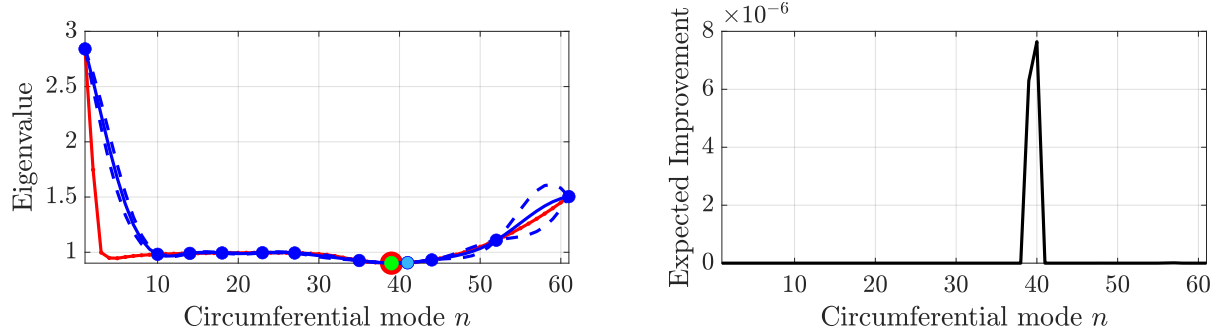


Figure 3.10: Fourth training step in the surrogate optimisation process.

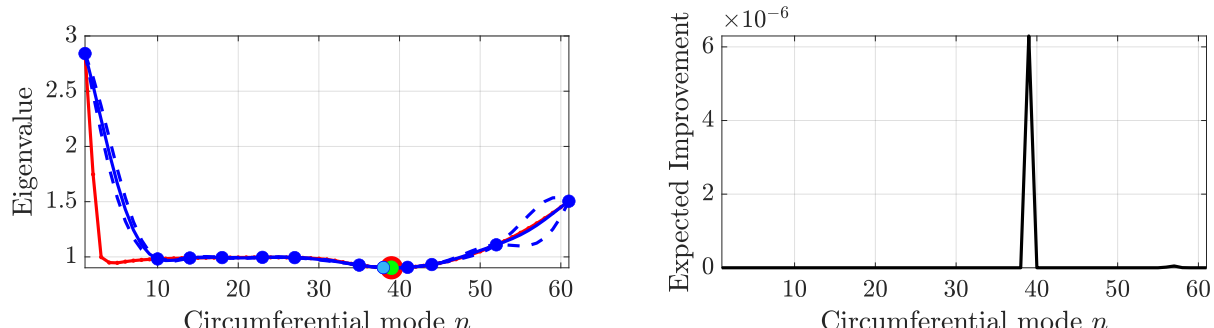


Figure 3.11: Fifth (and final) training step in the surrogate optimisation process.

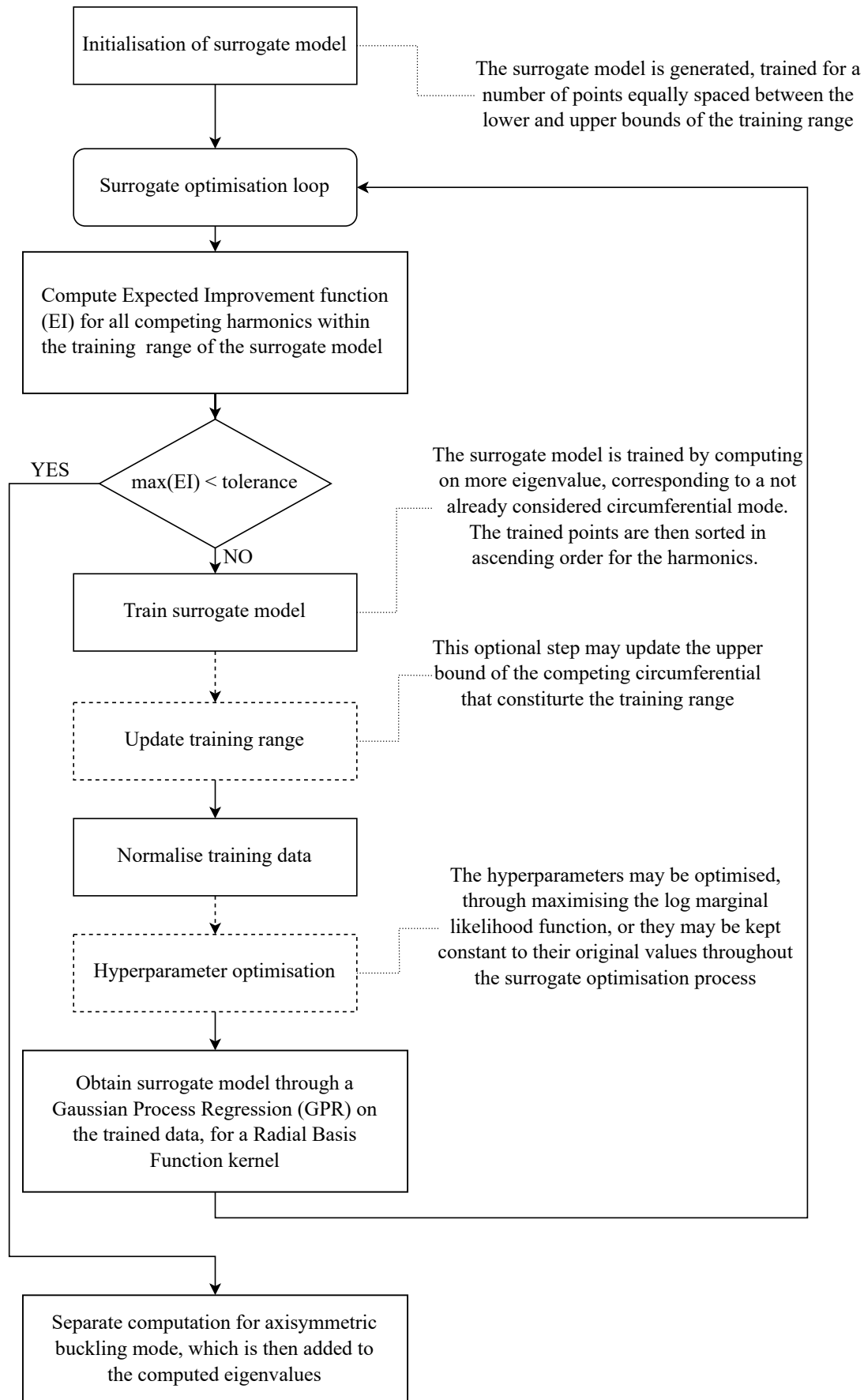


Figure 3.12: AQUINAS Surrogate Optimisation flowchart.

# Chapter 4

## Software architecture

Submitting a linear or nonlinear analysis with AQUINAS is facilitated with MATLAB’s [30] object oriented programming capabilities. An understanding of the way to define different AQUINAS objects, as well as the purpose they serve in any type of analysis, is important to the successful solution of an axisymmetric shell problem. The name-value pairs, either necessary or optional, for the generation of any object will be presented one by one with useful tips provided on the appropriate values that may be assigned to each.

### 4.1 Flow of control in AQUINAS

Before going into the individual study of the available AQUINAS objects, the general software architecture will be briefly presented so that the reader may familiarise themselves with its internal proceedings and stages of an analysis. Flow of control within AQUINAS is outlined in Figure 4.1, where some distinct levels in the solution process may be identified. The user instantiates a suite of objects representing the geometry, loads, constraints, materials, solver settings and output requests, and submits these as a `varargin` (variable-length argument list) to the `AQUINAS_Protocol.m` function which acts as a central control pipeline through the software. A series of error checks are then performed in the master script `AQUINAS_Protocol` to ensure their combination actually defines an axisymmetric shell problem. The reader is cautioned that these error checks do not exhaust all possible cases of ill-defined objects or axisymmetric shell problems and the actual understanding of the objects, in the context of different analysis types, is valuable.

Having confirmed the appropriate definition of the necessary components for an analysis to be submitted, control is passed to the relevant script. Adopting the terminology of prEN1993-1-6 [14], the different analysis scripts are `AQUINAS_LA.m`, `AQUINAS_LBA.m` and `AQUINAS_GMNA.m`. Geometric and material nonlinearities are taken into account in the same piece of code responsible for all nonlinear incremental types of analysis. While an interaction between `AQUINAS_GMNA.m` and `AQUINAS_LBA.m` may appear suspicious at first sight, the reader is reassured that this is just the name of the script and the current stress state of the shell is considered in the bifurcation checks performed on the last converged increment of a nonlinear analysis. `AQUINAS_S0.m` acts as a wrapper to either linear or nonlinear bifurcation checks with `AQUINAS_LBA.m` during a surrogate optimisation process (see the *Optimisation* section of Chapter 3).

The results of any analysis are then either organised in a structured output for the analyst to perform any post-processing and plotting in their master input scripts, or written into an ASCII text type of file to be processed at a later stage. This last capability

is not entirely functional and currently under development (hence the dashed lines in Figure 4.1), to be made available in a later release of AQUINAS.

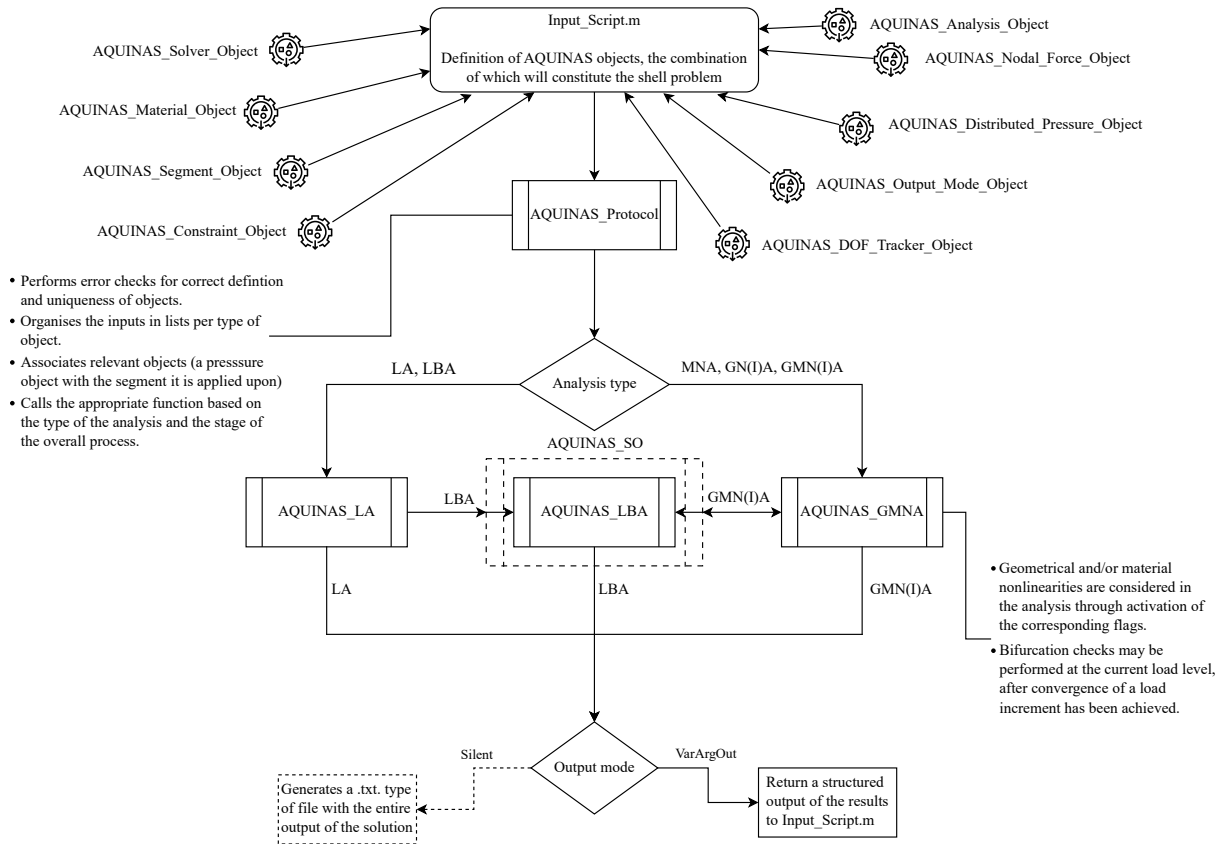


Figure 4.1: AQUINAS general flow of control diagram

## 4.2 Class descriptions

AQUINAS takes advantage of MATLAB's object oriented programming capabilities, using several different classes of objects for the analysis of an axisymmetric shell problem. Their assembly and organisation through `AQUINAS_Protocol` formulates a computationally defined shell model, to be processed by the appropriate AQUINAS script for the generation of the FE solution.

For all AQUINAS objects, the inputs parameters provided for their creation should be in name-value pairs. This allows for quickly testing the inputs, for both their type and value, using MATLAB's intrinsic argument validation tools. Any checks that cannot be handled through the argument validation functions are executed inside the constructor of each object, in case the potential issue corresponds to incompatible, missing or ill-defined name-value pairs for a single object definition, or in `AQUINAS_Protocol` if the potential error corresponds to incompatibilities between different AQUINAS objects for a given type of analysis. Failing any of these checks will lead to an error message and termination of execution.

The purpose that each AQUINAS class serves for every different type of analysis will be outlined in the following paragraphs. The necessary and optional name-value pairs for all objects will be presented, providing information on possible values that each may take and defaults that will be assigned if explicit definition is omitted.

### 4.2.1 AQUINAS Material Object

One of the objects that are absolutely necessary for defining an AQUINAS axisymmetric shell problem is the `AQUINAS_Material_Object`. The same class can be used for both materially linear (elastic) or nonlinear (elastic-plastic) analyses. The name-value pairs for a material object are the following:

**•♦ *name***

**Necessity:** Compulsory

**Description:** The name of the material object, to be used for associating with segment objects.

**Appropriate values:** Non-zero length character array.

**Default value:** none

**•♦ *E***

**Necessity:** Compulsory

**Description:** The Young's modulus *E* (modulus of elasticity) of the material.

**Appropriate values:** Positive real value.

**Default value:** none

**•♦ *nu***

**Necessity:** Compulsory

**Description:** The Poisson's ratio  $\nu$  of the material.

**Appropriate values:** Positive real value.

**Default value:** none

**•♦ *G***

**Necessity:** Compulsory

**Description:** The shear modulus of the material, defined for isotropic materials as  $G = \frac{E}{2(1+\nu)}$ .

**Appropriate values:** Positive real value.

**Default value:** none

**•♦ *sy***

**Necessity:** Compulsory for MNA and GMNA types of analysis, see the definition of `AQUINAS_Analysis_Object` below

**Description:** The stress values that correspond to a uniaxial stress-strain curve, to be used with the Von Mises yield criterion.

**Appropriate values:** 1D array of positive real values.

**Default value:** none

**•♦ *ep***

**Necessity:** Compulsory for MNA and GMNA types of analysis, see the definition of `AQUINAS_Analysis_Object` below

**Description:** The plastic strain values that correspond to a uniaxial stress-strain curve, to be used with the Von Mises yield criterion.

**Appropriate values:** 1D array of positive real values.

**Default value:** none

❖ *CurveDef*

**Necessity:** Compulsory for MNA and GMNA types of analysis, see the definition of `AQUINAS_Analysis_Object` below

**Description:** The type of the stresses-strains provided, can be either 'True' (Cauchy) or 'Engineering' (see Chapter 4.6 of [16]). If this argument is set to 'Engineering' then the stresses and plastic strains will be transformed to 'True' internally in the constructor of the object, according to the following formulae:

$$\sigma_{y,T} = \sigma_{y,E}(1 + \epsilon_{p,E}) \quad (4.1a)$$

$$\epsilon_{p,T} = \ln(1 + \epsilon_{p,E}) \quad (4.1b)$$

**Appropriate values:** 'True' or 'Engineering'

**Default value:** Undefined

On top of the arguments presented above, the reader may recognise by looking into the script for `AQUINAS_Material_Object` that there are also additional name-value pairs corresponding to the Young's modulus and Poisson's ratio for orthotropic materials, with different values along the meridional and circumferential directions of the shell. This functionality is currently under development and will be supported in a later release of the software.

## 4.2.2 AQUINAS Segment Object

As is the case with every other FE software, the geometric definition of the computational problem is a crucial component in a model's submission for analysis. For axisymmetric shell problems, this definition takes place in the 2D sub-space of positive radial coordinates. In the present computational toolbox, this is done by creating an `AQUINAS_Segment_Object` that will take care of generating all the necessary geometric properties and derivatives needed for axisymmetric shell elements according to the FE formulation of [50].

The name-value pairs that can be used for the definition of a segment object in AQUINAS are:

❖ *type*

**Necessity:** Compulsory

**Description:** The type of shell segment to be defined. Can be either a plate, a cone, an ellipse, an arc defined through 3 points or a meridian obtained by interpolating from a series of *r-z* points provided.

**Appropriate values:** 'Plate', 'Cone', 'Ellipse', '3pointArc' or 'Interp'

**Default value:** none

❖ *material*

**Necessity:** Compulsory

**Description:** The name of the `AQUINAS_Material_Object` which contains the computational definition of the material that the segment is made from.

**Appropriate values:** Character array.

**Default value:** none

❖ *formulation*

**Necessity:** Optional

**Description:** Whether to use a thin or thick formulation for the segment. Currently, only the thin shell theory option can be employed, with the alternative of a thick shell to be released at a later stage, for the analysis of segments where the transverse shear effects cannot be neglected.

**Appropriate values:** 'thin' or 'thick'

**Default value:** 'thin'

❖ *thickness*

**Necessity:** Compulsory

**Description:** The thickness of the shell meridian.

**Appropriate values:** Non-zero positive real value.

**Default value:** none

❖ *rzbot*

**Necessity:** Compulsory for shell segments of type 'Plate', 'Cone', 'Ellipse' or '3pointArc'

**Description:** The radial and axial coordinates of the 'bottom' of the segment's meridian. For 'Plate' types of segments the bottom end should be the outer edge.

**Appropriate values:** 1D array containing 2 values, corresponding to the radial  $r$  and axial  $z$  coordinates of the bottom edge. The radial coordinate should be greater or equal to zero, otherwise a violation of axisymmetry error will occur.

**Default value:** none

❖ *rztop*

**Necessity:** Compulsory for shell segments of type 'Plate', 'Cone', 'Ellipse' or '3pointArc'

**Description:** The radial and axial coordinates of the 'top' of the segment's meridian. For 'Plate' types of segments the top end should be the inner edge.

**Appropriate values:** 1D array containing 2 values, corresponding to the radial  $r$  and axial  $z$  coordinates of the top edge. The radial coordinate should be greater or equal to zero, otherwise a violation of axisymmetry error will occur.

**Default value:** none

❖ *rz3rd*

**Necessity:** Compulsory for shell segments of type '3pointArc'

**Description:** The radial  $r$  and axial  $z$  coordinates of the required 3rd point for the definition of a circular arc.

**Appropriate values:** 1D array containing 2 values, corresponding to the radial  $r$  and axial  $z$  coordinates of the 3rd point.

**Default value:** none

❖ *rzpts*

**Necessity:** Compulsory for shell segments of type 'Interp'

**Description:** A collection of radial and axial coordinates that will be used for the definition of the shell segment through application of an Akima interpolation [2].

**Appropriate values:** 2D array containing  $r$ - $z$  pairs of points. The points should be sorted in a top-down manner, in order to reflect the order of nodes in AQUINAS. If not then they will be re-ordered in the constructor of the segment, with a warning message outputted to the command window in order to inform the analyst.

**Default value:** none

#### ❖ *geom*

**Necessity:** Compulsory for shell segments of type 'Ellipse'

**Description:** Auxiliary geometric properties for the definition of elliptical meridians. The radial and axial coordinates of the centre of the ellipse, as well as the lengths of the major and minor axes  $a$  and  $b$ , are necessary for the definition of an elliptical segment. For circular segments the minor and major axes lengths should be equal to the radius  $r_\phi$  of the meridian. Rotated ellipses are currently not supported in AQUINAS (or at least not through this option).

**Appropriate values:** 1D array containing 4 values, corresponding to the radial and axial coordinates of the ellipse's centre and the major and minor axes lengths, taken along the radial  $r$  and axial  $z$  axes. The values need to be provided with this specific order in mind.

**Default value:** none

#### ❖ *els*

**Necessity:** Compulsory

**Description:** The number of elements used for the discretization of the shell's meridian.

**Appropriate values:** Positive non-zero integer.

**Default value:** none

#### ❖ *meshtype*

**Necessity:** Optional

**Description:** The type of grading to be applied on the mesh, in order to achieve higher discretisation at a specific portion of the shell's meridian. The grading can be applied towards either end of the meridian, with the single 'S' option, towards both ends with the edge 'E' option or towards the centre of the meridian with the middle 'M' option.

**Appropriate values:** 'S', 'E' or 'M'

**Default value:** 'S'

#### ❖ *g*

**Necessity:** Optional

**Description:** The grading parameter. For higher values of  $g$  the effect of the graded discretisation will be more pronounced. Negative values of  $g$  correspond to an inverted grading. For example, setting 'meshtype' to 'E' with a negative  $g$  will lead to a mesh that is graded towards the centre of the shell's meridian.

**Appropriate values:** Real values in the closed range of [ -1.0 , 1.0 ].

**Default value:** 0.0

### 4.2.3 AQUINAS Nodal Force Object

For axisymmetric shells, computationally modelled in the 2D space with the necessary kinematic assumptions along their circumference, a nodal force corresponds to a line load evenly distributed in the circumferential direction. Defining a nodal force in AQUINAS is done by using the `AQUINAS_Nodal_Force_Object`, with minimal inputs required.

For software architecture purposes, a nodal force may only be applied at the edge of a segment object. Therefore, the coordinates of the point where the force is applied must coincide with any of the edge of the segment objects included in the analysis submission. In case this does not hold, an error will occur.

In AQUINAS, the magnitude of the force object should be equal to that of the corresponding line load ( $F/L$  units), instead of the total force resultant ( $F$  units) that ABAQUS [1] users may be familiar with. Any necessary scaling based on the radial position that the load is applied to will be taken care by AQUINAS internally. It should also be noted that the magnitude is a signed algebraic value and should be negative if the applied force does not share the same direction as the global  $r - z$  axes.

The definition of this object is optional, since a shell problem can be generated without a line load applied anywhere on the FE model. The necessary name-value pairs for the definition of a `AQUINAS_Nodal_Force_Object` are the following:

**•♦ *type***

**Necessity:** Compulsory

**Description:** The direction that the force is applied along, can be either '`Fw`' for radial loads or '`Fw`' for axial ones. For forces that are not parallel to any of the two global axes, the load should be split into the individual components and two `AQUINAS_Nodal_Force_Object` should be submitted for analysis.

**Appropriate values:** '`Fu`' or '`Fw`'

**Default value:** none

**•♦ *rcoord***

**Necessity:** Compulsory

**Description:** The radial coordinate of the point that the nodal force (line load) is applied at.

**Appropriate values:** Positive real value.

**Default value:** none

**•♦ *zcoord***

**Necessity:** Compulsory

**Description:** The axial coordinate of the point that the nodal force (line load) is applied at.

**Appropriate values:** Real value.

**Default value:** none

**•♦ *magnitude***

**Necessity:** Compulsory

**Description:** The signed algebraic magnitude of the nodal force (line load) applied at the edge of a shell segment.

**Appropriate values:** Real value.

**Default value:** none

A reader who visits the script for the AQUINAS nodal force object may notice that there is an additional name-value pair corresponding to the origin of the object. This property is necessary for the internal workings of AQUINAS in case a nodal force object is applied at a point where two or more segments meet, and should not be altered by the users at the level of object creation.

#### 4.2.4 AQUINAS Distributed Pressure Object

On top of using a nodal force object to define the loading conditions of the axisymmetric shell problem, the analyst has the option to define a distributed pressure along the meridian. The `AQUINAS_Distributed_Pressure_Object` object may be used for defining a normal or tangential pressure (traction) in the meridional direction. The pressure is assumed to be uniform along the circumference of the shell, but may have any distribution along the meridian, provided that it can be defined through a function handle with respect to either the radial, axial or angle  $\phi$  coordinate of the meridian.

The name-value pairs that can be used for generating a pressure object are the following:

**•♦ *segments***

**Necessity:** Compulsory

**Description:** A cell array of `AQUINAS_Segment_Object` that the distributed pressure will be applied to (can be more than one).

**Appropriate values:** Cell array of `AQUINAS_Segment_Objects`.

**Default value:** none

**•♦ *type***

**Necessity:** Compulsory

**Description:** The pressure type applied, which can be either normal or tangential (traction).

**Appropriate values:** 'pn' for normal pressure and 'pt' for tangential.

**Default value:** none

**•♦ *functionHandle***

**Necessity:** Compulsory

**Description:** The function handle to be used for determining the magnitude of the distributed pressure on the nodes along each relevant segment's meridian. Even for constant pressure this property needs to be a function handle.

**Appropriate values:** A function handle, defined with respect to one variable at most.

**Default value:** none

**•♦ *withRespectTo***

**Necessity:** Optional

**Description:** The variable that the function handle is defined with respect to.

**Appropriate values:** '-' for constant pressures, 'r' for function handles with respect to the radial coordinate, 'z' for function handles with respect to the axial one and 'phi' if defined with respect to the meridional angle  $\phi$ .

**Default value:** '-'

### 4.2.5 AQUINAS Constraint Object

Boundary conditions and shell segment interactions alike are being handled by the constraint object in AQUINAS. The `AQUINAS_Constraint_Object` is responsible for generating appropriate Lagrange multiplier terms that will enrich the global stiffness matrix of the system. These terms will account for any kind of edge restraints, eccentric connections between segments or ensuring connectivity of segments that share an edge point (this last task is handled internally). Implementing boundary conditions with the method of Lagrange multipliers also allows for the definition of inclined roller restraints as well as conditions that may be linear combinations of nodal DOFs. For the same reasons outlined in the `AQUINAS_Nodal_Force_Object`, a boundary condition constraint may only be applied at the edge of a segment.

The name-value pairs that the `AQUINAS_Constraint_Object` supports are the following:

#### •♦ *type*

**Necessity:** Optional

**Description:** The type of the constraint condition that will be generated, can be either '`bc`' for a boundary condition constraint or '`ecc`' for an eccentric connection.

**Appropriate values:** '`bc`' or '`ecc`'

**Default value:** '`bc`'

#### •♦ *state*

**Necessity:** Optional, only relevant to boundary conditions ('`bc`')

**Description:** The state of the analysis that the boundary conditions will be applied at. Can be '`general`' for constraints that are applied at all the steps of an analysis, '`prebuckling`' for constraints that are only applied in the axisymmetric solution steps of the analysis or '`buckling`' for boundary conditions that are only taken into account during bifurcation checks of the FE model.

**Appropriate values:** '`general`', '`prebuckling`' or '`buckling`'

**Default value:** '`general`'

#### •♦ *rcoord*

**Necessity:** Compulsory for boundary conditions ('`bc`')

**Description:** The radial coordinate of the point that the boundary condition is applied at.

**Appropriate values:** Real positive value.

**Default value:** none

#### •♦ *zcoord*

**Necessity:** Compulsory for boundary conditions ('`bc`')

**Description:** The axial coordinate of the point that the boundary condition is applied at.

**Appropriate values:** Real value.

**Default value:** none

#### •♦ *dofs*

**Necessity:** Compulsory for boundary conditions ('`bc`')

**Description:** The DOF identifiers that are constrained by the current object, organised in a MATLAB cell array. Their identifiers for translational DOFs are '*u*' for the radial, '*w*' for the axial and '*v*' for the circumferential one, which is only relevant for the bifurcation checks of an analysis (like having default '*buckling*' state). The '*b*' or '*beta*' identifiers both refer to the rotation of the meridian. More than one DOFs may be included in the cell array input, in the same order that their LHS coefficients are ordered.

**Appropriate values:** '*u*', '*v*', '*w*', '*b*' or '*beta*'

**Default value:** none

❖ ***coeffLHS***

**Necessity:** Optional, only relevant for boundary conditions ('*bc*')

**Description:** The Left Hand Side (LHS) coefficients of the constraint, to be used according to the Lagrange multipliers method in the LHS of the equilibrium equation (stiffness matrix) during analysis. It is assumed that they follow the ordering of the '*dofs*' cell array.

**Appropriate values:** Cell array of real values (or just one value if there is just one type of DOF in the '*dofs*' option).

**Default value:** 1

❖ ***coeffRHS***

**Necessity:** Optional, only relevant for boundary conditions ('*bc*')

**Description:** The Right Hand Side (RHS) coefficient of the constraint, to be used according to the Lagrange multipliers method in the RHS of the equilibrium equation (force vector) during analysis.

**Appropriate values:** '*u*', '*v*', '*w*', '*b*' or '*beta*'

**Default value:** 0

❖ ***segments***

**Necessity:** Compulsory for eccentric connections '*ecc*'

**Description:** A cell array containing exactly two *AQUINAS\_Segment\_Object*, which will be treated as connected eccentrically.

**Appropriate values:** Cell array of *AQUINAS\_Segment\_Objects*.

**Default value:** none

❖ ***ends***

**Necessity:** Compulsory for eccentric connections '*ecc*'

**Description:** A cell array containing exactly two character arrays, corresponding to the ends of the segments to connect eccentrically. The '*ends*' cell array should have the same ordering as the '*segments*' cell array.

**Appropriate values:** Cell array containing '*bot*' or '*top*' entries.

**Default value:** none

The default values for the '*coeffLHS*' and '*coeffRHS*' name-value pairs allow for a classic restraint of a nodal DOF to be readily applied, provided that the user has only one DOF in the '*dofs*' cell array. On the other hand, if the constraint object corresponds to an eccentric connection between segments, then the magnitude of said eccentricity will be computed on the fly by AQUINAS as the distance between the associated ends of the connected segments.

As was the case with some of the previously defined objects, there is an additional name-value pair that is not to be provided by the analyst on creation of the object. By default, the '`origin`' of a constraint object is set to '`user`', but may also be '`auto`' for automatically generated constraints. This necessary internal process ensures that segments that share a common edge are rigidly connected. If a segment is all alone and unconnected in the 2D axisymmetric space then an error will occur.

Contrary to what the reader might think for a constraint in the FE model, this is actually a fully optional object in AQUINAS. A computational shell problem may be submitted for analysis without any constraints and result to a robust solution process. As an example, a cylinder under the effect of two opposing axial edge loads constitutes a problem that has been tested and solved with AQUINAS, even without the inclusion of constraints during the call to `AQUINAS_Protocol`. However, regardless of the possibility of being successful in dealing with ill-defined FE models, the Authors strongly advise to ensure a sufficiently constrained model is submitted for analysis in order to avoid numerical issues during the solution process.

#### 4.2.6 AQUINAS DOF Tracker Object

For purposes of output and post-processing, `AQUINAS_Output_Mode_Object` tracks the development of a specific DOF at any end of a segment object. The DOF to be tracked will also be used for visualising purposes of the nonlinear solution process (either it being GNA, MNA or GMNA), if the corresponding option in the solver object is activated. The equilibrium path tracked will also be stored for output and included in the structured output of AQUINAS. The name-value pairs that combined define a DOF tracker are:

- ♦ ***name***

**Necessity:** Compulsory

**Description:** A character array with the desired name for the DOF tracker.

**Appropriate values:** Character array.

**Default value:** none

- ♦ ***segment***

**Necessity:** Compulsory

**Description:** The `AQUINAS_Segment_Object` that the DOF tracker is applied to.

It can be either of the two ends of the segment.

**Appropriate values:** A single `AQUINAS_Segment_Object`.

**Default value:** none

- ♦ ***activeEnd***

**Necessity:** Compulsory

**Description:** The end of the segment that the DOF tracker is applied.

**Appropriate values:** '`top`' or '`bot`' / '`bottom`'

**Default value:** none

- ♦ ***typeOfDOF***

**Necessity:** Compulsory

**Description:** The type of DOF to be tracked by `AQUINAS_DOF_Tracker_Object`.

A tracker cannot be tasked to trace the circumferential DOF '`v`' since that is set to zero in the axisymmetric pre-buckling state of the shell.

**Appropriate values:** 'u', 'w' or 'b' / 'beta'

**Default value:** none

❖ *colour*

**Necessity:** Optional

**Description:** The colour to be used for plotting purposes of the equilibrium path for the DOF to be traced, only relevant if the nonlinear visualiser is enabled.

**Appropriate values:** Any colour format supported by MATLAB.

**Default value:** ['rand' 'rand' 'rand']

❖ *marker*

**Necessity:** Optional

**Description:** The marker to be used for plotting purposes of the equilibrium path for the DOF to be traced, only relevant if the nonlinear visualiser is enabled.

**Appropriate values:** Any marker option supported by MATLAB.

**Default value:** 'o'

❖ *markerSize*

**Necessity:** Optional

**Description:** The marker size to be used for plotting purposes of the equilibrium path for the DOF to be traced, only relevant if the nonlinear visualiser is enabled.

**Appropriate values:** Non-zero positive real value.

**Default value:** 3

## 4.2.7 AQUINAS Output Mode Object

While an analysis may be executed from start to finish without the inclusion of an `AQUINAS_Output_Mode_Object` in the submission to `AQUINAS_Protocol`, the results will be inaccessible for the analyst to examine. Currently, there is just one option for output in AQUINAS, that of a structured collection of result data, while there is an additional mode under development that will allow results to be written in a `.txt` file format, to be accessed after completion of the analysis. Most of the name-value pair options in this object correspond to the text version of the output, with the only two pair options that may be provided for the current version of AQUINAS being:

❖ *mode*

**Necessity:** Optional

**Description:** The output mode that AQUINAS will run in. Can be either '`Silent`' for no output or '`VarArgOut`' for AQUINAS to return a struct containing results. The '`WriteFile`' option, that the reader may see in the class definition for `AQUINAS_Output_Mode_Object` corresponds to the text output mode, that is currently not fully functional but will be made available at a later release of AQUINAS.

**Appropriate values:** '`Silent`' or '`VarArgOut`'

**Default value:** '`Silent`'

❖ *level*

**Necessity:** Optional

**Description:** The detail level of the output information in AQUINAS.

**Appropriate values:** 'basic' or 'extensive'

**Default value:** 'extensive'

#### 4.2.8 AQUINAS Analysis Object

A single `AQUINAS_Analysis_Object` has to be included in the submission of the model. The object carries the fundamental property '`type`', which corresponds to the type of analysis to be executed, and guides `AQUINAS_Protocol` to make the necessary calls to the appropriate scripts. Apart from the '`type`' property, this object is also relevant to analyses executing bifurcation checks at some point in their runtime by providing information on the circumferential wave-numbers that need to be trialled. The name-value pairs available for its definition are:

- ❖ ***type***

**Necessity:** Compulsory

**Description:** The type of analysis to be executed by AQUINAS, following the terminology of EN1993-1-6 [14].

**Appropriate values:** 'LA', 'LBA', 'GNA', 'MNA' or 'GMNA'

**Default value:** none

- ❖ ***circumferentialModes***

**Necessity:** Compulsory if bifurcation checks are to be executed. Redundant if bifurcation checks are to be executed with the Gaussian Process Regression minimisation option enabled (see `AQUINAS_Solver_Object` below)

**Description:** The circumferential wave-numbers to be trialled during each bifurcation checks step during analysis

**Appropriate values:** 1D array of positive integer values.

**Default value:** none

- ❖ ***noEigenvalues***

**Necessity:** Optional, redundant if the bifurcation checks are executed as part of a nonlinear analysis process (just the 1st eigenvalue for each trialled circumferential wave-number is needed)

**Description:** The number of eigenvalues obtained during the call to eigenvalue function '`eigs`' for each circumferential wave-number.

**Appropriate values:** Non-zero positive integer.

**Default value:** 1

- ❖ ***normalizeEigs***

**Necessity:** Optional, only relevant if eigenvectors are to be included in the output

**Description:** The method used for the normalisation of the eigenvectors. Can be either '-' if non normalisation is applied, 'SecondNorm' if the second norm of the eigenvector is used for its normalisation, or 'MaxValue' if the normalisation is to be performed according to the maximum value in the eigenvector (with this method the new maximum will have a value of 1.0).

**Appropriate values:** ' - ', 'SecondNorm' or MaxValue

**Default value:** ' - '

### 4.2.9 AQUINAS Solver Object

A crucial object, a single `AQUINAS_Solver_Object` is required for any type of analysis to be processed by AQUINAS. The solver contains all of the necessary computational choices that will determine whether the submitted shell problem is numerically well-defined and its results are to be trusted. While for the most part appropriate default values have been set for the different options of this object, care must be exercised to ensure that the underlying assumptions that these defaults are driven by do indeed hold for the shell model the analyst submits for analysis. Because of the large number of options this object has for its constructor, the name-value pairs are organised, both here as well as in the AQUINAS class, in families of relevant parameters. The options are the following:

- *Miscellaneous*

- ❖ *compiler*

**Necessity:** Optional

**Description:** The 'compiler' to be used for the numerically expensive computations of the stiffness matrices and internal force vectors (especially relevant to MNA-GMNA types of analysis). Can be either Matlab or C++, using the pre-compiled `mex` files. While C++ is substantially faster, the MATLAB option is still provided for users who would like to test and oversee the individual components of the solution process.

**Appropriate values:** 'Matlab' or 'C++'

**Default value:** 'Matlab'

- ❖ *consoleOutput*

**Necessity:** Optional

**Description:** A boolean value that determines whether messages like timings and intermediate results will be displayed in the command window during execution.

**Appropriate values:** true or false

**Default value:** false

- ❖ *noThreads*

**Necessity:** Optional, only relevant if the 'C++' compiler option is enabled

**Description:** The number of threads to be used by OpenMP for executing parallel computations of the stiffness or internal forces terms.

**Appropriate values:** Positive integer (ideally no more than the total number of available threads on the processor).

**Default value:** 1

- *Nonlinear analysis*

- ❖ *noGaussStations*

**Necessity:** Optional

**Description:** The number of Gauss stations for integration along the meridian of elements

**Appropriate values:** Positive integer, between 1 and 6. It is strongly suggested to use 3 to 4 Gauss stations for all segment - analysis types.

**Default value:** 3

- ❖ *noSimpsonStations*

**Necessity:** Optional, only relevant for materially nonlinear analysis

**Description:** The number of Simpson stations for through-thickness integration of elements according to Simpson's 1/3 rule.

**Appropriate values:** Positive odd integer, at least 3. In most cases 7 to 9 Simpson stations are sufficient to ensure appropriate integration of through thickness material points.

**Default value:** 7

- *Bifurcation analysis*

- ♦ *eigsSubspaceDimensionMultiplier*

**Necessity:** Optional, only relevant for analyses with bifurcation checks

**Description:** Can be used to set the value for the 'SubspaceDimension' option of the intrinsic `eigs` function. Some checks are executed to ensure that the user provided value does not lead to a subspace dimension higher than the number of DOFs in the system or lower than at least 2 x (no of requested eigenvalues).

**Appropriate values:** Positive non-zero integer

**Default value:** 2

- ♦ *eigsTolerance*

**Necessity:** Optional, only relevant for analyses with bifurcation checks

**Description:** Sets the value for the 'Tolerance' option of the intrinsic `eigs` function.

**Appropriate values:** Positive non-zero real value. Values should be kept between 1e-4 and 1e-8 to obtain reasonable results.

**Default value:** 1e-6

- ♦ *eigsNegativeTreatment*

**Necessity:** Optional, only relevant for analyses with bifurcation checks

**Description:** How negative eigenvalues should be treated. They may either be included in the bifurcation results or be dropped and set to `nan` values.

**Appropriate values:** 'Keep' or 'Drop'

**Default value:** 'Keep'

- ♦ *eigsForceReal*

**Necessity:** Optional, only relevant for analyses with bifurcation checks

**Description:** If this option is set to true then potentially complex eigenvalues will be treated as if they only consist of their real part, dropping the imaginary part. It should be reminded that the `eigs` function is an iterative solver for eigenvalues of sparse matrices and numerical issues should be expected in some cases. A warning will be displayed if eigenvalues are forced to be real and a complex one is encountered, in order to not only alert the analyst but also show that the imaginary/real ratio of the complex number is really small and the value is essentially real (as per the experience of the Authors).

**Appropriate values:** `true` or `false`

**Default value:** `true`

- ♦ *constrLagrMultF*

**Necessity:** Optional, only relevant for analyses with bifurcation checks

**Description:** The factor that the terms corresponding to the enforcement of boundary conditions according to the Lagrange multipliers method will be multiplied with. This multiplication will lead to eigenvalues corresponding to the constraints equal to  $-1/\text{constrLagrMultF}$ , giving the analyst the control to lead those eigenvalues as far as possible from the physically important ones. With an appropriate term of the '`eigsNegativeTreatment`' option, the eigenvalues that correspond to the Lagrange multipliers will be turned to `nan` values.

**Appropriate values:** Real non-zero values. Factors below `1e-8` should be avoided to ensure that the stiffness matrix does not become numerically ill-defined.

**Default value:** 1

- *Nonlinear analysis*

- ♦ *NonlinearSolver*

**Necessity:** Optional

**Description:** The solver to be employed for the incrementing the loads of the nonlinear analysis process. The available coded options are the classic load incrementation Newton-Raphson solver or the versatile Arc-Length (Riks) algorithm. The Arc-Length method may also trace equilibrium paths past potential limit points, provided they correspond to an axisymmetric state of the shell.

**Appropriate values:** '`ArcLength`' or '`NewtonRaphson`'

**Default value:** '`ArcLength`'

- ♦ *ArclengthMethod*

**Necessity:** Optional, only relevant if the '`ArcLength`' is to be used for the '`NonlinearSolver`'

**Description:** The method to be employed for computing the load proportionality factor change within an applied load increment. Either a Crisfield - Riks [17] or Ramm's [32] methods can be used, with an insightful discussion on the advantages and shortcomings of each presented in [19].

**Appropriate values:** '`Ramm`' or '`Crisfield`'

**Default value:** '`Ramm`'

- ♦ *noMaxSteps*

**Necessity:** Optional

**Description:** Maximum number of load steps that will be attempted by AQUINAS. The corresponding termination condition needs to be activated if this is to take effect and potentially stop execution (see `terminationConditions` option below)

**Appropriate values:** Non-zero positive integer

**Default value:** none

- ♦ *Jd*

**Necessity:** Optional, only relevant if the Arc-Length method is employed

**Description:** Number of desired iterations to achieve convergence of a load increment. This option can be used to reduce the arc-length  $l_i$  step of the solver in highly nonlinear parts of the equilibrium path, or even accelerate

in linear-like steps, according to the equation:

$$l_i = l_{i-1} \sqrt{J_d/J_{i-1}} \quad (4.2)$$

**Appropriate values:** Non-zero positive integer.

**Default value:** 3

❖ ***Jmax***

**Necessity:** Optional

**Description:** Maximum number of iterations allowed to achieve convergence of a load increment

**Appropriate values:** Non-zero positive integer.

**Default value:** 20

❖ ***LPFmax***

**Necessity:** Maximum value of the Load Proportionality Factor (LPF) that AQUINAS will attempt to reach. The corresponding termination condition needs to be activated if this is to take effect and potentially stop execution (see terminationConditions option below)

**Appropriate values:** Positive real value.

**Default value:** Inf

❖ ***dLPF***

**Necessity:** Compulsory for GNA, MNA or GMNA types of analysis

**Description:** The initial load increment that will be attempted by AQUINAS.

If the 'NewtonRaphson' options is used this will be kept constant throughout all the steps (except if a step fails to converge and the option to attempt with a smaller step is activated), while if the 'ArcLength' algorithm is used then this will be turned internally to an equivalent arc-length increment that will be updated after every load step

**Appropriate values:** Positive real value.

**Default value:** none

❖ ***dLPFmax***

**Necessity:** Optional

**Description:** Maximum value of the LPF increment that AQUINAS is allowed to attempt. Relevant for cases where there is acceleration of the solution process by increasing the dLPF increment through Eq. 4.2 for the ArcLength method

**Appropriate values:** Positive real value.

**Default value:** Inf

❖ ***zetaT***

**Necessity:** Optional

**Description:** Tolerance  $\zeta_t$  for testing convergence of a load increment

**Appropriate values:** Positive real value, should range between 2e-3 to 2e-4 for most shell problems (also see [50]).

**Default value:** 1e-3

❖ ***zetaD***

**Necessity:** Optional

**Description:** Tolerance  $\zeta_d$  for testing divergence of a load increment

**Appropriate values:** Positive real value, the default value of  $\zeta_d = 2$  is suggested (also see [50]).

**Default value:** 2

❖ ***epsilon\_s***

**Necessity:** Optional

**Description:** Effective strain for computing the number of sub-increments for a given strain increment

**Appropriate values:** Positive real value, the default value of  $\epsilon_s = 0.0002$  is suggested (also see [50]).

**Default value:** 0.0002

❖ ***max\_epsilon\_bar***

**Necessity:** Optional

**Description:** Maximum effective strain increment that may be attempted to be solved for with the sub-increment method (corresponding to a number of sub-increments  $N_{sb} = \bar{\epsilon}_{max}/\epsilon_s$  sub-increments).

**Appropriate values:** Positive real value

**Default value:** 0.02

❖ ***ksi***

**Necessity:** Optional, relevant if bifurcation checks are activated

**Description:** The tolerance  $\xi$  to accept an eigenvalue as equal to 1, at which point buckling is assumed to occur.

**Appropriate values:** Positive real value, values of  $\xi \approx 0.001 - 0.0001$  are suggested (also see [51], where the notation  $\xi$  is adopted).

**Default value:** 0.001

❖ ***simultaneousBifurcationTreatment***

**Necessity:** Optional, relevant if bifurcation checks are activated

**Description:** The treatment that should be adopted if more than one eigenvalues are found to be in the range  $[1 - \xi, 1 + \xi]$

**Appropriate values:** Can be either 'none' for an analysis where a load increment will be reattempted until there is just one eigenvalue within the  $[1 - \xi, 1 + \xi]$  range, 'pickSmallestWithinRange' to allow the solver to select the smallest eigenvalue within that range (provided that there are none below  $1 - \xi$ ) or 'divideKsiBy10' to reduce the value of  $\xi$  and therefore the range of accepted eigenvalues.

**Default value:** 'none'

❖ ***maxAttempts***

**Necessity:** Optional

**Description:** Number of consecutive failed (not converged) steps to be reattempted, before giving up and aborting execution.

**Appropriate values:** Positive integer.

**Default value:** 0

❖ ***reattemptCutback***

**Necessity:** Optional

**Description:** Factor to multiply the LPF increment (for classic load incrementation, through the 'NewtonRaphson') or arc-length increment (for arc-length method, enabled through the 'ArcLength' option, for both

variations of the method considered) with, when a load step is deemed as failed and going to be re-attempted.

**Appropriate values:** Any real value within the open range (0,1).

**Default value:** 0.25

❖ ***DOFTrackerForCIP***

**Necessity:** Optional

**Description:** Name of AQUINAS\_DOF\_Tracker\_Object to be used for the calculations relevant to the convergence indicator plot, as presented in [41].

**Appropriate values:** A non-zero length character array.

**Default value:** '-'

❖ ***visualiseNonlinear***

**Necessity:** Optional

**Description:** Option that enables the generation of on the fly plots for the analyst to track the progress of the nonlinear solution process

**Appropriate values:** true or false

**Default value:** false

❖ ***terminationConditions***

**Necessity:** Optional

**Description:** Character 1D array that contains letters corresponding to the criteria that will determine the termination of the nonlinear analysis. Potential conditions, with their corresponding code letters, are:

- 'A' - Maximum number of load steps reached.
- 'B' - Maximum LPF exceeded.
- 'C' - Bifurcation check, terminate at first event. The circumferential modes to be considered should either be found by turning on the minimization algorithm (Gaussian Process Regression, see following properties) or provided through the AQUINAS\_Analysis\_Object.
- 'D' - Limit point, where the global stiffness matrix is not positive definite any more.
- 'E' - Prediction of plateauing region, based on the development of the Convergence Indicator Plot (CIP), as outlined in [41].

**Appropriate values:** Matlab character array with any combination of letters A to E.

**Default value:** '-'

– ***Surrogate Optimisation***

❖ ***surrogate\_optimisation***

**Necessity:** Optional

**Description:** A boolean value that activates the automatic search for the critical circumferential wave-number employing a Surrogate Optimisation algorithm, using a Gaussian Process Regression method.

**Appropriate values:** true or false

**Default value:** false

❖ ***so\_Auto\_Bounds***

**Necessity:** Optional

**Description:** Boolean value that enables the automatic determination of the circumferential wave-number bounds where the Surrogate Optimisation algorithm will be applied. If this option is set to true then the values provided through the '`so_circWave_lb`' and '`so_circWave_ub`' (see below) options will be ignored.

**Appropriate values:** true or false

**Default value:** true

❖ **`so_circWave_lb`**

**Necessity:** Optional

**Description:** The lower bound of the range of circumferential wave-numbers where the Surrogate Optimisation algorithm will be applied, in an attempt to identify the critical mode. This option will be neglected if '`so_Auto_Bounds`' is set to true.

**Appropriate values:** Positive non-zero integer, should be lower than the value of the '`so_circWave_ub`' option. The zero-th harmonic is treated separately and is not included in these bounds.

**Default value:** 1

❖ **`so_circWave_ub`**

**Necessity:** Optional

**Description:** The upper bound of the range of circumferential wave-numbers where the Surrogate Optimisation algorithm will be applied, in an attempt to identify the critical mode. This option will be neglected if '`so_Auto_Bounds`' is set to true.

**Appropriate values:** Positive non-zero integer, should be higher than the value of the '`so_circWave_lb`' option.

**Default value:** 100

❖ **`so_circWave_bound_step`**

**Necessity:** Optional, only relevant if '`so_Auto_Bounds`' is set to true

**Description:** The step that will be used when attempting to automatically extend the range of circumferential wave-numbers to be trialled.

**Appropriate values:** Positive non-zero integer.

**Default value:** 10

❖ **`so_Hyperparameter_Optimisation`**

**Necessity:** Optional

**Description:** Boolean value that determines whether to optimise the hyper-parameters of the surrogate optimisation algorithm at each step of the process.

**Appropriate values:** true or false

**Default value:** true

❖ **`so_Hyperparameters`**

**Necessity:** Optional

**Description:** The hyper-parameters to be used in the Gaussian process regression of the surrogate optimisation algorithm. The values provided in this input argument will be ignored if the hyper-parameters are to be optimised during training of the surrogate model ('`so_Hyperparameter_Optimisation`' set to true).

**Appropriate values:** 1D array holding two entries for the two hyper-parameters.

**Default value:** none

❖ ***so\_Hyperparameters\_Optimisation\_Grid\_Stations***

**Necessity:** Optional

**Description:** Number of nodes to be used for the grid where the log marginal likelihood will be computed, for the purposes of hyper-parameters optimisation.

**Appropriate values:** 1D array holding two entries for the number of nodes along the x-y directions of the grid.

**Default value:** [50 50]

❖ ***so\_No\_Initial\_Points***

**Necessity:** Optional

**Description:** Number of training points to be used for the initial generation of the surrogate model. The points correspond to harmonics, equally distributed with the training range, as defined from 'gpr\_circWave\_lb' and 'gpr\_circWave\_ub'.

**Appropriate values:** Positive integer number of points, at least 2 are needed for initialisation of the surrogate model.

**Default value:** 10

❖ ***so\_Hyperparameters\_Optimisation\_lbf***

**Necessity:** Optional, only relevant if the 'so\_Hyperparameter\_Optimisation' argument is set to true.

**Description:** Lower bound on the hyper-parameters, to be obtained during their optimisation step, corresponding to the normalised training range.

**Appropriate values:** 1D array of two positive real values, corresponding to the hyper-parameters. The lower bound for the first hyper-parameter should be within the range of (0,1).

**Default value:** [0.05 0.5]

❖ ***so\_Hyperparameters\_Optimisation\_ubf***

**Necessity:** Optional, only relevant if the 'so\_Hyperparameter\_Optimisation' argument is set to true.

**Description:** Upper bound on the hyper-parameters, to be obtained during their optimisation step, corresponding to the normalised training range.

**Appropriate values:** 1D array of two positive real values, corresponding to the hyper-parameters. The upper bound for the first hyper-parameter should be within the range of (0,1).

**Default value:** 1e-10

❖ ***so\_noise***

**Necessity:** Optional

**Description:** Noise to be added in the diagonal of the RBF kernel during the Cholesky decomposition step of Gaussian process in order to avoid numerical problems

**Appropriate values:** Positive real value, suitably small in magnitude.

**Default value:** 1e-10

❖ ***so\_alpha***

**Necessity:** Optional

**Description:** Significance level value  $\alpha$ , used to determine the confidence interval of the Gaussian process as  $1 - \alpha$ .

**Appropriate values:** Positive real value within the range (0,1).

**Default value:** 0.05

❖ ***so\_EI\_tol***

**Necessity:** Optional

**Description:** Tolerance to compare the Expected Improvement (EI) function's values within the training range of the surrogate optimisation process and determine whether the algorithm has converged.

**Appropriate values:** Positive real value.

**Default value:** 1e-5

❖ ***so\_Max\_Steps***

**Necessity:** Optional

**Description:** Maximum number of steps to be allowed before the surrogate optimisation algorithm is terminated.

**Appropriate values:** Positive integer.

**Default value:** 100000

## 4.3 Procedure descriptions

Having presented the architecture of the software, in a rather abstract manner, but also all of the available objects that may be defined as an axisymmetric shell problem is generated, it is time to discuss what is actually happening when an analysis is submitted with AQUINAS. As showcased in the flowchart of Figure 4.1, there are three basic analysis scripts that handle the linear or nonlinear solution process. Each of them will be outlined in the following sections, where the focus is on the considerably more complex `AQUINAS_GMNA.m` script, responsible for geometric and/or material nonlinear analyses.

### 4.3.1 AQUINAS LA

The most generic type of a FE solution, a Linear Analysis consists of a single analysis increment that only considers linear kinematics (small displacement theory) and purely elastic material law. Once the error checking and organising parts of `AQUINAS_Protocol.m` have been completed, a call is made to `AQUINAS_LA.m`. Inside this LA script, the material stiffness matrices of the element are computed and after the condensation process (see section *Condensation of nodal variables* of Chapter 2) has been applied, the global stiffness matrix for the axisymmetric shell system is assembled, taking into account its sparsity patterns. This assembly may be done either through the relevant MATLAB scripts or pre-compiled C++ files, using MATLAB's MEX capability. The global stiffness matrix is enriched with the appropriate Lagrange multipliers terms to ensure the boundary conditions are applied to the model.

Once the equilibrium equation has been solved, the condensed-out degrees of freedom of an element's nodes are recovered. Control is returned to `AQUINAS_Protocol`, where the midsurface strain and generalised stress resultants may now be computed. The inner-middle-outer fibre strains-stresses can also be evaluated from the relevant midsurface components. The results are be organised in the way desired by the analyst as defined

through an `AQUINAS_Output_Mode_Object`, and at this stage the analysis has successfully been completed.

### 4.3.2 AQUINAS LBA

Bifurcation analyses may be performed through a call to `AQUINAS_LBA.m`. The name of this script may be deceiving, as bifurcation is checked at the current stress state of the shell, as provided through an array of membrane stress resultants evaluated at the midsurface Gauss integration points along the elements. For an actual LBA to be executed, an LA will be submitted beforehand, so that the stress resultants have been computed and the linear bifurcation checks may be executed.

Both the material and geometric stiffness matrices need now be computed. If the bifurcation checks are performed as part of a geometrically nonlinear analyses, the nonlinear components of the strain-displacement matrix will also be considered in the formulation of the material stiffness of an element. The stiffness matrices will then be condensed, with the condensation process of the geometric stiffness being also described in the corresponding section of Chapter 2. Two global stiffness matrices are now formed, with the Lagrange multipliers added after multiplication with an input provided factor (see `AQUINAS_Solver_Object` and the '`constrLagrMultF`' name-value pair above) that ensures that eigenvalues corresponding to the boundary conditions (the boundary conditions lead to additional rows-columns in the stiffness matrices) are positioned as far as possible from the load related ones. MATLAB's sparse eigenvalue solver `eigs` is employed in order to calculate the eigenvalues and corresponding eigenmodes of the shell problem. The eigenmodes will then not be put through the recovery process to obtain the full set of element nodal variables, as the computation of strains-stresses is not sensible in the context of a bifurcation analysis.

### 4.3.3 AQUINAS GNA - MNA - GMNA

A fully nonlinear analysis may be executed through a call to `AQUINAS_GMNA.m`. Geometric and material nonlinearities are included in the FE solution through appropriate boolean flags, based on the type of analysis that was being submitted, evaluated before entering the main load incrementation loop.

Before proceeding with the exploration of the load bearing capacity development for an axisymmetric shell problem, on the way to its failure mode, certain operations are required to ensure the solution process runs as efficiently as possible. These include the initialisation of storage arrays for the stiffness terms, strains and stresses, but also the computation of the nodal geometric properties of Eq. (2.1) so that they don't have to be re-calculated on every iteration of the process. If the user desires the visualisation of the nonlinear solution procedures, the corresponding MATLAB windows will be generated at this point. The total LPF achieved and number of load steps converged are set to zero.

Once all the necessary initialisations have been completed, the solution may now enter the main load incrementation loop. For each load step attempted some further initialisations need to be made, corresponding to the accumulated results within the step and auxiliary convergence related fields. A set of iterations is now attempted for each load increment, aiming at achieving convergence through minimisation of the residual forces in the shell model. To aid with the following discussion, the index  $i$  will be referring to the attempted load increment, while index  $j$  to the nonlinear iteration en route to convergence

of load step  $i$ .

On the very first iteration  $j$  of an increment  $i$ , the tangent stiffness matrix of the axisymmetric shell model needs to be computed, as well as the externally applied forces vector. The stiffness terms will not be evaluated on any subsequent iteration for the same load step, leading to a ‘modified Newton-Raphson’ kind of approach to the solution process. The element tangent stiffness matrices  $[K_T]_e$  will include the effects of nonlinear strains on the strain-displacement matrix  $B$  of Eq. (2.49), as well as geometric stiffness terms  $[K_\sigma]_e$  on  $[K_T]_e$ , if geometric nonlinearities are to be considered in the analysis. On the other hand, if the effects of material nonlinearities are to be included, the tangent modulus matrix  $[D_T]$  for each Gauss station along the shell’s meridian will need to be integrated according to Eq. (2.36). This integration is performed numerically, through the application of Simpson’s 1/3 rule. The  $\gamma_i$  nodal variable will be condensed out of the stiffness matrix of each element according to Eq. (2.67), before assembly into the global tangent stiffness matrix. There is no need to condense out the  $(\partial v / \partial s)_i$  nodal variable, as both the  $v$  and  $\partial v / \partial s$  degrees of freedom are set to zero by default in the purely axisymmetric pre-buckling path of the shell that AQUINAS aims to trace. Once the global stiffness matrix and force vector have been formulated for the current increment  $i$ , the reference solution may be obtained through the equilibrium equation as:

$$\{\delta_I\}_i = [K_T]_i^{-1} \{F_I\}_i \quad (4.3)$$

On subsequent iterations, the equilibrium equation is only solved for the vector of residual forces  $\{\Phi\}_i^j$  in the system, with the correction to the displacement vector found by:

$$\{\Delta\delta_R\}_i^j = [K_T]_i^{-1} \{\Phi\}_i^j \quad (4.4)$$

If the arc-length method is to be used for the load incrementation, the change of the LPF will have to be evaluated after solution of the equilibrium equation. The vector of accumulated displacement  $\{\Delta\delta_a\}_i^j$  for the current increment  $i$  will have to be updated, based on the displacement solution obtained on iteration  $j$ . The full set of element nodal degrees of freedom of Eq. (2.37) will also need to be recovered according to Eq. (2.65), and the transformation of Eq. (2.63) applied, with the circumferential ones still omitted due to the convention discussed above. As a final step before proceeding to the computation of the element’s residual forces, the change in the nodal displacement magnitudes  $\zeta$  is evaluated, for purposes of checking against a tolerance parameter to test for converge or divergence of the current load step  $i$ , as

$$\zeta = \frac{(\Delta_i^j)^2 - \Delta_i^{j-1})^2}{\Delta_i^j)^2} \quad (4.5)$$

with  $\Delta_i^j$  defined as

$$\Delta_i^j = \sqrt{(u_i^j)^2 + (w_i^j)^2} \quad (4.6)$$

The midsurface strains  $\{\epsilon\}$  along the shell’s meridian may now be evaluated, at all available Gauss stations, according to Eq. (2.11). In an analysis where geometric nonlinearities are neglected, the nonlinear terms of Eq. (2.11), as given by Eq. (2.14), are omitted. The increment of the strain vector for iteration  $j$  is evaluated as the change from the previous strain state of the midsurface point.

If materially nonlinear effects are not included in the FE model, the computation of the stress resultants of Eq. (2.34) is a straight forward process, with the modulus matrix of Eq. (2.36) including only the elastic rigidity matrix  $[D_e]$  of eq. (2.30). If plasticity is to be considered however in tracing the nonlinear behaviour of the shell, the through-thickness stress distribution for all Gauss points has to be computed in order to calculate the stress resultants. The first step in this process is to evaluate the strain increments for the iteration  $j$  across the fibres of the shell wall, as given by Eq. (2.9). For each of these material points the corresponding stress increment is to be evaluated, following the sub-incremental procedure outlined in section *Constitutive relations* of Chapter 2. Once the stresses are found to be on the yield surface of the material, the stress resultants are evaluated by applying Simpson's 1/3 rule of integration for the through thickness stations that were used.

The residual forces can now be evaluated as the difference between the externally applied forces with those that develop internally for each element. The condensation process is once again necessary in order to construct the global residual force vector. It is important to note that in the process of condensing the residual forces for every element the condensed tangent stiffness matrices are also calculated and the global stiffness matrix is reformulated. Even though the stiffness terms themselves are not calculated again at this point, the global matrix  $[K_T]$  that was set up in the first iteration of the increment cannot be used again, as the condensed element stiffness arrays are affected by the different force vectors used during the condensation. Not doing so would lead to erroneous displacements in the process of recovering the full set of nodal displacement for the elements.

If this is not the first iteration for the running load step, convergence will be tested on the basis of comparing the maximum change in the  $\zeta$  vector with a tolerance  $\zeta_t$ . Divergence may also be tested by comparing with a tolerance  $\zeta_d$ , and potentially abort the current increment attempt and apply cutbacks on the load (or arc-length) applied for the step. In the case that convergence is achieved bifurcation checks may be performed for a set of competing harmonics  $n$ , provided that geometric nonlinearities are included in the problem and the associated termination condition (see '`terminationConditions`' name-value pair for `AQUINAS_Solver_Object` above) has been provided. Bifurcation checks may not be executed for an MNA in AQUINAS, as this is a counter-intuitive process that is not in accordance with the geometrically nonlinear nature of buckling. If any of the termination conditions provided has been satisfied the analysis process will be concluded and control will be returned to `AQUINAS_Protocol`.

The internal processes of `AQUINAS_GMNA` are presented in Figure 4.2 of the following page. An attempt to distinguish steps that are specific to a geometrically or materially nonlinear solution is made, so that the reader may appreciate the way AQUINAS handles the both types of nonlinearity within the same script.

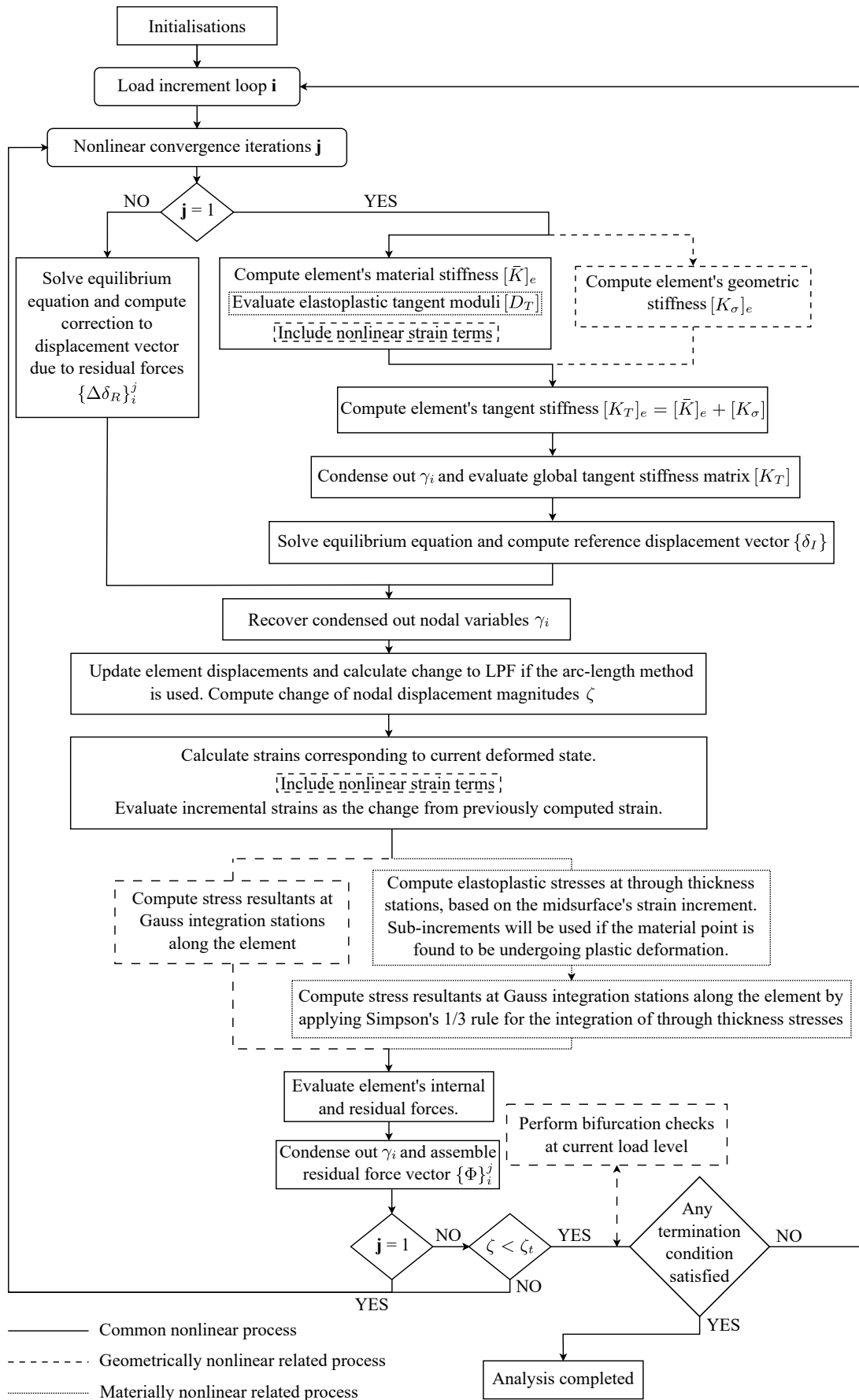


Figure 4.2: AQUINAS Geometrically and/or Materially Nonlinear Analysis flowchart.

# Chapter 5

## Example library

AQUINAS comes with an extensive example library of ‘input’ files which take the form of simple Matlab .m files. They are intended to act in part as tutorials in how various analyses and problems can be set up and solved, and in part as a repository of verification and validation exercises to establish the correctness of the software.

In what follows, two complementary classification schemes for axisymmetric shell edge boundary conditions will be used, that of Yamaki [61] and prEN 1993-1-6 [14] presented in Tables 5.1 - 5.2 and 5.3 respectively. The reader is cautioned that the notation used here is specialised for the current finite element formulation, where  $w$  and  $u$  are the nodal displacements in the radial  $r$  and axial  $z$  directions respectively. This is different to notation typically adopted in the algebraic shells literature, where  $w$  and  $u$  are the shell midsurface displacements in the normal and meridional directions respectively. It is equally important to state that while both in the work of Yamaki and in EN 1993-1-6 the boundary conditions are expressed in terms of local degrees of freedom (normal-meridional displacements), AQUINAS only allows the definition of boundary conditions in the global system (global radial-axial directions), as most commonly encountered in FE software.

Table 5.1: Classification of shell clamped boundary conditions from Yamaki [61]

Clamped BC	Restrictions
C1	$\bar{u} = v = \bar{w} = 0, \frac{d\bar{w}}{ds} = 0$
C2	$\bar{u} = \bar{w} = 0, \frac{d\bar{v}}{ds} = 0, N_{\phi\theta} = 0$
C3	$v = \bar{w} = 0, \frac{d\bar{v}}{ds} = 0, N_\phi = 0$
C4	$\bar{w} = 0, \frac{d\bar{v}}{ds} = 0, N_\phi = N_{\phi\theta} = 0$

Table 5.2: Classification of shell simply supported boundary conditions from Yamaki [61]

Simply Supported BC	Restrictions
S1	$\bar{u} = v = \bar{w} = 0, \frac{d^2\bar{w}}{ds^2} = 0$
S2	$\bar{u} = \bar{w} = 0, \frac{d^2\bar{v}}{ds^2} = 0, N_{\phi\theta} = 0$
S3	$v = \bar{w} = 0, \frac{d^2\bar{v}}{ds^2} = 0, N_\phi = 0$
S4	$\bar{w} = 0, \frac{d^2\bar{v}}{ds^2} = 0, N_\phi = N_{\phi\theta} = 0$

There is however a way to restrict a local DOF of the shell’s meridian with the options provided in the `AQUINAS_Constraint_Object`. Before going into the necessary process for

Table 5.3: Classification of shell boundary conditions from prEN 1993-1-6 [14]

BC code	Simple term	Restrictions
BC1r	Clamped	$\bar{u} = v = \bar{w} = 0, \beta = 0$
BC1f	-	$\bar{u} = v = \bar{w} = 0, \beta \neq 0$
BC2r	-	$v = \bar{w} = 0, \beta = 0, \bar{u} \neq 0$
BC2f	Pinned	$v = \bar{w} = 0, \bar{u} \neq 0, \beta \neq 0$
BC3r		$\bar{u} = v = \bar{w} \neq 0, \beta = 0$
BC3f	Free edge	$\bar{u} = v = \bar{w} \neq 0, \beta \neq 0$

such a boundary condition to be defined, the reader is reminded of the transformations that associate the global and local DOFs of Figure 2.3. As presented in [50]:

$$\begin{Bmatrix} \bar{u} \\ \bar{v} \\ \bar{w} \end{Bmatrix} = \begin{bmatrix} \cos(\phi) & 0 & -\sin(\phi) \\ 0 & 1 & 0 \\ \sin(\phi) & 0 & \cos(\phi) \end{bmatrix} \begin{Bmatrix} u \\ v \\ w \end{Bmatrix} = [T] \begin{Bmatrix} u \\ v \\ w \end{Bmatrix} \quad (5.1)$$

Similar relations can also be found in Annex D of [14]. Taking into account the above Eq. 5.1, the analyst can define a boundary condition in the local system by providing the left hand side parameters of the corresponding relation. These left hand side parameters will then be added to the stiffness matrix of the problem, hence the desired relation will be considered during solution of the equilibrium problem. For example, in order to restraint the local degree of freedom  $\bar{u}$  it is enough to create a constraint object that links the global  $u$  and  $w$  DOFs with LHS factors equal to  $\cos(\phi)$  and  $-\sin(\phi)$  respectively, while leaving the RHS factor at its default value of zero. In code, this would look like:

```
ubarConstraint = AQUINAS_Constraint_Object('coordR',r,'coordZ',z,...  
    'dofs',{'u','w'},'coeffLHS',[cos(phi),-sin(phi)]);
```

The reader is cautioned that the notation of prEN 1993-1-6 will be adopted to define the axisymmetric shell problems, over any symbols used in relevant resources, at least for the cylindrical and conical models examined (with an effort made to also use the notation for other models, wherever applicable). Details on the discretisation of the axisymmetric shell problems may be found on the individual MATLAB example scripts, included in the distribution of AQUINAS. Most of the examples presented here require seconds to run, some take minutes while a handful (e.g. LBA05, GNA01, GNIA01, GNIA02, GMNA01 and GMNA02) may take significantly longer.

## 5.1 LAs

AQUINAS can accurately and efficiently execute linear elastic analyses (LAs) for a variety of multi-segment axisymmetric shell geometries. Due to the axisymmetric nature of the expected solution, the circumferential degree of freedom  $v$  is omitted from the analysis, allowing for a reduction in the computational effort. Once an LA has been completed, the analyst is able to view and extract for post-processing the degrees of freedom, the strains and curvatures, the stresses and the membrane and bending stress resultants, all expressed at the nodes of the shell segments.

The LA results of AQUINAS are put to the test through comparison with various trustworthy solutions, either algebraic, found in relevant literature on the mechanics of thin shells, or computational ones obtained through available scientific software. Over the following sections of this chapter, unless explicitly mentioned otherwise, the material that the axisymmetric shells are made of is steel, with a Young's modulus of  $E = 200000\text{ N/mm}^2$  and a Poisson's ratio of  $\nu = 0.3$ . Due to the axisymmetric nature of the LA solutions, the circumferential degree of freedom is zero by default and will therefore be omitted.

### 5.1.1 Example LA01: Thin cylinder under axial compression and internal pressure

The first LA example is that of a cylindrical shell subject to axial compression and uniform internal pressure which may be found in the script `input_Example_LA01.m`. A BC1r / C1 boundary condition is considered at the base edge of the cylinder and a BC2f / S3 condition at the top edge. The cylinder is under the effect of an axially compressive edge load of magnitude  $N = 1000.0\text{ N/mm}$  and of internal pressure  $p_n = 1.0\text{ N/mm}^2$ . Its height and radius are  $L = 500.0\text{ mm}$  and  $r = 500.0\text{ mm}$  respectively, while the shell wall has a thickness of  $t = 5.0\text{ mm}$ . The geometry of the problem is also presented in Figure 5.1.

The finite element solution is compared against an algebraic bending and membrane theory solution for thin axisymmetric shells as detailed most accessibly in Rotter and Sadowski [36] though also elsewhere [20, 55]. A brief but insightful comparison of the stresses between AQUINAS and the analytical solutions, obtained through both membrane and bending theories, is presented in the following Figures 5.2 - 5.3. By running the input script the reader can also view a comparison of the radial and axial displacements or the strains arising in the cylinder, or even for another set of material properties and loading of their choice.

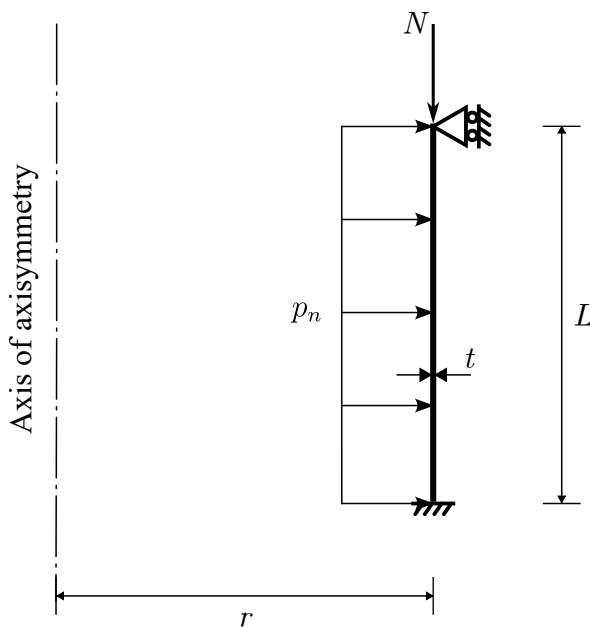


Figure 5.1: LA01 - System diagram.

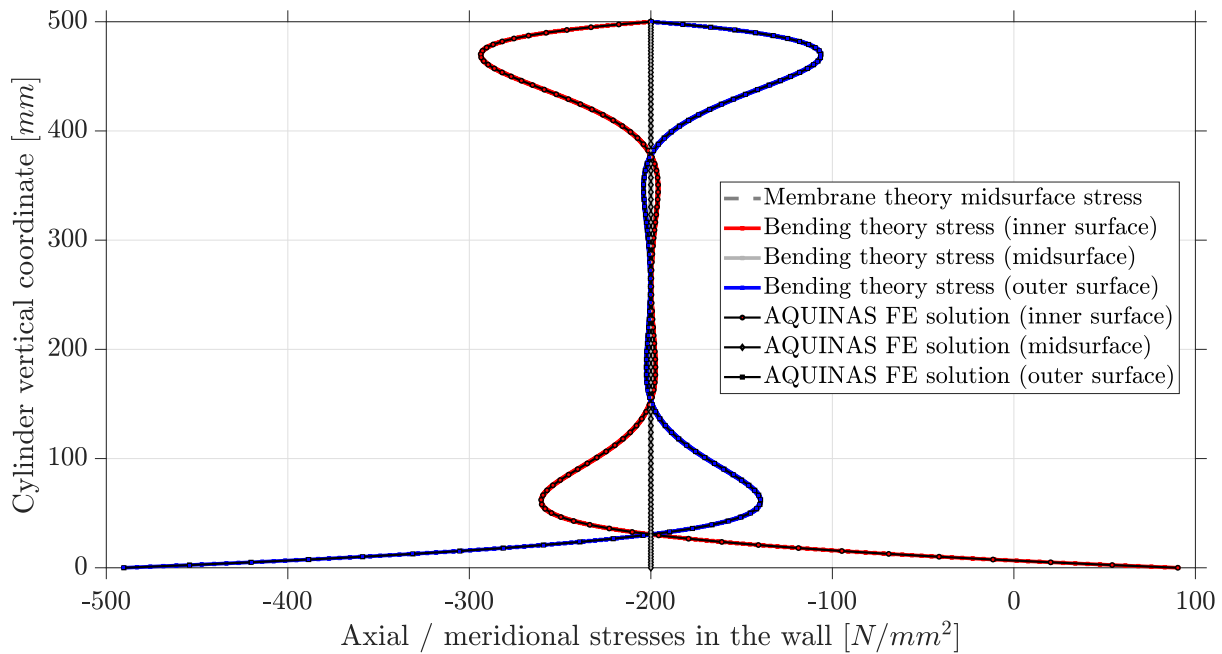


Figure 5.2: LA01 - Comparison of axial stresses in the inner, middle and outer surface of the shell wall.

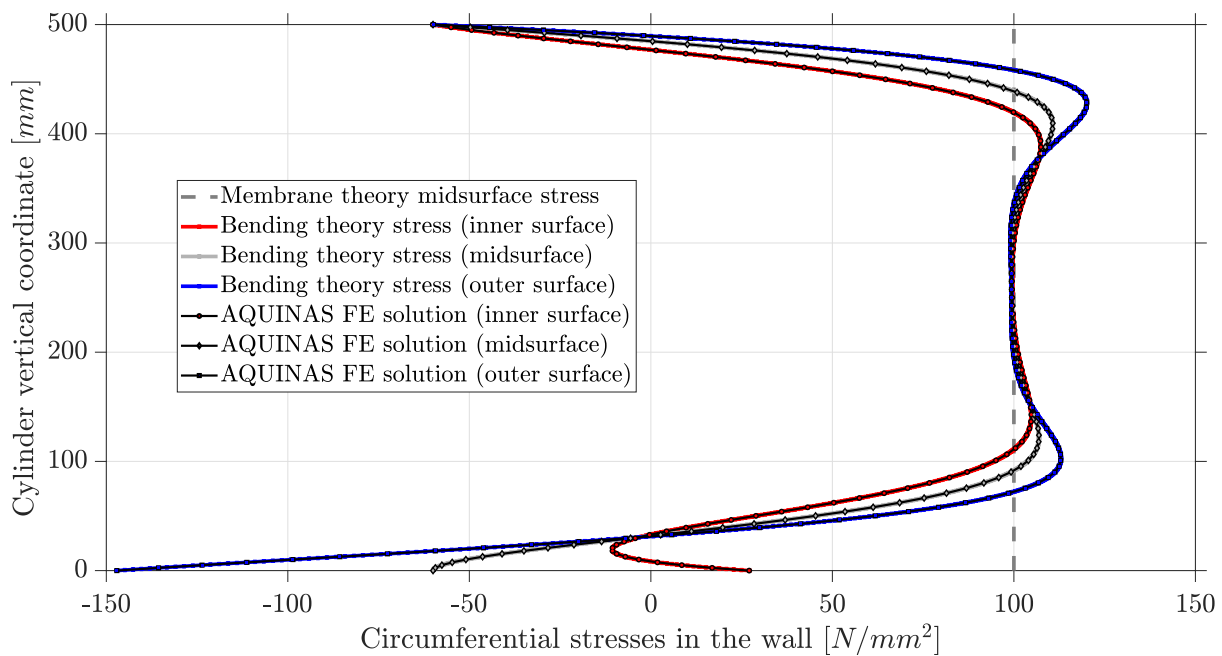


Figure 5.3: LA01 - Comparison of circumferential stresses in the inner, middle and outer surface of the shell wall.

### 5.1.2 Example LA02: Thin cylinder with midsurface eccentricity under axial compression and internal pressure

This second LA example builds up on the previous cylindrical shell problem by introducing an eccentricity along the mid-height of the meridian, testing the software's capability to analyse eccentrically connected segments, in the `input_Example_LA02.m`

script. A BC1f boundary condition is considered at the bottom edge of the cylindrical shell and a BC2f at the top. The cylinder is under the effect of an axially compressive edge load  $N = 300.0 \text{ N/mm}$ , applied at its top edge, and internal pressure  $p_n = 1.0 \text{ N/mm}^2$ . Its total length is  $L = 500.0 \text{ mm}$  and the shell wall is of thickness  $t = 1 \text{ mm}$ . The eccentrical connection, of magnitude  $e = 1.0 \text{ mm}$ , is located at the mid-height of the cylinder's meridian, leading to a radius of  $r_B = 100.0 \text{ mm}$  for the bottom half and of  $r_T = r_B - e = 99 \text{ mm}$  for the top one. The geometry of this axisymmetric shell problem can be seen in Figure 5.4, where the eccentricity is exaggerated to aid understanding.

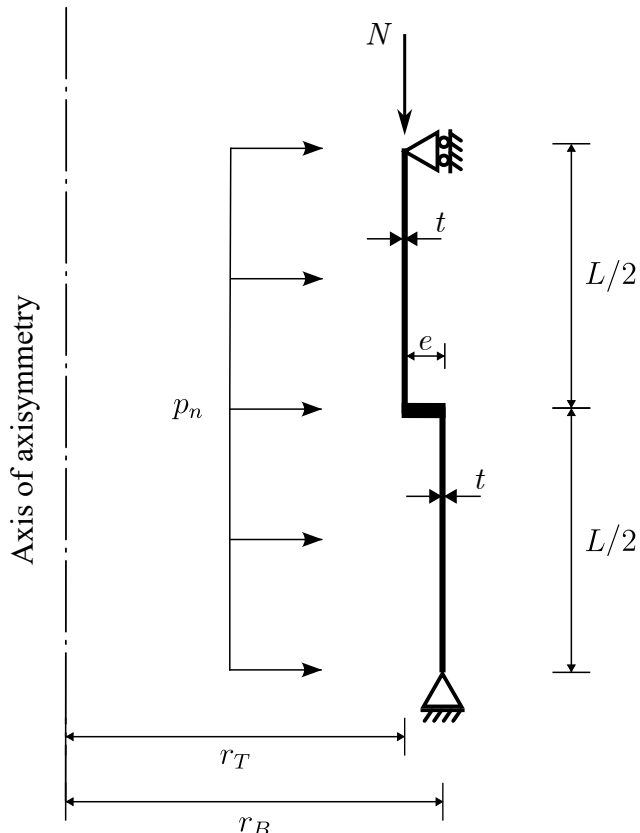


Figure 5.4: LA02 - System diagram.

The finite element solution is once again compared against an analytical bending and membrane theory solution for thin axisymmetric shells based on the shell theory principles presented in [36, 20, 55]. The inner-middle-outer surface meridional and circumferential stresses of AQUINAS are plotted against the corresponding analytical results in Figures 5.5 - 5.6. By running the input script the reader may also examine a full comparison of the radial and axial displacements, meridional or circumferential strains developing in the cylinder, or perhaps for another set of material, geometric or loading properties of their choice.

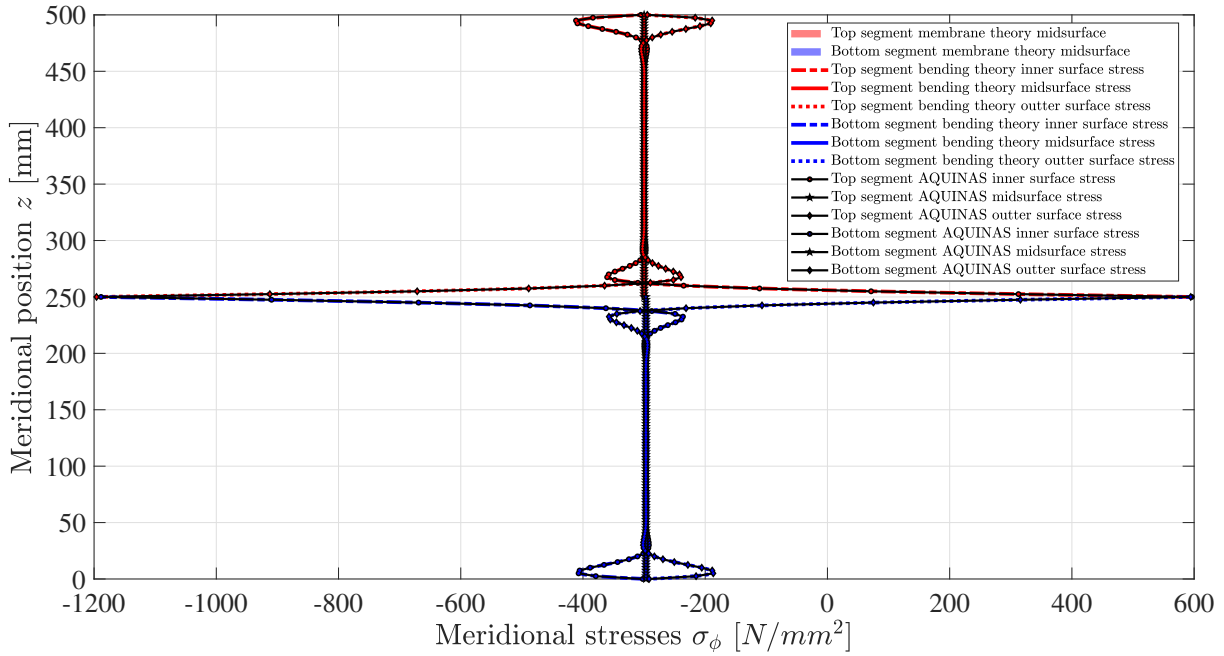


Figure 5.5: LA02 - Comparison of axial stresses in the inner, middle and outer surface of the shell wall.

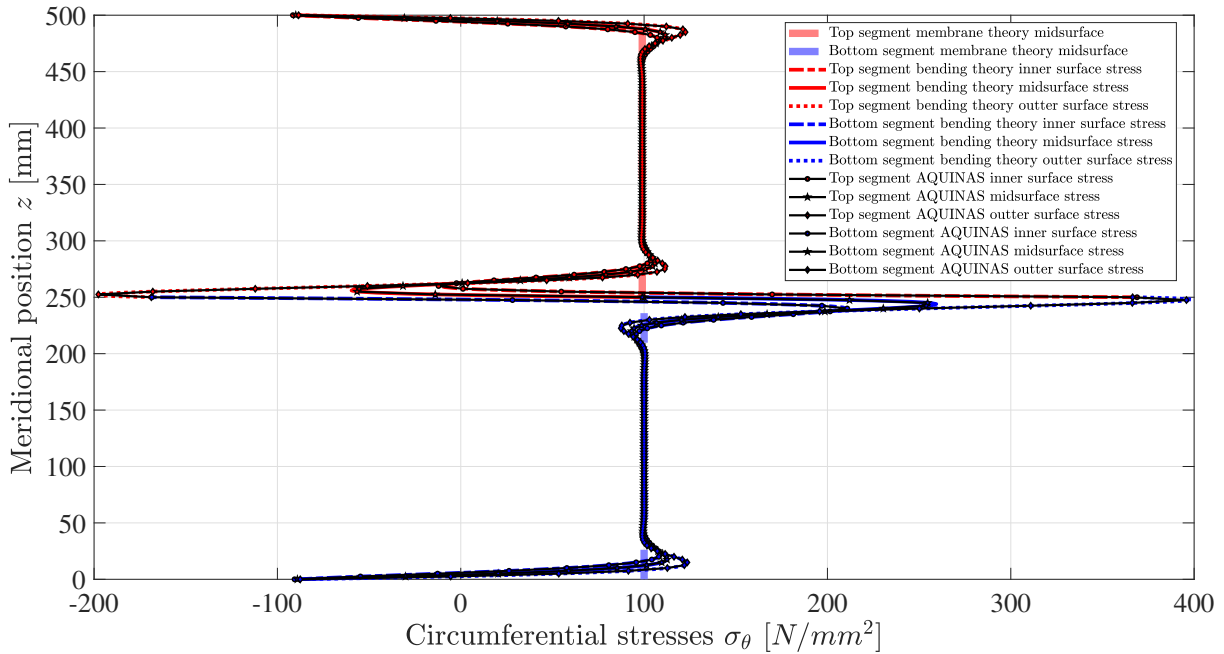


Figure 5.6: LA02 - Comparison of circumferential stresses in the inner, middle and outer surface of the shell wall.

### 5.1.3 Example LA03: Multi-strake cylindrical silos with step-wise varying thickness under nonlinear loading

The linear elastic response of five different cylindrical isotropic silos under nonlinear pressure and traction distributions is investigated and compared against the work of Boyez et al [7]. The five silos have different height over diameter ( $H/D$ ) aspect ratios and

number of segments along their meridian. The segments have an integer wall thickness that increases towards the base of the silos. The geometries of the five silos are presented in Figure 5.7, with the lengths of the different segments of the meridian summarized in Table 5.4. The silos serve as storage units for granular solid which exerts a nonlinear normal pressure  $p_n$  and a frictional traction  $p_z$ , where the distribution that these loading patterns follow depend on the H/D ratio of the silos. A Jansen or modified Reimbert axisymmetric pressure distribution is used to model the loading of the silos. The interested reader may find a more in depth discussion on these pressure distributions, as well as the individual parameters that govern their variation along the meridians of the silos, in A.J. Sadowski and M.J. Rotter [43].

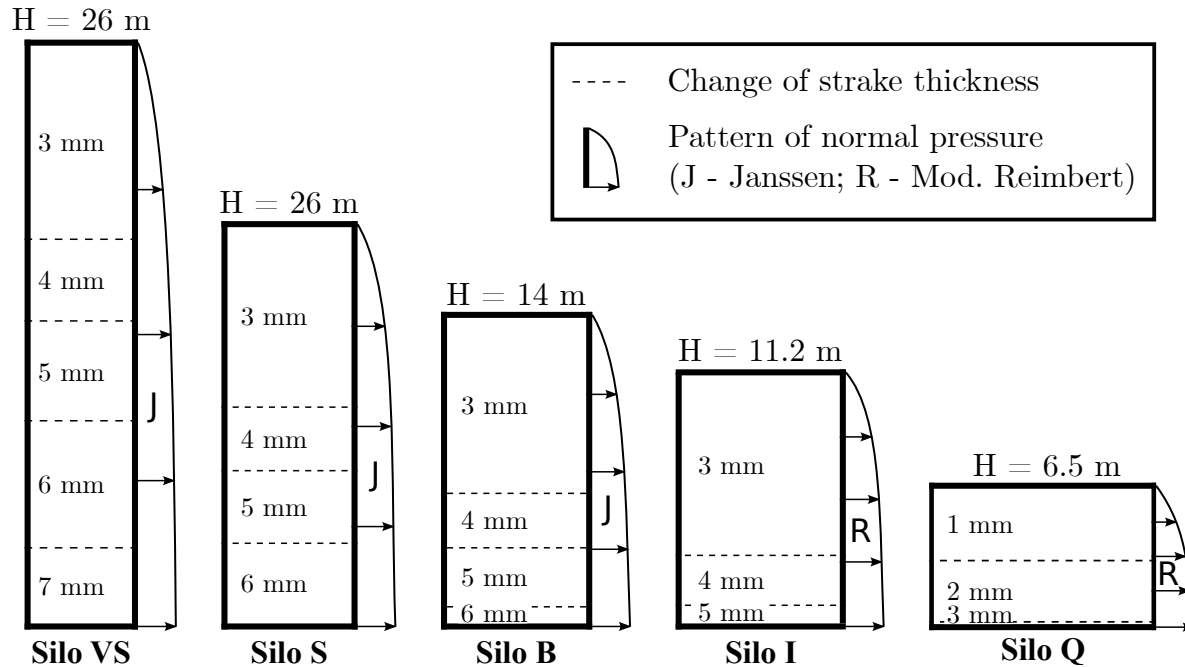


Figure 5.7: LA03 - System diagram.

Table 5.4: LA03 - Length  $h$  and thickness  $t$  of cylindrical segments

Silo VS		Silo S		Silo B		Silo I		Silo Q	
$D = 5.0\text{ m}$	$D = 6.0\text{ m}$	$D = 6.0\text{ m}$	$D = 6.8\text{ m}$	$D = 6.8\text{ m}$	$D = 7.6\text{ m}$	$D = 7.6\text{ m}$	$D = 10.0\text{ m}$	$D = 10.0\text{ m}$	
$t$	$h$	$t$	$h$	$t$	$h$	$t$	$h$	$t$	$h$
3	8800								
4	3600	3	8200	3	8000				
5	4400	4	2800	4	2400	3	8200	1	3300
6	5600	5	3200	5	2600	4	2200	2	2700
7	3600	6	3800	5	1000	5	800	3	500

It is important to note that the CSBL element, as developed by Boyez et al [7] and used for the LAs of the silos in that reference, can accurately model up to a quadratic pressure per element due to the nature of the shape functions adopted. Taking into account that there is just one CSBL element to model each segment (one of the benefits of the corresponding formulation) of the silos, some discrepancies are expected (the reader is

reminded that pressures in AQUINAS are split into trapezoids per element, but more than one elements are used per segment). These discrepancies will be more or less subtle depending on how close the original distribution function and the quadratic fit are. Some key stress results are presented in Figures 5.8 - 5.9, where the good agreement between the two computational approaches is illustrated. More result plots regarding the displacements, strains or curvatures can be generated by running the `input_Example_LA03.m` script.

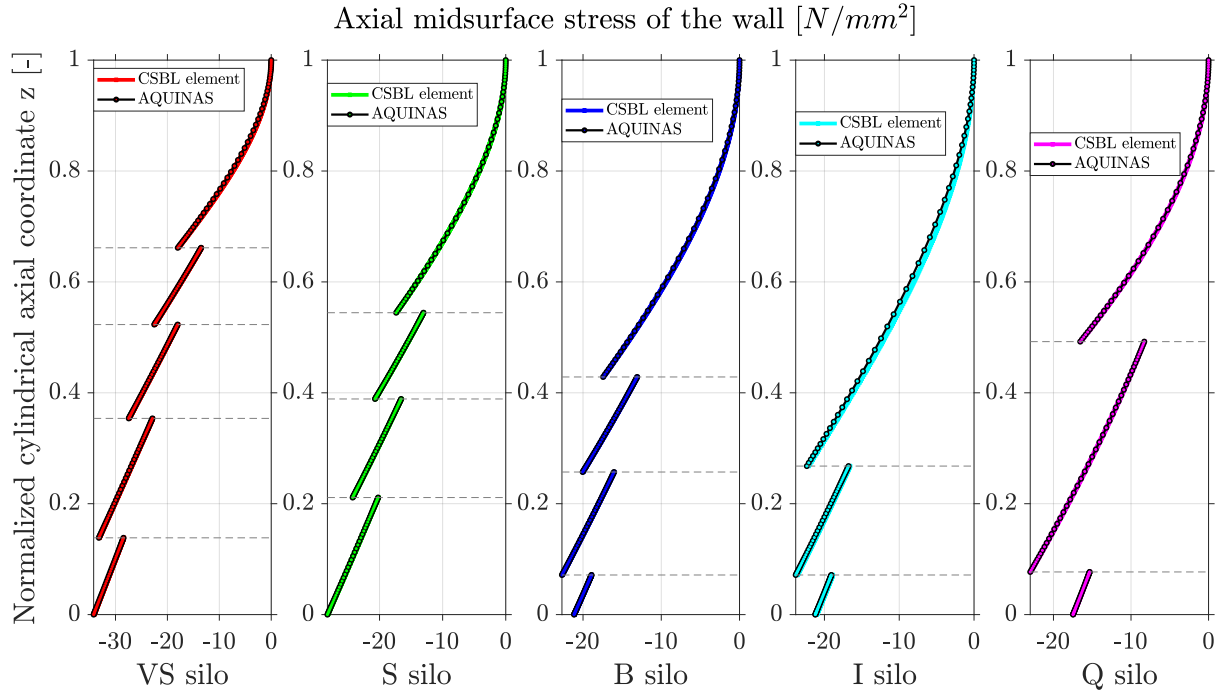


Figure 5.8: LA03 - Comparison of midsurface axial stresses of the shell wall.

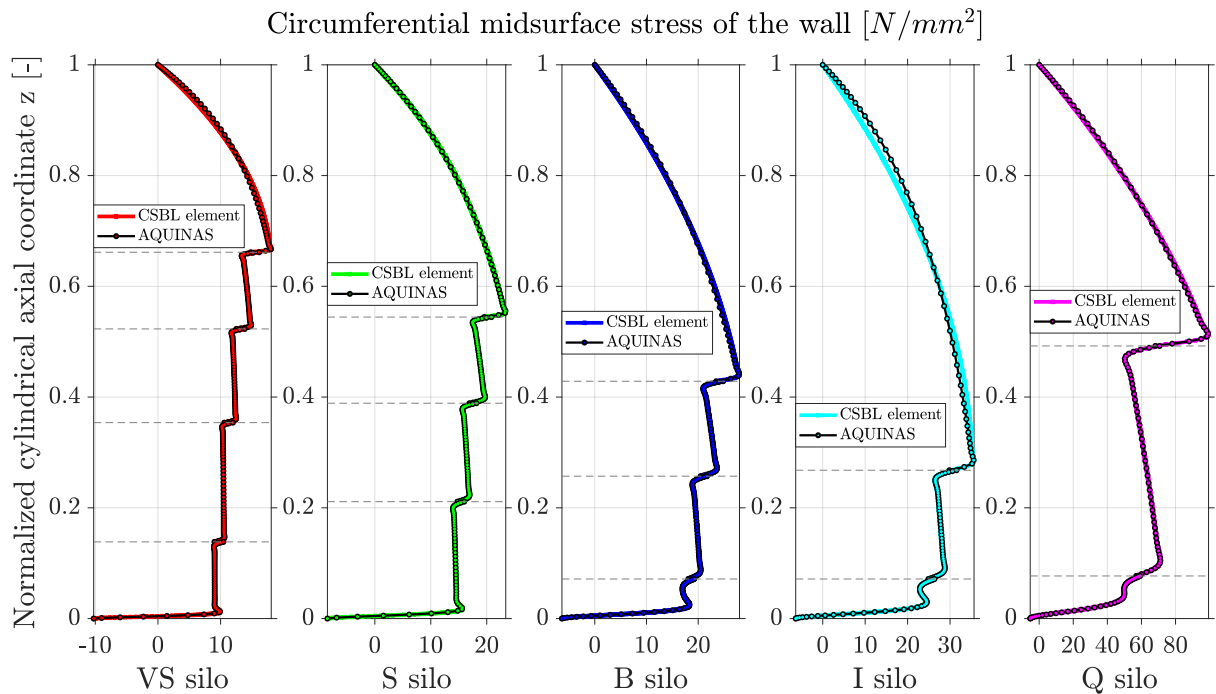


Figure 5.9: LA03 - Comparison of midsurface circumferential stresses of the shell wall.

### 5.1.4 Example LA04: Conical shell under axial uniform pressure

In this LA example, as presented in the `input_Example_LA04.m` script, the FE results of a conical shell under unit axial (vertical) uniform axisymmetric pressure  $q = 1.0 \text{ N/mm}^2$  are compared against corresponding membrane and bending theory analytical solutions. The cone is closed at its apex, with the half apex angle being  $\alpha = 30^\circ$ . The meridian of the cone has a length of  $L = 200 \text{ mm}$  with a BC1f - S2 support applied at its base ( $u = w = 0$  equivalent to  $\bar{u} = \bar{w} = 0$ ), while the wall of the axisymmetric shell has a thickness of  $t = 5 \text{ mm}$ . The geometric properties of the cone are presented in Figure 5.10.

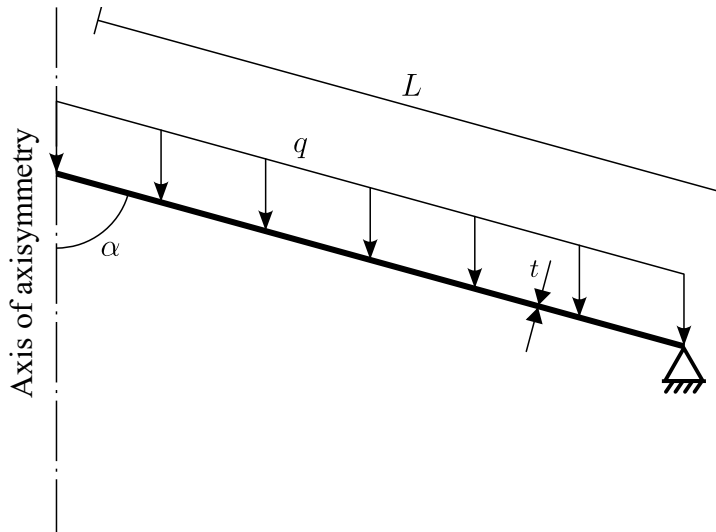


Figure 5.10: LA04 - System diagram.

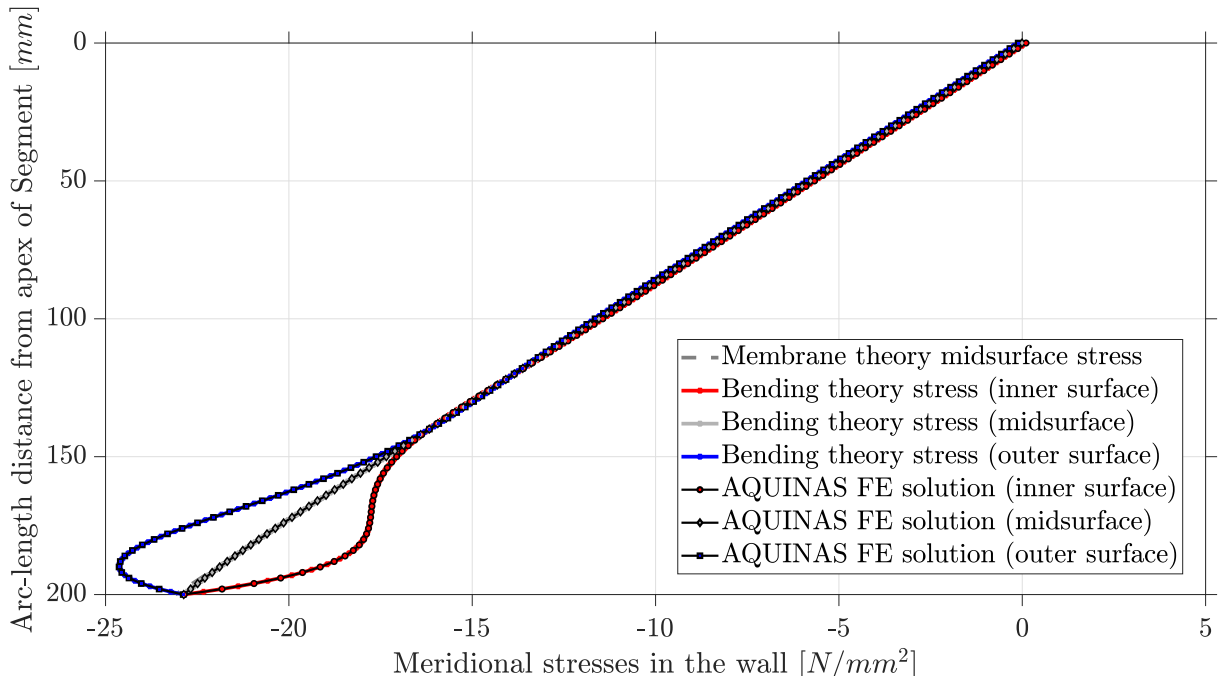


Figure 5.11: LA04 - Comparison of inner, middle and outer surface meridional stresses of the conical shell wall.

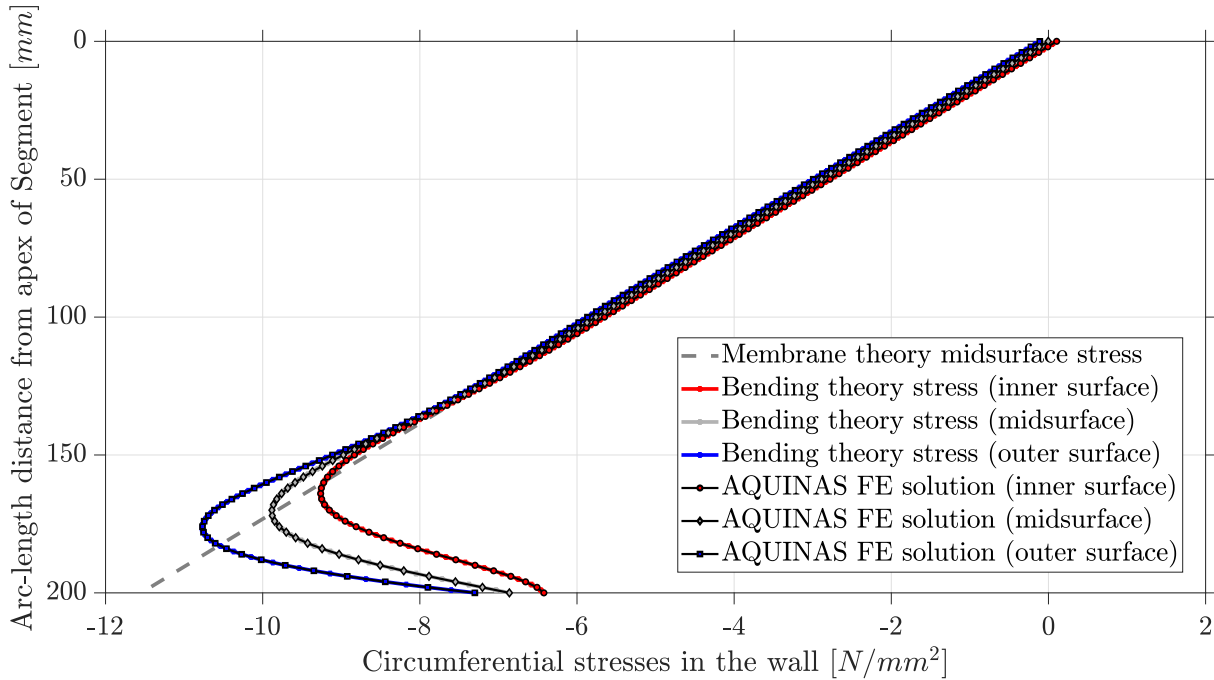


Figure 5.12: LA04 - Comparison of inner, middle and outer surface circumferential stresses of the conical shell wall.

The membrane and bending theory analytical solutions used for comparison purposes here can be found in Article 133 of Timoshenko and Woinowsky-Krieger [55]. The inner, middle and outer surface stresses of the cone are displayed in Figures 5.11 - 5.12 where the AQUINAS FE results show a great agreement with the bending theory analytical solution. The membrane theory results are also included, despite the considerable deviations from the more accurate bending theory solution near the exposed edge of the shell, where bending effects are dominant.

### 5.1.5 Example LA05: Spherical shell segment with an outward radial edge load

The first LA example of an axisymmetric shell without a straight meridian is that of a spherical segment subjected to a radial edge load  $H$ . The analytical membrane and bending theory solutions, used for comparison purposes with AQUINAS' results, can be found in '*Stresses in Shells*' by W. Flugge [20]. The same parameters of the problem used in the book (radius of the sphere, thickness of the wall etc.) are also adopted in the `input_Example_LA05.m` script, with the only exception that [mm] are used as length units and [N] for force. The spherical zone, truncated at both ends, is symmetric about the horizontal axis with a total angle span of  $2\alpha$ , where  $\alpha = 10^\circ$ . Taking into account the horizontal symmetry of the problem, only the upper half of the meridian is modelled, with appropriate boundary conditions at its base. The radius of the spherical segment is  $a = 381.0 \text{ mm} (= 15.0 \text{ in.})$  and the shell wall has a thickness of  $t = 25.4 \text{ mm} (= 1.0 \text{ in.})$ . A unit line load  $H$  is applied at both truncated ends of the axisymmetric shell. The geometry of the spherical shell is displayed in Figure 5.13, while a brief comparison of the meridional and circumferential stress results is made in Figures 5.14 - 5.15.

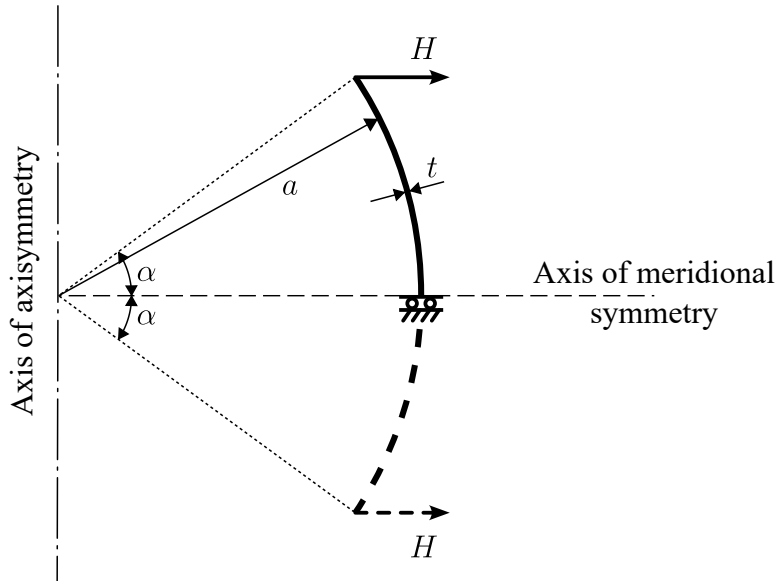


Figure 5.13: LA05 - System diagram.

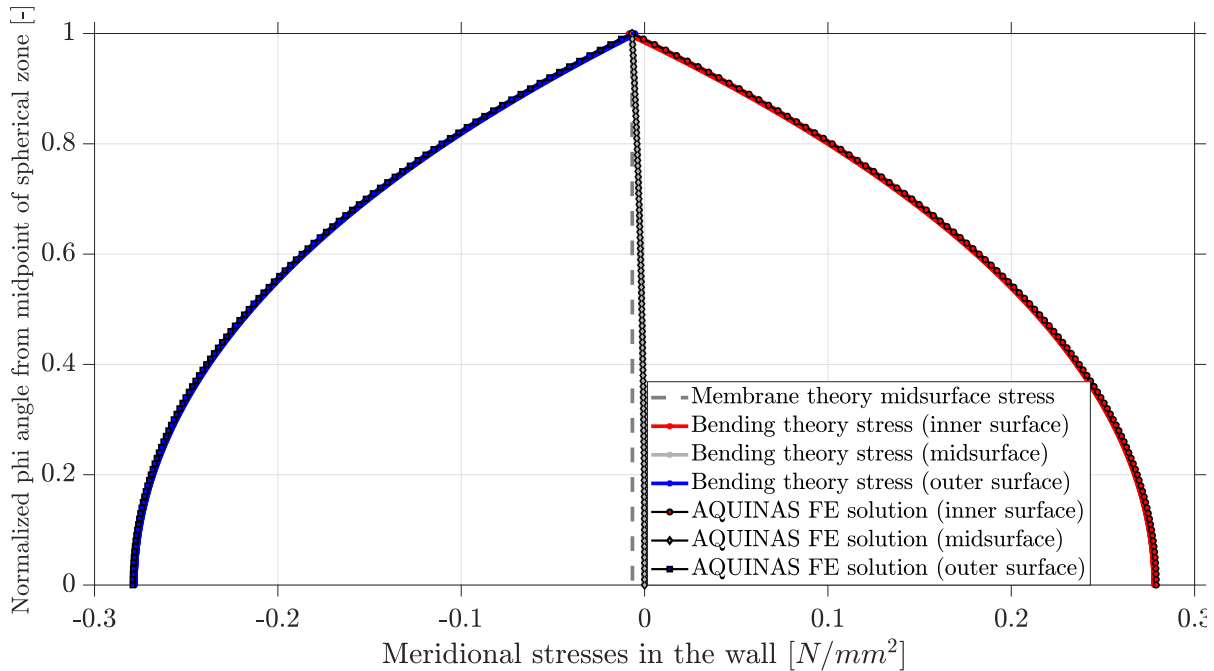


Figure 5.14: LA05 - Comparison of inner, middle and outer surface meridional stresses of the spherical zone.

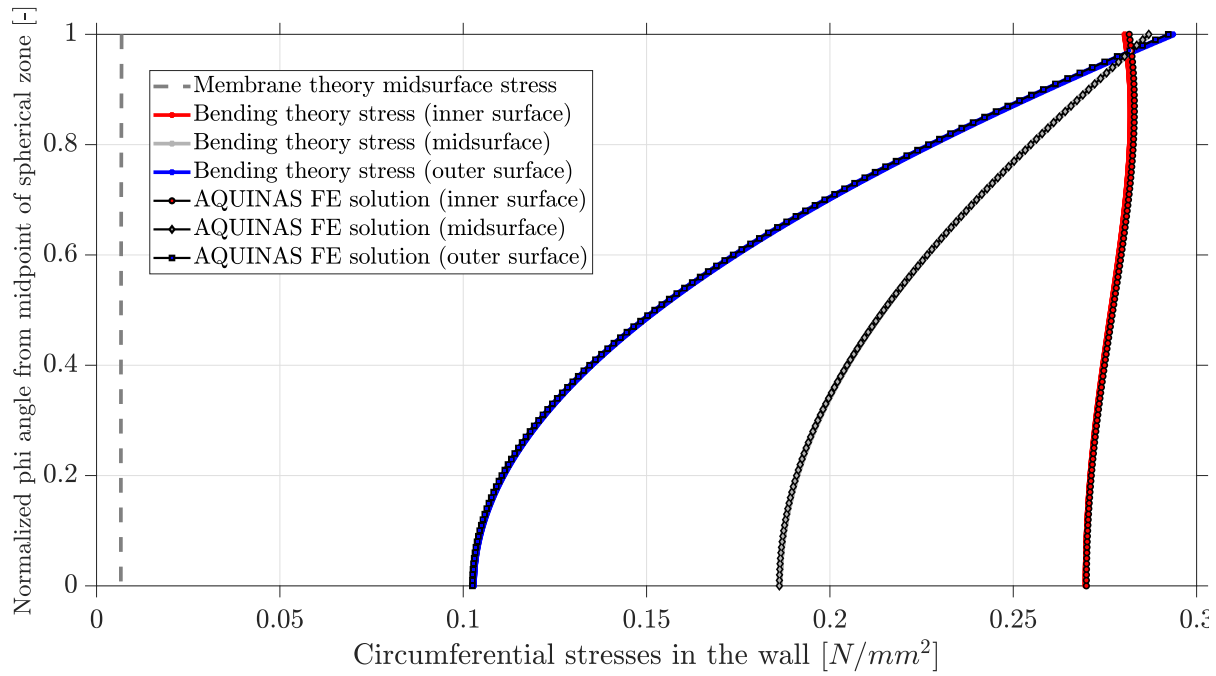


Figure 5.15: LA05 - Comparison of inner, middle and outer surface circumferential stresses of the spherical zone.

### 5.1.6 Example LA06: Spherical cap subjected to uniform vertical pressure

It is interesting to also explore the response of a different kind of axisymmetric spherical shell, though one that is commonly encountered in real life problems, that of a spherical cap under uniform vertical pressure. This problem closely relates to the spherical cap ‘hats’ used in silo containers. The spherical cap considered here has an angle span of  $2\alpha$ , where  $\alpha = 10^\circ$ , and a radius of  $a = 500.0 \text{ mm}$ . The wall of the spherical cap has a thickness of  $t = 1.0 \text{ mm}$  and a uniform vertical pressure (similar to the effect of the self-weight) is applied along its meridian. The geometry of the spherical cap and the pressure that is applied on it are displayed in Figure 5.16.

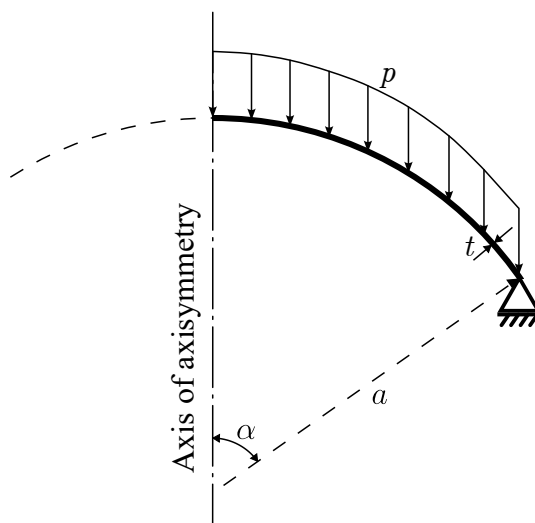


Figure 5.16: LA06 - System diagram.

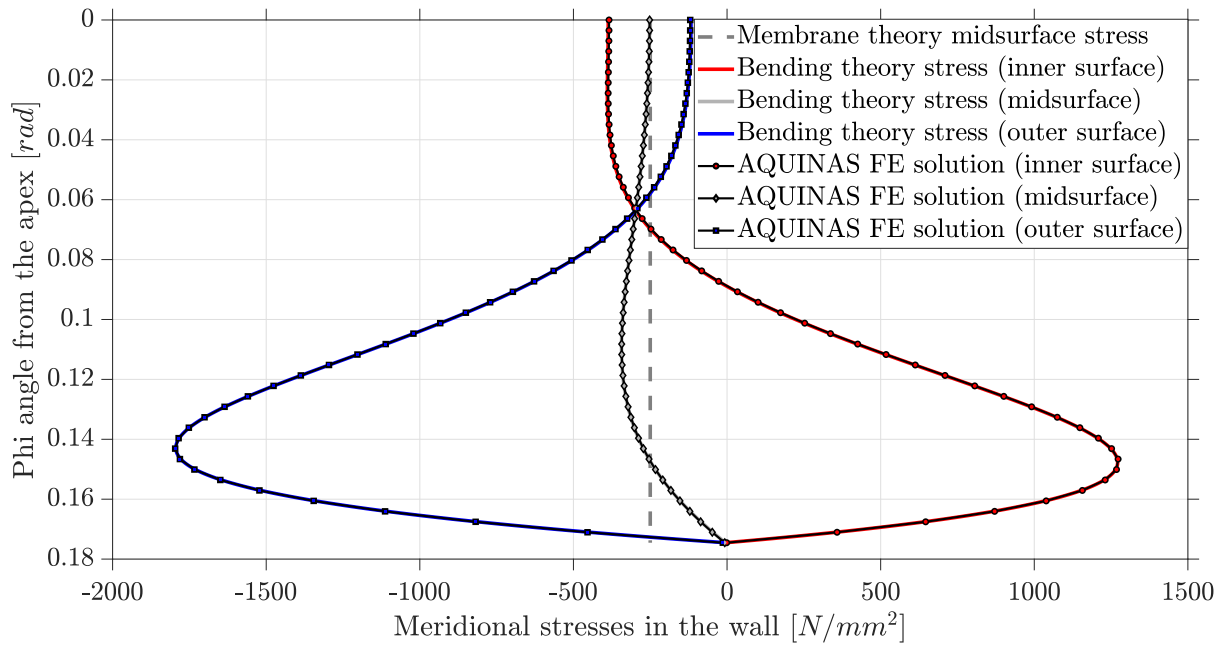


Figure 5.17: LA06 - Comparison of inner, middle and outer surface meridional stresses of the spherical cap.

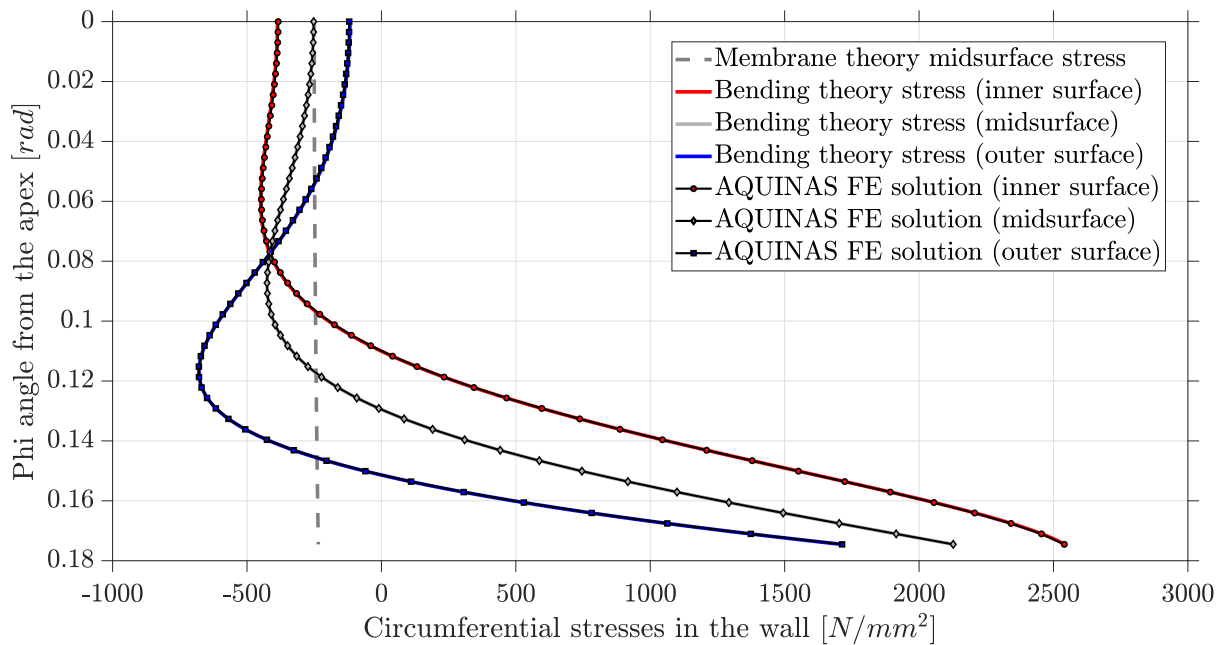


Figure 5.18: LA06 - Comparison of inner, middle and outer surface circumferential stresses of the spherical cap.

An analytical solution has also been coded in the example script `input_Example_LA06.m` for comparison with the AQUINAS LA results. The membrane and bending theory solutions there are taken from W. Flugge's work *Stresses in shells* [20], where a similar problem is considered. It is important to note however that in the problem discussed there the Poisson's ratio used is equal to  $\nu = 0$ , in contrast to the Poisson's ratio considered in all of the examples of this chapter, including this one, of  $\nu = 0.3$ . Hence, if comparison with the results in the book by W. Flugge is intended, a minor alteration is in order. A brief

presentation of the meridional and circumferential stresses is given in Figures 5.17 - 5.18 below. More results or different combinations of the input parameters can be examined by running the example script `input_Example_LA06.m`.

### 5.1.7 Example LA07: LA of a thin elliptical shell cap under uniform pressure

In order to fully test the capability of AQUINAS to analyse elliptical shell segments, a simplification of which are the axisymmetric spherical shell problems of the two previous examples, the LA of a thin elliptical shell cap under uniform compression is examined in `input_Example_LA07.m`. The upper half of the ellipse that is modelled here has a meridional displacement restraint at its bottom edge. Its geometry is defined by its major and minor radius,  $a = 1000.0 \text{ mm}$  and  $b = 500.0 \text{ mm}$  accordingly, while the shell wall has a thickness of  $t = 1.0 \text{ mm}$ . The normal internal pressure applied has a unit magnitude of  $p = 1.0 \text{ N/mm}^2$ . The definition of this axisymmetric shell problem is illustrated in Figure 5.19.

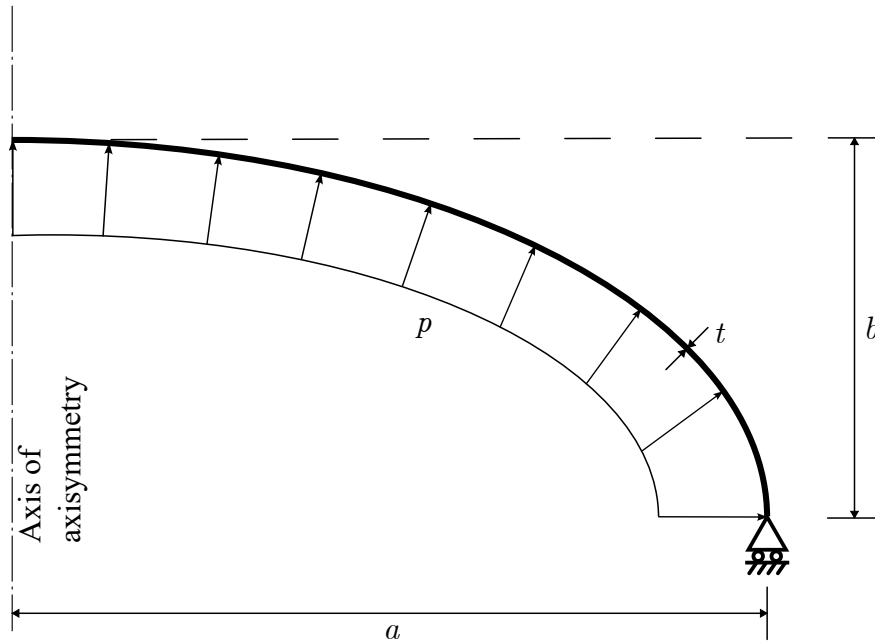


Figure 5.19: LA07 - System diagram.

Due to the complexity of a potential bending theory analytical solution in this case, only a membrane theory algebraic solution is provided for reference. The membrane theory results can be found in chapter '2.2.2.2 Boiler End' of '*Stresses in Shells*' by W. Flugge [20]. Instead, the AQUINAS FE results are compared against those of another FE software, established through decades of extensive use by the scientific community, ABAQUS. Its results for the problem definition described above are stored in `input_Example_LA07.csv` and will not be regenerated for different geometric, material or loading inputs in the corresponding script. Hence, a user who is interested in a comparison with any of the properties altered will only have the membrane theory results readily available, and may have to compute their own ABAQUS (or any other axisymmetric FE solver) solution for the problem if they seek a more precise answer to this example. The stress results for the

inner, middle and outer fibre of the shell wall are presented in Figures 5.20 - 5.21, where the good agreement between AQUINAS and ABAQUS can be appreciated, as well as with the membrane theory solution for the region of the shell's meridian that is sufficiently distant from the bending boundary layer of the ellipsoid's edge.

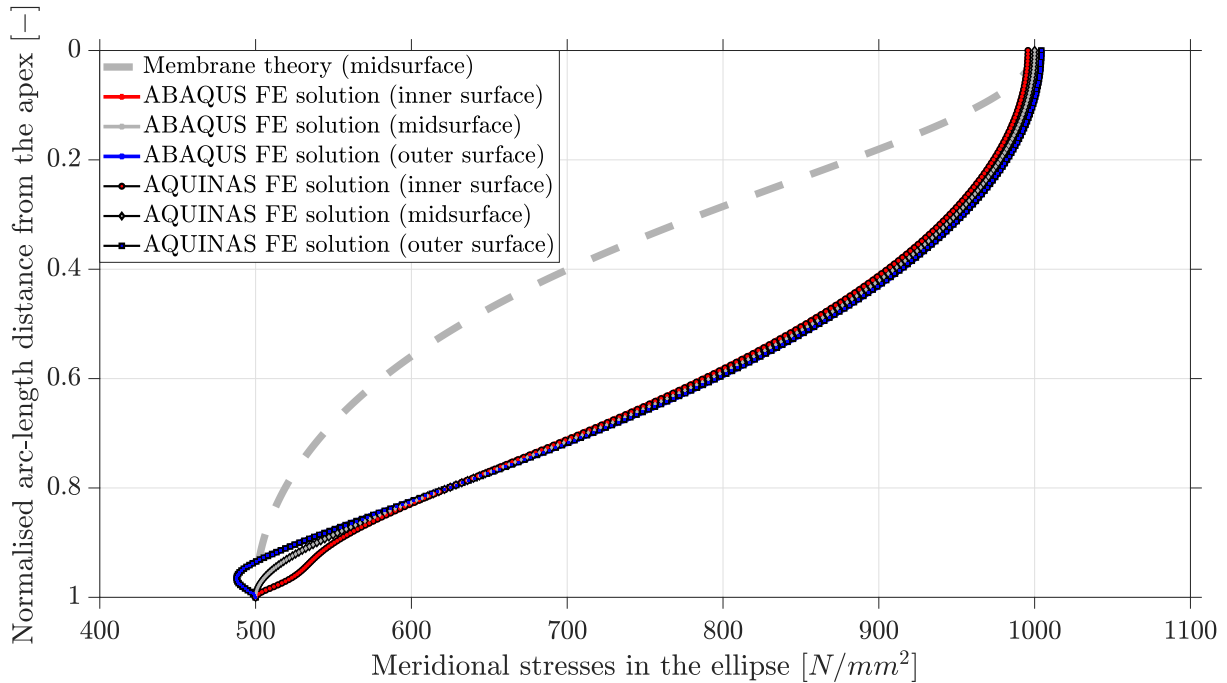


Figure 5.20: LA07 - Comparison of inner, middle and outer surface meridional stresses of the spherical cap.

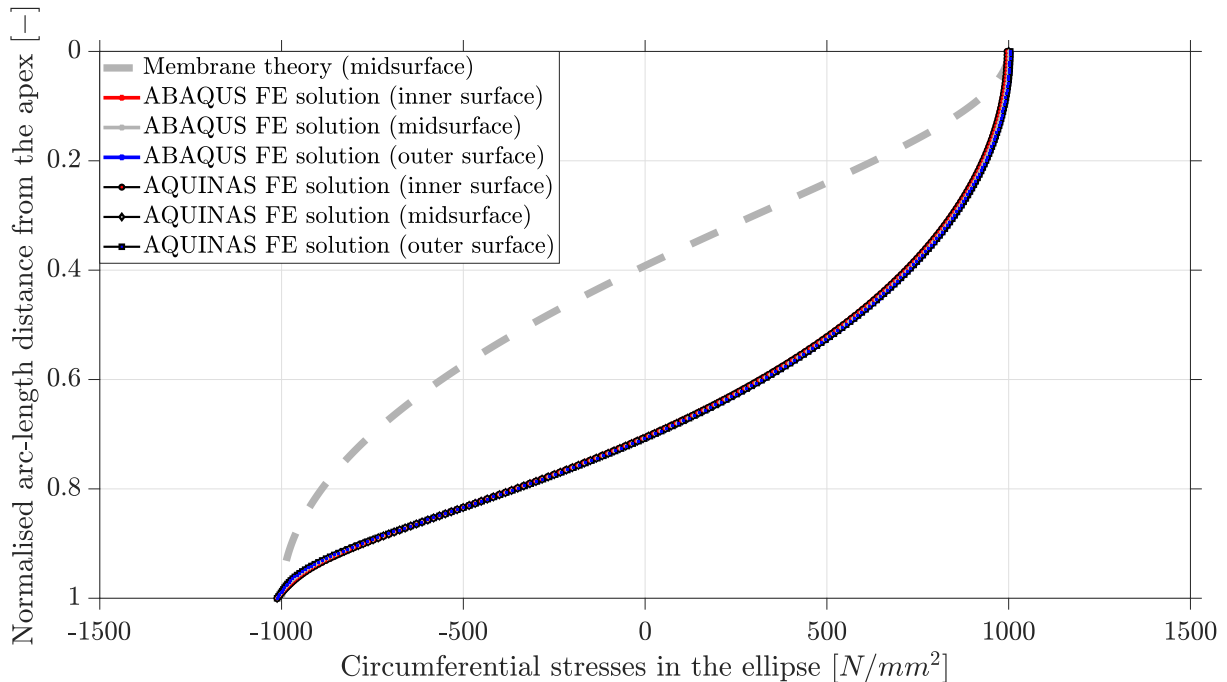


Figure 5.21: LA07 - Comparison of inner, middle and outer surface circumferential stresses of the spherical cap.

### 5.1.8 Example LA08: LA of a thin ogival shell under self weight pressure

There are two ways to define an ogival in AQUINAS. The analyst can either use the 'Ellipse' option of the segment object and provide a centre for the ellipse (in this case sphere) that has a negative radial coordinate (behind the axis of axisymmetry), or use the '3pointArc' option and have as input 3 points along the curved meridian of the shell. In `input_Example_LA08.m` the '3pointArc' option was employed. The ogival's meridional curvature radii is  $a = 1000.0 \text{ mm}$  while its truncation angle is  $\phi_0 = 20^\circ$ . A meridional displacement restraint applied at its base. A unit self weight loading  $q = 1.0 \text{ N/mm}^2$  is considered along the meridian of the shell, defined as a combination of a normal pressure and traction (tangential pressure) that vary along the meridian of the shell. This shell problem is displayed in Figure 5.22.

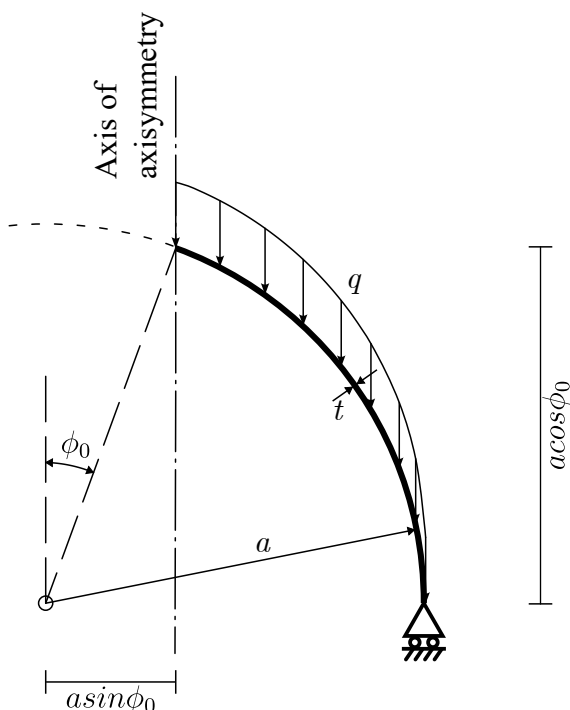


Figure 5.22: LA08 - System diagram.

Once again, the stresses throughout the shell wall obtained from AQUINAS and ABAQUS are compared against each other, as well as the corresponding membrane theory results, in Figures 5.23-5.24. The algebraic solution coded in the `input_Example_LA08.m` script is obtained from chapter 2.2.2.3 *Pointed Shells* of '*Stresses in Shells*' by W. Flugge [20]. More comparison plots may be generated by running the input script, while for values of the input variables used only the membrane theory solution can be expected to still be valid.

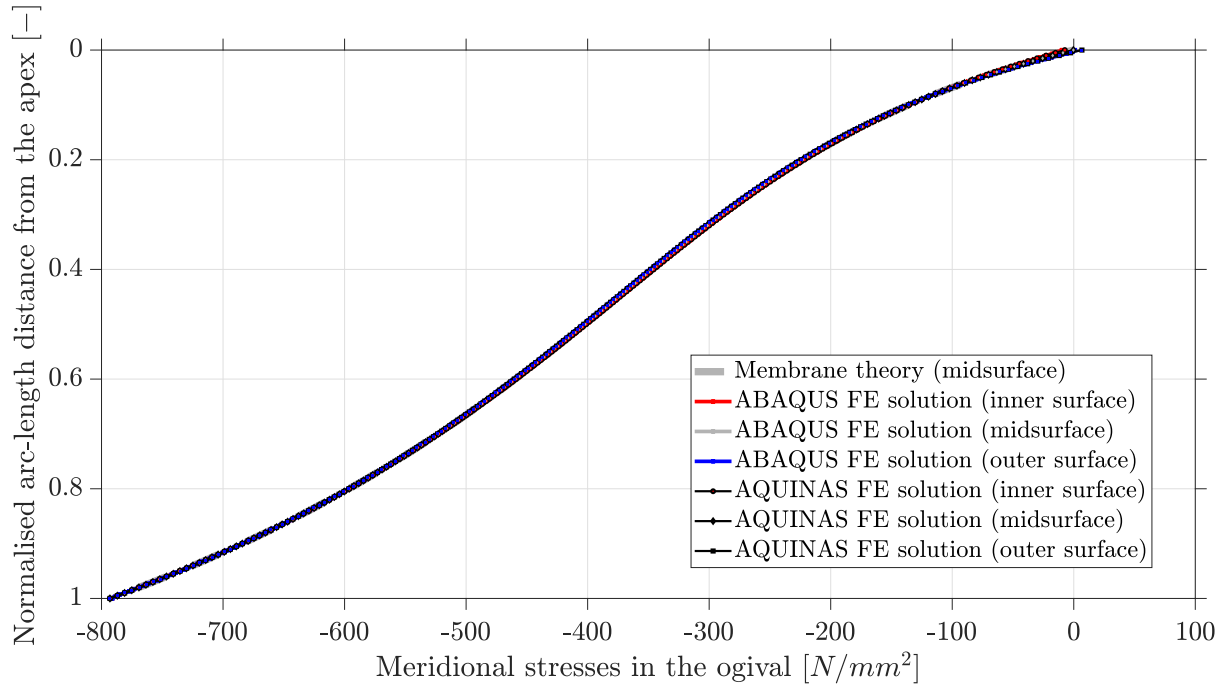


Figure 5.23: LA08 - Comparison of meridional stresses in the inner, middle and outer surface of the shell wall.

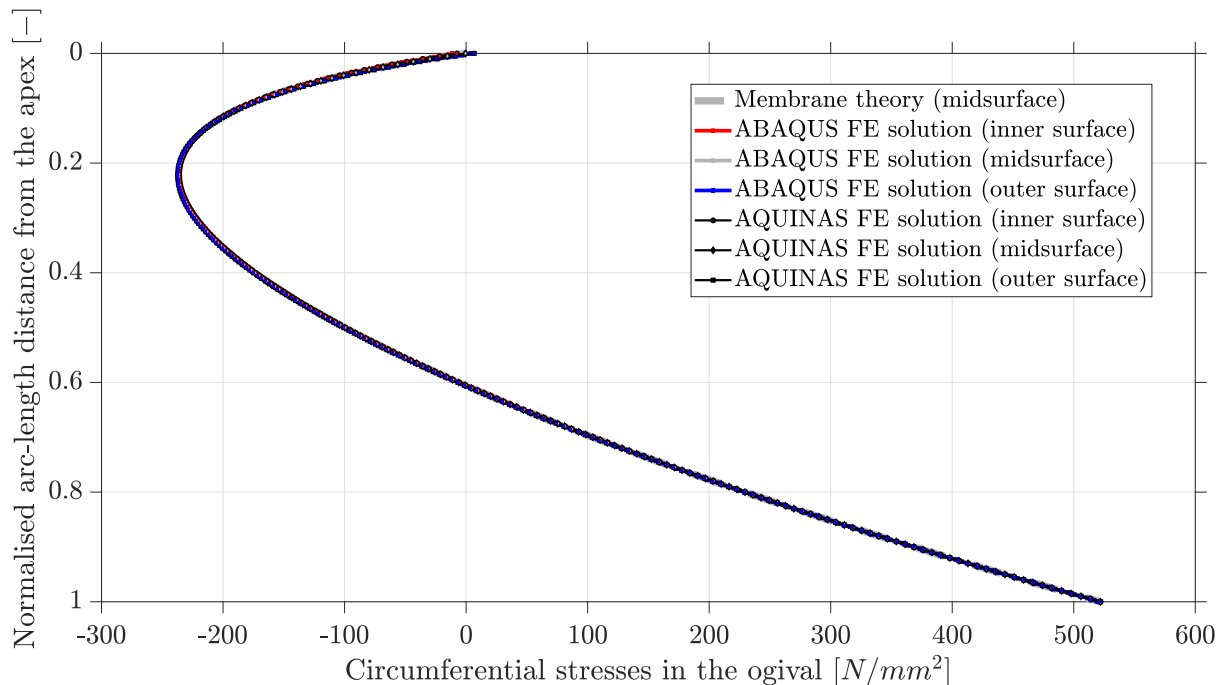


Figure 5.24: LA08 - Comparison of circumferential stresses in the inner, middle and outer surface of the shell wall.

### 5.1.9 Example LA09: LA of a thin hyperboloid under an axial edge load

AQUINAS is also able to accurately model and analyse shell segment with negative meridional curvature, such as the hyperboloid of this LA example. The meridian is

constructed with the use of the '*3pointArc*' option, with a total height of  $h = 1000.0\text{ mm}$  and a radius that ranges from  $r_{edge} = 1000.0\text{ mm}$  at the edges to  $r_{in} = 750.0\text{ mm}$  at the point closest to the axis of revolution. The axisymmetric hyperboloid has a BC1r - C1 boundary condition applied at its base, while the top edge is completely free, with an edge load  $N = 1000.0\text{ N/mm}$  acting axially downwards. The shell wall has a thickness of  $t = 1.0\text{ mm}$ . The geometry of this shell problem is presented in Figure 5.25.

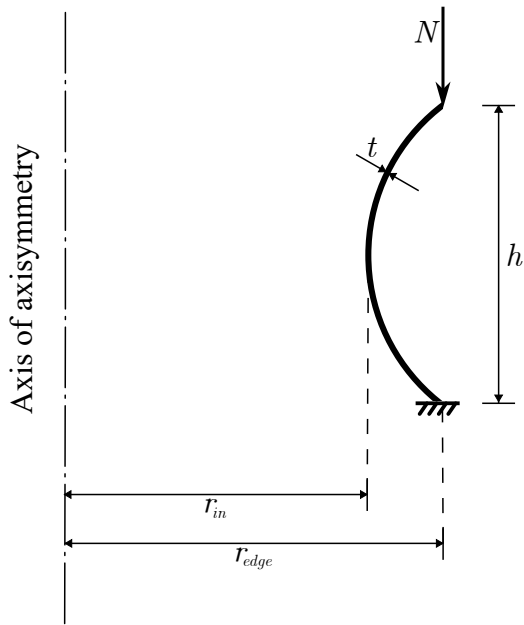


Figure 5.25: LA09 - System diagram.

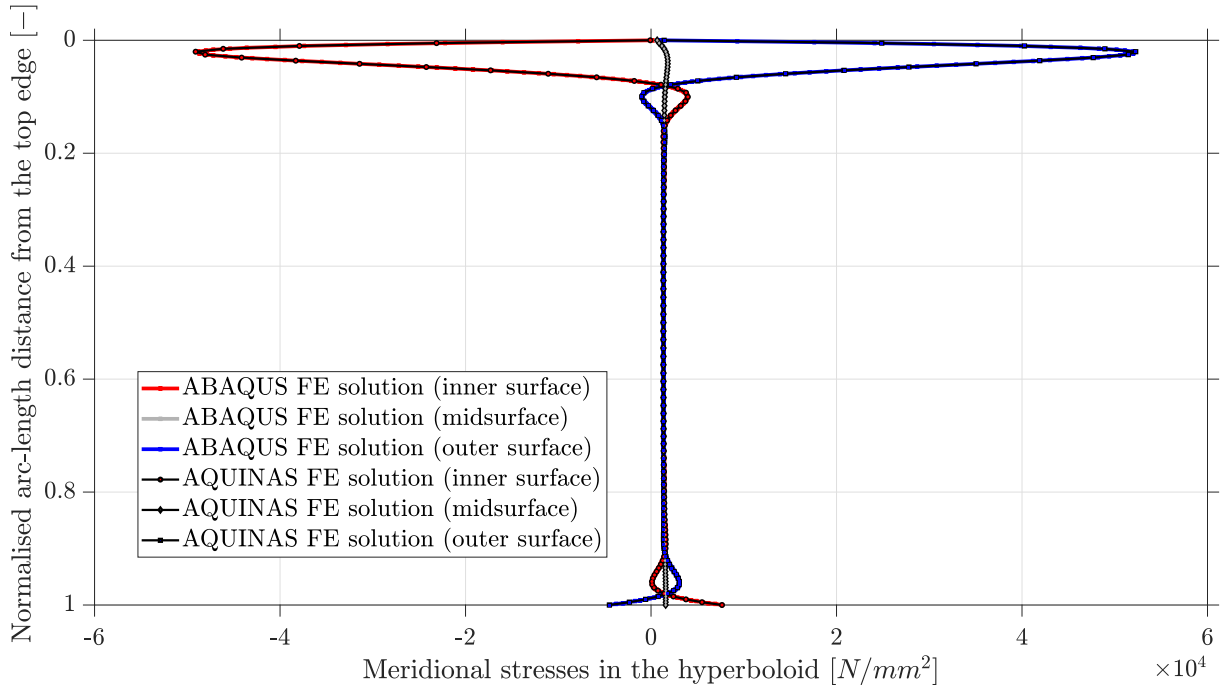


Figure 5.26: LA09 - Comparison of meridional stresses in the inner, middle and outer surface of the shell wall.

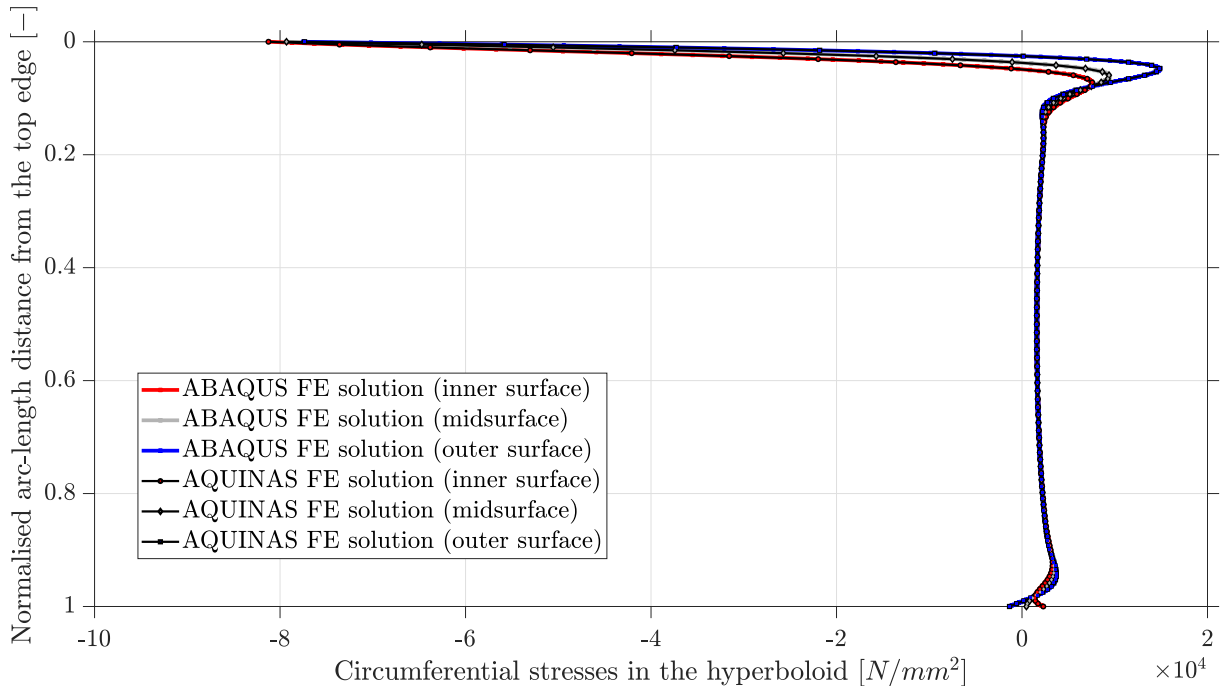


Figure 5.27: LA09 - Comparison of circumferential stresses in the inner, middle and outer surface of the shell wall.

In this example only an FE comparison with ABAQUS was attempted, owing to the scarcity of relevant axisymmetric shell problems in classic literature resources. The inner-middle-outer surface stress distributions along the hyperboloid's meridian are plotted for the two FE solvers in Figures 5.26-5.27, adding to the cases where AQUINAS demonstrates an excellent agreement with already established solutions, either computational or algebraic.

### 5.1.10 Example LA10: LA of a thin multi-segment shell under normal pressure

The multi-segment shell of this LA example is inspired by the corresponding axisymmetric shell problem presented in *Equilibrium of shell structures* by J. Heyman [23]. While a membrane theory solution is presented in [23], the shortcomings of the approach are acknowledged as there are evidently incompatibilities of circumferential stresses at shell junctions. The meridian of the pressure vessel modelled in `input_Example_LA10.m` consists of spherical caps, toroidal and barrel sections, and is symmetric about the equator of the axisymmetric shell, as can be appreciated from Figure 5.28. For the FE modelling of the probably most demanding LA problem thus far, the  $a$  reference radius parameter is set to  $a = 200.0 \text{ mm}$  and the thickness of the shell wall at  $t = 1.0 \text{ mm}$ . The angle  $\alpha$  can be found to be  $\alpha = 24.3^\circ$  [23] from basic geometry considerations. A unit internal pressure  $p = 1 \text{ N/mm}^2$  is considered, with the plane of meridional symmetry utilised to reduce the required discretisation for a computational solution of adequate quality to be obtained.

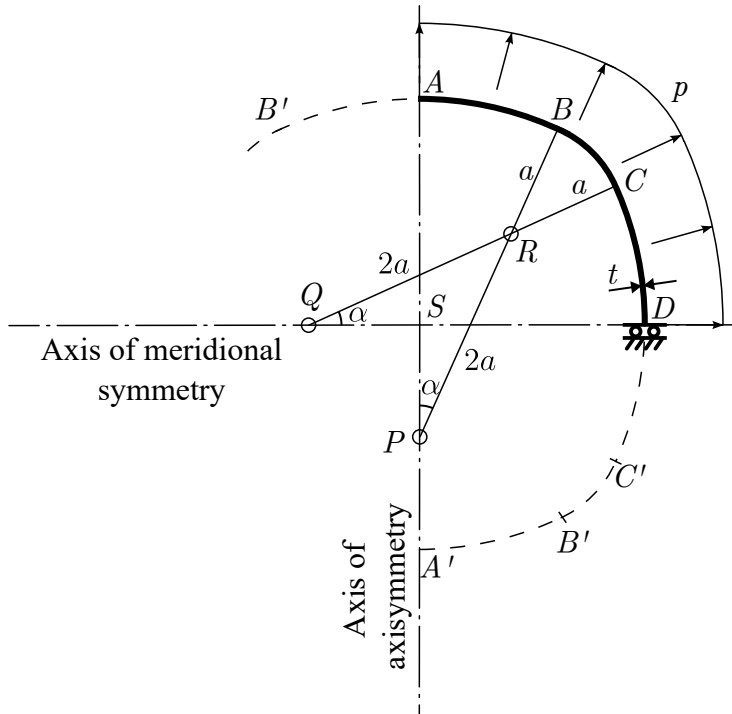


Figure 5.28: LA10 - System diagram.

Due to the inability of a membrane theory solution to accurately describe the stress distribution along the shell's meridian, and the overall complexity of the problem that makes the prospect of a bending theory solution rather uninviting, a computationally obtained distribution of the stresses, through submission of an ABAQUS FE [1] model, will be used for comparison with the AQUINAS results. The meridional and circumferential stress distributions are displayed in Figures 5.29 - 5.30, where the reader may appreciate the significance of the bending boundary layers between junctions of the pressure vessel, but also another perfect agreement between the two FE solutions. The membrane theory solution is also presented in Table 5.5, specialised for the specific  $a$  reference radius and  $p$  pressure used in the current implementation, as obtained from Table 2.1 of [23]. The reader can visually compare these with the mid-surface results of Figures 5.29 - 5.30 as a further cross check of the validity of the AQUINAS solution.

Table 5.5: LA10 - Meridional and circumferential membrane stress resultants at the shell junctions, obtained from Table 2.1 of [23], with reference to Figure 5.28.

Point	$A$	$B^-$	$B^+$	$C^-$	$C^+$	$D$
$r_\phi$ [mm]	600	600	600	380	380	400
$r_\theta$ [mm]	600	600	200	200	600	600
$N_\phi$ [N/mm]	300	300	300	190	190	200
$N_\theta$ [N/mm]	300	300	-300	20	260	266.6

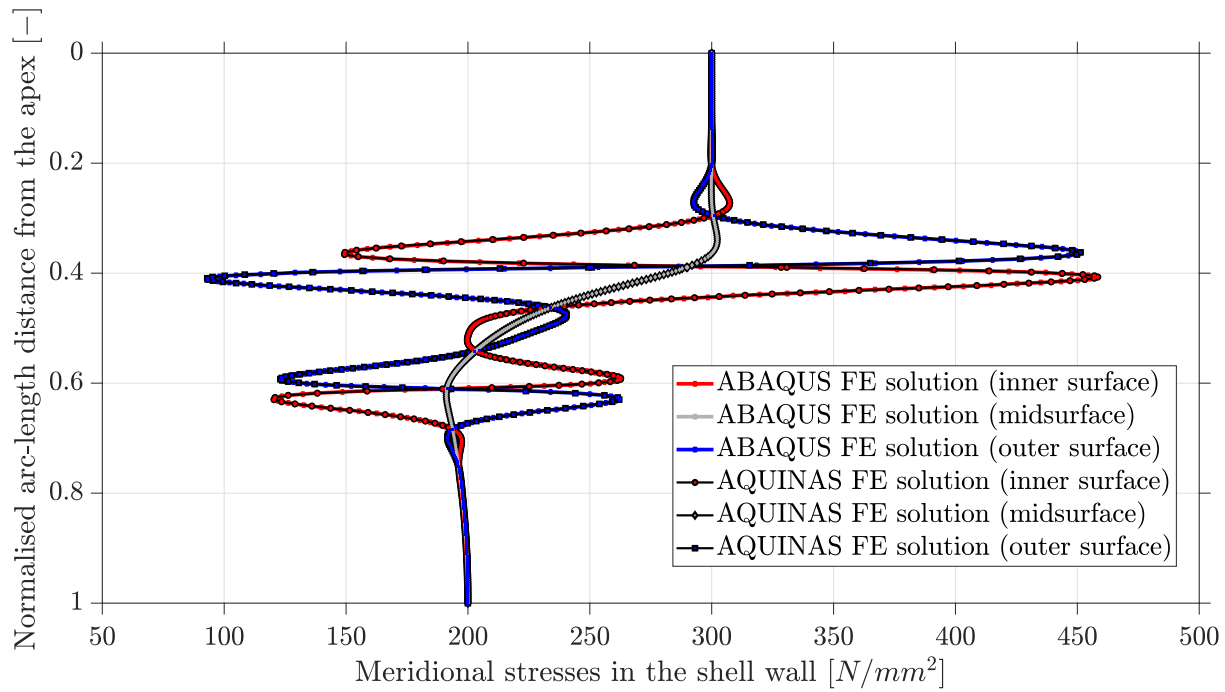


Figure 5.29: LA10 - Comparison of meridional stresses in the inner, middle and outer surface of the shell wall.

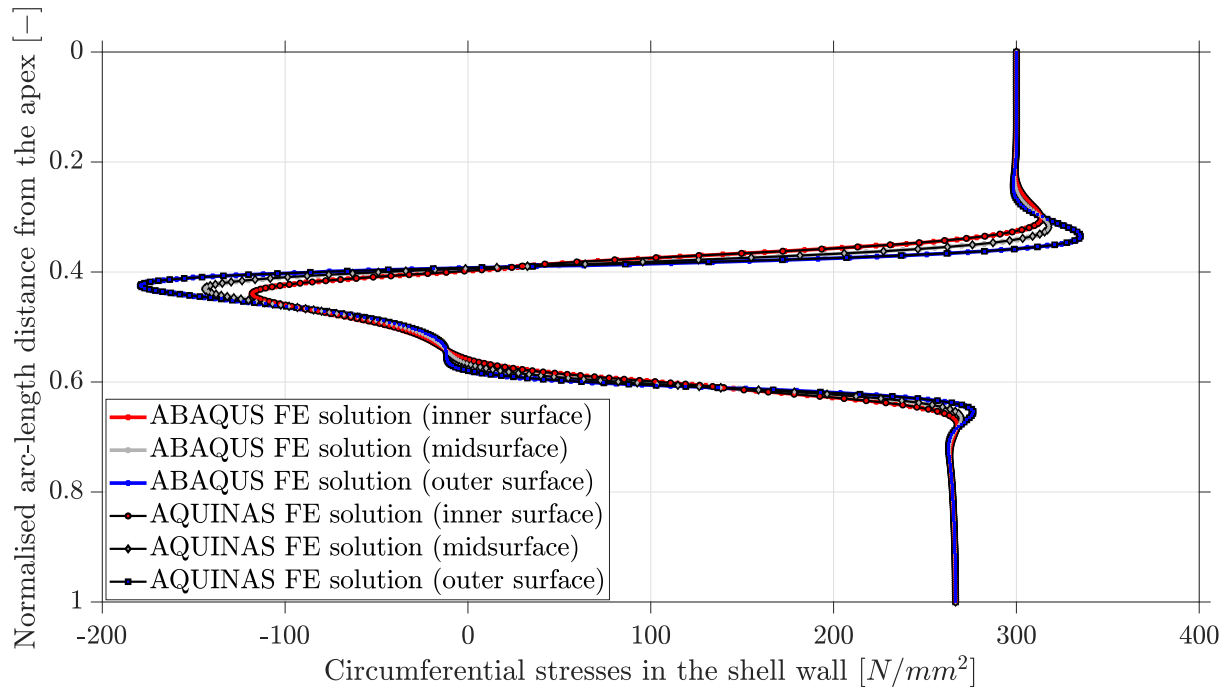


Figure 5.30: LA10 - Comparison of circumferential stresses in the inner, middle and outer surface of the shell wall.

### 5.1.11 Example LA11: Thin circular plate with clamped edges under uniform pressure

AQUINAS also provides the option for an explicit definition of an axisymmetric circular plate segment. The FE results obtained with the use of such a segment are tested in this

LA example, where the focus is on a circular plate subjected to a uniform unit pressure. The ends of the plate are clamped, with no hole considered at the its centre. Its outer edge has a radius of  $r = 50.0 \text{ mm}$  and its thickness is  $t = 1.0 \text{ mm}$ . The geometry of the plate, as well as the pressure applied, are presented in the following Figure 5.31. Comparison is made with a bending theory analytical solution, found in S. Timoshenko and S. Woinowsky-Krieger [55]. There is no point in a membrane theory for this example since there is no radial / meridional force acting on the plate and hence it only resists the uniform normal pressure through bending. Once more, stress results are presented in Figures 5.32 - 5.33 to illustrate the excellent agreement between the analytical solution and AQUINAS, while more can be found by running the `input_Example_LA11.m` script.

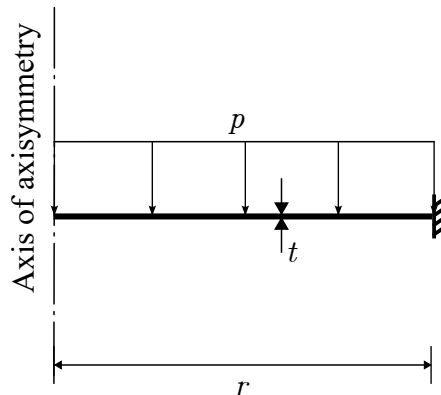


Figure 5.31: LA11 - System diagram.

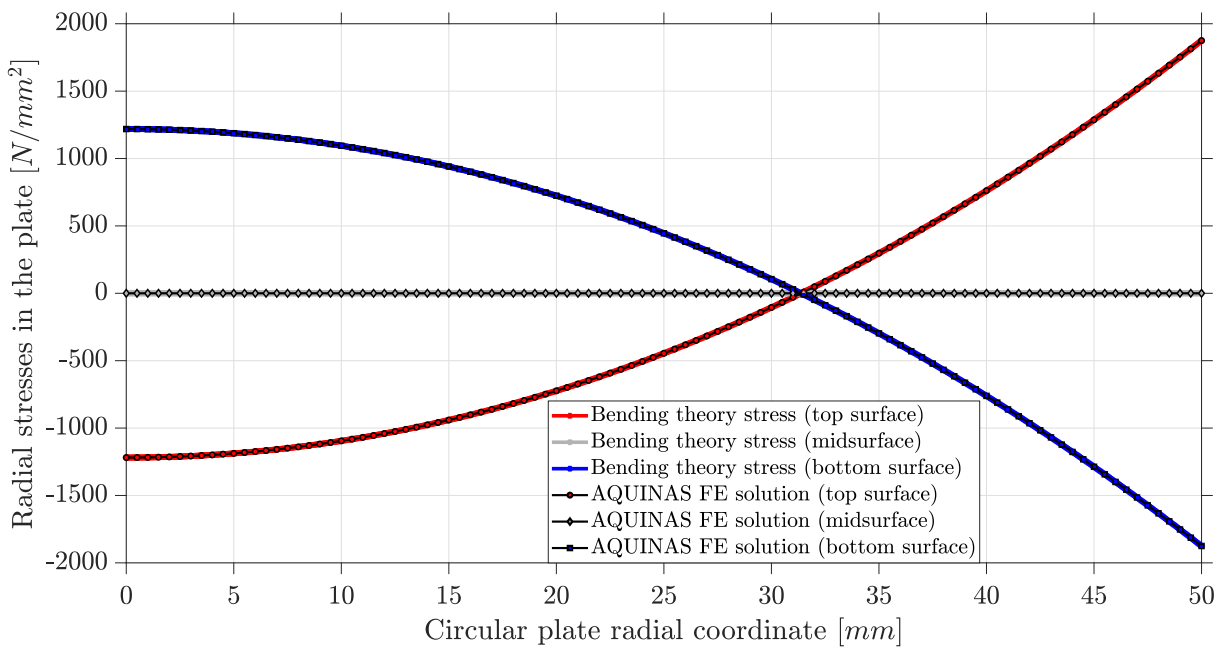


Figure 5.32: LA11 - Comparison of top, middle and bottom surface radial stresses of the circular plate.

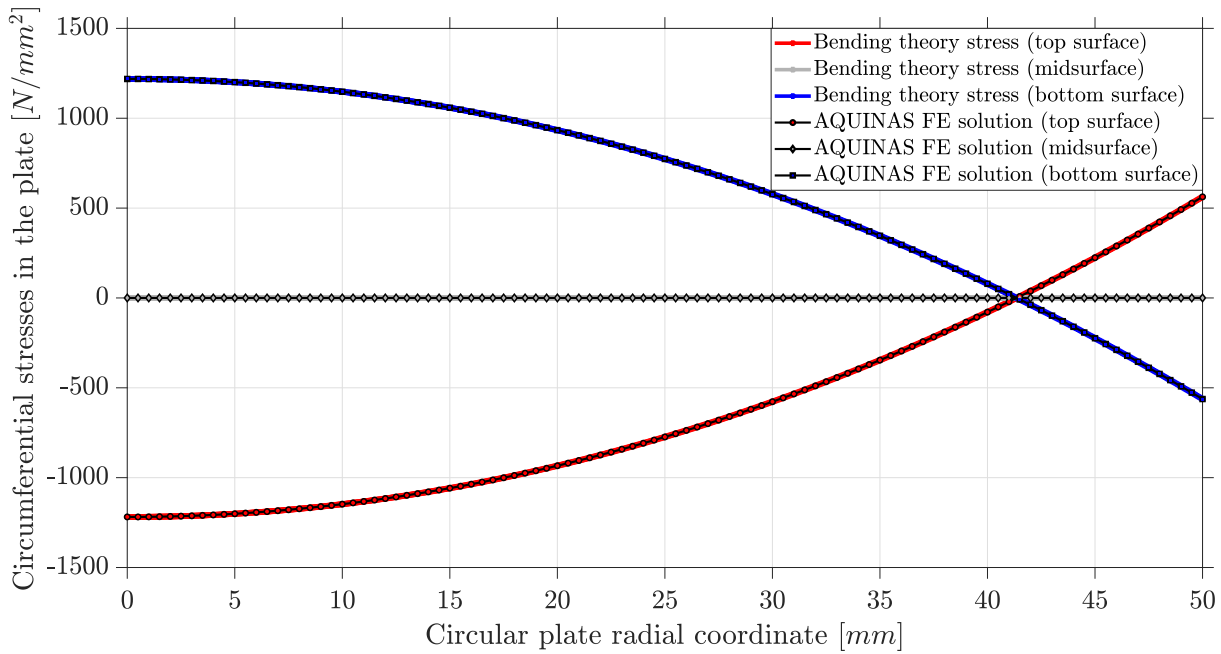


Figure 5.33: LA11 - Comparison of top, middle and bottom surface circumferential stresses of the circular plate.

### 5.1.12 Example LA12 : LA of a thin toroid shell with uniform internal pressure

This LA example can be found in `input_Example_LA12.m`, where the focus is on a thin toroid under uniform internal pressure. The geometry of this doughnut shell problem is illustrated in Figure 5.34.

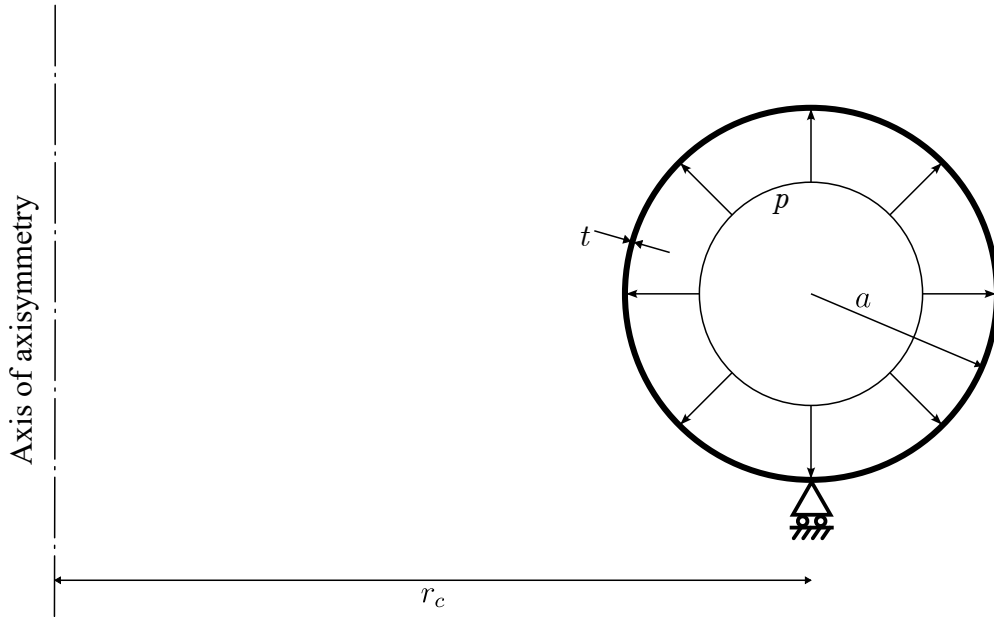


Figure 5.34: LA12 - System diagram.

The meridional radius of the shell is  $a = 500.0 \text{ mm}$  and its centre is located at a radial coordinate of  $r_c = 2000.0 \text{ mm}$ . The bottom apex of the circular closed meridian has BC2f

- S3 boundary condition and a unit normal internal pressure  $p_n = 1.0 \text{ N/mm}^2$  is uniformly distributed along the shell's meridian. The shell wall has a uniform thickness  $t = 1.0 \text{ mm}$ .

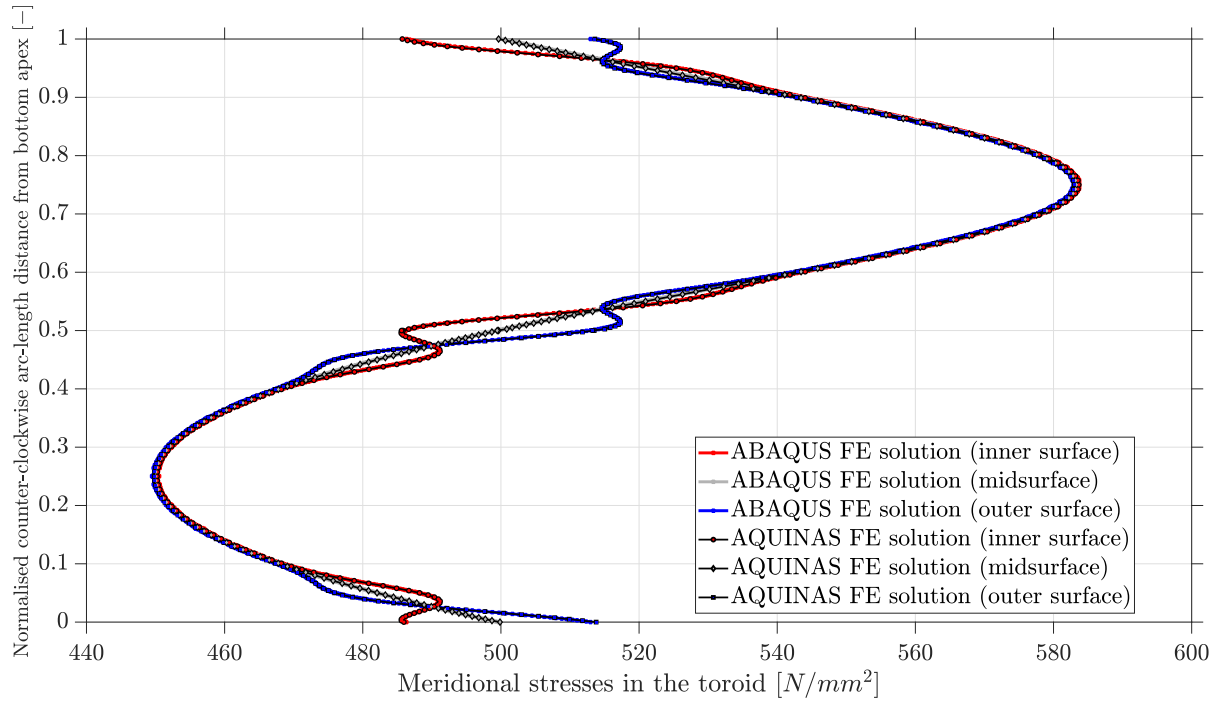


Figure 5.35: LA12 - Comparison of circumferential stresses in the inner, middle and outer surface of the shell wall.

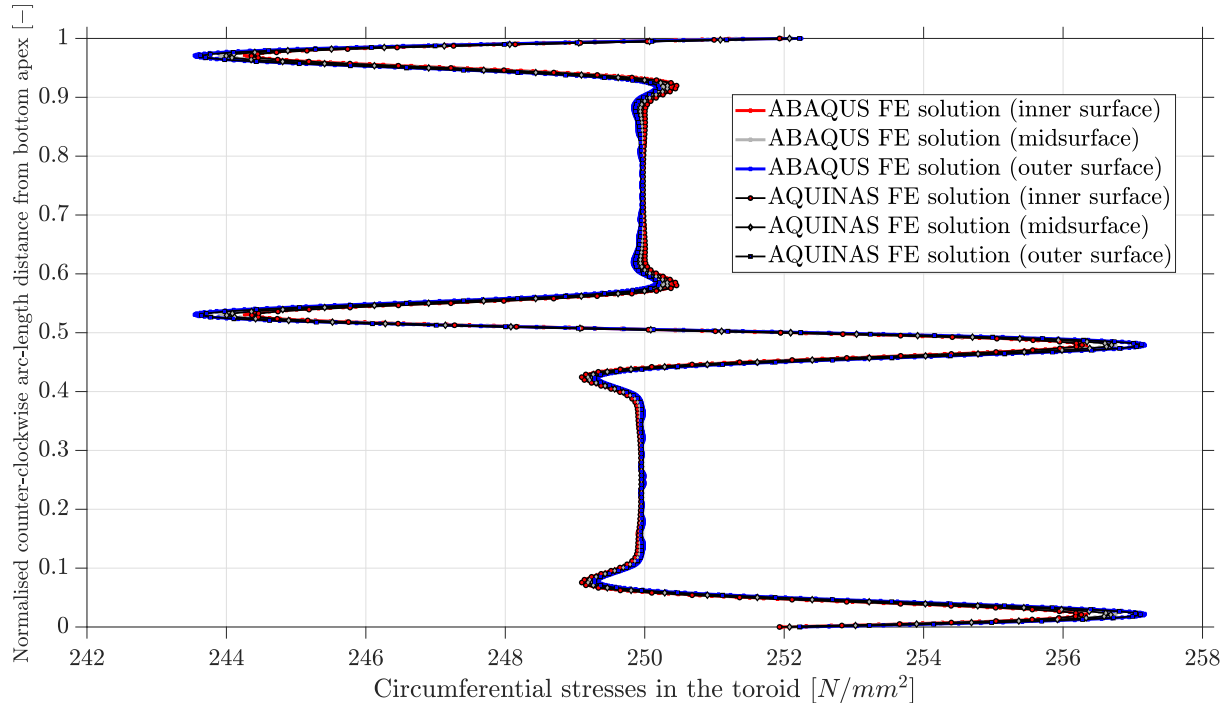


Figure 5.36: LA12 - Comparison of circumferential stresses in the inner, middle and outer surface of the shell wall.

ABAQUS is employed for one more time to generate the necessary results that will

allow a visual comparison with AQUINAS. The meridional and circumferential stress distributions can be examined in Figures 5.35-5.36 below, allowing the reader to appreciate the solid performance of AQUINAS throughout each of these LA examples. Deformed shape and strain results may be generated by running the input script `input_Example_LA12.m`.

## 5.2 LBAs

The chief motivation for the development of AQUINAS has been the accurate and efficient identification of the unsymmetrical bifurcation buckling mode for axisymmetric shell problems. The LA examples of the previous section have generated confidence in the correctness of the geometric definition of shell meridians and calculations of strains-stresses in AQUINAS. The present section proceeds to the more demanding computational procedures of the software, the bifurcation analyses of axisymmetric shells. Unless stated otherwise the material considered is steel, with a Young's modulus of  $E = 200000 \text{ N/mm}^2$  and a Poisson's ratio of  $\nu = 0.3$ .

### 5.2.1 Example LBA01: LBA of a thin cylindrical shell of varying length under uniform axial compression

In this LBA example, the response of thin unpressurised cylindrical shells under uniform compression is examined. The cylinders are of varying length, characterised by a dimensionless parameter  $\Omega$ , given as:

$$\Omega = \frac{L}{r} \sqrt{\frac{t}{r}} \quad (5.2)$$

An axially compressing edge load  $N_{cl}$  is applied at the top edge of the cylinders, the magnitude of which is related to the classical elastic critical stress  $\sigma_{cl}$  for the bifurcation of cylinders under axial compression, given as

$$\sigma_{cl} = \frac{E}{\sqrt{3(1 - \nu^2)}} \frac{t}{r} \quad (5.3)$$

so that  $N_{cl} = \sigma_{cl} t$ , or in expanded form:

$$N_{cl} = \frac{Et^2}{r\sqrt{3(1 - \nu^2)}} \quad (5.4)$$

The derivation of the classical elastic critical stress  $\sigma_{cl}$  has been based on a uniform membrane pre-buckling stress state. This however does not hold in the current example, due to the restraint applied for the radial displacement  $u$  at both ends of the cylinder. A BC2f boundary condition is applied at the top edge of the cylinder and a BC1f at its base. While the length of the cylinders vary, their radius and thickness is set to  $r = 500.0 \text{ mm}$  and  $t = 1.0 \text{ mm}$  accordingly, leading to an  $r/t$  ratio of 500. The geometry, loading and boundary conditions of the cylinder are presented in Figure 5.37. Several values of the  $\Omega$  parameter are explored, from rather short ones, where plate-like buckling is expected to be critical, to very long tubes that behave like a column, with the Euler buckling load being very close to the FE prediction by AQUINAS. The critical buckling loads computed, normalised by the classical buckling load of Eq. (5.4) for all values of  $\Omega$  considered, are plotted in Figure 5.38.

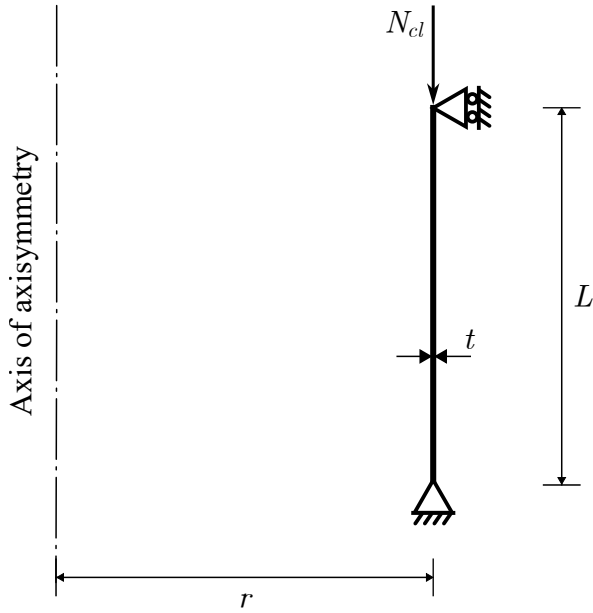
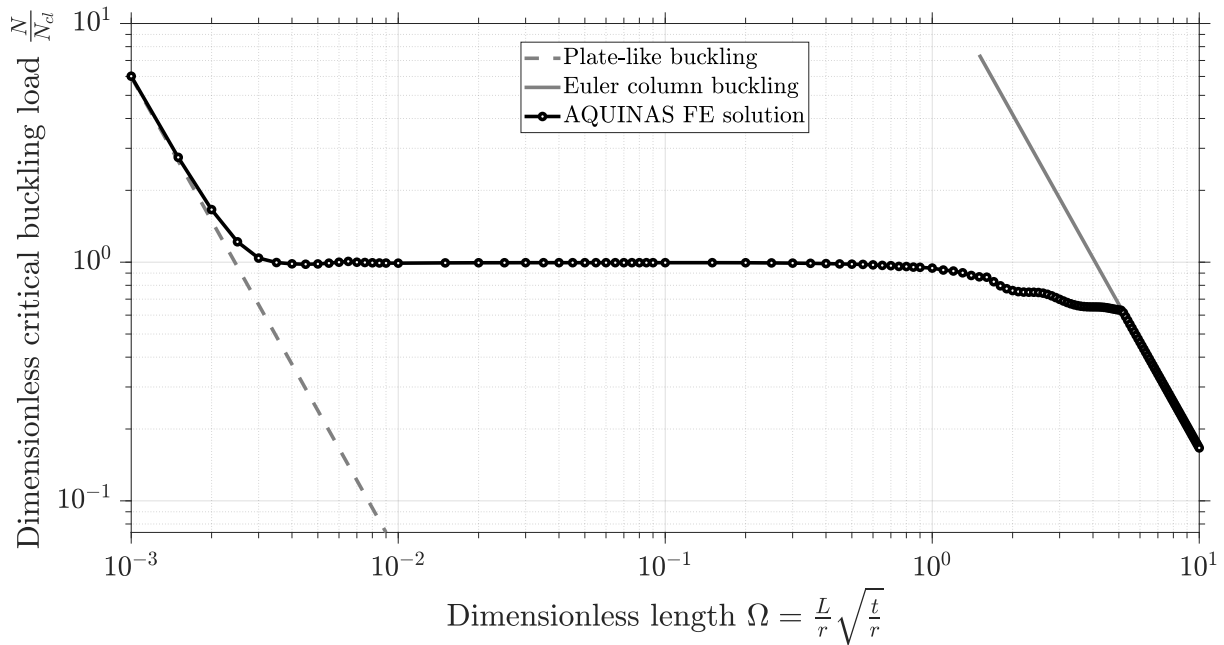


Figure 5.37: LBA01 - System diagram.

Figure 5.38: LBA01 - Development of critical bifurcation load with respect to the dimensionless length parameter  $\Omega$ .

The reader may appreciate that the good agreement between the analytically derived buckling loads and the FE results of AQUINAS. Medium-length cylinders showcase a critical bifurcation edge load that is equal to the classical value of Eq. (5.4). Even though the condition of a uniform pre-buckling membrane stress state is violated with the edge restraints applied, the effect of this violation is negligible due to how short the bending boundary layers span in a medium-length cylinder. In cases where the cylinders can be characterised as either very short or very long, the critical bifurcation loads are consistent with the theoretical values of plate and Euler column buckling accordingly.

On top of the critical bifurcation loads, and their corresponding circumferential modes, AQUINAS may also output the Load Proportionality Factor that will cause buckling into any circumferential mode  $n$ . Capitalising on this feature, the user can obtain curves that showcase the development of the critical buckling load with respect to the harmonic number  $n$ , or in cases where there is a set of parametrised models, as is here with the dimensionless length parameter  $\Omega$ , surfaces like the one of the following Figure 5.39.

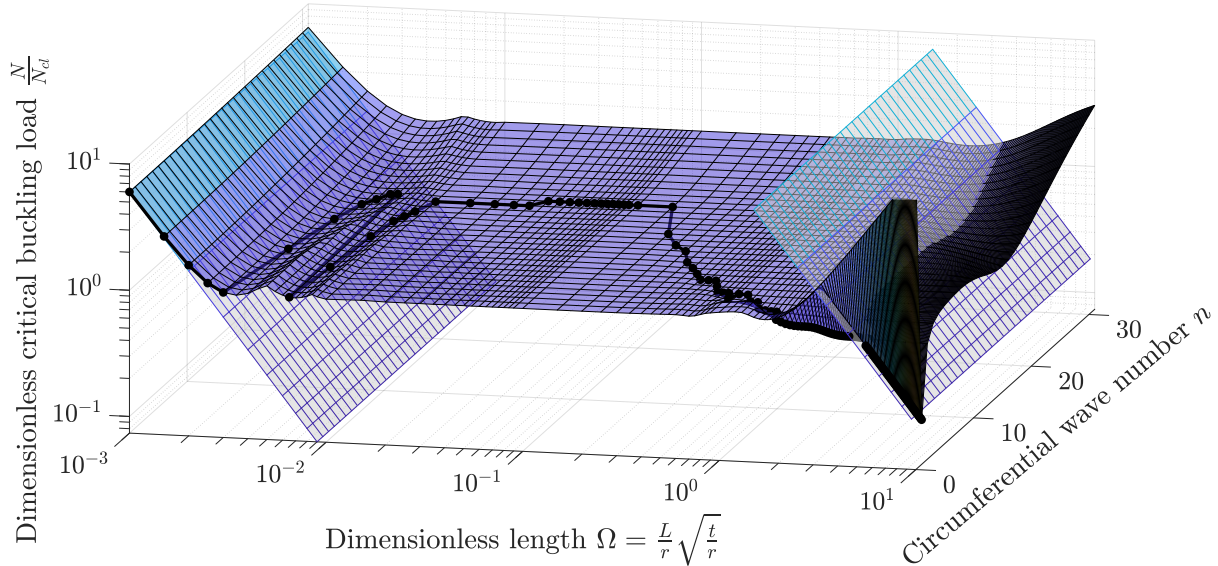


Figure 5.39: LBA01 - Buckling loads for various values of the dimensionless length parameter  $\Omega$  and circumferential modes  $n$ .

If the optimisation option is enabled, with AQUINAS employing its surrogate model optimisation algorithm, the 3D surface of Figure 5.39 will not be displayed at the end of the analysis, since only a select few circumferential modes are trialled per  $\Omega$ . The reader may wish to run the `input_Example_LBA01.m` script, potentially exploring a wider range of length parameters or  $r/t$  ratios or performing any other parametric study.

### 5.2.2 Example LBA02: LBA of a thin cylinder under axial compression and direct comparison with the Koiter circle

This second LBA example serves as a continuation of the first one, investigating the locus of circumferential full waves  $n$  and meridional half waves  $m$  for the bifurcation modes corresponding to elastic buckling load  $N_{cl}$  of Eq. (5.4). This locus has been found in [27] to be a circle, termed as the ‘Koiter circle’ in shell buckling related literature, with the relationship between the bifurcation load  $N_{m,n}$  of an  $m$ - $n$  pair being for pin-ended boundary conditions given as [42]

$$N_{m,n} = \frac{Et^3}{12(1-\nu^2)}\eta^2 + \frac{Et}{r^2\eta^2} \quad (5.5)$$

with the  $\eta^2$  parameter above being defined as:

$$\eta^2 = \left( \frac{(m\pi/L)^2 r^2 + n^2}{(m\pi/L)r^2} \right)^2 \quad (5.6)$$

The buckling load of equation (5.4) has been derived through a minimisation procedure of (5.5) [42], assuming that  $m$  and  $n$  may take any value. As the reader may suspect, this cannot be the case when discussing the number of waves occurring in a bifurcation mode of an axisymmetric shell, either them being circumferential full waves or meridional half waves. Only positive integers are potential values for  $m$  or  $n$ . A consequence of the integer nature of the circumferential and meridional wave-numbers is that the actual buckling load obtained for  $m$ - $n$  pair from (5.5) may be higher than  $N_{cl}$  if the pair does not satisfy the equation of the Koiter circle, as derived in [27]. The equation for the Koiter circle, simplified for the material properties used here ( $E = 200000 \text{ N/mm}^2$ ,  $\nu = 0.3$ ), is given as [42]:

$$(m \frac{\pi}{L} r)^2 + n^2 - 1.818r \sqrt{\frac{r}{t}} (m \frac{\pi}{L}) \approx 0 \quad (5.7)$$

In Figure 4 of [42] it is illustrated that the bifurcation loads  $N_{m,n}$  increase the further the corresponding  $m$ - $n$  pair is from the Koiter circle, both in terms of their analytically obtained value or FE computed one. This result is reproduced in Figure 5.40, where the source of computationally obtained critical buckling loads is AQUINAS. The single cylinder considered here is of length  $L = 1000.0 \text{ mm}$  and shares the rest of its geometric properties, as well as loading and boundary conditions, with the cylinders of `input_Example_LBA01.m`, as displayed in Figure 5.37.

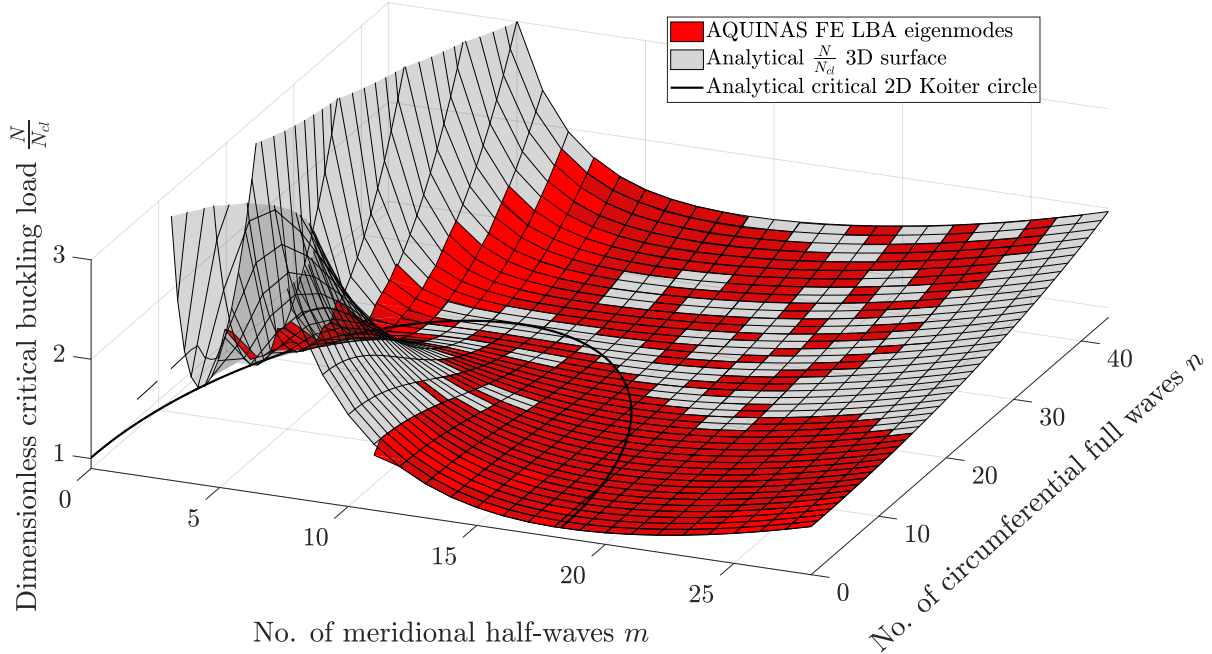


Figure 5.40: LBA02 - Analytically and computationally obtained buckling loads  $N_{m,n}$  for a cylinder under axial compression.

It should be noted that while determining the circumferential mode  $n$  that the cylinder is bifurcating into in AQUINAS is a straightforward process, since  $n$  is explicitly included in the formulation of the stiffness matrices for the eigenvalue problem of Eq. (2.82), the number of meridional half waves  $m$  is obtained through a post-processing fitting of harmonics on the computed eigenmodes for each  $n$ . As such, a level of error in this automated fitting is inevitable and can lead to meridional-half waves  $m$  being unrepresented

for a circumferential harmonic  $n$  in Figure 5.40, even for pairs that would fall very close to the Koiter circle of Eq. (5.7).

### 5.2.3 Example LBA03: LBA of a thin cylindrical shell under uniform lateral pressure

Having established the appropriate behaviour of the linear bifurcation solver in AQUINAS for cylinders under axial compression, it is time to move on to another regularly encountered case in shell buckling literature, that of cylinders under uniform external normal pressure. An analytical solution for the bifurcation loads of the cylinders is also present for comparison purposes here, coded in `input_Example_LBA03.m` based on the formulations of the classical shell buckling textbook of N. Yamaki ‘*Elastic Stability of Circular Cylindrical Shells*’ [61]. It is important to note that the analytical derivations of the bifurcation pressure associated with a circumferential mode in [61] are preformed on the basis of a uniform membrane pre-buckling stress state along the meridian of the cylinders, regardless of the boundary conditions that would be considered for the bifurcation checks themselves. Assuming different boundary conditions for the pre-buckling/buckling states of axisymmetric shell problems is a technique often encountered in literature resources of the past, usually due to the obvious reduction of the problem’s complexity through omission of the bending effects near the edges. While it can be appreciated that this is not a very realistic approach to the design of axisymmetric shells against buckling, as it would be rather unlikely for the restraints applied to a shell to change just before it buckles, the capability to handle different cases of boundary conditions for different states of the shell’s response has been added to AQUINAS, for the software to have all the necessary tools for a direct comparison with established textbook solutions. Several cylinders are examined, with their radius and thickness being constant at  $r = 1000.0\text{ mm}$  and  $t = 1.0\text{ mm}$ , and their length  $L$  varying according to the Batdorf parameter:

$$Z = \sqrt{1 - \nu^2} \frac{L^2}{rt} \quad (5.8)$$

Critical buckling pressure results for a few combinations of boundary conditions are displayed in [61], using the terminology of Tables 5.1 and 5.2. Here, only the C1-C1 (equivalent to a BC1r condition) case for the bifurcation modes is considered for all of the Batdorf parameters trialled, with the `input_Example_LBA03.m` script being readily extensible to explore any alternative combination of boundary conditions for the cylinders. The classical elastic critical buckling pressure, applied on the meridian of the cylindrical models, can be found to be [53]

$$p_{cl} = 0.92E \frac{r}{\sqrt{rtZ/\sqrt{1 - \nu^2}}} \left(\frac{t}{r}\right)^2 \quad (5.9)$$

where  $Z$  here is the Batdorf parameter of Eq. (5.8) and does not refer to the axial coordinate of the shell’s meridian of Eq. (2.1b).

The geometry and boundary-loading conditions of the cylindrical shells are illustrated in Figure 5.41, where as discussed above different restraints are applied for the pre-buckling stress state and the buckling modes. Only an axial restraint ( $w = 0$ ) is applied at the base of the cylinders in order to allow for the axisymmetric models to deform without introducing bending behaviour for compatibility purposes at the edges, allowing a uniform pre-buckling stress state to develop.

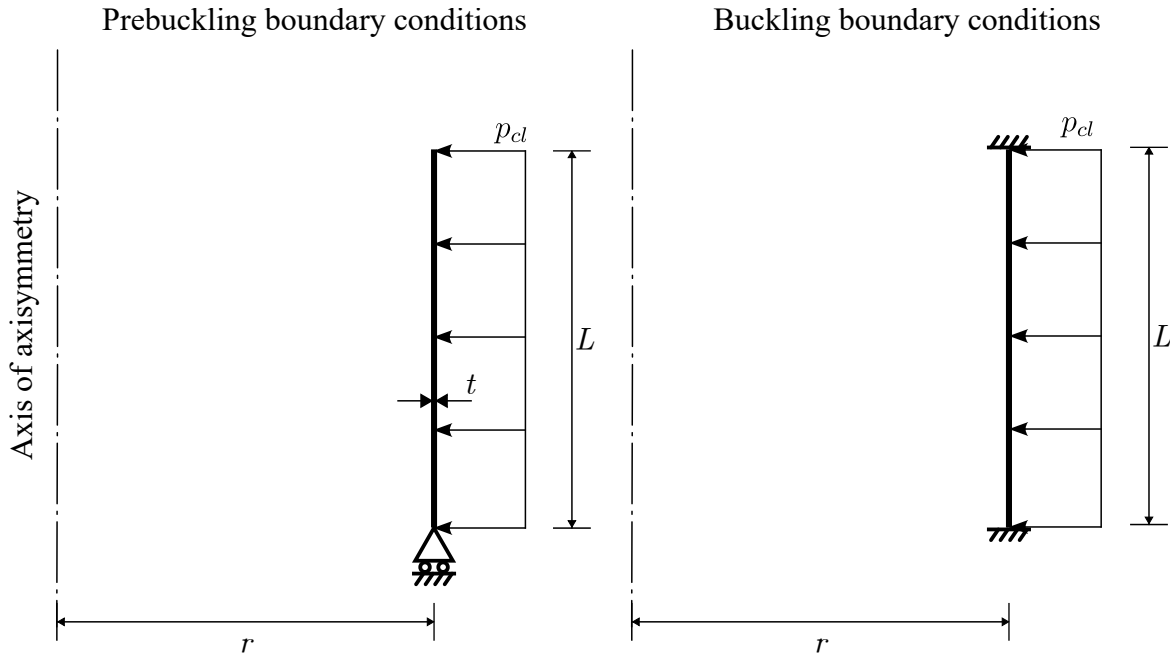


Figure 5.41: LBA03 - System diagram.

In Figure 5.42 the analytically derived critical bifurcation pressure and the associated circumferential mode  $n$  of [61] is shown to have an excellent agreement with the corresponding computationally obtained results from AQUINAS, with Yamaki's  $k_p$  and  $\beta$  parameters being adopted for this comparison. The critical buckling pressure  $p_{cr}$  normalised by the classical result for cylinder's under external pressure  $p_{cl}$  of Eq. (5.9) is also plotted against the  $\omega$  parameters that are equivalent to the Batdorf ones considered for this example in Figure 5.43. A benefit of the capability of AQUINAS to obtain an eigenvalue for any circumferential mode to be considered is the computation of a surface of results, showcasing the development of the pressure and associated harmonic  $n$  that would lead to bifurcation as the cylinders increase in height, through a value of the dimensionless parameter  $\Omega$ . This third plot may only be generated though by disabling the surrogate optimisation option, as only a select few harmonic's are trialled when the minimisation algorithm is enabled. While in [61] only the critical pressure and mode is presented, the derivations have been coded in the script to obtain a result for any circumferential mode of interest, allowing for a further comparison in this 3D surface space of Figure 5.44. A reader who examines the `input_Example_LBA03.m` script can appreciate how complex these derivations actually are, even with the simplification of a uniform pre-buckling stress state, making the analytical approach completely impracticable for the design of cylinders under normal pressure.

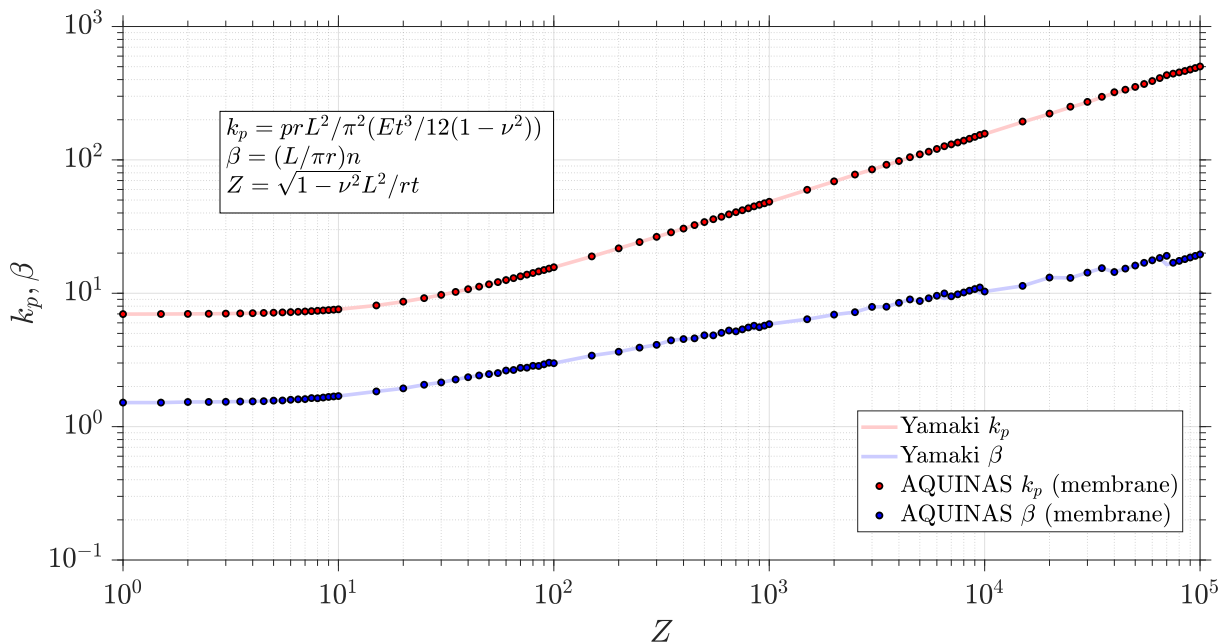


Figure 5.42: LBA03 - Variation of  $k_p$  and  $\beta$  with the Batdorf parameter  $Z$  for a C1-C1 boundary condition case.

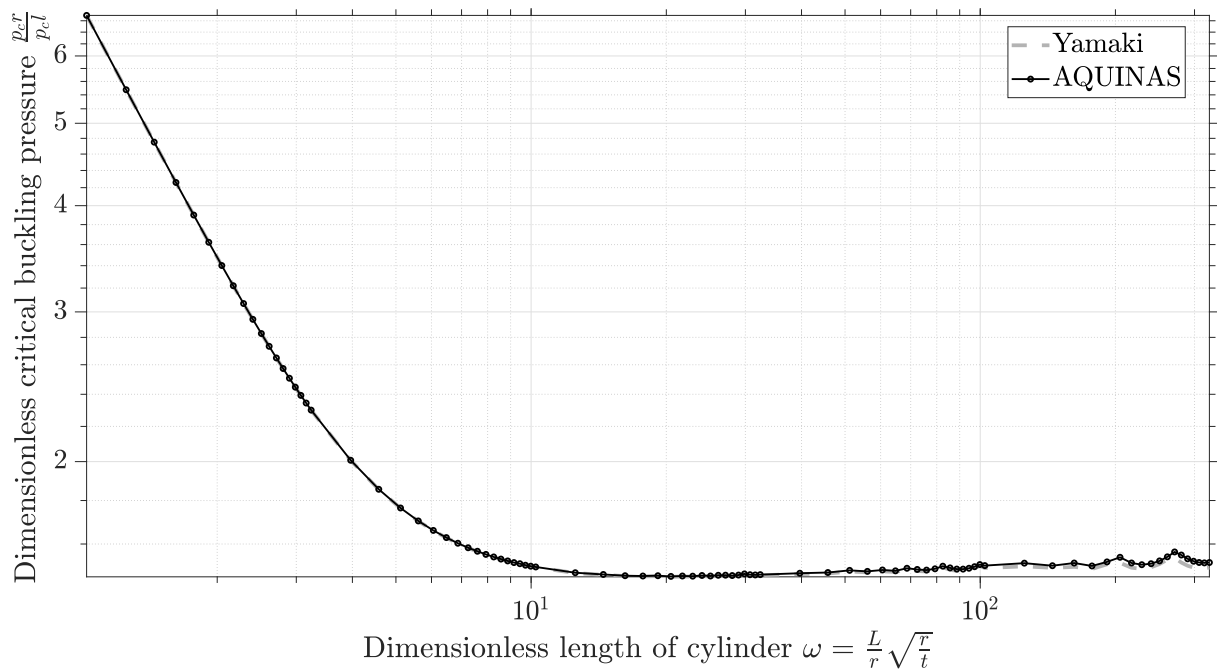


Figure 5.43: LBA03 - Development of critical buckling pressure ratio  $p_{cr}/p_{cl}$  with respect to the dimensionless length parameter  $\Omega$ .

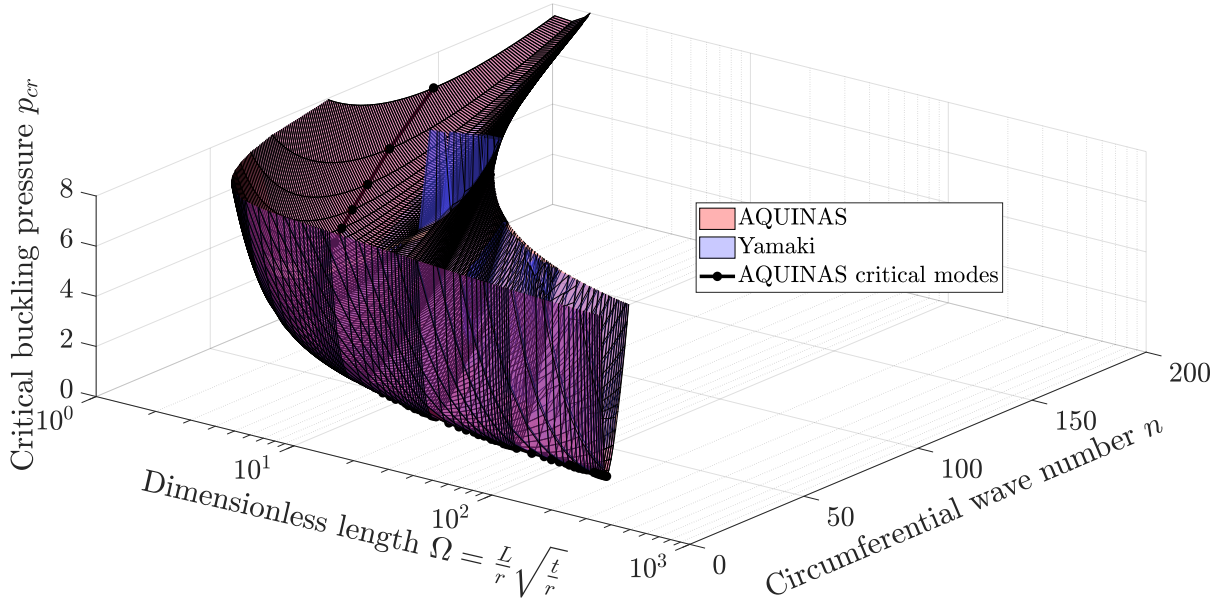


Figure 5.44: LBA03 - Buckling pressures for various values of the dimensionless length parameter  $\Omega$  and circumferential modes  $n$ .

#### 5.2.4 Example LBA04: Koiter ellipse for a thin truncated cone under uniform axial compression

A computational investigation of the bifurcation loads and modes for truncated conical shells under an axially compressive stress state by A. Spagnoli in [47] has shown that the locus of circumferential full waves  $n$  against meridional half waves  $m$  can be approximated by an ellipse, when these are plotted in a dimensionless  $\bar{\beta}_c$ - $\bar{\beta}_m$  space. The dimensionless wave-numbers are defined in [47] as

$$\bar{\beta}_m = \frac{\bar{\lambda}}{\bar{l}_m} \quad (5.10a)$$

$$\bar{\beta}_c = \frac{\bar{\lambda}}{\bar{l}_c} \quad (5.10b)$$

where

$$\bar{l}_m = \frac{L}{m} \quad (5.11a)$$

$$\bar{l}_c = \frac{\pi \bar{\rho}}{n} \quad (5.11b)$$

and

$$\bar{\lambda} = \frac{\pi}{\sqrt[4]{3(1-\nu^2)}} \sqrt{\bar{\rho}t} \quad (5.12)$$

The  $\bar{\lambda}$  parameter corresponds to the average half-wavelength according to the linear bending theory for cones, with  $\bar{\rho}$  being the average radius of curvature. The derivations

of the equations that will eventually lead to the elliptical locus for the dimensionless wave-numbers  $\bar{\beta}_c$  and  $\bar{\beta}_m$  may be found in A. Spagnoli's work in [47].

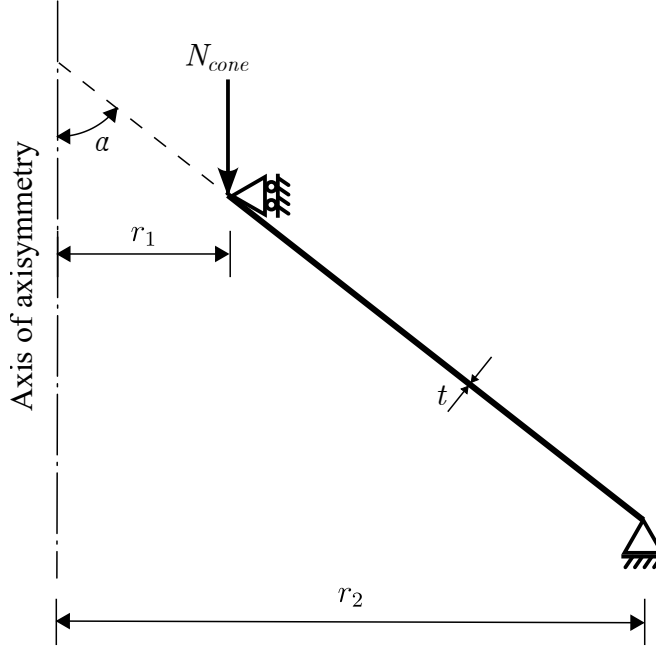


Figure 5.45: LBA04 - System diagram.

For each run of `input_Example_LBA04.m`, the LBA of a single truncated conical shell under axial compression is executed, with the results then post-processed in order to obtain the meridional half wave-number  $m$ . The cones are characterised from their tapering angle  $\alpha$  which can vary from  $\alpha = 0^\circ$ , for a cone that is essentially a cylinder, up to  $\alpha = 90^\circ$  for a plate-like cone. The shell wall has a constant thickness of  $t = 1.0 \text{ mm}$ , while the inner (top) edge of the conical segment has a radius of  $r_1 = 1000.0 \text{ mm}$ . The meridian of the cone has a length of  $L = 3000.0 \text{ mm}$ , which can be used to compute the radial and axial coordinates of the outer (bottom) edge of the segment as a function of the tapering angle  $\alpha$ . A BC1f restraint is applied at the outer edge of the cone and a BC2f at the top, with the circumferential DOF  $v$  restrained at both ends. The reader is cautioned that the notation used in [47] is not the one adopted by AQUINAS and care should be exercised in interpreting the boundary conditions. The classical buckling compressive axial edge load, applied at the top edge of the cone, is derived on the basis of a membrane pre-buckling state and is given as:

$$N_{cone} = \frac{Et^2}{r_1 \sqrt{3(1 - \nu^2)}} \cos^2 \alpha \quad (5.13)$$

The geometric definition for this LBA example is illustrated in Figure 5.45, while in Figure 5.46 the AQUINAS FE results are plotted in the dimensionless wave-number space and compared against the Koiter ellipse locus for a tapering angle of  $\alpha = 15^\circ$ . While the agreement may seem good but not ideal here, it should be noted that the calculation of the meridional half wave-number  $m$  is done through a fitting of harmonic, equally spaced waves, running along the meridian of the cones. This is a scheme that can lead to rather accurate computations for cylinders under axial compression (see `input_Example_LBA01.m`), but is only a rough approximation in the case of cones where the meridional half waves are

generally not equally spaced. An even better agreement can be observed if the meridional half waves are manually counted one by one, a process that is much more strenuous compared to the automated approximation used here. Additionally, running this example may take some time.

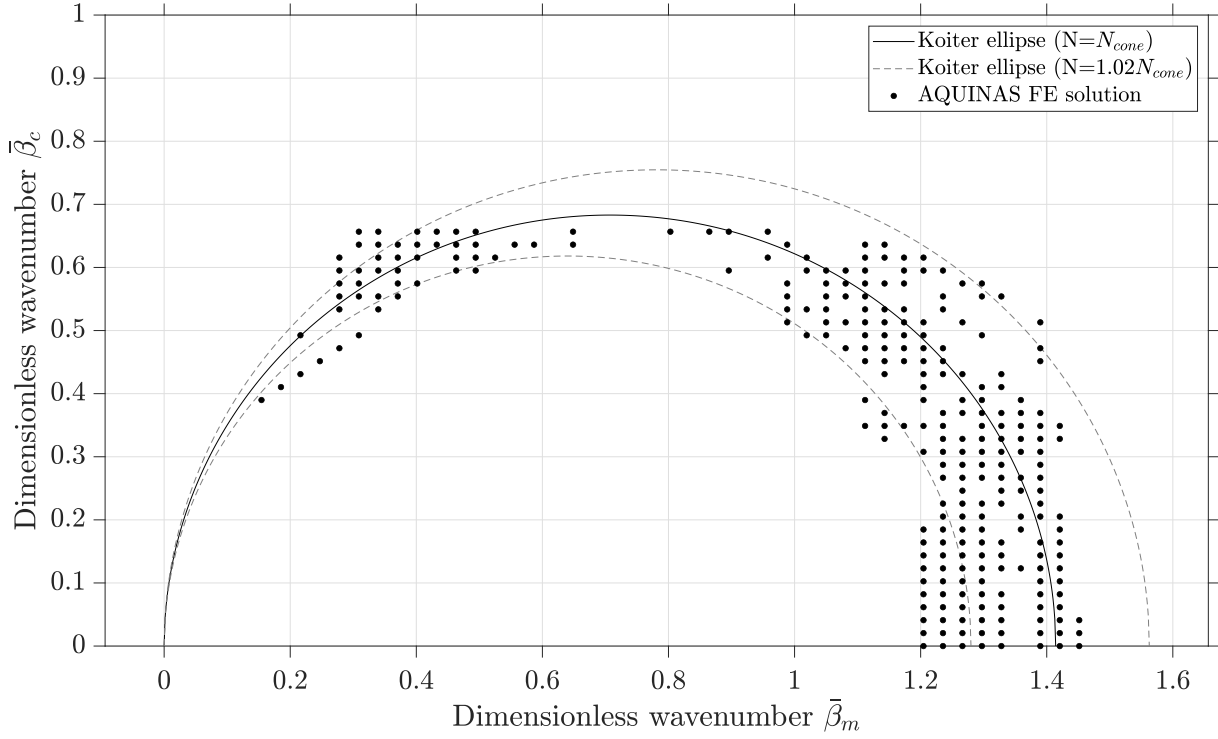


Figure 5.46: LBA04 - Locus of simultaneous buckling modes with  $N \leq 1.02N_{cone}$  for a cone with a tapering angle  $\alpha = 15^\circ$  in the  $\bar{\beta}_m$  -  $\bar{\beta}_c$  dimensionless wave-number space.

### 5.2.5 Example LBA05: Bifurcation modes of a thin spherical shell under uniform external pressure

Moving on to the LBA of axisymmetric shell problem with curved meridians, the circumferential and meridional modes of thin spherical shells under uniform external pressure are explored in `input_Example_LBA05.m`. As discussed by Hutchinson in ‘*Buckling of spherical shells revisited*’ [25], the bifurcation modes of closed spheres under external pressures may be described through the spherical harmonics  $S_{mn}$ , given as

$$S_{nm} = \cos(m\omega)P_n^m(\sin\theta) \quad (5.14)$$

where  $P_n^m$  is the associated Legendre function of degree  $n$  and order  $m$ . The reader is cautioned that the notation used for this example, as adopted from [25], should not be confused with the number of meridional half waves  $m$  and circumferential full waves  $n$  used throughout AQUINAS, but instead they refer the associated Legendre polynomials. The meridional angle  $\theta$  is zero at the equator of the spheres, and  $\omega$  is used for the circumferential angle. While the order  $m$  of  $P_n^m$  is equivalent to the circumferential wave-number, the degree  $n$  should not be viewed as a parameter equivalent to the meridional wave-number. The  $\sin(m\omega)$  term is omitted in this example, as antisymmetric bifurcation terms are not included in AQUINAS’ FE formulation (see discussion in Chapter 2).

The buckling modes for spherical shells of different radius over thickness ratios are examined, running from an  $r/t = 50$  up to  $r/t = 2000$  with the shell wall being kept at a unit thickness  $t = 1.0\text{mm}$ . The classical elastic buckling pressure  $p_{cl}$  [25] is applied, given by

$$p_{cl} = \frac{2E}{\sqrt{3(1 - \nu^2)}} \left(\frac{t}{r}\right)^2 \quad (5.15)$$

for which the degree  $n$  of the associated Legendre function can be found from:

$$n(n + 1) = \sqrt{12(1 - \nu^2)} \frac{r}{t} \quad (5.16)$$

Both the degree  $n$  and the order  $m$  are restricted to be of integer nature [25], with  $(0 \leq m \leq n)$ . An axial displacement  $w$  restraint is applied at the base of the spheres, while the circumferential displacement  $v$  is restrained at both apexes. The geometry of this spherical shell problem is presented in Figure 5.47.

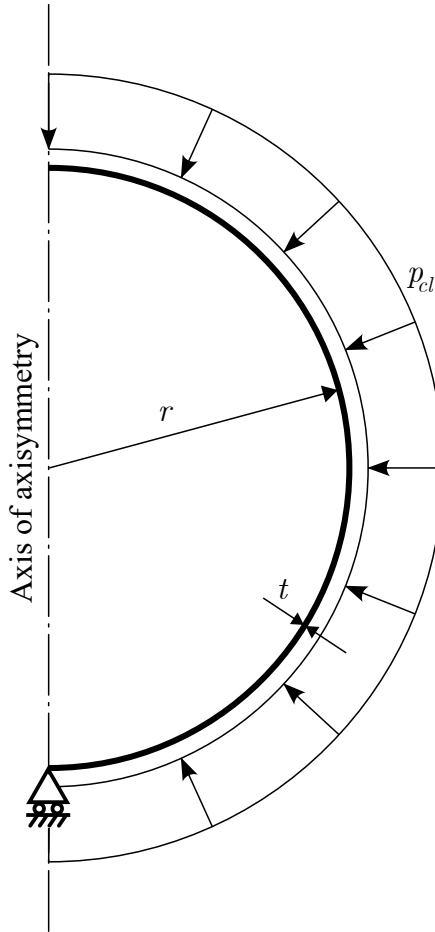


Figure 5.47: LBA05 - System diagram.

The bifurcation modes obtained for each  $r/t$  ratio from AQUINAS are then post-processed in order to identify which spherical harmonic of Eq. (5.14) best fits the mode, and determine the degree  $n$  and order  $m$  of the Legendre polynomial. The normalised critical pressure, as well as the degree of the associated Legendre polynomial obtained from the FE solution here, are plotted and compared against the classical theory presented

in [25] in Figures 5.48 and 5.49. An additional figure can be obtained if the surrogate Optimisation option is disabled, where the 3D surface of degrees  $n$  and order  $m$  for every  $r/t$  ratio are computed and showcased in Figure 5.50.

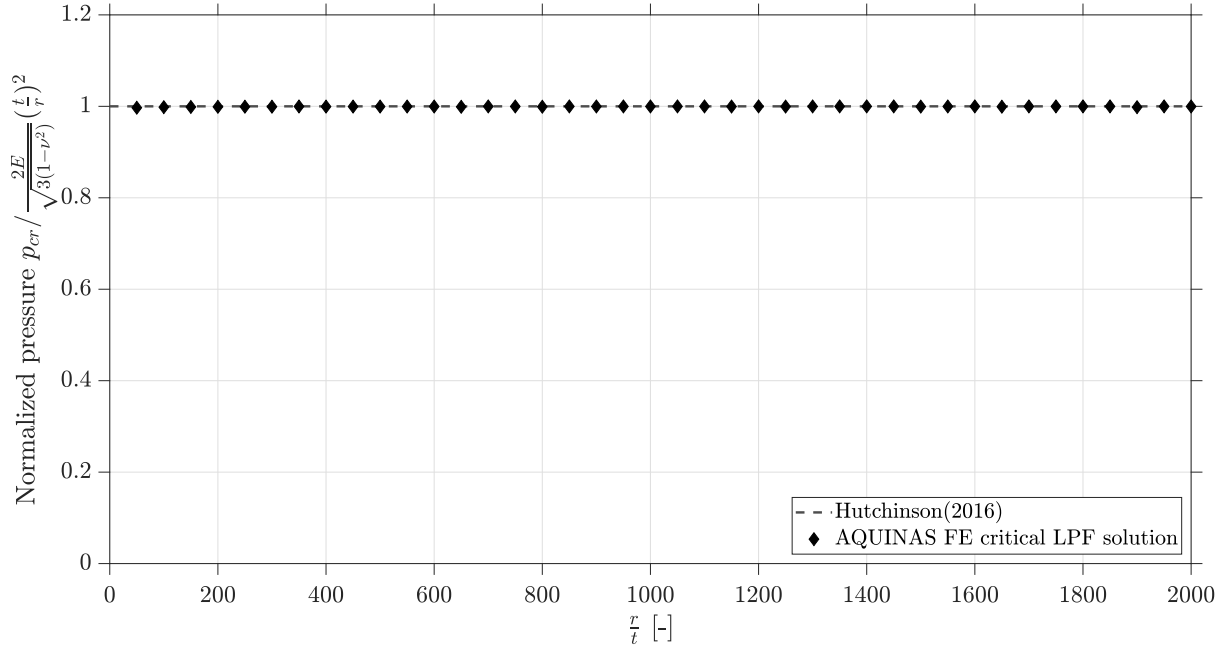


Figure 5.48: LBA05 - Normalised critical bifurcation pressure for varying  $r/t$  ratios of full spherical shells.

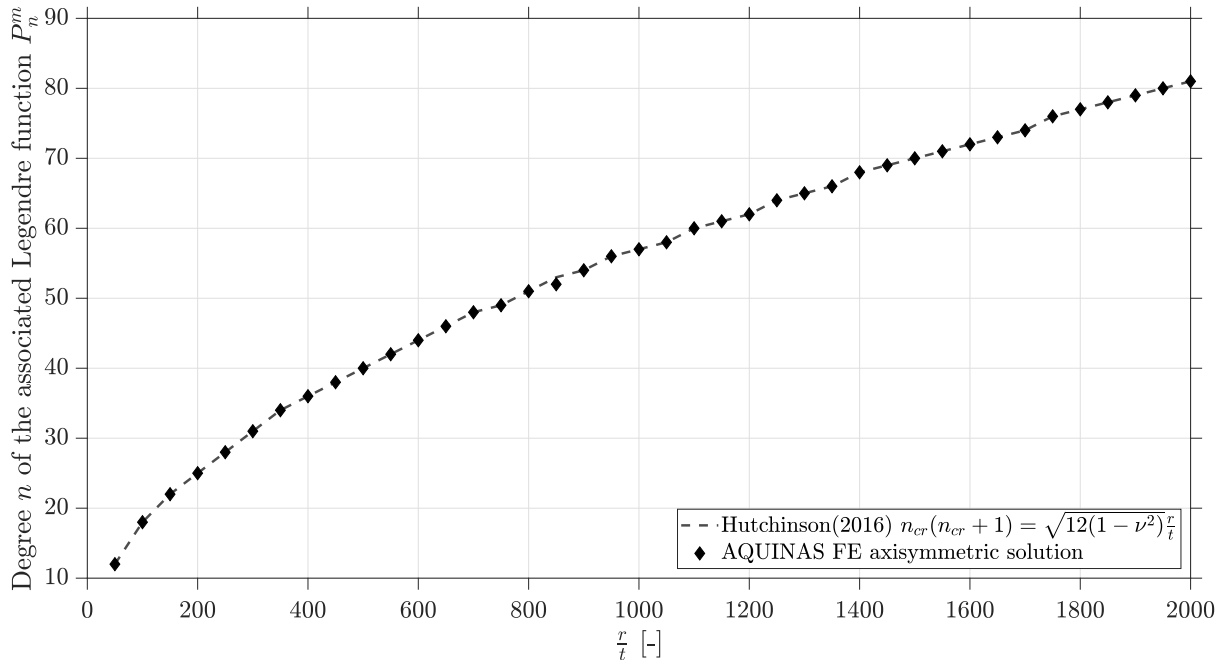


Figure 5.49: LBA05 - Critical circumferential mode for varying  $r/t$  ratios of full spherical shells under external pressure.

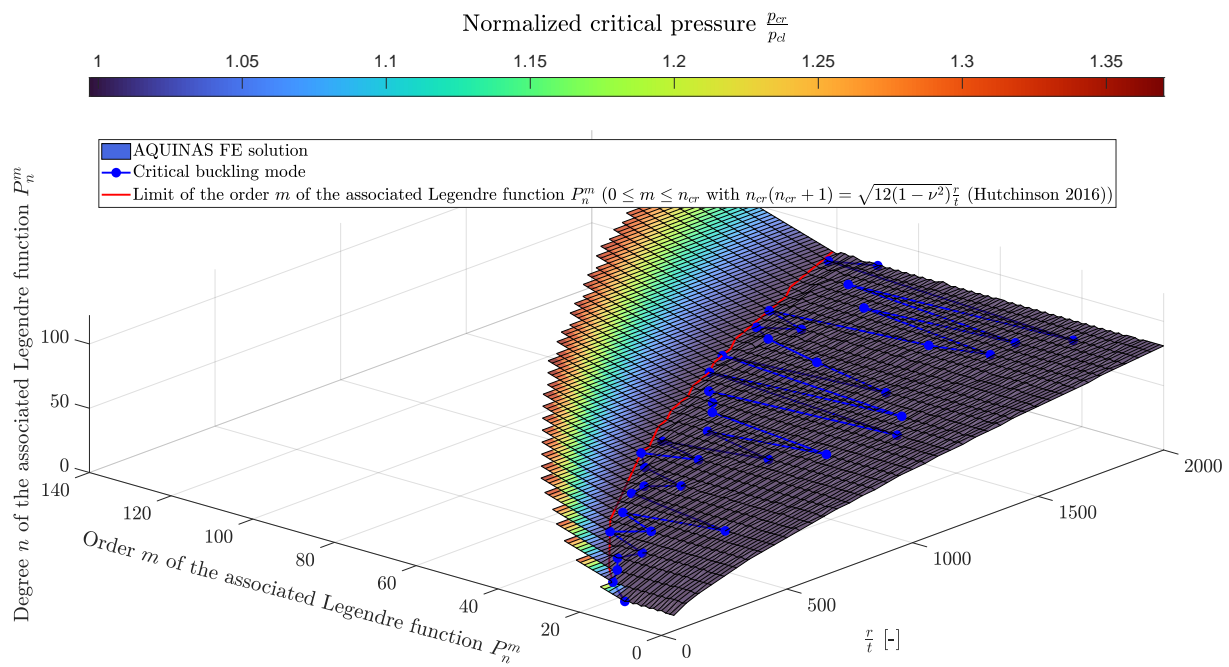


Figure 5.50: LBA05 - Order  $m$  and degree  $n$  of associated Legendre polynomials for spheres of varying  $r/t$  ratios under external pressure.

The LBA results of AQUINAS seem to very accurately predict not only the critical pressure  $p_{cr}$ , but also the bifurcation modes. The reader should not be alarmed if on consecutive runs of `input_Example_LBA05.m`, with and without the surrogate optimization algorithm employed, the order  $m$  (circumferential mode) is found to vary, as this is a consequence of all the competing circumferential modes essentially coexisting at the same load level (provided they refer to an order  $m$  that is less than the degree  $n$  of the associated Legendre polynomial).

### 5.3 MNAs

Axisymmetric shells may exhibit yielding, either local or global, as they are incrementally loaded to failure. Neglecting the effects of geometric nonlinearities, an MNA may be executed with AQUINAS through the `AQUINAS_GMNA` script, following the procedure presented in section *AQUINAS GNA - MNA -GMNA* of Chapter 4. The stresses are computed on the through thickness fibres of the shell wall, checking for yielding of each individual point. In the case that elastic trial stress increment for a material point is found to be outside the yield surface, the corresponding strain increment will be applied through sub-increment that will allow the integration of the elastic-plastic strains. A correction will be applied at the end of the sub-increments that will bring the stresses closer to the yield surface, within a specified tolerance.

A series of examples will be presented in this section, exploring the materially nonlinear behaviour of axisymmetric shells models. The computed elastic-plastic stress distributions can be found to develop in an irregular pattern, especially in the case of a circular plate under bending for `input_Example_MNA02.m`. While this is the case, the Load Proportionality Factor (LPF) that leads to a plastic collapse mechanism seems to be accurately predicted, even for this second MNA problem. As stated in the beginning of the current manual, AQUINAS is meant to be an active, ongoing project with constant

updates in its repository. The oscillating stress distributions that are currently computed for axisymmetric shells deep into plasticity constitute a chief reason for such an update, to be addressed at a later release of AQUINAS.

### 5.3.1 Example MNA01: MNA of a thin cylinder under uniform axial compression

A cylindrical shell model will be once again used as the first benchmark to present the AQUINAS FE results, in this case in the challenging domain of materially nonlinear analyses. The cylinder under investigation has a radius  $r = 1000.0\text{ mm}$  and its total length is set to  $L = 1000.0\text{ mm}$ , with a shell wall of unit thickness  $t = 1.0\text{ mm}$ . A BC2f / S3 restraint is applied at its top edge and a BC1f / S1 at its base. An elastic perfectly plastic material is considered, with a yield stress  $f_y = 250\text{ N/mm}^2$ . Its elastic properties are identical to those used in previous examples ( $E = 200000.0\text{ N/mm}^2$  and  $\nu = 0.3$ ). The compressive line edge load  $N$  applied at the top end of the shell is incremented using the arc-length method, as plasticity gradually extends from the bending boundary layers of the cylinder to the membrane region of its meridian. The geometry and boundary conditions are presented in Figure 5.51.

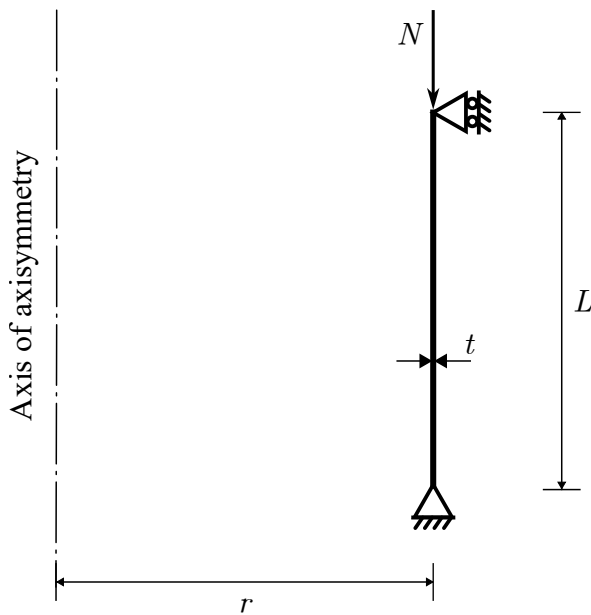


Figure 5.51: MNA01 - System diagram.

For this example there is no external source of comparison, as the validity of the resulting equilibrium path can be assessed on intuition alone. A purely elastic behaviour is to be expected of the cylinder until the von Mises stress at any of the material points used for tracking plasticity in the shell wall crosses the yield surface. This will mark the onset of plasticity, leading to a plateauing behaviour for the cylinder where it continues to deform for very small changes in the line load  $N$  applied. For the elastic-perfectly plastic material that is considered for the present model, the plateau in the equilibrium path should correspond to an edge line load of  $N = f_y t$ . This exact behaviour is illustrated in Figure (5.52) through the equilibrium path for the cylinder under compression as obtained from an AQUINAS MNA. The reader may appreciate both the initial elastic behaviour and the plastic plateau of the cylindrical shell model, deep into which yielding has spread across

the entirety of the shell's meridian and the arc-length increments applied are associated with minimal changes of the LPF.

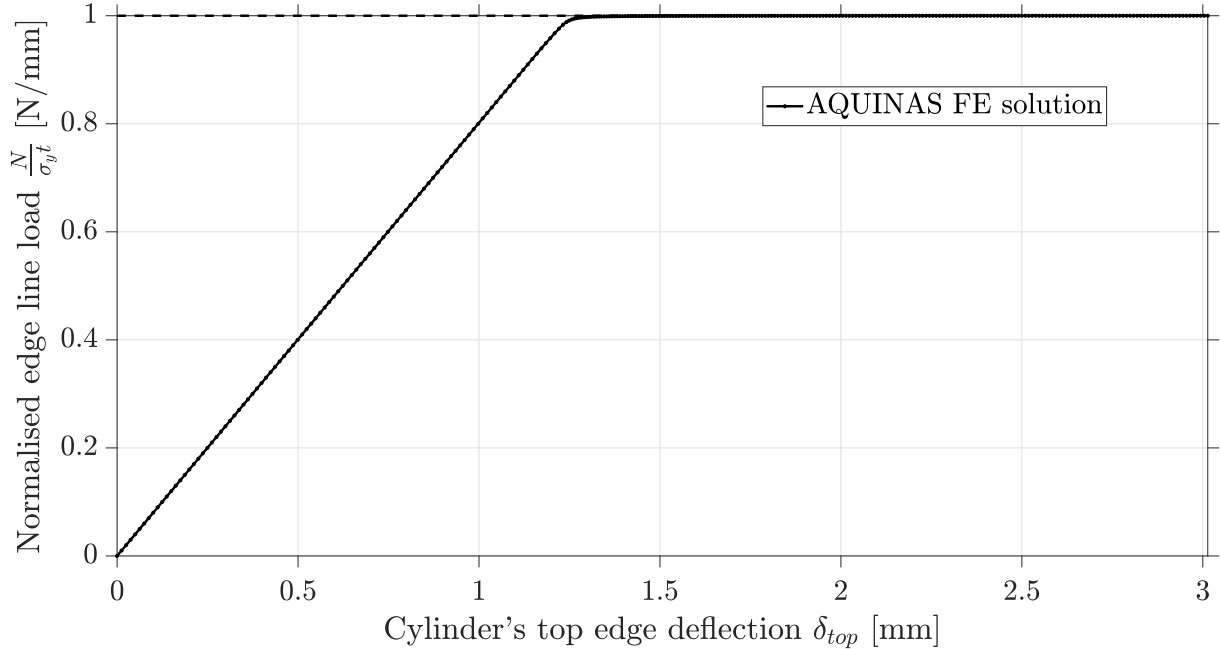


Figure 5.52: MNA01 - Top edge deflection equilibrium path for a thin unpressurised cylinder under axial compression.

### 5.3.2 Example MNA02: MNA of a simply-supported circular plate under concentrated load

This MNA example serves to illustrate the ability of AQUINAS to predict another axisymmetric shell's strength, but also as a demonstration of the occasional ruggedness of the stress distributions obtained deep into plasticity.

The model under investigation is a circular plate of radius  $r = 100.0\text{ mm}$  with a shell wall of thickness  $t = 10.0\text{ mm}$ . The material is once again elastic perfectly plastic, with its yield stress set to  $f_y = 250\text{ N/mm}^2$ . A BC1f boundary condition is applied at the edge of the plate, as can be seen in Figure 5.53 where the geometry of this materially nonlinear shell problem is illustrated.

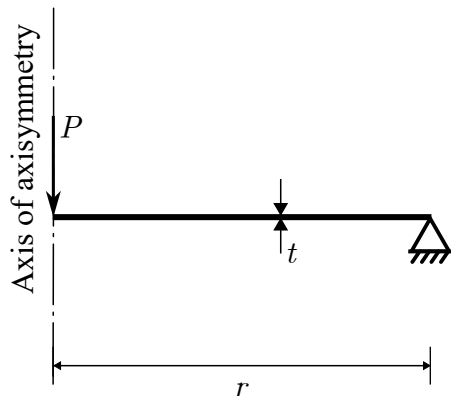


Figure 5.53: MNA02 - System diagram.

The equilibrium response of the circular plate's centroid is presented in Figure 5.54, illustrating a similar nonlinear and slowly plateauing behaviour that can be seen in Figure 4 of Teng and Rotter (1989a) [50], the source publication of the AQUINAS FE toolbox. Plasticity spreads from the centre of the plate towards its BC1f edge, with the middle fibre of the cross section remaining completely unstressed for every integration station along the meridian. Larger deformations occur as the plate is fully yielded and the externally applied concentrated force asymptotically tends to  $P = 2\pi M_p$ . While this first result is very promising for the implementation of the AQUINAS' materially nonlinear solution process, the distributions of the bending stress resultants  $M_\phi$  and  $M_\theta$  appears to be irregular, as the reader may observe from Figures 5.55 - 5.56. As yielding spreads across the meridian of the circular plate, 'residual' bending stress resultants arise where elements meet, with this effect being considerably more significant towards the centre of the axisymmetric shell model. This behaviour does not seem to occur in [50], where the bending stress resultant distributions are smooth, even deep into plasticity where the plate has fully yielded. The Authors of the current document, responsible for the development of the AQUINAS toolbox, will keep looking into this materially nonlinear stress patterns, aiming at an update of the current section, as well as of the source code's repository.

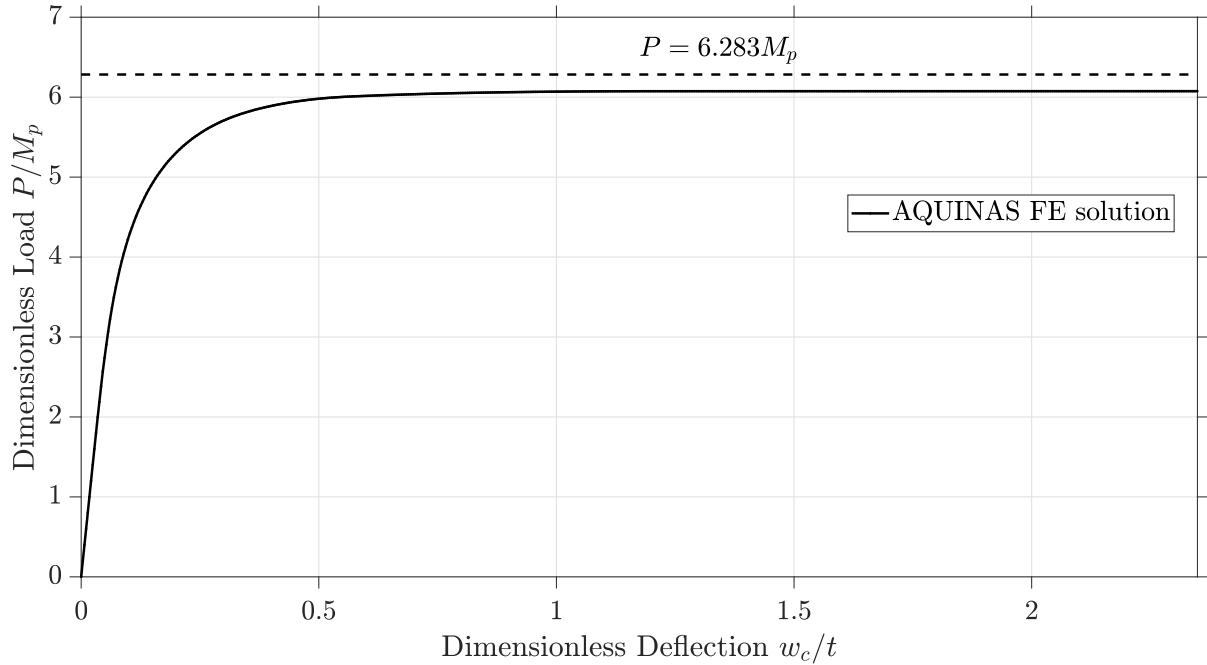


Figure 5.54: MNA02 - Dimensionless deflection equilibrium path of circular plate's centroid  $w_c$ .

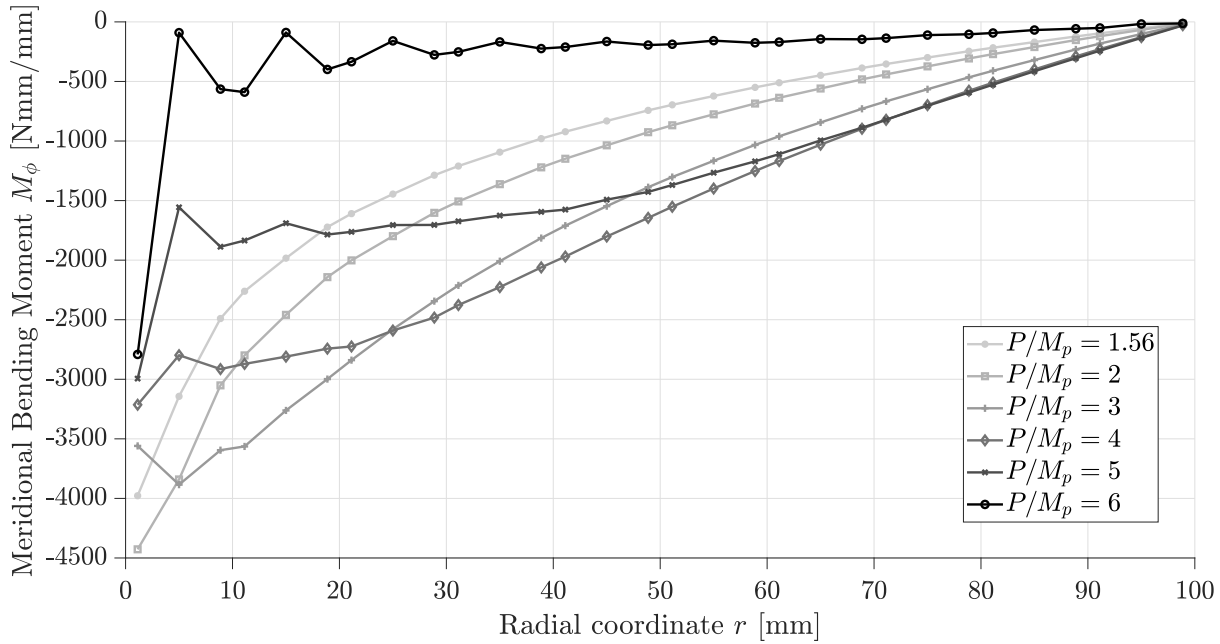


Figure 5.55: MNA02 - Development of meridional membrane stress resultants  $M_\phi$ .

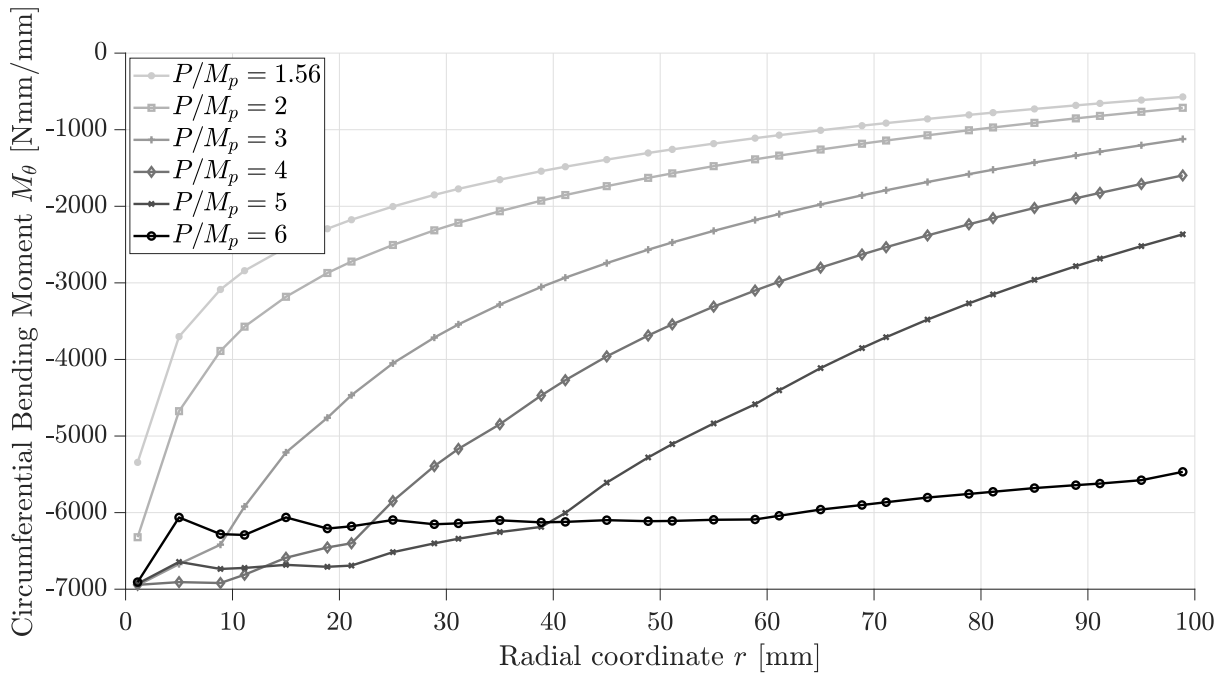


Figure 5.56: MNA02 - Development of circumferential membrane stress resultants  $M_\theta$ .

### 5.3.3 Example MNA03: MNA of a clamped spherical caps under uniform external pressure

In `input_Example_MNA03.m`, the limit loads of spherical caps under external pressure are obtained for a series of meridional angle spans  $\phi_0$ . The shell wall is of unit thickness  $t = 1.0 \text{ mm}$  for all of the spherical models with their radius of meridional curvature set to  $r = 12.5 \text{ mm}$ . A BC1r - C1 boundary condition is applied at the edge of the spherical caps, as illustrated in Figure 5.57.

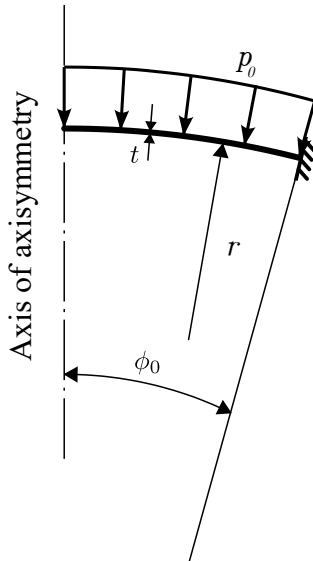


Figure 5.57: MNA03 - System diagram.

The material is characterised by a yield stress of  $f_y = 250 \text{ N/mm}^2$ , with no strain hardening considered. Comparison is made with the limit loads obtained through digitisation from Teng and Rotter (1989a) [50], computed with the same underlying shell formulation. The reader may appreciate the good agreement between the FE solutions, as presented in Table 5.6, subject to the quality of a digitisation process.

Table 5.6: MNA03 - Limit loads of clamped spherical caps under uniform pressure.

$\phi_0$	Teng and Rotter (1989a) [50]	AQUINAS
15°	75.897	77.65
20°	56.296	53.587
30°	43.077	43.173
40°	41.937	41.359
50°	41.026	40.669
60°	41.026	40.353

## 5.4 GNAs

The inherently nonlinear load bearing response of thin axisymmetric shells is analysed in AQUINAS through the master script `AQUINAS_GMNA.m`, responsible for the execution of both geometrically and materially nonlinear analyses. In this section, the equilibrium paths of axisymmetric FE shell models are explored, with the added consideration of geometrical nonlinearities as they are incrementally loaded to failure. The effects of geometrical nonlinearities as they bifurcate into a circumferential mode  $n$  will also be investigated, since the critical circumferential harmonic, associated with the lowest buckling load, may change as the analysis progresses and the shell models stress and deform.

As a special case of GNAs, GNIAs of shells will also be examined in the following section, with the imperfect shape of the shell's meridian being modelled through the segment object rather than being defined as a perturbation shape at the level of submitting an analysis.

With analytical results being scarce on the topic, the focus will be on comparisons with established computational solutions in relevant literature.

### 5.4.1 Example GNA01: GNA of a thin cylindrical shell under uniform axial compression

Thin cylinders under axial compression are once again put to the test, in the form of a benchmark example, with the aim of establishing the accuracy of geometrically nonlinear solutions with AQUINAS. Cylinders of various lengths, parametrised with respect to the Batdorf parameter of Eq. (5.8) are submitted for a GNA that aims at computing the nonlinear buckling load, as well as the associated circumferential mode  $n$ .

All of the cylinders have a constant radius  $r = 1000.0 \text{ mm}$  and thickness of  $t = 1.0 \text{ mm}$ . A BC2f-S3 boundary condition is applied at the top edge of the cylinders and a BC1f-S1 at their base. An edge load of magnitude equal to the buckling load of Eq. (5.4) is applied at their top edge. The geometry, loading and boundary conditions of the cylinders are identical to those of LBA01 as illustrated in Figure 5.37. Comparison is made with results obtained through the ‘panel analysis’ technique , with ABAQUS [1] being the FE solver of choice of the analysts in [42]. Axisymmetric shell models, that may only bifurcate into a zeroth harmonic mode  $n = 0$ , are also included in the comparison, as well as analytical ones based on the derivations of Yamaki [61]. As a consequence of Yamaki’s solutions assuming a meridional symmetry of the boundary conditions, which is not the case for the cylinders analysed in AQUINAS or in [42], they are treated as an upper-lower bound for the obtained for the critical buckling loads  $N_{GNA}$  computed. The comparison for the range of Batdorf parameters considered is shown in Figure 5.58.

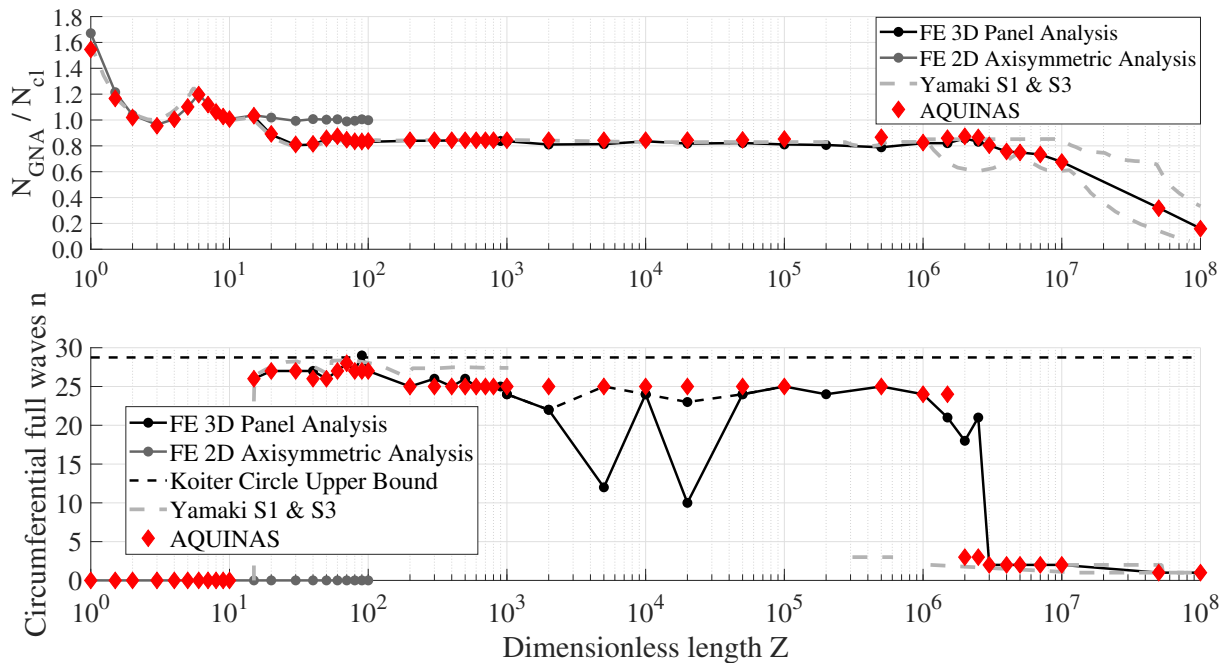


Figure 5.58: GNA01 - Comparison of geometrically nonlinear critical bifurcation loads and associated circumferential modes for cylinders of varying length under axial compression.

The reader may appreciate that the predictions made by AQUINAS for the critical buckling load  $N_{GNA}$  and the associated circumferential mode  $n$  fall very close to those of

the rest of the results included in the comparison. As discussed earlier, Yamaki's S1 and S3 solutions serve as upper-lower limits for the S1-S3 models analysed by AQUINAS, and indeed the FE computed results keep within all available bounds. Furthermore, AQUINAS illustrates a robust behaviour in the medium-length range of cylinders, where as explained in [42] the 'panel analysis' technique faces numerical problems. A further exploration of how the bifurcation loads related to competing circumferential modes  $n$  develop alongside the Batdorf parameters  $Z$  is presented in Figure 5.59, obtained using the capability of AQUINAS to consistently obtain an eigenvalue for a trialled harmonic  $n$ . The reader is cautioned however at this point that any AQUINAS result other than the one associated with the actually critical harmonic  $n$  for each cylindrical model is an estimate rather than a computation. AQUINAS will terminate the nonlinear analysis at the first bifurcation event, which corresponds to an eigenvalue equal to unity for any of the trialled circumferential modes. Hence, while AQUINAS has traced the nonlinear path of the axisymmetric shell model all the way to bifurcation into a specific mode with an eigenvalue of one, the rest of the competing harmonics have a higher associated eigenvalue. This result can be viewed as kind of a modified LBA, where the equilibrium path for the shell is traced up to some non-critical load level. As is the case with LBA results, the further the eigenvalue is from unity the higher the potential error in the critical load level prediction. Nevertheless, the reader can appreciate that for the most part of the surface presented in Figure 5.59, the bifurcation loads predicted for the non-critical modes are reasonably close to the harmonic computed as critical, validating to some extent the estimations presented these surfaces. The AQUINAS surface is smooth for all Batdorf parameters analysed, a result that could have been only obtained due to the inclusion of the circumferential mode  $n$  into the FE formulation.

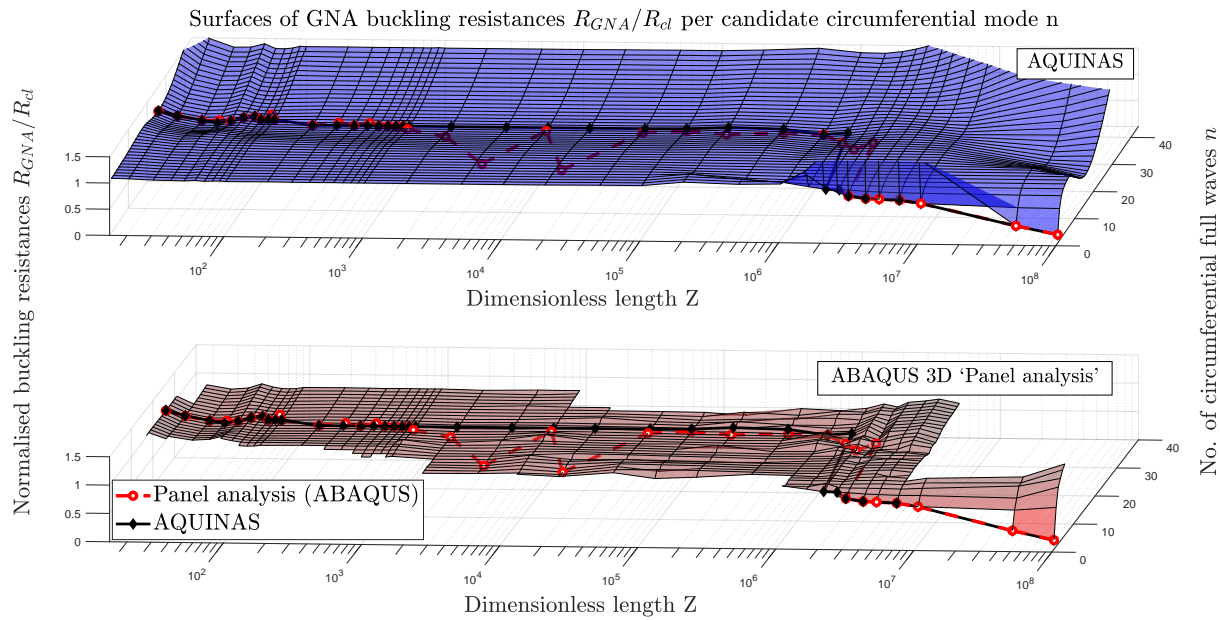


Figure 5.59: GNA01 - Automated identification of the critical geometrically nonlinear GNA bifurcation buckling load for a thin cylindrical shell under uniform meridional compression as a function of the Batdorf dimensionless length parameter  $Z$ , with comparison against the 3D 'panel models' from ABAQUS.

As is always the case with the example scripts presented in the current document, the

reader may wish to run the script for themselves and examine the solution, or perhaps alter some of the parameters that define these cylindrical shell problems. Caution should be exercised in interpreting the generated plots if any of the parameters are altered, since the results included for comparison are loaded from a .csv file for the geometry, loading and boundary conditions discussed here. Additionally, running this example may take some time.

### 5.4.2 Example GNA02: GNA of the Belleville spring

An example that makes direct comparison with results presented in the publication from which AQUINAS shell formulation originates [50], `input_Example_GNA02.m` explores the equilibrium path of the Belleville spring. The snap-through behaviour of the conical shell structure assesses the nonlinear Riks solver in AQUINAS, as it has to identify the limit point and then trace the descending portion of the equilibrium path all the way until the stiffness turns positive again. The Belleville spring, which essentially is a shallow conical shell with its apex truncated, has an outer edge radius of  $r_1 = 7.62\text{ cm}$  and an inner one of  $r_2 = 2.54\text{ cm}$ . The shell wall has a thickness of  $t = 0.508\text{ cm}$  and the height of the conical segment is  $h = 1.27\text{ cm}$ . The material does not share its properties exactly with the steel material considered thus far, with its modulus of elasticity being  $E = 2.1 \times 10^3\text{ kg/cm}^2$  (Poisson's ratio is still  $\nu = 0.3$ ). A vertical line load  $N$  is applied at the top/inner edge of the spring, the base of which is fully clamped. The geometry, loading and boundary conditions are displayed in Figure 5.60.

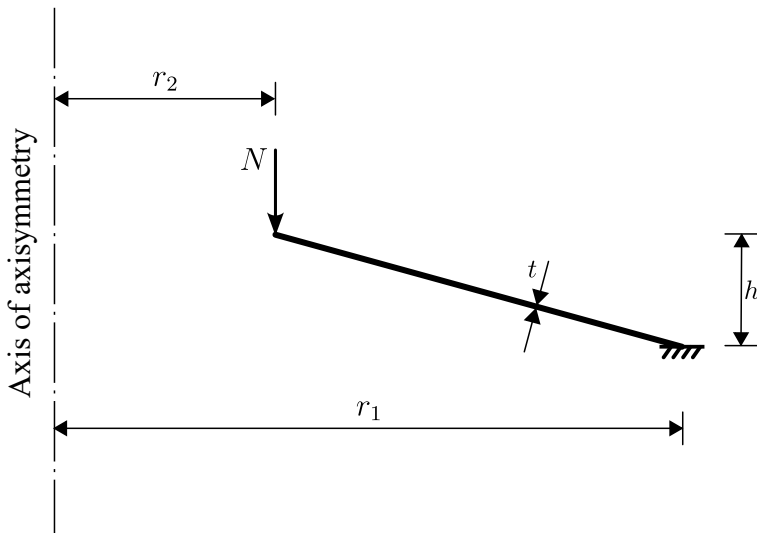


Figure 5.60: GNA02 - System diagram.

The equilibrium path for the inner edge deflection  $\delta$  obtained from AQUINAS is compared in Figure 5.61 against the data points from Surana [48] and the FE solution from J.G. Teng and J.M. Rotter [50], both digitised from [50]. The reader may appreciate the great agreement between the AQUINAS solution and [50], a consequence of the two FE software sharing the same shell formulation, and the discrepancies with the results of [48] that were observed in [50] also occur here.

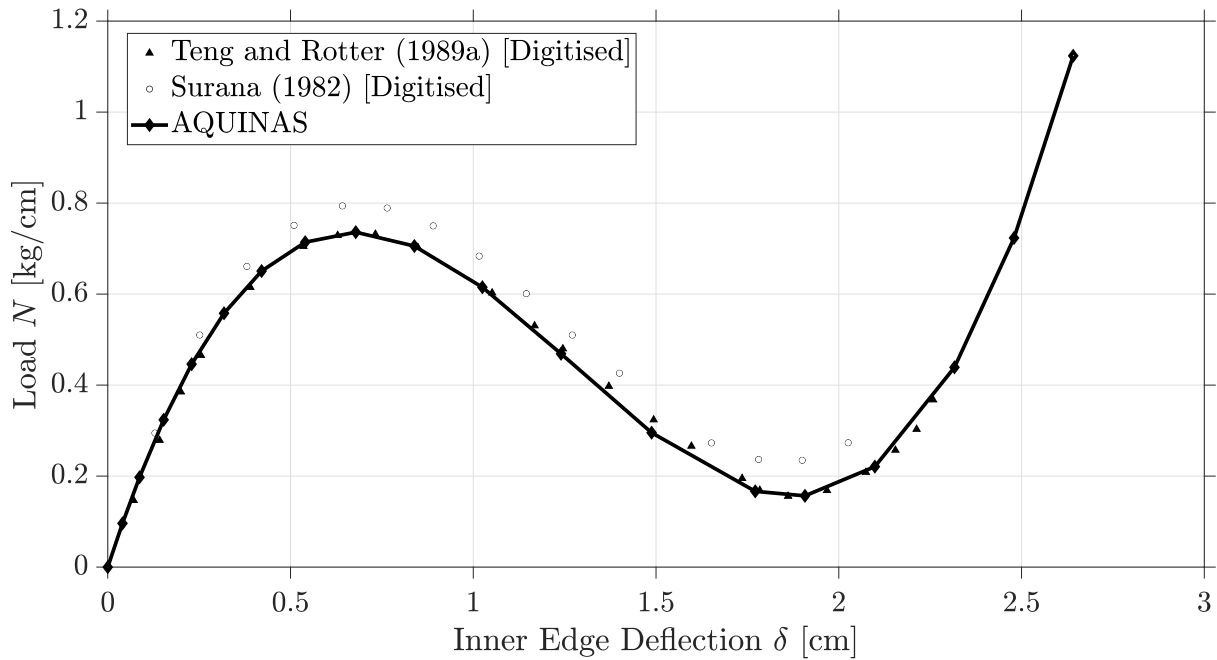


Figure 5.61: GNA02 - Equilibrium path for the Belleville spring.

### 5.4.3 Example GNA03: GNA of a thin spherical cap under uniform external pressure

After exploring a couple of geometrically nonlinear analyses of axisymmetric shells with straight meridians, it is time to move on to doubly-curved shells. In `input_Example_GNA03.m`, the load-deflection path of a spherical cap's apex deflection under the effect of uniform external normal pressure is examined. The definition of this nonlinear shell problem is illustrated Figure 5.62.

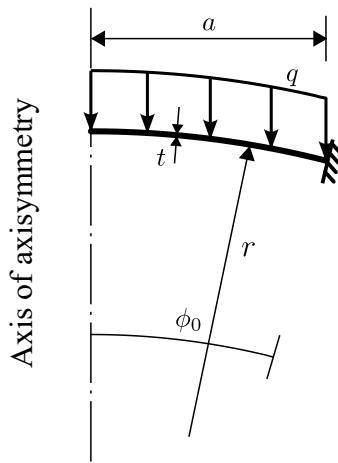


Figure 5.62: GNA03 - System diagram.

Comparison is once again made with the FE results from [50], but also from the established solution of Bathe et al. [6], both obtained through digitisation from [50]. The spherical cap has a radius of  $r = 2540.0\text{ mm}$  and a thickness of  $t = 12.7\text{ mm}$ , with its outer edge located at a meridional angle of  $\phi_0 = 7.1^\circ$ . The material used in this GNA example is slightly different from the one used in most of the previous examples, with its Young's

modulus being  $E = 207000 \text{ N/mm}^2$  and its Poisson's ratio still set at  $\nu = 0.3$ . A BC1r boundary condition is applied at its edge. The excellent agreement between AQUINAS and both FE solutions is illustrated in Figure 5.63.

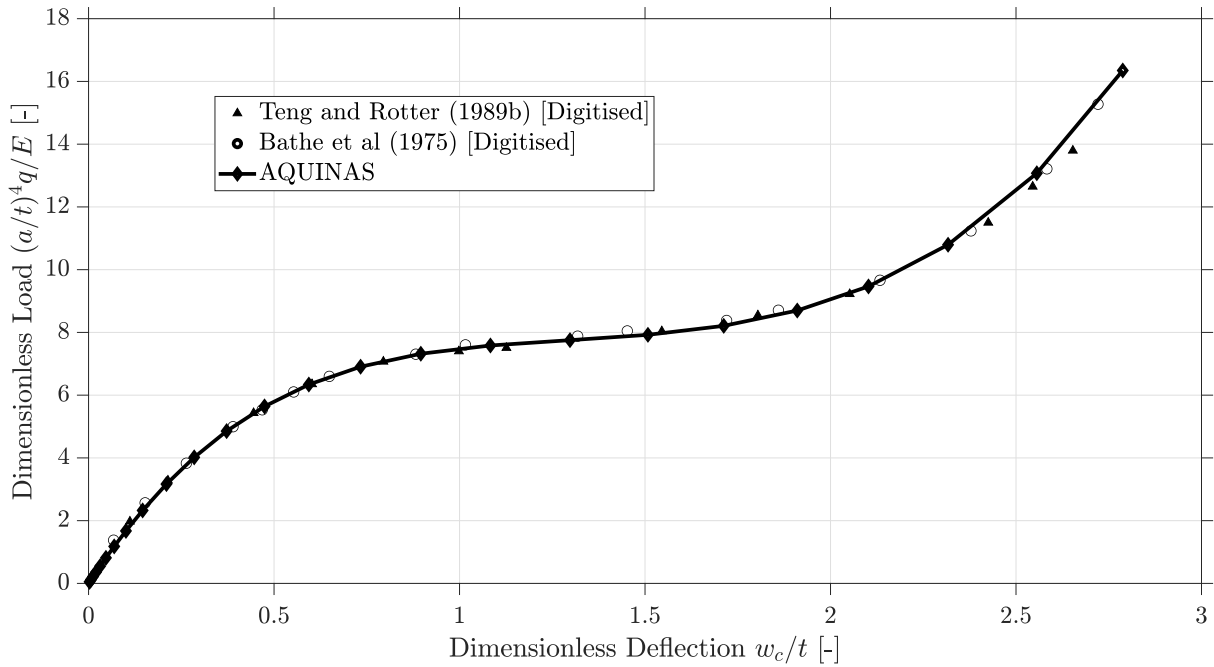


Figure 5.63: GNA03 - Equilibrium path for apex deflection of shallow spherical cap under external

#### 5.4.4 Example GNA04: GNA of a ring-loaded thin spherical cap

Another benchmark test that makes direct comparison with results from the source [50] of the AQUINAS shell formulation, `input_Example_GNA04.m` explores the equilibrium path of a ring-loaded thin spherical cap apex's deflection as illustrated in Figure 5.64.

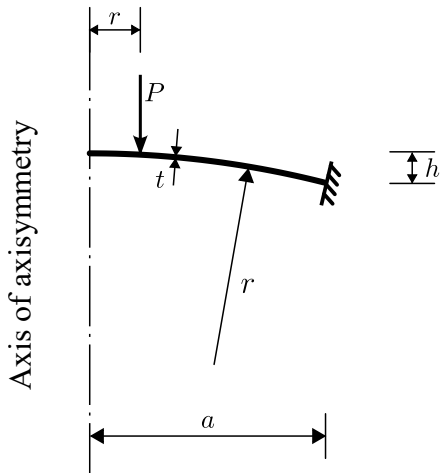


Figure 5.64: GNA04 - System diagram.

Two load cases are considered, one where the load  $P$  is applied directly at the apex of the spherical cap ( $r = 0$ , concentrated load) and a second one where the load is applied

as a ring load a distance  $r = 0.42a$ , where  $a$  is the projection of the spherical cap to the radial coordinate axis. The radius and thickness of the spherical cap's meridian are set to  $r = 4.758 \text{ in}$  and  $t = 0.01576 \text{ in}$  accordingly, while the projection  $a$  of the cap into the radial axis is  $a = 0.9 \text{ in}$ . The edge of the spherical cap is fully clamped. The two load-deflection paths of the spherical cap's apex deflection  $w_c$  are presented in Figure 5.65. Comparison is made not only with the FE results of the source publication [50], but also with the computational solution of Wood and Zienkiewicz [60]. All three approaches seem to be in perfect agreement, for both the load cases considered, regardless of whether a limit point is observed on the equilibrium path of the spherical cap.

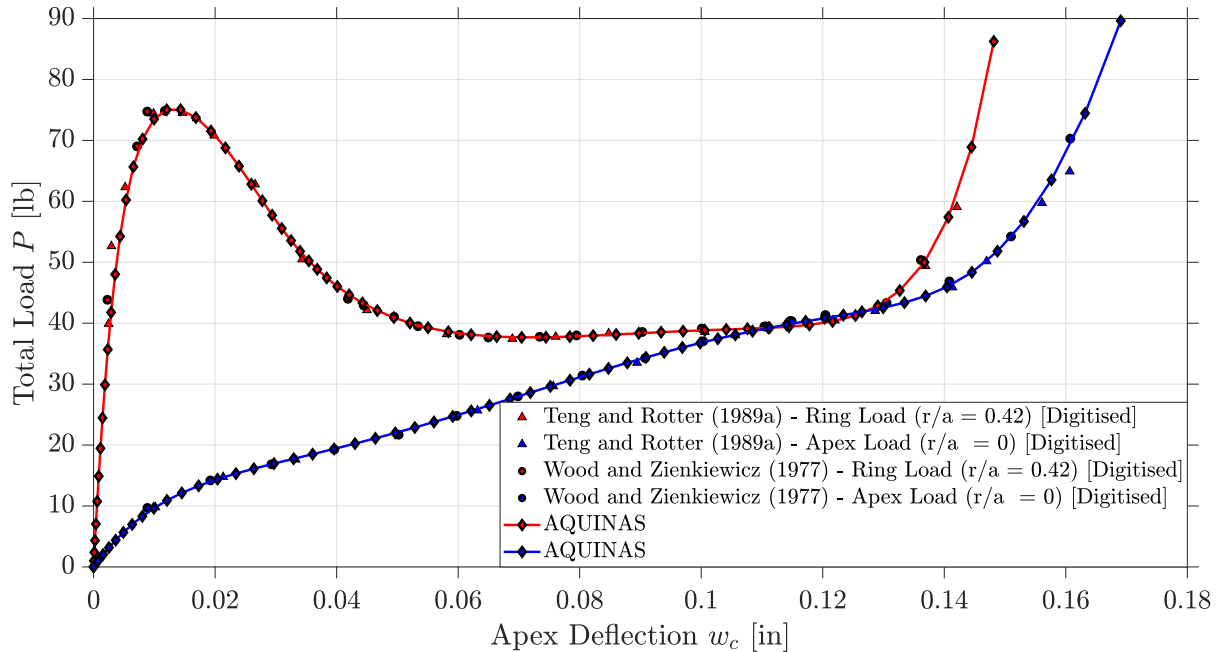


Figure 5.65: GNA04 - Load-deflection curves of ring loaded spherical caps

#### 5.4.5 Example GNA05: Snap-through of a shallow spherical cap

Computing the snap-through load of an axisymmetric shell in AQUINAS is equivalent to the evaluation of the limit point in the shell's response, identified as the point where the determinant of the tangent stiffness changes sign. In `input_Example_GNA05.m`, the snap-through loads for a range of shallow spherical caps are computed and compared against those obtained from the works of Budiansky [8] and Dumir and Nath [18]. The caps are parametrised with respect to a rise parameter  $\lambda$  (not to be confused with the bending boundary layer half-wavelength  $\lambda$ ), given as:

$$\lambda = 2[3(1 - \nu^2)]^{1/4} \sqrt{h/t} \quad (5.17)$$

The radius and thickness of the spherical caps are constant for all models at  $r = 100.0 \text{ mm}$  and  $t = 1.0 \text{ mm}$  accordingly, with only the height  $h$  of the caps (projection on to the axial coordinate axis  $z$ ) varying according for each  $\lambda$  of Eq. (5.17). The characteristic pressure  $p_0$  applied on the spherical caps is set to:

$$p_0 = \frac{2Et^2}{r^2 \sqrt{3(1 - \nu^2)}} \quad (5.18)$$

The edge of the spherical caps considered are fully clamped. The geometry, loading and boundary conditions of the cap models are presented in Figure 5.66, while the numerical comparison of the snap-through loads for each rise parameter  $\lambda$  is summarised in Table 5.7. As expected, the AQUINAS results are very close its parent publication [50], with any minor discrepancies attributed to differences in the implementation or discretisation of the spherical caps.

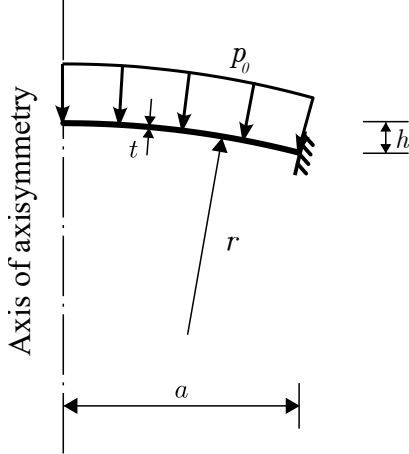


Figure 5.66: GNA05 - System diagram.

Table 5.7: GNA05 - Snap-through loads  $\frac{p_{cr}}{p_0}$  of shallow clamped spherical caps for a range of rise parameters  $\lambda$ .

$\lambda$	Budiansky [8]	Dumir and Nath [18]	Teng and Rotter [50]	AQUINAS
4	0.578	0.580	0.563	0.560
5	0.629	0.630	0.615	0.619
5.5	0.789	0.785	0.746	0.754
6	0.995	0.986	0.972	0.968
7	1.068	1.042	1.046	1.040
8	1.130	1.115	1.109	1.103

#### 5.4.6 Example GNA06: Nonlinear buckling analysis of a clamped shallow spherical cap under uniform external pressure

As discussed earlier, the critical circumferential mode that the axisymmetric shell wants to bifurcate into may change as the nonlinear analysis proceeds yielding a different result to the LBA prediction. The script `input_Example_GNA06.m` identifies the critical buckling pressures and associated modes  $n$  of shallow spherical shell models, similar to the ones analysed in these last GNA examples. The geometry of the caps is once again characterised with the aid of the rise parameter  $\lambda$  of Eq. (5.17), with the magnitude of the external pressure  $p_0$  applied determined from Eq. (5.18). The radius and thickness of the spherical caps is  $r = 100.0 \text{ mm}$  and  $t = 1.0 \text{ mm}$ , constant for all models, while their outer edge is fully clamped. This nonlinear axisymmetric shell problem is presented in Figure 5.67, with the critical buckling pressure ratios  $p_{cr}/p_0$  and associated modes  $n_{cr}$  showcased in Table 5.8. The FE results obtained from AQUINAS are not only compared with those of [51],

but also with the computational solution of Huang [24]. A good agreement between the three nonlinear computations is showcased, with minor differences that may be attributed to the critical circumferential mode identification scheme applied (see discussion in [51]), as well as to the inclusion of antisymmetric bifurcation terms.

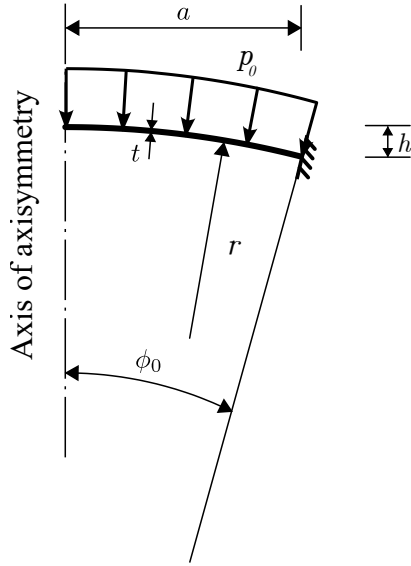


Figure 5.67: GNA06 - System diagram.

Table 5.8: GNA06 - Critical nonlinear buckling pressure ratios  $p_{cr}/p_0$  and associated circumferential mode  $n_{cr}$  for a range of rise parameters  $\lambda$ .

$\lambda$	$\frac{p_{cr}}{p_0}$ of [24]	$n_{cr}$ of [24]	$\frac{p_{cr}}{p_0}$ of [51]	$n_{cr}$ of [51]	AQUINAS $\frac{p_{cr}}{p_0}$	AQUINAS $n_{cr}$
6	0.775	2	0.777	2	0.768	2
7	0.760	3	0.763	3	0.754	3
8	0.766	4	0.769	4	0.762	4
9	0.777	4	0.778	4	0.773	5
10	0.776	5	0.778	5	0.772	5
12	0.780	7	0.782	7	0.778	7
14	0.782	9	0.787	9	0.784	9
16	0.790	11	0.792	11	0.789	10

## 5.5 GNAs

Midsurface imperfections can be explicitly defined in AQUINAS at the level of generating an axisymmetric shell segment. The imperfect shape is approximated through an Akima interpolation [2] that fits a polynomial of up to cubic order on the series of points provided as input to the `AQUINAS_Segment_Object`. It is important to remember that these imperfection shapes are purely axisymmetric, since AQUINAS neglects any circumferential displacements in tracing the pre-buckling response of any shell. The analysis submitted shares all of its formulation and processing aspects as those of the GNAs presented in the previous section.

### 5.5.1 Example GNIA01: GNIA of a thin unpressurised cylinder under uniform axial compression with a weld depression imperfection

The first GNIA example to be presented explores the effect of a weld depression imperfection on the strength of cylinders under axial compression. The weld depression is positioned at the mid-height of the cylindrical shell models, where the shape of the imperfection itself is given as

$$\delta = \delta_0 e^{-\pi x/\lambda} \left( \cos \frac{\pi x}{\lambda} + k \sin \frac{\pi x}{\lambda} \right) \quad (5.19)$$

with the  $\delta_0$  being the amplitude of the weld imperfection,  $x$  being the distance from the position of the weld along the meridian of the cylinder and  $k$  a parameter that is  $k = 1$  for a TYPE A weld and  $k = 0$  for a TYPE B [37]. The linear meridional bending half wavelength  $\lambda$  may be found as:

$$\lambda = \frac{\pi \sqrt{rt}}{\sqrt[4]{3(1 - \nu^2)}} \quad (5.20)$$

Following the modelling guidelines of J.M. Rotter and J.G. Teng (1989) [37], different boundary conditions are considered for the pre-buckling analysis of the axisymmetric FE models and the bifurcation checks. Boundary conditions that represent continuity at the ends of the cylindrical model are considered, with the radial displacement  $u$  being free and the rotation of the meridian  $\beta$  fixed. For the buckling configuration however, a BC2f - S3 boundary condition is considered at both ends, with an axial displacement  $w$  restraint applied at the position of the weld instead of the base of the cylinder (where it is applied for the pre-buckling state), to ensure that numerical issues that may arise from computation of geometric definitions through an interpolation scheme are avoided. The external load applied on top edge of the cylinders is related to the classical elastic critical stress of Eq. (5.3) so that  $N = \sigma_{ct} t$ .

The geometric definition of a cylinder with a TYPE A weld depression imperfection, as given by Eq. (5.19) at mid height is presented in Figure 5.68 (where the boundary conditions, alternating between pre-buckling/buckling configurations of the shells, are omitted). The reader may also wish to run `input_Example_GNIA01.m` for a TYPE B weld, but should be warned that the included results for comparison are only relevant to a TYPE A imperfection shape. All of the cylindrical models are of constant unit thickness  $t = 1.0 \text{ mm}$ , with their radius set to  $r = 1000.0 \text{ mm}$ . The length of the cylindrical shell models is chosen such that  $L/r = 3$ .

In Figures 5.69 - 5.70, the nonlinear critical bifurcation loads and associated circumferential modes are plotted for a series of increasing amplitudes  $\delta_0$  for a weld depression imperfection at the mid-height of the cylindrical shell models. An almost perfect agreement is illustrated between the results presented in Rotter and Teng (1989) [37] and Rotter and Teng (2004) [53], with the first one obtained through a computational analysis with the FELASH software [50]. On the other hand, the panel analysis results of [42] display a considerable deviation from those of the three other FE solutions (AQUINAS included), making the case for the existence of the current software even stronger. The disagreement between AQUINAS and [37] - [53] for the critical circumferential mode of a perfect cylinder is not considered alarming, as numerous competing harmonics  $n$  essentially coexist for the same critical level of load. The results of `input_Example_GNA01.m`, presented ear-

lier, provide enough proof for the ability of AQUINAS to accurately predict the critical circumferential modes of cylinders under axial compression.

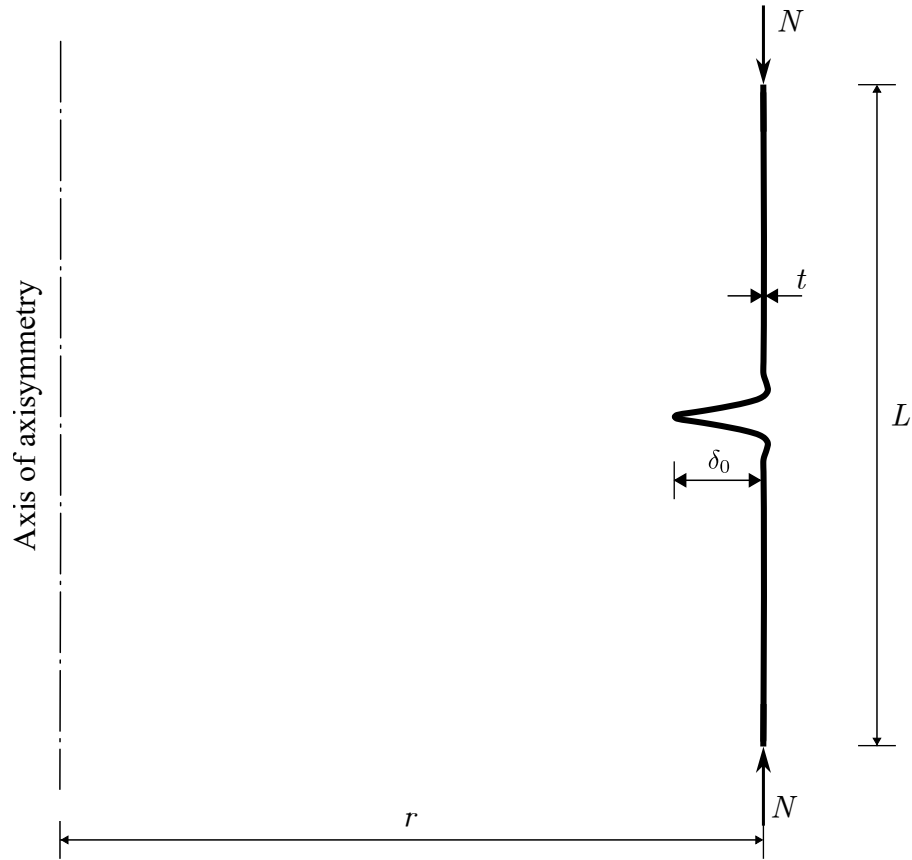


Figure 5.68: GNIA01 - System diagram.

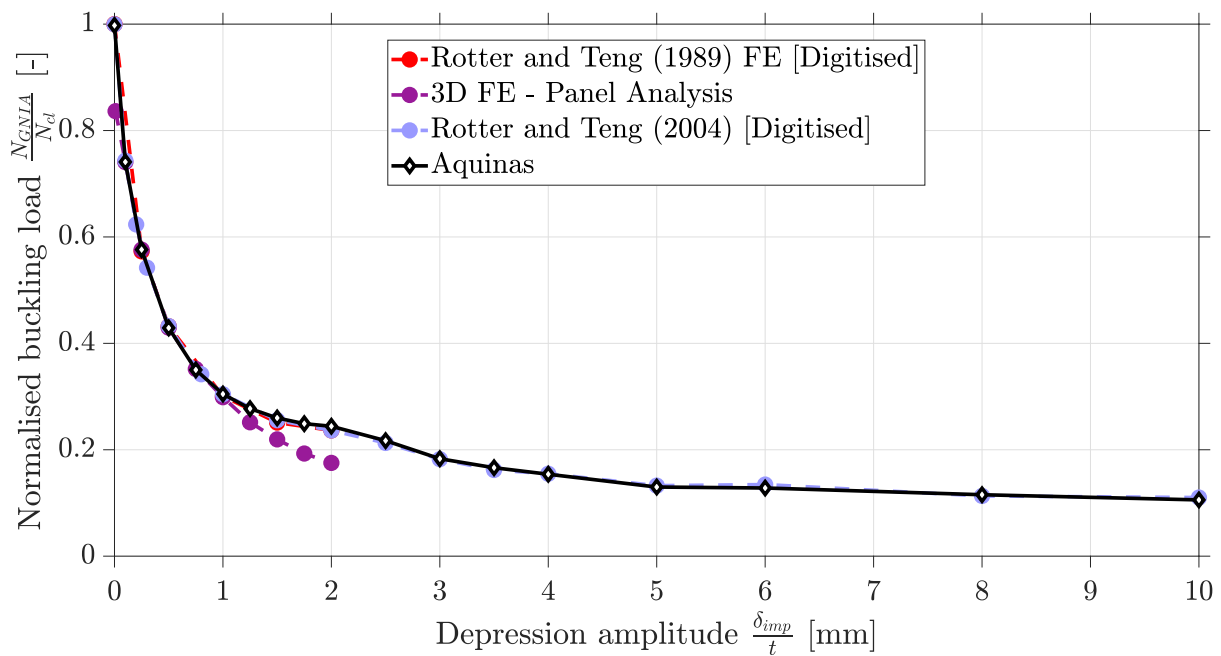


Figure 5.69: GNIA01 - Critical dimensionless loads for increasing amplitudes of a TYPE A weld depression imperfection.

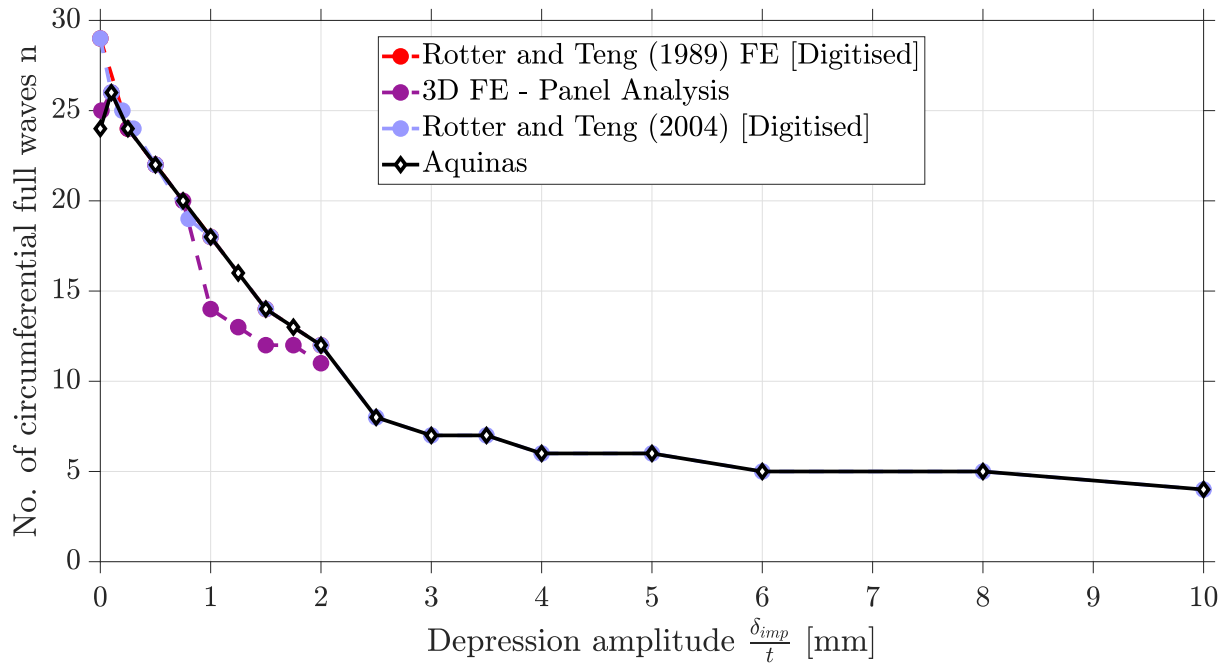


Figure 5.70: GNIA01 - Critical circumferential bifurcation modes for increasing amplitudes of a TYPE A weld depression imperfection.

The bifurcation modes for a selected few imperfection amplitudes  $\delta_0$  are also presented in Figure 5.71, with the shapes normalised so that the peak modal displacement is equal to unity and scaled by a factor of 10. The reader may wish to compare those against the corresponding shapes presented in [37] and confirm that the bifurcation modes obtained from AQUINAS are indeed valid. The reader is cautioned that this example may take some time to run.

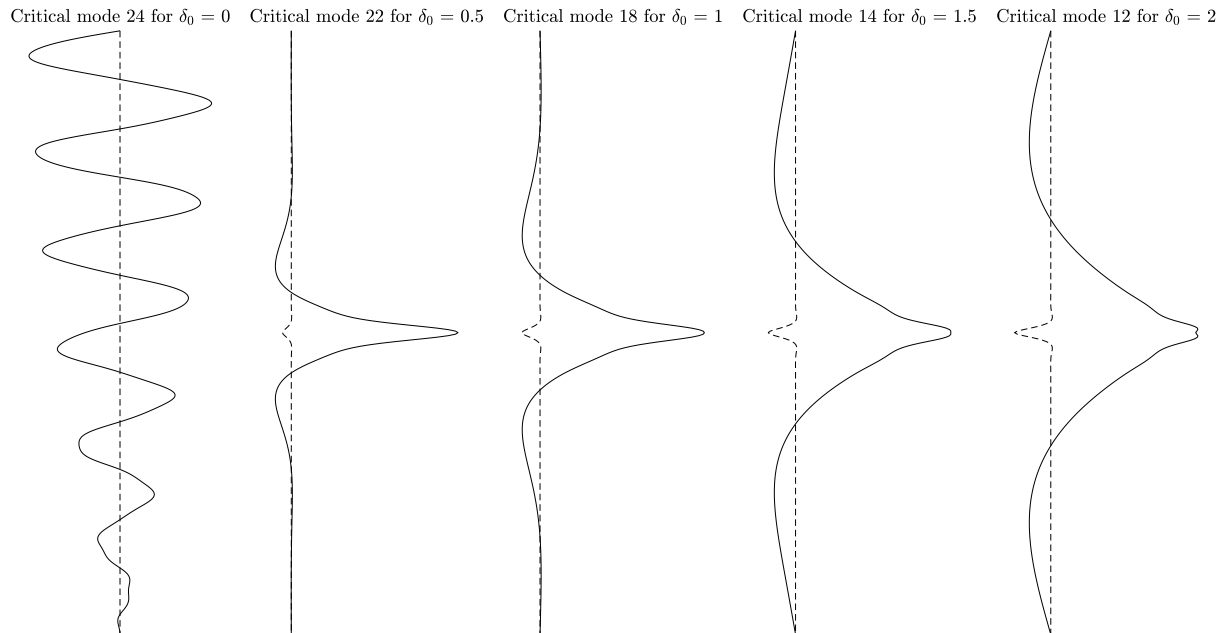


Figure 5.71: GNIA01 - Bifurcation modes for selected imperfection amplitudes of a TYPE A weld depression.

### 5.5.2 Example GNIA02: GNIA of a thin pressurised cylinder under uniform axial compression with a weld depression imperfection

Continuing the topic of computing the strength of cylinders with weld depression imperfections, `input_Example_GNIA02.m` examines the development of thin cylindrical models' resistance under the combined effect of axial compression and internal pressure. A few selected imperfection amplitudes  $\delta_0$  are considered for the imperfect geometry of the cylinders, but also different characterisation parameters  $\bar{p}$  for the internal normal pressure, given as

$$\bar{p} = \frac{pr}{\sigma_{el}t} \quad (5.21)$$

with the classical elastic critical stress given in Eq. (5.3). The geometry and boundary conditions are similar to those of `input_Example_GNIA01.m` ( $t = 1.0 \text{ mm}$ ,  $r = 1000.0 \text{ mm}$  and  $L/r = 3$ ), with the loading now including a varying internal pressure, illustrated in Figure 5.72.

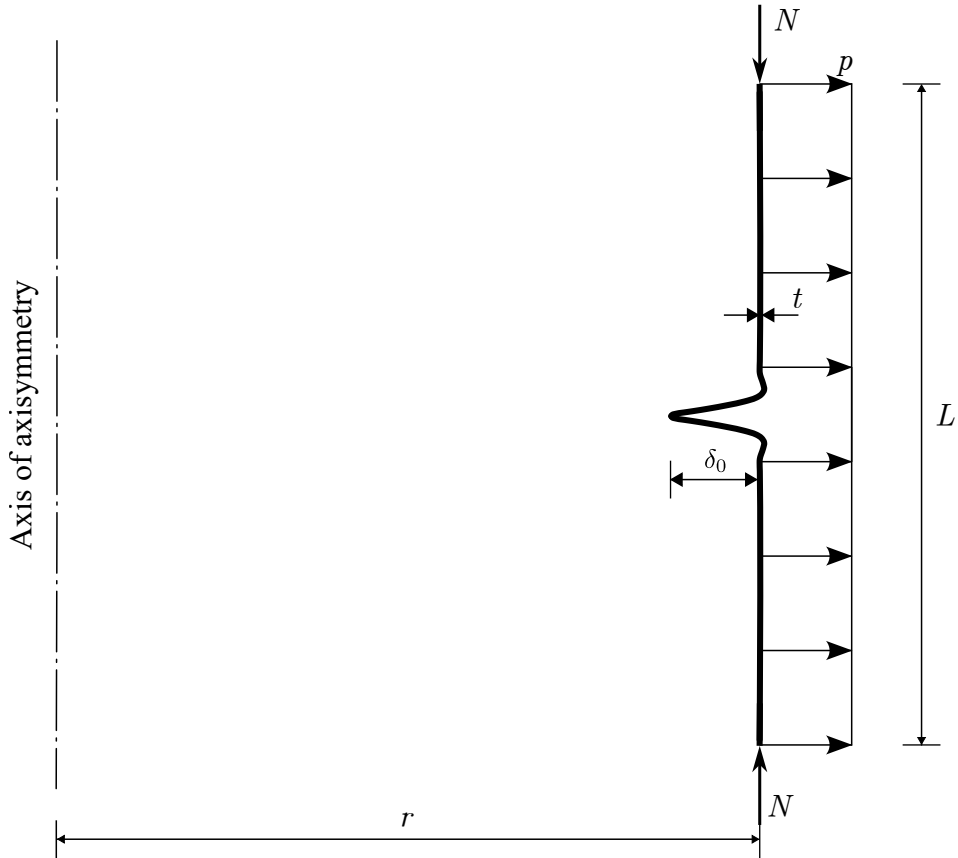


Figure 5.72: GNIA02 - System diagram.

For comparison purposes, the results of Rotter and Teng (1989) [37] have been digitised, as obtained with the use of the FELASH [50] - [51] suite of software. The results of the two FE toolboxes (that share the same axisymmetric shell formulation) are plotted in Figure 5.73, illustrating the beneficial effects of internal pressure on the response of cylinders with varying weld depression imperfections under axial compression. Discrepancies that are

visible for the higher dimensionless pressure ratios  $\bar{p}$  considered are attributed to potential differences in the definition of the geometric derivatives ( $\frac{\partial\phi}{\partial s}$ ,  $\frac{\partial^2\phi}{\partial s^2}$  etc.) associated with the imperfect geometry, for which an Akima interpolation scheme has been used here [2], but also on discretisation choices along the meridian of cylindrical shell models. While it is mentioned in [37] that a ‘very fine finite element mesh was used in the neighbourhood of the weld depression, with elements of length only  $0.25\sqrt{rt}$ ’, it is unclear what is the extent of the ‘neighbourhood of the weld depression’, and consequently what was the discretisation for the rest of the meridian. The reader is encouraged to run the input script with a lower meridional discretisation than the one used for the generation of Figure 5.73 and notice that there is a better agreement for the higher end dimensionless pressure parameters  $\bar{p}$ .

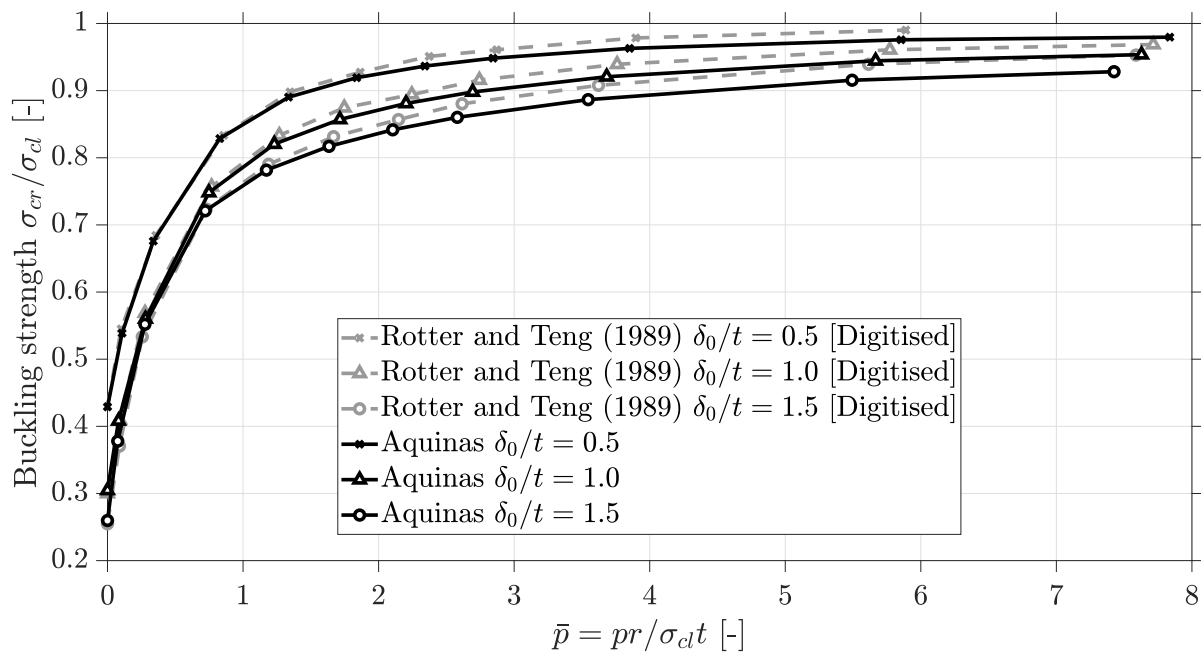


Figure 5.73: GNIA02 - Critical dimensionless loads for increasing amplitudes of a TYPE A weld depression imperfection for cylinders under combined axial compression and internal pressure.

The bifurcation modes for selected values of the dimensionless pressure parameter  $\bar{p}$  of cylinders with a weld imperfection amplitude ratio of  $\delta_0/t = 1.5$  are also presented in Figure 5.74, where the reader may appreciate the similarity of the computed shapes and those of Figure 12 in [37]. Once again, the modes are normalised and scaled, and should not be treated as an actual deformed shape. The reader is cautioned that this example may take some time to run.

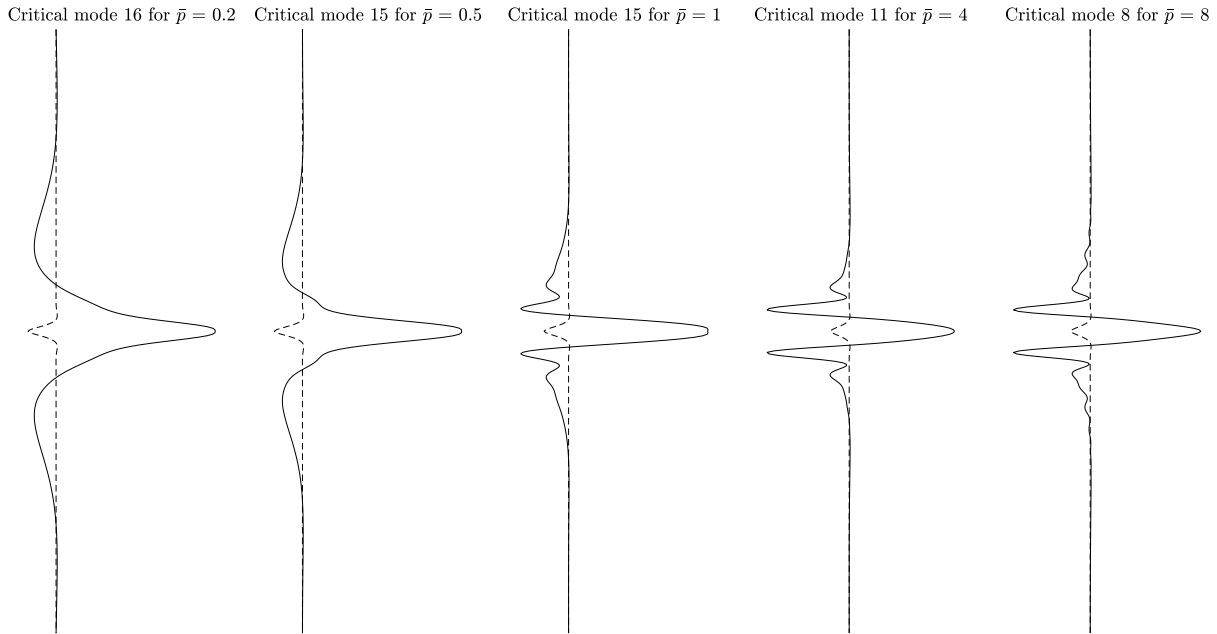


Figure 5.74: GNIA02 - Bifurcation modes for selected dimensionless pressure ratios  $\bar{p}$  of cylinders with a TYPE A weld imperfection shape, with an amplitude ratio of  $\delta_0/t = 1.5$ , under combined axial compression and internal pressure.

## 5.6 GMNAs

All the individual pieces of the FE formulation and computational schemes are coordinated in `AQUINAS_GMNA.m`, for the geometrically and materially nonlinear analysis of axisymmetric shells with a uniform pre-buckling stress state, according to the European Standard prEN 1993-1-6 [14]. As was the case with the geometrically nonlinear benchmark examples presented earlier, a series of competing circumferential modes  $n$  may be trialled, for each converged load increment applied, to check for bifurcation into an axisymmetric or non-axisymmetric mode.

In the following exploration of the two cylindrical GMNA problems, the very good behaviour of AQUINAS for solving advanced nonlinear problems will be showcased, while the reader can appreciate the almost effortless execution of GMNA type of problem by having a look through the relevant scripts. At the same time, the necessity for a computational tool that can accurately detect bifurcation into any circumferential mode, with just a single axisymmetric shell model, will be highlighted as the only sensible option for the generation of nominal ‘capacity curves’ for reference shell systems. These curves are of paramount importance for the application of prEN 1993-1-6 [14] for the design of shell problems, especially in the context of the LBA-MNA [34] or Reference Resistance Design [39] - [41] methodologies.

### 5.6.1 Example GMNA01: Nominal capacity curve generation for cylinders of varying slenderness under uniform axial compression

The fully nonlinear resistance of cylindrical shells of varying slenderness under axial compression is examined in `input_Example_GMNA01.m` for the computation of a capacity

curve for this reference system, aiming to reveal the underlying relationships of material and geometric nonlinearities as the cylindrical models become increasingly more slender. The cylinders considered in this GMNA example are characterised by a unit dimensionless length parameter  $\Omega = 1$ , as defined by Eq. (5.2). While the thickness of the shell wall is kept constant at a unit thickness of  $t = 1.0\text{ mm}$ , the radius of the meridian's midsurface varies for the cylindrical models through a series of considered  $r/t$  ratios. The elastic-perfectly plastic material law is characterised by a yield stress  $f_y = 250\text{ N/mm}^2$ , even though the relationships of normalised resistances presented through the construct of a capacity curve are unaffected by the yield stress of the material. The base of the cylinders are fully clamped with a BC1r-C1 boundary condition, while the top edge, where the compressive line load  $N$  is applied, is restrained through a BC2r-C3 condition. The cylindrical shell model is presented in Figure 5.75.

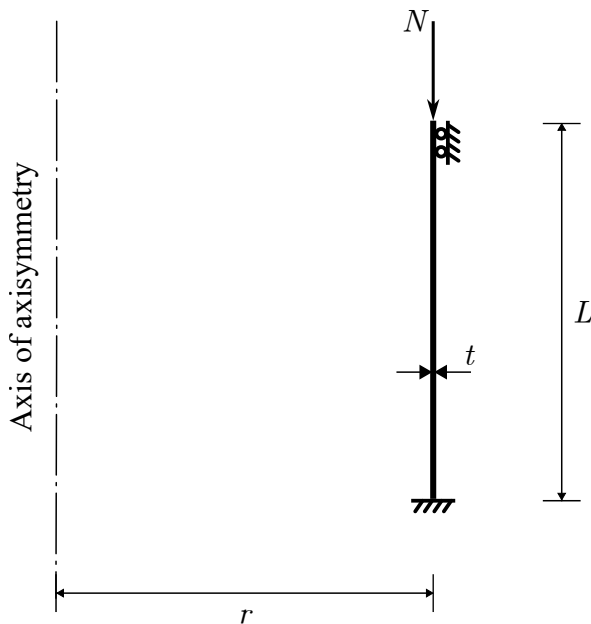


Figure 5.75: GMNA01 - System diagram.

Three different sets of AQUINAS analyses are executed for each  $r/t$  ratio, in an attempt to isolate the nonlinear effects that dominate the resistance of the cylinders as they transition from thick, stocky models to very slender ones. A geometrically and materially nonlinear model that is only allowed to fail through an axisymmetric failure mode is expected to accurately identify the strength of the cylinders for low intermediate slenderness models, but is also expected to be under-conservative for the thinner models, where elastic bifurcation into any one of the competing circumferential modes  $n$  is anticipated to be the determining factor of the shell's resistance. An attempt to also capture the completely elastic bifurcation into a non-axisymmetric mode  $n$  is made, for the higher end of the  $r/t$  ratio range, by submitting a GNA for each of the cylindrical model. Finally, an AQUINAS nonlinear solution with both types of nonlinearities included and bifurcation checks for all potentially competing harmonics  $n$  is included in `input_Example_GMNA01.m`, with the expectation to be capable of accurately converging to the appropriate resistance for cylindrical shells of low, intermediate or high slenderness. The very different failure modes that are critical for the slendernesses considered constitute a very demanding benchmark test not only for AQUINAS, but for any FE solver.

These three AQUINAS analyses required more than 24-hours on an 8 core AMD

Ryzen 7 4800h CPU. It is apparent that if an analysis where only the meridian requires discretisation is of such computational expense, then the generation of the same capacity curve with a ‘panel analysis’, as demonstrated by Sadowski et al (2017) [42], can be deemed as completely impractical in terms of time efficiency (without mentioning the other potential computational pitfalls discussed in [42]). In Figure 5.76, the capacity curve for the cylindrical shell problem under consideration is presented, where the relationships between the normalised resistance  $R_{GMNA}/R_s$  of a system against either its dimensionless slenderness  $\lambda = \sqrt{R_s/R_{cl}}$  (the ‘traditional’ form Fig. 5.76 left), and against an alternatively normalised resistance  $R_{GMNA}/R_{cl}$  (the ‘modified’ form Fig. 5.76 right as conceived by Rotter [38]), are explored. A reader taking a closer look in the publications presenting the capacity curves construct in the context of axisymmetric shell analyses may notice that an LBA and MNA need to be executed for the computation of the corresponding resistances, namely  $R_{LBA}$  and  $R_{MNA}$ . Instead  $R_{cl}$  and  $R_s$  have been used in `input_Example_GMNA01.m` as the reference resistances in their place, computed through the classical elastic bifurcation load  $P_{cl} = 2\pi r t \sigma_{cl}$  (relevant to the classical elastic critical stress  $\sigma_{cl}$  of eq. (5.3)) and a simple membrane theory prediction of the plastic load  $P_s = 2\pi r f_y t$  that would lead to extensive membrane yielding, and therefore collapse. This simplification, and associated economy in computational time, is only possible in this case due to the extensive research and availability of background results on the topic of cylindrical shell buckling under axial compression. In the absence of a sufficient scientific background for a shell problem, the analyst would have to actually compute the LBA and MNA resistances.

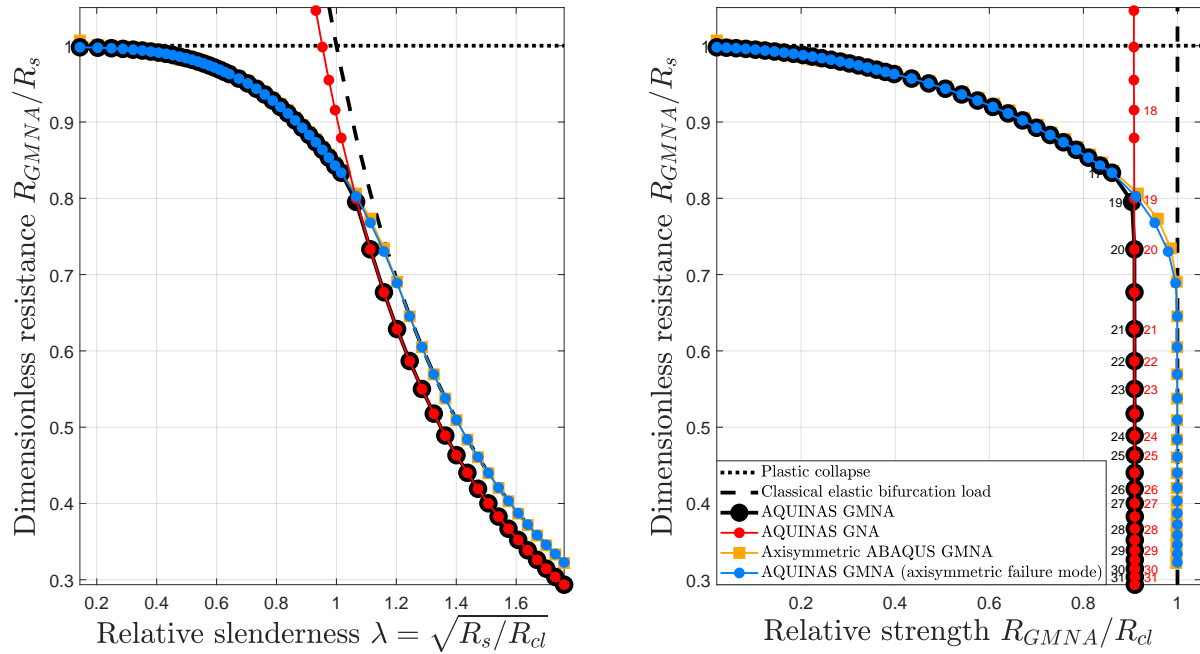


Figure 5.76: GMNA01 - Traditional (left) and modified (right) capacity curves for cylinder under axial compression for a dimensionless length  $\Omega = 1$ .

An axisymmetric GMNA ABAQUS [1] model is also examined for each cylinder, not only to verify the result obtained from an AQUINAS ‘axisymmetric failure only’ analysis, but also to illustrate the consistent overestimation of the shells’ strength by this well established, commercial software, as there is no way to detect bifurcation into a non-axisymmetric harmonic mode  $n$ . The reader may also appreciate how clean the generated capacity curve appears to be, with its form being exceptionally similar to the characteristic

capacity curve presented in Sadowski et al. (2017) [41]. The full GMNA AQUINAS result has an excellent agreement with the axisymmetric ABAQUS GMNA (and of course with its very own axisymmetric failure GMNA), and gradually starts to agree with the elastic GNA result, as the cylinders become thinner and thinner. The predicted bifurcation modes are also in excellent agreement between the AQUINAS GMNA and AQUINAS GNA (black and red numbers on modified capacity curve accordingly) solutions for the high-slenderness cylinders, indicating that there is little to no yielding occurring as the cylindrical models deform. The reader is cautioned that this example may take some time to run.

### 5.6.2 Example GMNA02: Elastic-plastic collapse load predictions for a pressurised cylinder under uniform axial compression

The elastic-plastic collapse loads of pressurised and axially-compressed cylinders will be examined in this GMNA validation example, where the focus is still on axisymmetric shells of infinite meridional radius of curvature. Four different  $r/t$  ratios will be considered for the cylindrical models, ranging from rather thick and stocky ( $r/t = 250$ ) to very thin and slender ( $r/t = 2000$ ). The applied internal pressure  $p$  will also be varying with respect to the applied axial load  $N$ , as a higher internal pressure may lead to uniform circumferential yielding faster and significantly undermine the strength of the cylinders under axial compression. This behaviour is thoroughly investigated in Rotter (1990) [33], where the finite difference BOSOR5 program [10], very popular for shell analyses in this past era of extensive shell research, is used for computing the solution of this demanding geometrically and materially nonlinear problem. This will allow AQUINAS to compare its full GMNA results with a very different, yet well established, approach to the solution of axisymmetric shell problems.

As discussed in [33], the shell models studied are chosen to represent the bases of cylindrical on-ground silos and tanks. The length of the cylinders' meridian is chosen to be equal to five elastic bending half-wavelengths  $\lambda$  as defined by Eq. (5.20), leading to a length of approximately  $L \approx 12\lambda$  or a Batdorf parameter  $Z = 142$ . Their base is fully clamped (BC1r-C1), while a BC3r boundary condition is applied at their top edge to represent meridional continuity, as illustrated in Figure 5.77. The wall is of unit thickness  $t = 1.0\text{ mm}$  for all  $r/t$  ratios, with the fabrication material having a yield stress of  $f_y = 250\text{ MPa}$  with no strain hardening considered. The magnitude of the internal pressure is related to the axial compressive stress  $\sigma_x$ , as defined through the applied line edge load  $N = \sigma_x t$ , so that a series of  $pr/\sigma_x t$  ratios are submitted for a nonlinear analysis for each  $r/t$  ratio examined.

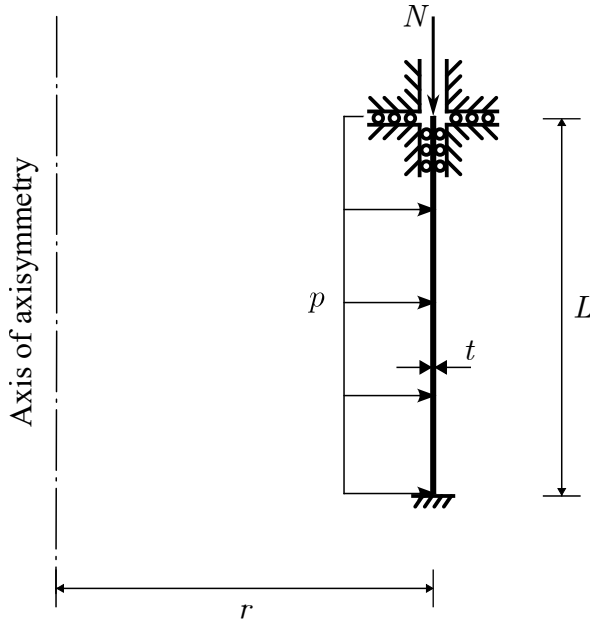
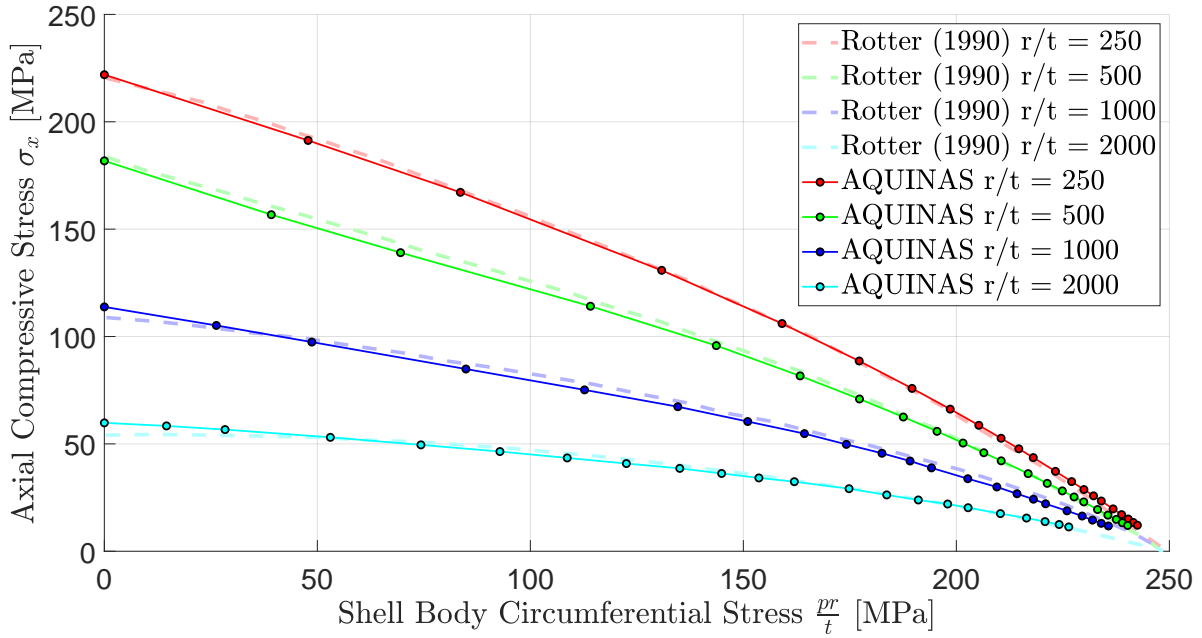


Figure 5.77: GMNA02 - System diagram.

The GMNA results of this exploration are presented in Figure 5.78, with the digitised collapse loads obtained in [33] with the BOSOR5 suite included for comparison. A very good agreement is illustrated between the two very different computational approaches, where some minor discrepancies are to be expected due to the inevitably poor quality of a digitisation result. The reader is cautioned that this example may take some time to run.

Figure 5.78: GMNA02 - Collapse load predictions for pressurised cylinders under axial compression for  $r/t = 250, 500, 1000, 2000$  ratios.

## 5.7 GMNIAs

No Geometrically and Materially Nonlinear Analysis are included with the AQUINAS documentation at this time, although undertaking one is possible with only trivial changes to the GNIA and GMNA examples presented above. Once such a model has been explored to the same standard of detail showcased for the previous validation examples of the current document, this section of the AQUINAS manual will be updated.

## 5.8 Miscellaneous

### 5.8.1 Example MISC01: Parallel scaling analysis

The script `input_Example_MISC01.m` file implements a simple ‘strong’ scaling analysis of the parallel performance of the AQUINAS C++ version for the FE assembly on a generic LA problem, the geometry of which is of no interest in this case as it is not the quality of the FE solution that is examined. The system stiffness matrix and the distributed force vector assembler is currently parallelised, the operation involving a computationally expensive `for` loop with independent iterations, using threading with OpenMP. The results are presented in 5.79, as generated with an 8-core AMD Ryzen 7 4800H CPU. The reader is cautioned that the data presented strongly depend on the number of processors, clock speed and background processes in an analyst’s computer, and replication of the distributions presented might not be possible. The serial fraction of the AQUINAS runtime is evaluated through application of Amdahl’s law [3], demonstrating the significance of the parallel OpenMP loop in speeding-up the solution process.

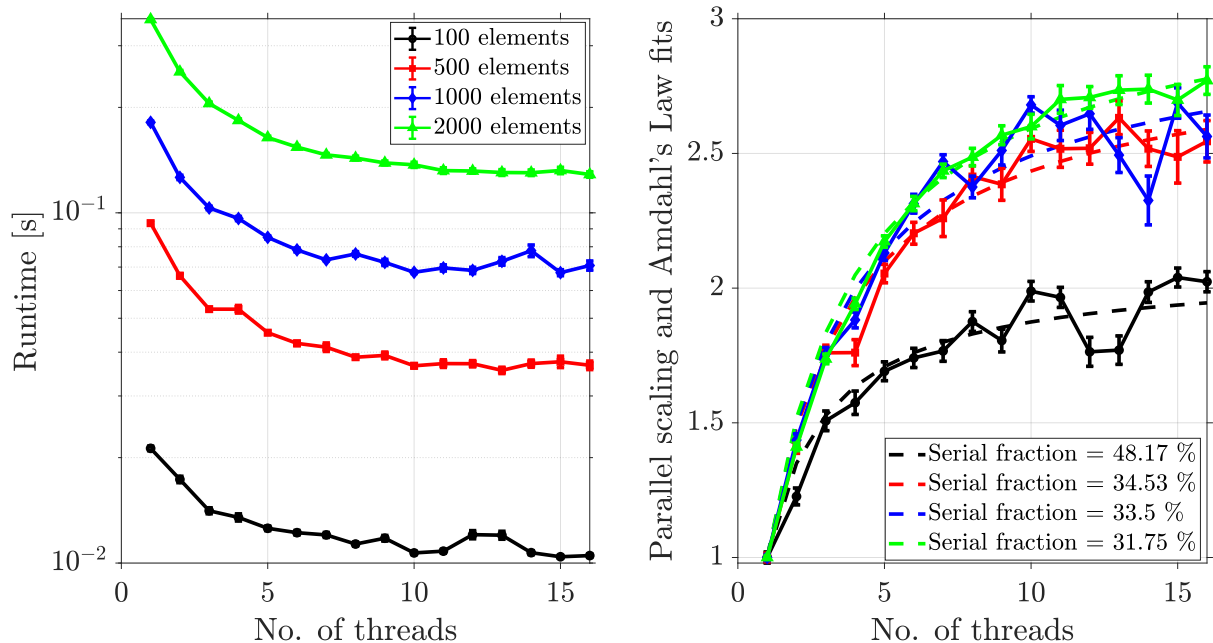


Figure 5.79: MISC01 - Parallel scaling analysis of AQUINAS on a simple LA problem, where the source of concurrency is the matrix assembler.

Analysts wishing to use the C++ capabilities are advised to perform this analysis first to establish an approximately optimal number of threads beyond which performance has reached a plateau and requesting additional parallel resources offers little further benefit.

# Bibliography

- [1] ABAQUS. *ABAQUS 2017 Commercial Finite Element Software and Documentation*. Dassault Systèmes Simulia Corp, United States, 2017.
- [2] H. Akima. A new method of interpolation and smooth curve fitting based on local procedures. *J. ACM*, 17(4):589–602, oct 1970.
- [3] Gene M Amdahl. Validity of the single processor approach to achieving large scale computing capabilities. In *Proceedings of the April 18-20, 1967, spring joint computer conference*, pages 483–485, 1967.
- [4] ANSYS. *ANSYS 2021 R2*. ANSYS Inc., 2021.
- [5] Ch. Baillis, J.F. Jullien, and A. Limam. An enriched 2d modelling of cooling towers.: Effects of real damage on the stability under self weight and on the strength under wind pressure. *Engineering Structures*, 22(7):831–846, 2000.
- [6] Klaus-Jürgen Bathe, Ekkehard Ramm, and Edward L Wilson. Finite element formulations for large deformation dynamic analysis. *International journal for numerical methods in engineering*, 9(2):353–386, 1975.
- [7] A. Boyez, A.J. Sadowski, and B.A Izzuddin. A novel ‘boundary layer’ finite element for the efficient analysis of thin cylindrical shells. *Computers & Structures*, 182:573–587, 2017.
- [8] B. Budiansky. Buckling of clamped shallow spherical shells. Technical report, HARVARD UNIV CAMBRIDGE MA, 1959.
- [9] David Bushnell. Stress, stability and vibration of complex, branched shells of revolution. *Computers & Structures*, 4(2):399–424, 1974.
- [10] David Bushnell. B0S0R5 - program for buckling of elastic-plastic complex shells of revolution including large deflections and creep. *Computers & Structures*, 6(3):221–239, 1976.
- [11] David Bushnell, Bo.O. Almroth, and Frank Brogan. Finite-difference energy method for nonlinear shell analysis. *Computers & Structures*, 1(3):361–387, 1971.
- [12] C.R. Calladine. *Theory of shell structures*. Cambridge University Press, 1983.
- [13] CEN. *prEN 1993-1-14 Eurocode 3: Design of steel structures - Part 1-14: Design assisted by finite element analysis*, Brussels, 2021. CEN.
- [14] CEN. *prEN 1993-1-6 Eurocode 3: Design of steel structures - Part 1-6: Strength and stability of shell structures*, Brussels, 2021. CEN.

- [15] A. Combescure and E. Pernette. Linear and nonlinear buckling of discrete supported cooling towers using special axisymmetric shell elements. *Nuclear Engineering and Design*, 111(2):217–225, 1989.
- [16] M.A. Crisfield. *Non-linear Finite Element Analysis of Solids and Structures*. John Wiley and Sons, 1991.
- [17] MA1913032 Crisfield. An arc-length method including line searches and accelerations. *International journal for numerical methods in engineering*, 19(9):1269–1289, 1983.
- [18] P.C. Dumir, M.L. Gandhi, and Y. Nath. Axisymmetric static and dynamic buckling of orthotropic shallow spherical caps with flexible supports. *Acta Mechanica*, 52(1):93–106, 1984.
- [19] M Fafard and B12081290773 Massicotte. Geometrical interpretation of the arc-length method. *Computers & structures*, 46(4):603–615, 1993.
- [20] W. Flügge. *Stresses in shells*. Springer-Verlag, 2nd edition edition, 1962.
- [21] M Geradin. Error bounds for eigenvalue analysis by elimination of variables. *Journal of Sound and Vibration*, 19(2):111–132, 1971.
- [22] G Gusic, A Combescure, and J.F Jullien. The influence of circumferential thickness variations on the buckling of cylindrical shells under external pressure. *Computers & Structures*, 74(4):461–477, 2000.
- [23] J. Heyman. *Equilibrium of shell structures*. Oxford Engineering Science Series, 1977.
- [24] Nai-Chien Huang. Unsymmetrical buckling of thin shallow spherical shells. *Journal of Applied Mechanics*, 31, 1964.
- [25] John W Hutchinson. Buckling of spherical shells revisited. *Proceedings of the Royal Society A: Mathematical, Physical and Engineering Sciences*, 472(2195):20160577, 2016.
- [26] Paul Thomas Jumikis. *Stability problems in silo structures*. PhD thesis, Department of Civil and Mining Engineering, University of Sydney, 1987.
- [27] W.T. Koiter. *On the stability of elastic equilibrium*. PhD thesis, Delft University, May 1945.
- [28] H. Kraus. *Thin Elastic Shells*. John Wiley and Sons, 1st edition edition, 1967.
- [29] Maple. *Maple 2022*. Maplesoft, a division of Waterloo Maple Inc., Waterloo, Ontario, 2022.
- [30] MATLAB. *version 9.12.0 (R022a)*. The MathWorks Inc., Natick, Massachusetts, 2022.
- [31] David Roger Jones Owen. *Finite elements in plasticity, theory and practice*. Pineridge press, 1980.

- [32] Ekkehard Ramm. Strategies for tracing the nonlinear response near limit points. In *Nonlinear Finite Element Analysis in Structural Mechanics: Proceedings of the Europe-US Workshop Ruhr-Universität Bochum, Germany, July 28–31, 1980*, pages 63–89. Springer, 1981.
- [33] J Michael Rotter. Local collapse of axially compressed pressurized thin steel cylinders. *Journal of Structural Engineering*, 116(7):1955–1970, 1990.
- [34] J Michael Rotter. Shell buckling design and assessment and the lba-mna methodology. *Stahlbau*, 80(11):791–803, 2011.
- [35] J. Michael Rotter, Greig Mackenzie, and Martin Lee. Spherical dome buckling with edge ring support. *Structures*, 8:264–274, 2016. Advances in the Analysis, Behaviour and Design of Steel Structures.
- [36] J Michael Rotter and Adam J Sadowski. Cylindrical shell bending theory for orthotropic shells under general axisymmetric pressure distributions. *Engineering Structures*, 42:258–265, 2012.
- [37] J Michael Rotter and Jin-Guang Teng. Elastic stability of cylindrical shells with weld depressions. *Journal of Structural Engineering*, 115(5):1244–1263, 1989.
- [38] J.M. Rotter. Shell buckling and collapse analysis for structural design: the new framework of the european standard. In *New Approaches to Structural Mechanics, Shells and Biological Structures*, Eds. Drew H.R. and Pellegrino S., pages 355–378. Kluwer Academic, 2002.
- [39] JM Rotter. The new method of reference resistance design for shell structures. *Proc. SDSS*, pages 623–630, 2016.
- [40] J.M. Rotter and P.T. Jumikis. Nonlinear strain-displacement relations for thin shells of revolution. *School of Civil and Mining Engineering, University of Sydney*, 1987.
- [41] Adam J. Sadowski, O. Kunle Fajuyitan, and Jie Wang. A computational strategy to establish algebraic parameters for the reference resistance design of metal shell structures. *Advances in Engineering Software*, 109:15–30, 2017.
- [42] A.J. Sadowski, L. Pototschnig, and P. Constantinou. The ‘panel analysis’ technique in the computational study of axisymmetric thin-walled shell systems. *Finite Elements in Analysis and Design*, 152:55–68, 2018.
- [43] A.J. Sadowski and J.M. Rotter. Steel silos with different aspect ratios: I — behaviour under concentric discharge. *Journal of Constructional Steel Research*, 67(10):1537–1544, 2011.
- [44] P. Seide. *Small Elastic Deformations of Thins Shells*. Springer Dordrecht, 1st edition edition, 1975.
- [45] Juan C Simo and Thomas JR Hughes. *Computational inelasticity*, volume 7. Springer Science & Business Media, 2006.
- [46] András Sóbester, Alexander Forrester, and Andy Keane. *Engineering design via surrogate modelling: a practical guide*. John Wiley & Sons, 2008.

- [47] Andrea Spagnoli. Koiter circles in the buckling of axially compressed conical shells. *International Journal of Solids and Structures*, 40(22):6095–6109, 2003.
- [48] K.S. Surana. Geometrically nonlinear formulation for the axisymmetric shell elements. *International Journal for Numerical Methods in Engineering*, 18(4):477–502, 1982.
- [49] J.G. Teng. Nonlinear and buckling analysis of complex branched shells of revolutions. In *Computational Mechanics in Structural Engineering*, pages 309–324. Elsevier, 1999.
- [50] J.G. Teng and J.M. Rotter. Elastic-plastic large deflection analysis of axisymmetric shells. *Computers & Structures*, 31(2):211–233, 1989.
- [51] J.G. Teng and J.M. Rotter. Non-symmetric bifurcation of geometrically nonlinear elastic-plastic axisymmetric shells under combined loads including torsion. *Computers & Structures*, 32(2):453–475, 1989.
- [52] JG Teng and JM Rotter. Plastic buckling of rings at steel silo transition junctions. *Journal of Constructional Steel Research*, 19(1):1–18, 1991.
- [53] Jin-Guang Teng and J Michael Rotter. *Buckling of thin metal shells*. CRC Press, 2004.
- [54] Jin-Guang Teng and J. Michael Rotter. Buckling of pressurized axisymmetrically imperfect cylinders under axial loads. *Journal of Engineering Mechanics*, 118(2):229–247, 1992.
- [55] S. Timoshenko and S. Woinowsky-Krieger. *Theory of plates and shells*. Engineering Societies Monographs, 1959.
- [56] H.N.R. Wagner, C. Hühne, and S. Niemann. Robust knockdown factors for the design of spherical shells under external pressure: Development and validation. *International Journal of Mechanical Sciences*, 141:58–77, 2018.
- [57] H.N.R. Wagner, C. Hühne, S. Niemann, and R. Khakimova. Robust design criterion for axially loaded cylindrical shells - simulation and validation. *Thin-Walled Structures*, 115:154–162, 2017.
- [58] Jie Wang, O. Kunle Fajuyitan, M. Anwar Orabi, J. Michael Rotter, and Adam J. Sadowski. Cylindrical shells under uniform bending in the framework of reference resistance design. *Journal of Constructional Steel Research*, 166:105920, 2020.
- [59] Christopher KI Williams and Carl Edward Rasmussen. *Gaussian processes for machine learning*. MIT press Cambridge, MA, 2006.
- [60] Richard D Wood and OC Zienkiewicz. Geometrically nonlinear finite element analysis of beams, frames, arches and axisymmetric shells. *Computers & Structures*, 7(6):725–735, 1977.
- [61] N. Yamaki. *Elastic stability of circular cylindrical shells*. North-Holland, 1984.
- [62] O.C. Zienkiewicz and R.L. Taylor. *The finite element method for solid and structural mechanics*. Elsevier, 2005.
- [63] R. Zoelly. *Ueber ein knickungsproblem an der kugelschale*. PhD thesis, ETH Zürich, 1915.